SELF-FITTING CRANIOMAXILLOFACIAL (CMF) BONE SCAFFOLDS WITH TUNABLE PROPERTIES

A Dissertation

by

MICHAELA R. PFAU

Submitted to the Office of Graduate and Professional Studies of
Texas A&M University
in partial fulfillment of the requirements for the degree of

DOCTOR OF PHILOSOPHY

Chair of Committee,	Melissa A. Grunlan
Committee Members,	Duncan J. Maitland
	Daniel L. Alge
	W. Brian Saunders
Head of Department,	Michael J. McShane

May 2021

Major Subject: Biomedical Engineering

ABSTRACT

The use of self-fitting scaffolds based on thermoresponsive shape memory polymers (SMPs) offers a potential solution to treat craniomaxillofacial (CMF) bone defects via regenerative healing. Porous SMP scaffolds were previously prepared by Grunlan and coworkers with poly(ε-caprolactone)-diacrylate (PCL-DA, M_n ~10 kg/mol). In this present work, the *in vivo* healing potential of PCL-DA self-fitting scaffolds was assessed using a rabbit calvarial defect model. The scaffolds did not impede bone tissue formation, and further showed successful peripheral tissue integration, both histologically and by push-out testing, when compared to a PEEK implant.

PCL-DA self-fitting scaffolds are limited by a slow degradation rate as well as a high transition temperature ($T_{trans} = T_{m,PCL}$ ~55 ºC) required for press-fitting. To accelerate degradation, a semi-interpenetrating (semi-IPN) scaffold composition was previously prepared with PCL-DA and poly(L-lactic acid) (PLLA, M_n ~ 15 kg/mol) (75/25 wt%). Herein, osteogenesis of human mesenchymal stem cells (hMSCs) *in vitro* was assessed for PCL-DA versus PCL-DA/PLLA semi-IPN scaffolds, both with and without a bioactive polydopamine (PD) coating. PD-coated scaffolds promoted hydroxyapatite (HAp) mineralization and the PD-coated PCL-DA/PLLA semi-IPN scaffolds exhibited enhanced osteogenic differentiation versus the PD-coated PCL-DA scaffolds. The accelerated degradation of PCL-DA/PLLA semi-IPNs was explored by substituting PLA-based thermoplastic polymers of varying molecular weight (M_n), crystallinity, and hydrophilicity. Degradation rates under base-catalyzed and neutral, non-catalyzed

conditions were correlated to annealing temperature and phase separation. To lower the SMP scaffold's T_{trans}, macromers with 4-arm star architecture were substituted into the PCL-DA/PLLA semi-IPN design. This resulted in a reduced T_{trans} ($T_{m,star\text{-}PCL}$ ~45 °C) for improved tissue safety during implantation, as well as a reduced macromer solution viscosity that was shown to improve fabrication of larger scaffolds via SCPL.

Lastly, PCL-DA-based SMP scaffolds were prepared as co-networks with poly(propylene fumarate) (PPF). Low M_n PCL and poly(D,L-lactic acid) (PDLLA) were used as macroinitiators to prepare compatibilized diblock PPF copolymers: PPF-PCL and PPF-PDLLA. These afforded facile incorporation into PCL-DA networks over analogous PPF homopolymers. These scaffolds uniquely exhibited tunable hydration while retaining mechanical properties throughout a 4-month non-catalyzed degradation study.

DEDICATION

To My Grandparents

Thank you for recognizing the curious scientist in me as a little girl and instilling in me the confidence needed pursue my dreams. I am so grateful for your love & support, and most of all, for your unwavering belief that I could.

ACKNOWLEDGEMENTS

First and foremost, I would like to thank my committee chair Prof. Melissa Grunlan. I am incredibly grateful for the opportunities she has made accessible to me and for her continued support throughout various challenges that I endured. It is difficult to put into words just how appreciative I am of the positive impact Prof. Grunlan has had on my life, but I thank her profoundly.

Next, I would like to thank my committee members Prof. Duncan Maitland, Prof. Daniel Alge, and Prof. Bryan Saunders who have each imparted their unique advice to me. Thank you to Prof. Maitland for offering research suggestions and collaborative opportunities, to Prof. Alge for future faculty mentorship, and to Prof. Saunders for encouraging me to think outside of my usual wheelhouse and many collaborative efforts.

I am also thankful to previous and current students in the Grunlan Lab family; I could not have asked for a better group of people to work with. Thank you to my best friend Ping Dong, my grad school experience would not have been the same without you. To my undergraduate students who contributed to work herein: Kelly McKinzey, Abbey Roth, Emily Rayer and Rabia Ali, thank you for your enthusiasm and all your hard work.

Last but certainly not least, I would like to say thank you to all my family members, including my best friend Alix and my family in-law, for your love and support throughout this endeavor. To my fiancé, Kevin Cloud, thank you taking on so much in order for us to reach this milestone, and for your optimism & enthusiasm toward supporting all of my career goals. I love you and am so excited for our future together!

CONTRIBUTORS AND FUNDING SOURCES

Contributors

This work was supervised by a dissertation committee consisting of Professor Melissa Grunlan [advisor] and Professors Duncan Maitland and Daniel Alge of the Department of Biomedical Engineering and Professor Brian Saunders of the Department of Small Animal Clinical Sciences.

In Chapter II, the *in vivo* studies were performed with Prof. Brian Saunders and microCT quantification/analyses used in Figures 2-9 and 2-10 were performed by Dr. Lauren Dobson, of the Department of Small Animal Clinical Sciences. The animal study was approved by the Texas A&M University IACUC (AUP 2015-0240/2018-0403). Gross examination and histological analyses used in Figures 2-6 and 2-8 were performed by pathologist Dr. Maureen O'Brien of Prof. Brad Weeks lab in the Department of Veterinary Pathobiology at Texas A&M. Biomechanical testing and corresponding statistical analyses used in Figure 2-11 were completed by Zachary Lawson, Dr. Andrew Robbins and Dr. Michael Moreno of the Mechanical Engineering Department at Texas A&M. In Chapter 3, all *in vitro* stem cell studies were performed by Ahmad Arabiyat under supervision of Dr. Mariah Hahn of the Department of Biomedical Engineering at Rensselaer Polytechnic Institute. Figures 3-2, and 3-9 to 3-12 and statistical analyses were also prepared by Ahmad Arabiyat. In Chapter VI, radial force testing (Figure 6-10-d) was performed by Lance Graul under the supervision of Prof. Duncan Maitland of the Biomedical Engineering Department at Texas A&M. The use of the Microscopy and

Imaging Center at Texas A&M is acknowledged for use of the Tescan Vega SEM, EDS analyses, and the Leica DM 6B for imaging used in Chapters III-VI.

All other work for the dissertation was completed by the student, under the advisement of Professor Melissa Grunlan of the Department of Biomedical Engineering.

Funding Sources

Graduate study was supported by a graduate teaching fellowship (GTF) from Texas A&M University. This work was made possible in part by the National Institute of Dental and Craniofacial Research (NIDCR) under 1R01DE025886-01A1 and the Texas A&M Engineering Experiment Station (TEES). Its contents are solely the responsibility of the authors and do not necessarily represent the views of the institutions.

TABLE OF CONTENTS

Page

LIST OF FIGURES

LIST OF TABLES

Page

1. INTRODUCTION

1.1. Overview

Smart scaffolds based on shape memory polymer (SMPs) have been increasingly studied in tissue engineering. The unique shape actuating ability of SMP scaffolds has been utilized to improve delivery and/or tissue defect filling. In this regard, these scaffolds may be self-deploying, self-expanding, or self-fitting. Smart scaffolds are generally thermoresponsive or hydroresponsive wherein shape recovery is driven by an increase in temperature or by hydration, respectively. Most smart scaffolds have been directed towards regenerating bone, cartilage, and cardiovascular tissues. A vast variety of smart scaffolds can be prepared with properties targeted for a specific tissue application. This breadth of smart scaffolds stems from the variety of compositions employed as well as the numerous methods used to fabricated scaffolds with the desired morphology. Smart scaffold compositions span across several distinct classes of SMPs, affording further tunability of properties using numerous approaches. Specifically, these SMPs include those based on physically cross-linked and chemically cross-linked networks and include widely studied shape memory polyurethanes (SMPUs). Various additives, ranging from nanoparticles to biologicals, have also been included to impart unique functionality to smart scaffolds. Thus, given their unique functionality and breadth of tunable properties, smart scaffolds have tremendous potential in tissue engineering.

1.2. Smart Scaffolds: Shape Memory Polymers (SMPs) in Tissue Engineering (TE)

1.2.1. Introduction

Shape memory polymers (SMPs) are a class of smart materials capable of responding to external stimuli with a shape change. This response encompasses shape fixity (deformation followed by fixation into a temporary shape), and shape recovery (a return to the original, permanent shape). Thermoresponsive SMPs, whose shape is modulated by application of heat, have been widely studied. The “netpoints” are chemical or physical crosslinks that determine the permanent shape whereas the “switching segments” maintain the temporary shape and recover the permanent shape when heated above their thermal transition temperature (T_{trans}). The T_{trans} may either be a glass transition temperature (T_g) or a melting transition temperature (T_m). Thus, a temporary shape formed by deformation at $T > T_{trans}$ can be fixed by cooling to $T < T_{trans}$ and subsequently recovered by heating to $T > T_{trans}$ again. For SMPs, the shape memory effect is entropically driven.[1-3]

The unique shape shifting capabilities of SMPs have been used toward advancing numerous biomedical applications.[4-11] In the 1940s, thermoplastic polymer resins with “elastic memory” were developed as dental fillings that could be thermally triggered to expand into tooth cavities.[12] Today, several FDA-approved SMP devices exist, including DYNACORD™ (a self-tightening suture),[13] Eclipse™ (a soft tissue anchor),[14] and Morphix® (an orthopedic suture anchor).[15] More recently, IMPEDE-FX, based on a shape memory polyurethane (SMPU) foam, was approved as an embolization plug. Crimped for catheter delivery, the foam plug undergoes shape recovery (i.e. expansion) within the vasculature as it is hydrated and warmed to body temperature.[16, 17] Bioresorbable SMPs have also been explored extensively, beginning with efforts to develop self-tightening sutures.[4] However, the interest in tissue engineering (TE) has prompted the exploration of biodegradable SMPs as smart scaffolds.[7, 18] Scaffolds play a critical role to regenerate healthy tissues lost to injury, disease, or congenital defects (**Figure 1-1**). Exogenous growth factors and/or pre-seeded cells are frequently incorporated into the scaffold to better promote neotissue formation. Scaffold chemical and physical properties have also been shown to potently direct cellular regeneration. Additionally, scaffolds with tailored mechanical properties and degradation profiles are sought to afford the necessary mechanical support and to match the rate of neotissue formation, respectively.[19-21] As smart scaffolds, SMPs offer unique and differentiating characteristics. Namely, this is related to their shape shifting ability, allowing them to fill tissue defects of varying and sometimes irregular geometries with fidelity. Most typically, the shape change is triggered by heat ("thermoresponsive"). Electrically conductive and magnetic scaffolds permit thermally-induced shape actuation via resistive heating and application of a magnetic field, respectively. [22, 23] Some SMP scaffolds that have appreciable hydrophilicity and water-absorbing abilities (e.g. hydrogels) undergo shape change in the form of swelling upon hydration ("hydroresponsive"). [24] In some cases, the absorption of water acts as a plasticizer to reduce the scaffold's T_{trans} (T_g), resulting in shape recovery.[25, 26] Herein, we highlight recent advances in the use of smart scaffolds with translational potential in TE.

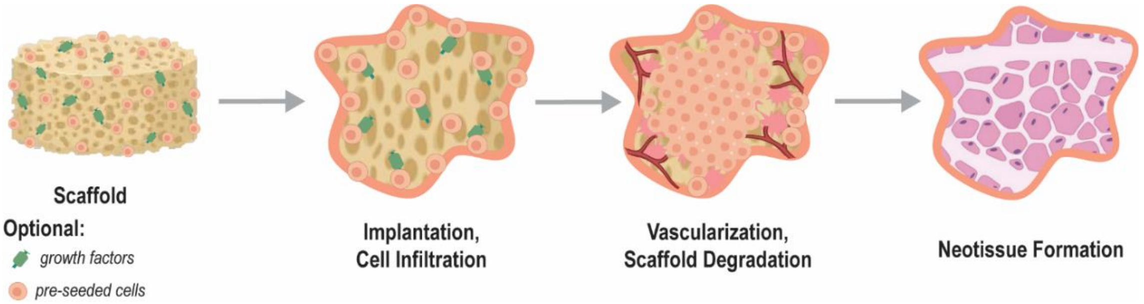

Figure 1-1. Schematic showing the general stages of tissue engineering (TE) whereby a highly porous scaffold, optionally loaded with growth factors and/or pre-seeded with cells, promotes tissue healing. Eventually the scaffold construct degrades and is replaced with healthy neotissue.

.

1.2.2. Smart Scaffold Functionality

Smart SMP scaffolds may be classified according to the nature of functional delivery into tissue defects afforded by shape memory behavior, including self-deploying, self-expanding, and/or self-fitting (**Figure 1-2**). These scaffolds leverage their shape fixity and recovery for their minimally invasive delivery, triggered volumetric filling, and/or conformal fitting within irregularly shaped spaces. SMP scaffolds afford the opportunity to achieve excellent contact with adjacent tissue, an integral aspect of tissue integration and healing. Filling of irregular spaces is a feature usually associated with *in situ* forming materials (e.g. bone cements, injectable hydrogels, etc.). However, these are associated with various limitations including exothermic cures, slow setting times, low pore interconnectivity, and shrinkage resulting in loss of contact with adjacent tissues. [27-35] In some cases, the permanent shape and size of the SMP scaffolds is designed to match that of the tissue defect. Alternatively, the SMP scaffold is of a generic geometry but is used to fill various and even irregularly shaped defects.

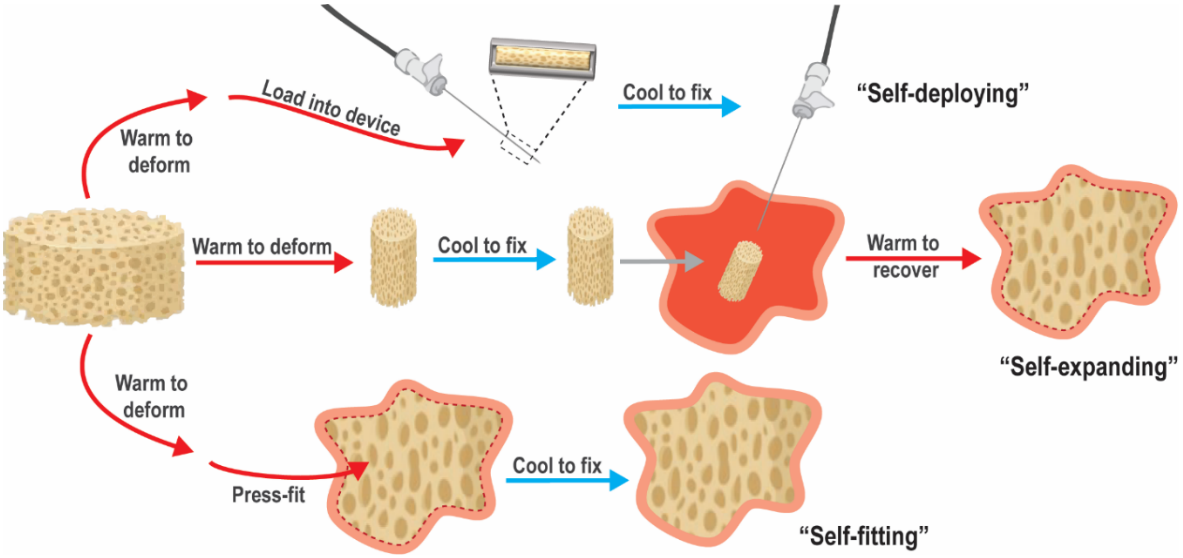

Figure 1-2. Classes of SMP scaffolds based on mode of delivery to tissue defect.

1.2.2.1. Self-Deploying Scaffolds

Smart SMP scaffolds that self-deploy are typically warmed to their T_{trans} to permit crimping into a compact geometry and subsequently cooled to fix this shape, affording loading into a catheter or needle. Thus, these shape fixed scaffolds can be delivered in a minimally invasive fashion. Self-deploying scaffolds typically have a T_{trans} near body temperature (T_{body} ~37 °C), such that upon delivery, the scaffold is triggered to shape recover (i.e. expand). Hydration that occurs after delivery can also trigger shape recovery.

1.2.2.2. Self-Expanding Scaffolds

While not delivered via minimally invasive techniques, self-expanding scaffolds also undergo shape recovery in tissue defects or voids. The scaffold, previously fixed in a relatively compressed shape, is triggered to expand within the tissue space via shape recovery. Likewise, shape recovery can be initiated by warming to T_{body} and/or hydration upon implantation.

1.2.2.3. Self-Fitting Scaffolds

Self-fitting scaffolds are often based on SMPs having a T_{trans} slightly above T_{body}. These may be warmed (e.g. with saline; $T > T_{trans}$) to cause softening, allowing the scaffold to be press-fitted into the tissue defect. Shape recovery then drives expansion of the scaffold within the defect, including those with irregular geometries. As the scaffold cools to T_{body} ~37 °C, it becomes shape fixed in this new geometry. If cooling occurs too rapidly to permit expansion to defect edges, irrigation with warm saline, if at an acceptably tissue-safe temperature, could be used to promote continued shape recovery. Hydration can also drive self-fitting of a SMP scaffolds into a defect, pending non-brittle mechanical properties permit press-fitting.

1.2.3. Smart SMP Scaffolds for Targeted Tissue Regeneration

The advantages associated with delivery, conformal fitting, and/or integration with surrounding host tissue make smart scaffolds excellent candidates for engineering a large variety of tissues (**Figure 1-3**). Most particularly, smart scaffolds have been evaluated for bone, cartilage, and cardiovascular tissue regeneration. Herein, we primarily highlight smart scaffolds that have been shown to support the differentiation and proliferation of human mesenchymal stem cell (hMSCs) and/or have advanced to *in vivo* studies.

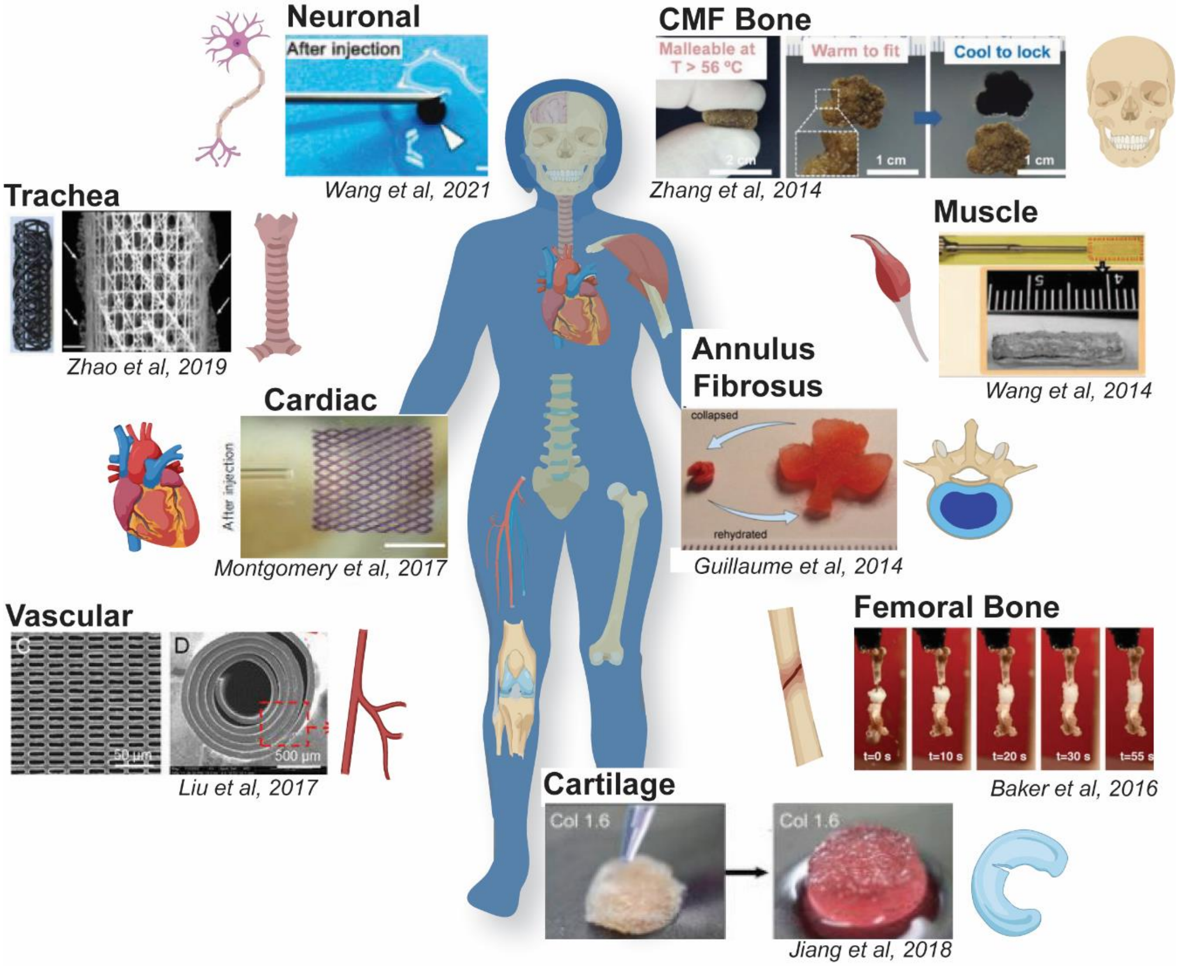

Figure 1-3. Utility of smart SMP scaffolds in the regeneration of various tissues.[36-44]

1.2.3.1. Bone Tissue

Several smart scaffolds have been developed for bone TE. SMPU scaffolds containing PCL and poly(L-lactic acid) (PLLA) soft segments were blended with poly(ethylene glycol) (PEG) or gelatin to adjust viscosity for fused deposition modeling (FDM) fabrication. Due to water uptake by the PEG or gelatin, the T_{trans} ($T_{g,\ PLLA}$ ~50 °C) was lowered via plasticization to T_{body}, affording a self-expanding scaffold. These scaffolds supported osteogenesis of hMSCs, which was further enhanced via incorporation of superparamagnetic iron oxide (SPIO) nanoparticles (NPs).[45] Another SMPU, prepared using 6-arm star PLLA with an aniline trimer incorporated for electroactivity, showed improved osteogenic differentiation of myoblasts versus those prepared without aniline.[46] SMP films based on UV-curable PCL-dimethacrylate (MA) (PCL-MA) ($T_{trans} = T_{m,\ PCL}$ ~54 °C) supported hMSC differentiation into osteoblasts, even following thermally-triggered shape recovery.[47] Using solvent casting particulate leaching (SCPL), PCL-based scaffolds were prepared with diol-terminated PCL, dextran, and a carbodiimide linker, and then coated with bioactive hydroxyapatite (HAp) via solution precipitation. By adjusting the PCL/dextran ratio, the T_{trans} ($T_{m,\ PCL/dextran}$) was adjusted to ~ T_{body} to support self-expansion, and the scaffolds were shown to support bone MSC (BMSC) osteogenesis. *In vivo* degradation was also monitored in a rat subcutaneous model, and scaffolds were shown to degrade fully within ~6 months.[48]

Other bone TE smart scaffolds have been developed for more targeted scenarios. We have reported self-fitting scaffolds for treatment of irregularly-shaped craniomaxillofacial (CMF) bone defects. PCL-diacrylate (PCL-DA) scaffolds ($T_{trans} = T_{m,\ PCL}$ ~55 °C) were prepared via SCPL with a fused salt template for pore interconnectivity, and subsequently coated with a bioactive polydopamine coating.[37] Scaffolds exhibited HAp mineralization *in vitro*, and, when modified with a cell adhesive peptide, were shown to support osteogenic hMSC differentiation.[49] Intended to treat femoral segmental bone defects, self-expanding scaffolds were prepared from acrylate monomers and a crosslinker (tetraethylene glycol dimethacrylate) using SCPL. The ratio of tert-butyl acrylate (tBA) and butyl acrylate (BA) (92:8 wt%) was tuned to achieve a $T_{trans} \sim T_{body}$. These scaffolds were fixed into a compressed shape, and subsequent irrigation with 45 °C saline triggered scaffold expansion into a mouse femoral defect. Overall, these SMP grafts showed integration with native bone after 12 weeks, and torsional mechanical properties comparable to an allograft.[43] To treat a confined femoral bone defect, a PCL-HAp SMP scaffold ($T_{trans} = T_{m,\,PCL} \sim 40$ ºC) was prepared via gas foaming. A shape fixed, compressed scaffold was implanted into a rabbit femoral defect, where irrigation with warm saline prompted self-expansion. After 12 weeks, bone ingrowth at the periphery and neovascularization was observed.[50]

1.2.3.2. Cartilage Tissue

Several smart scaffolds have been designed to repair cartilage, including the various types found in joints, ears, intervertebral discs, and trachea. Many of these are hydrogels and so are hydroresponsive. Targeted for articular cartilage repair, a self-expanding alginate gel, cross-linked via carbodiimide chemistry, was prepared with aligned pores via directional freezing. These scaffolds exhibited robust mechanical properties and were capable of reversible compression. Aligned pores allowed for improved collagen deposition by cultured hMSCs and was further improved with a Type II collagen coating.[51] Another self-expanding hydrogel scaffold, prepared with collagen or denatured collagen and a carbodiimide cross-linker, was used to treat full thickness defects in the knee joints of NZ white rabbits. These smart scaffolds, optionally pre-seeded with chondrocytes, promoted cartilage and subchondral bone repair. Smart scaffolds were prepared via SCPL using poly(glycerol sebacate) (PGS) and poly(1,3-propylene sebacate)

(PGS) as well as bioactive kartogenin (KGN). These acellular scaffolds could be prepared with a broad T_{trans} ($T_{m, PGS}$ ~35-45 ºC), and so exhibited excellent shape recovery at T_{body} as well as supported chondrogenic differentiation of BMSCs. Furthermore, acellular scaffolds were self-deployed into full-thickness defects of the rat femoropatellar groove where they supported chrondrogenic differentiation and formation of neocartilage.[44] A smart scaffold was developed to mimic the complexly shaped auricular cartilage of human ears. PLLA threads were woven into mesh tubes that, upon heating above the T_{trans} ($T_{g, PLLA}$ ~60 °C), could be molded into helical shapes like those of human ears. These scaffolds were seeded with cartilaginous particles derived from human pluripotent stem (iPS) cells and implanted subcutaneously into a mouse model where the shape and cartilage features were maintained for one year.[52] For tracheal repair, a smart scaffold was prepared from a PLLA iron-oxide (Fe_3O_4) nanocomposite ($T_{trans} = T_{g, PLLA}$ ~ 65 °C) using FDM. The Fe_3O_4 NPs were shown to permit magnetically-induced thermal actuation when exposed to a 30 kHz alternating magnetic field.[38] Targeted for the repair of annulus fibrosus (AF) tissue in herniated intervertebral discs, a hydroresponsive, alginate/carbodiimide-linked self-expanding hydrogel scaffold was evaluated. These were shown to support AF cell proliferation and adhesion with extracellular matrix (ECM) secretion after 21 days in culture with transforming growth factor beta 3 (TGF-β3) supplementation.[41]

1.2.3.3. Cardiovascular Tissues

Smart scaffolds have been frequently directed towards cardiovascular TE, including in the form of cardiac patches, vascular grafts, and vascular wraps. Smart cardiac patches were prepared from a soybean oil epoxidized acrylate network as thin film with complex porous micropatterns using stereolithography. These patches were designed to be self-expanding (T_{trans} ~ T_{body}) and were shown to support hMSC cardiomyogenic differentiation.[53] To permit minimally invasive delivery, a smart scaffold was prepared as an injectable cardiac patch from elastic poly(octamethylene maleate (anhydride) citrate)) microfabricated with a diamond-shaped lattice which drives shape recovery. These smart patches were seeded with rat cardiomyocytes (CMs) and were self-deployed (i.e. injected) into a myocardial infarction rat model where they were shown to increase wall thickness. The same type of cardiac patches, but seeded with human stem cell derived CMs and scaled up in size, were also successfully delivered via minimally invasive surgical techniques into a porcine model.[40]

Smart scaffolds have also been utilized to prepare vascular grafts. A 6-armed poly(ethylene glycol)-PCL-acrylate (PEG-PCL-Ac) was melt casted and UV-cured over a mold to afford micropatterned pores of different geometries on each side. To permit minimally invasive delivery, the scaffold (T_{trans} ~ T_{body}) was shape fixed into a tightly rolled conformation and expansion (i.e. shape recovery) triggered by body temperature. These were successfully implanted into the cervical artery of NZ white rabbits and supported endothelial cells (ECs) on the surface with vascular smooth muscle cells (VSMCs) on the inner surface.[42] A smart vascular scaffold based on 4D-printed biodegradable poly(glycerol dodecanoate)-Ac (PGD-Ac) exhibited a tunable T_{trans} (20-37 °C), depending on the duration of thermal curing. In this way, the scaffold was successfully implanted as a self-expanding vascular graft into a mouse aorta and supported endothelial and smooth muscle cell proliferation.[54] A perivascular smart wrap based on PCL-*co*-(α-allyl carboxylate ε-caprolactone) (PCL-*co*-ACPCL) was UV-cured into a film and then porated via laser ablation. Following implantation into mouse subcutaneous tissue, the microporous scaffolds showed upregulated neovascularization, fibrogenesis, and angiogenesis. Having a $T_{trans} \sim T_{body}$, these scaffolds are expected to actuate upon implantation to afford self-wrapping.[55]

1.2.3.4. Other Tissues

For skeletal muscle, a freeze-dried alginate/carbodiimide-linked self-deploying hydroresponsive scaffold was delivered via minimally invasive techniques in a severe skeletal muscle mouse injury model. The dehydrated scaffold was loaded into a needle and the syringe then filled with myoblasts and growth factors (e.g. insulin-like growth factor 1 (IGF-1) and vascular endothelial growth factor (VEGF)) to improve cell engraftment and muscle contraction.[39] To treat neuronal tissue damage caused by severe ischemic stroke, hydroresponsive scaffolds based on carbon nanotube (CNT)-doped silkworm sericin were prepared with geometries to match that of an irregularly-shaped cavity in an ischemic stroke mouse model. Following pre-seeding with BMSCs, these scaffolds were delivered via minimally invasive procedures and were shown to support neuronal differentiation.[36]

1.2.4. SMP Materials, Scaffold Fabrication Considerations and Property Tunability

As evidenced by the many smart scaffolds evaluated for various TE applications, a variety of SMP materials have been utilized (**Figure 1-4**). All SMPs must include two functional design elements: netpoints (responsible for the memorized shape or "shape recovery") and switching segments (responsible for the temporary programmed shape or "shape fixity"). These elements can be achieved via differing network designs, including physically cross-linked, chemically cross-linked, or PUs, which may rely on physical and/or chemical cross-linking. Variations of each of these affords additional tunability of shape memory behavior, and important material properties (e.g. modulus, and degradation rate). Moreover, fabrication methods can be used to further enhance SMP scaffold efficacy.

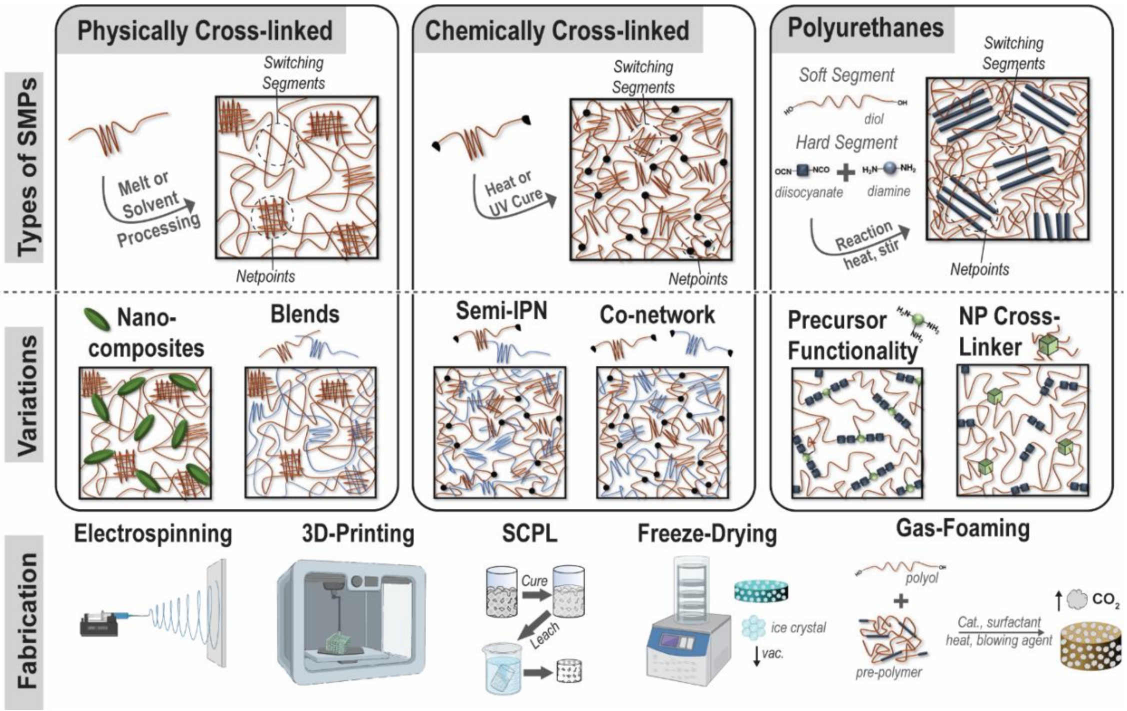

Figure 1-4. (top) Classes of SMPs used to prepare smart scaffolds: physically cross-linked, chemically cross-linked, and PU systems. (middle) Variations to these main SMP classes that afford property tunability. (bottom) Different fabrication methods used to achieve smart scaffolds with targeted morphological features.

1.2.4.1. Physically Cross-linked

As noted above, two examples of PLLA-based physically cross-linked smart scaffolds were developed toward the regeneration of ear cartilage and tracheal tissue. For thermoplastic PLLA, where crystalline lamellae serve as netpoints and amorphous chain segments act as switching segments. Typically, T_g of PLLA (T_g ~ 50-65 °C, depending on molecular weight)[56] serves as the T_{trans}, and so body temperature cannot trigger shape recovery. However, this T_{trans} range is ideal for maintaining a fixed shape upon implantation, as for Uto's ear regeneration study.[52] Alternatively, incorporating magnetic nanoparticles, as in the tracheal scaffold study, can provide remote shape actuation of PLLA-based smart scaffolds.[38]

Physically crosslinked SMPs may be refined via copolymerization, formation of nanocomposites, and by blending. Poly(D,L-lactide)-*co*-trimethylene carbonate (PDLLA-TMC) and poly(lactide-glycolide)-TMC (PLGA-TMC) copolymers were electrospun into scaffolds for bone and vascular TE, respectively. The TMC was used to tune the T_g to ~ T_{body} and physical cross-links were afforded by chain entanglements.[57, 58] Likewise, biodegradable amorphous poly(propylene carbonate) (PPC) exhibits shape memory (T_{trans} ~ T_g ~ 60 °C) that was shown to be enhanced following the addition of microfibrillated cellulose as a composite.[59] PLA-based composites have also been prepared with chitosan for potential antimicrobial activity[60] as well as with graphene for electrical SMP activation.[61] Blending PLA with PCL has been commonly used as a strategy to improve PLA toughness, and depending on the PLA/PCL weight percent, has also been shown to exhibit shape memory with PCL crystalline lamellae as the switching segment (T_{trans} ~

$T_{m,PCL}$ ~55 °C).[62] PLA/PCL blends have also been combined with nanohydroxyapatite (nHA) as bioactive nanocomposites.[63] Physically immiscible blends, like the PLA/PCL constructs, attain shape memory behavior due to phase separation, which allows one phase (PLA) to behave as the netpoints, while the other phase (PCL) behaves as the switching segment. PLLA has also been blended, but in a miscible system, with poly(3-hydroxybutarate-co-hydroxyvalerate) (PHBV) to lower T_{trans} toward T_{body} and PLLA/PHBV blends prepared as scaffolds via electrospinning were shown to support osteogenesis of BMSCs.[64, 65] Miscible PLLA/poly(methyl-methacrylate) (PMMA) blends have been shown to have a broad T_g that allows for triple shape memory.[66] PLLA/poly(vinyl acetate) (PVAc) blends were also shown to be miscible but the incorporation of nanohydroxyapatite (nHA) or graphene can lead to phase separation and induce triple shape memory via two distinct thermal transitions.[61, 67] The addition of nHA may also be advantageous to bone TE in providing an osteoconductive environment for mineralization, while nanocarbons like graphene may allow for electrical trigger of shape memory via resistive heating.

1.2.4.2. Chemically Cross-linked.

Various chemically cross-linked SMPs have been used to prepare smart scaffolds for TE, as noted above. In these systems, chemical cross-links act as netpoints while polymer segments between cross-links act as switching segment. Like physically cross-linked systems, shape memory can be actuated thermally and/or via hydration but chemically cross-linked systems tend to have more robust shape recovery. Acrylate (Ac)- or methacrylate (MA)-based networks, prepared from macromers with these terminal crosslinkable groups, have been commonly used toward both bone and cardiovascular TE.[37, 47, 49, 53, 55] These form networks comprised of crosslinks (i.e. netpoints) consisting of hydrolysable esters. Semi-crystalline PCL has been particularly utilized, since the T_m (~43-60°C) generally decreases with decreased molecular weight (M_n), the T_{trans} (T_m) may be tuned.[68] Additional modifications to PCL-network scaffolds can afford properties useful to regeneration. For instance, we have made numerous modifications to smart scaffolds for CMF defects formed from PCL networks using SCPL fabrication.[37, 69] To impart bioactivity, a polydopamine coating was applied to PCL-DA scaffolds.[49] In another approach, SMP scaffolds were likewise prepared as co-networks with macromers comprised of PCL and polydimethylsiloxane (PDMS) segments.[70] Attributed to the silicon-based and hydrophobic nature of the PDMS, these PCL-PDMS scaffolds exhibited HAp mineralization *in vitro*. Using a semi-interpenetrating network (semi-IPN) design based on PCL-DA and thermoplastic PLLA (75:25 wt%), scaffolds were also prepared with accelerated degradation and increased modulus.[71] Lastly, using a star-PCL architecture, we showed that the T_{trans} could be reduced to ~45 ºC ($T_{m,PCL}$) for improved tissue safety during thermally driven self-fitting. Cardiovascular TE scaffolds based on PGD-Ac networks represent another type of acrylate network with PGD switching segments having a T_{trans} ($T_{g,\ PGD}$) that can be readily tuned to ~T_{body} via cure time.[54] Acrylate-based networks have also been used to form other chemically crosslinked SMP scaffolds. These include bone TE scaffolds based on butyl-based monomers as well as soybean epoxidize acrylate. As noted above, the T_{trans} (T_g) can be tuned to ~ T_{body} with monomer ratio[43] and could also be formed with acrylated PEG to afford plasticization (i.e.

T_g lowering) due to hydration.[72] Similarly, methacrylate (MA) macromers were used to form PCL/PEG ("CLEG") co-network hydrogels with shape memory properties.[73] PTMC-MA macromers have also been used to form chemically cross-linked SMPs, and have been combined as nanocomposites with PLA fibers,[74] plasticized with PEG co-networks, and copolymerized with PDLLA to tune properties.[75] Chemical cross-linking moieties based on radical crosslinking can also be introduced into polymer repeat unit pendant groups or backbone. For instance, PCL-based copolymer having crosslinkable pendant allyl groups were used to prepare SMP scaffolds for vascular TE and whose T_{trans} (T_m) could be adjusted to ~ T_{body} based on the ratio of ε-caprolactone (CL) to α-allyl carboxylate-CL.[55, 76] Co-polyesters containing fumaric acid (FA) segments, bearing crosslinkable double bonds in the backbone, have been prepared as hydroresponsive scaffolds via SCPL.[77] SMP scaffolds for bone TE were recently prepared by 4D printing of poly(propylene fumarate) (PPF). These PFF scaffolds exhibited a tunable T_{trans} (T_g ~30-40 °C) depending on cure time.[78]

Chemically cross-linked networks have been prepared with other cross-linking chemistries as well. Examples include, PTMC cross-linked with a bis(cyclic carbonate) via ring opening polymerization (ROP),[79] PCL/PEG co-networks cross-linked via thiol-ene chemistry,[80] and alginate or collagen hydrogels cross-linked with via carbodiimide chemistry.[39, 41, 44, 48, 51, 81] Several other carbodiimide cross-linked hydrogel scaffolds were described earlier, often prepared via freeze-drying or lyophilization.[39, 41, 51] Smart hydrogel scaffolds have also been prepared as interpenetrating networks (IPN) cryogels consisting of covalently and permanently crosslinked polyacrylamide (PAAm) and covalently and dynamically crosslinked oligoethylene glycol (OEG)-based dendronized polymers. The Schiff-base cross-linking allow for dynamic, pH-modulated control over shape memory.[82]

1.2.4.3. Polyurethanes

SMPUs are a distinct class of widely studies SMPs, relying on physical cross-linking (thermoplastics) or chemical cross-linking (thermosets). SMPUs are generally characterized by thermodynamically immiscible soft segments (switching segments) and hard segments (netpoints). These are connected via urethane linkages formed through reactions of alcohol and isocyanate moieties. Chain extenders, low molecular weight diols (or diamines), may be reacted with diisocyanates to increase the length of the hard segments.[83] Thermoplastic PUs (TPUs) are formed into physically cross-linked PU scaffolds frequently via electrospinning or 3D-printing, where the molecular weight of these types of chains yields conducive rheological properties. TPUs have been modified in many common ways that have been previously described for other SMP systems, including: PCL-based co-polymers,[84, 85] PLA-based blends,[86, 87] bio-based (i.e. castor oil) precursors,[7] combining with hydrophilic polymers,[45] and nanocomposites. CNT,[88] HAp,[89] and iron-based NPs[86] seen in previous systems have been employed in TPUs. One nanocomposite SMP not previously discussed is a PLA-based TPU with nanosilicates, shown to induce HAp mineralization for bone TE.[90]

Chemically cross-linked SMPU porous scaffolds are frequently formed via gas foaming. In this process, pre-polymers with isocyanate moieties react with polyols to produce PU linkages, and carbon dioxide (CO_2) generation occurs as a by-product of the reaction between excess isocyanates and water. This process also usually employs a combination of catalysts, surfactants, heat, and blowing agents.[91, 92] Maitland et al. utilized gas foaming to create smart SMPU embolization devices,[25, 93, 94] including those that are modified with tungsten NPs for radio-opacity.[95] Other chemically cross-linked SMPUs have used NPs that are functionalized to act as chemical cross-linkers. For instance, oxidized CNTs[96] and star-shaped polyester having a polyhedral oligomeric silsesquioxane (POSS)core[97, 98] have been employed as multifunctional cross-linkers.

Polymers typically used to construct smart scaffolds and methods to achieve tunability of properties are summarized in **Figure 1-5**. In addition to thermoresponsive and hydroresponsive SMP scaffolds, another class of SMPs are elastomers that can be fabricated into mesh lattices (typically via 3D printing) whose geometries support SMP abilities, as previously noted for the cardiac patch example.[40, 99] To participate in cell-like signaling, other SMP scaffolds may leverage dynamic linkages, including those based on Schiff bases[82] and ionic chemistries. One major class of these are chitosan-based SMP systems as chitosan can crosslink via link via physical, chemical, or ionic linkages.[100, 101] The ionic linkages have the potential to be controlled by pH, [102] and so could be utilized to produce shape memory behavior.

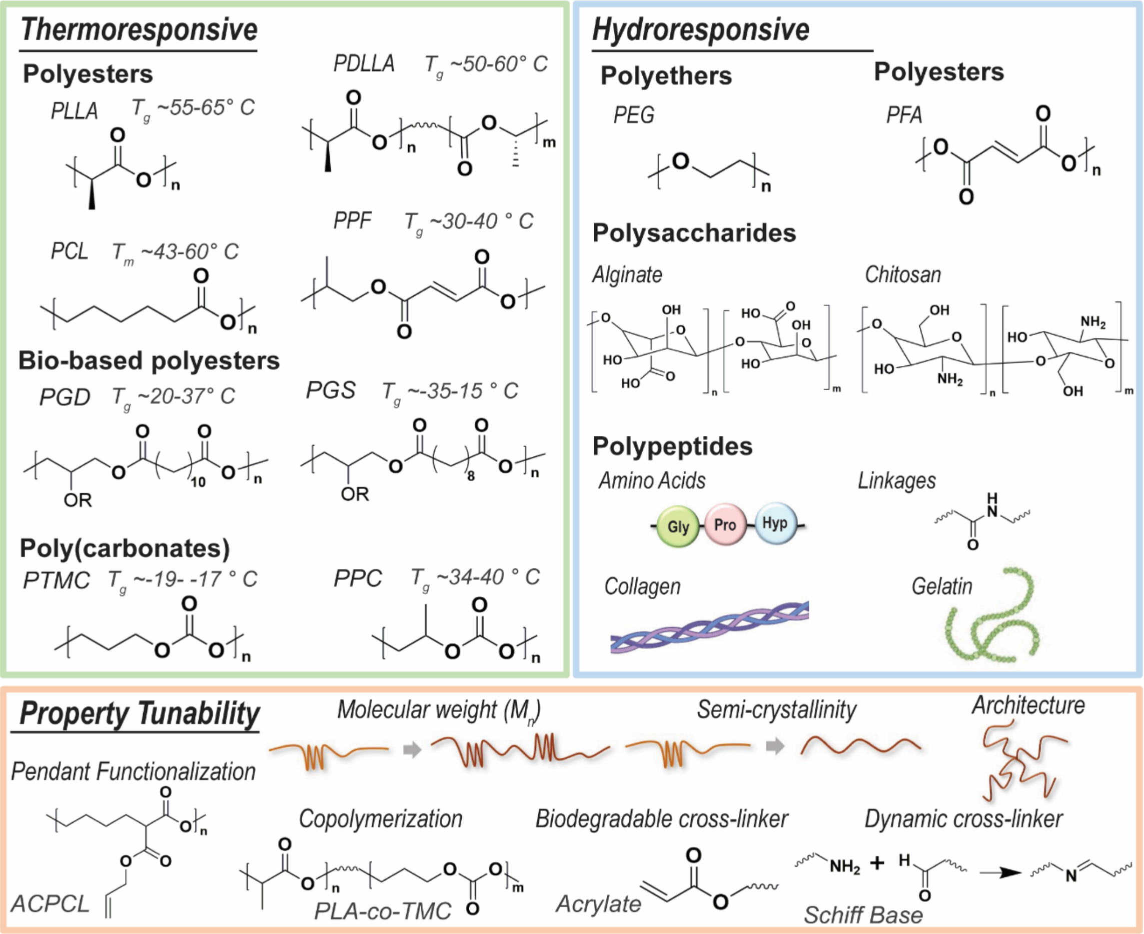

Figure 1-5. SMPs typically used to achieve smart scaffolds with thermoresponsive and/or hydroresponsive behaviors, and additional ways that SMP scaffold properties may be tuned.

1.2.5. Conclusions

Smart scaffolds based on thermoresponsive and hydroresponsive SMPs hold vast potential to advance the regeneration of numerous tissues, particularly bone, cartilage, and cardiovascular tissues. The shape memory ability of smart scaffolds has largely been leveraged to achieve tissue defect filling, either via self-deploying, self-expanding, or self-fitting. This unique feature affords convenient routes for implantation as well as superior scaffold-tissue contact to promote healing. More recently, the shape shifting ability of SMPs has been utilized to respond to cellular triggers[103] or for on/off switching of cell behavior (e.g. alignment and differentiation).[104-106] Such SMPs have the potential to create smart scaffolds with greater control over directing tissue regeneration. Collectively, SMP scaffolds possess a breadth of useful properties that afford further tunability through a variety of strategies. Smart scaffolds are based on several classes of SMPs, and include physically cross-linked, chemically cross-linked, and SMPUs. Within each of these classes of SMPs, a variety of fabrication methods are also used to prepare smart scaffolds with specific morphological features. Additional functionality can be achieved with further modifications, such as the incorporation of additives (e.g. various NPs, growth factors, and antimicrobials), or application of coatings. Increasing evidence of the utility of smart scaffolds is supported by a growing body of work with cultured stem cells as well as with animal models. Thus, the development of smart scaffolds is making promising headway towards clinical translation in regenerative engineering.

2. PRE-CLINICAL EVALUTAION OF SELF-FITTING PCL SCAFFOLDS IN RABBIT CALVARIAL DEFECTS

2.1. Overview

Self-fitting scaffolds composed of cross-linked poly(ε-caprolactone)-diacrylate (PCL-DA) have been developed for the treatment of craniomaxillofacial (CMF) bone defects. These scaffolds possess the requisite properties for successful bone healing including porosity, biodegradability, and the ability to achieve a conformal fit within the defect via thermoresponsive shape memory polymer (SMP) behavior. Here, a preclinical *in vivo* study was performed using 12 New Zealand white rabbits (three groups of four animals) with 8 mm diameter non-critical bilateral calvarial defects. The SMP scaffolds were implanted and were compared to untreated defects; healing was assessed at 4 and 16-weeks using histology to examine bone formation. Quantification of bone volume and surface area from microCT yielded no significant differences between the SMP scaffold and untreated defect, showing that the SMP scaffolds do not impede bone growth. For the 16 week group, poly(ether ether ketone) (PEEK) samples were also compared to the PCL-DA SMP scaffolds using a biomechanical push-out. SMP scaffold stiffness was improved by 85.3 N/mm and failure was improved by 85.7 N compared to the PEEK control. These superior biomechanical properties correspond to histology and microCT data and may be attributed to successful osseointegration imparted by the SMP scaffolds self-fitting ability.

2.1.1. Statement of Significance

This study was intended to assess the performance of the self-fitting PCL scaffolds *in vivo* CMF bone healing potential for the first time. For this reason, a pilot study was performed herein to gain an initial understanding of scaffold biocompatibility, and quantity/quality of bone ingrowth over time. In addition to establishing scaffold implantation viability, the PCL scaffolds showed **(1)** evidence of osteoconduction, **(2)** favorable interactions with surrounding tissue, and **(3)** enhanced implant stability due to successful osseointegration. Moreover, the self-fitting PCL scaffolds support improved CMF bone healing and may offer distinct advantages over existing devices on the market.

2.2. Introduction

Confined, craniomaxillofacial (CMF) bone defects arise from a variety of clinical scenarios, including trauma, tumor resection, congenital deformities, surgical burr holes, or craniotomy.[107] Their prevalence is significant, and in the USA, annually include >400,000 facial fractures [108] and 1 in every 1,700 live births.[109] As a result, the global CMF device market was valued at 1.6 billion USD in 2020 and is predicted to grow 9.0% annually.[110] It was previously reported that over 6% of a total of 1.6M bone grafts implanted annually were craniofacial bone grafts.[111] Indeed, autografting remains the "gold standard" of treatment, despite numerous drawbacks, including surgical harvesting, donor site morbidity, and limited availability.[112-116] Additionally, CMF defects frequently exhibit irregular geometries, such that rigid autografts are difficult to shape and position within the defect, often resulting in insufficient bone-to-graft contact and subsequent graft resorption.[117-119]

The limitations of autografting have prompted alternative approaches, particularly those based on biomaterials that can achieve a conformal fit.[113, 114, 120, 121] Capable of *in situ* cure, bone cements and putties that are typically comprised of poly(methyl methacrylate) (PMMA) and a bioactive glass or glass ceramic filler emerged in the 1940s.[33, 122-125] These are limited by their slow setting times, brittle nature (leading to post-surgical fracture), and exothermic cures as high as 90 ºC (leading to tissue necrosis). Moreover, a lack of porosity and biodegradability prohibits regeneration of bone tissue within the defect. Patient-specific implants (PSIs) have more recently been developed, wherein an implant matching the defect geometry is created by preoperative processing a patient's CT-scans, computer-aided design (CAD) of a virtual implant, and 3D printing of the actual implant.[126-130] Polyetheretherketone (PEEK) is most often utilized, favored due to its similar mechanical properties to bone tissue (e.g. modulus and yield strength). However, in addition to the time intensive process to prepare PEEK CMF PSIs, the lack of porosity and biodegradable can lead to pore integration with adjacent bone and furthermore does not lead to tissue regeneration throughout the defect.

Tissue or regenerative engineering is a promising alternative to treat CMF bone defects.[131, 132] The scaffold plays an essential role to the success of this approach and must exhibit key properties, including: (1) biodegradability and interconnected pores for osteoconduction, (2) mechanical robustness to prevent collapse or brittle fracture, and (4) conformal fit within the defect to permit osseointegration. To achieve conformal fitting, *in situ* forming scaffolds are most often evaluated but generally suffer from exothermic cures, insufficient porosity and pore interconnectivity, brittleness, and post-cure shrinkage resulting in diminished tissue contact.[29, 133, 134]

To address this unmet need in CMF bone regeneration, we have reported “self-fitting” shape memory polymer (SMP) scaffolds based on biodegradable poly(ε-caprolactone)-diacrylate (PCL-DA).[37, 135] The crystalline lamellae (T_m or “T_{trans}” ~55 ºC) serve as the switching segments and the crosslinks form the netpoints. Thus, the porous scaffold becomes malleable when exposed to warm saline or air (T ~55 ºC) due to the lamellae melting. This allows the scaffolds to be press-fit into regular- or irregularly-shaped defects, wherein shape recovery promotes scaffold expansion to the perimeter. With cooling ($T < T_{trans}$), the lamellae recrystallize and the scaffold undergoes shape fixity, locking it in its new shape within the defect. In addition to the conformal fit and perimeter contact (for osseointegration) afforded by the scaffold’s shape memory behavior, several other beneficial properties were also realized. Fabrication using solvent-casting particulate leaching (SCPL) with a fused salt template produced scaffolds with pores sizes associated with osteogenesis and also as pore interconnectivity for cellular and neotissue infiltration.[136] The scaffolds were mechanically robust, and lacked brittleness, withstanding 85% strain without fracture.[70, 71, 137] PCL-DA scaffolds were also shown to be non-cytotoxic and to support the adhesion and proliferation of human osteoblasts.[37] However, upon coating the scaffolds with a bioactive polydopamine coating, there was approximately a 5-fold increase in cellular adhesion and proliferation as well a 1.6-fold increase in expression of runX2. The polydopamine-coated scaffolds also formed deposits of hydroxyapatite (HAp) upon exposure to simulated body fluid (SBF, 1X). In subsequent studies, we demonstrated that the PCL-DA scaffolds could be fabricated with an incorporated cell adhesion peptide (NH_2-Arg-Gly-Asp-Ser-COOH; RGD).[49] When seeded with bone marrow-derived human mesenchymal stem cells (h-MSCs) and cultured in the absence of osteogenic supplements, polydopamine-coated scaffolds improved osteogenesis relative to uncoated scaffolds.

In this work, a pilot *in vivo* study was performed using a rabbit calvarial defect model to assess the healing potential of these "self-fitting" PCL-DA scaffolds (**Figure 2-1**). To assess the inherent bone healing capacity of the scaffold, a cell adhesive peptide and a polydopamine coating, were both excluded. Furthermore, exogeneous cells and growth factors were also not included. In this way, the scaffold represents a biologic-free and bioactive coating-free, off-the-shelf surgical product. A rabbit calvarial defect model is well-established the literature.[120, 138] Bilateral calvarial defects (d ~8 mm) were created in New Zealand white rabbits. While not critically sized, this scenario enabled us to assess scaffold osseointegration and neotissue infiltration along the perimeter. Moreover, it reduced the number of animals utilized as two bilateral defects could be produced, rather than one central, critical-size defect (d ~15 mm). Using microCT and histological analysis, healing was assessed compared to untreated control defects at both 4- and 16- weeks. For the 16-week timepoint, a custom biomechanical testing system was used to conduct push-out force tests to assess osseointegration and implant stability compared to PEEK implant controls.

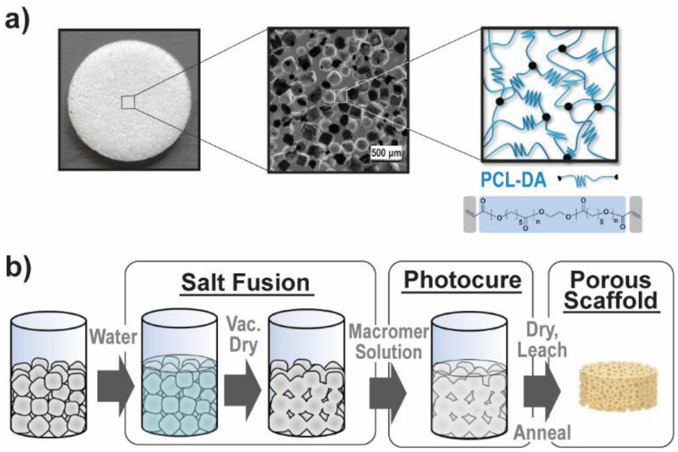

Figure 2-1. (a) SMP scaffold with interconnected pores made of 100% PCL-DA, prepared via (b) solvent casting particulate leaching (SCPL).

2.3. Materials and Methods

2.3.1. Materials

PCL-diol (M_n = 10 kg/mol per manufacturer specifications), 4-(dimethylamino)pyridine (DMAP), triethylamine (Et_3N), acryloyl chloride, potassium carbonate (K_2CO_3), anhydrous magnesium sulfate ($MgSO_4$), sodium chloride (NaCl, salt) 2,2-dimethoxy-2-phenyl acetophenone (DMP), 1-vinyl-2-pyrrolidinone (NVP), dichloromethane (DCM), and other solvents were purchased from Sigma-Aldrich. All solvents were dried over 4 Å molecular sieves prior to use and all reagents were vacuum dried overnight prior to use. Salt was sieved using an ASTM E-11 no.40 sieve with 425 µm openings; scanning electron microscopy (SEM) and ImageJ showed an average salt size of 460 ± 70 µm.

2.3.2. Device Development and Characterization

Self-fitting scaffolds with interconnected pores based on a PCL-DA SMP polymer network (Fig. 1a) were prepared via solvent casting particulate leaching (SCPL, Fig. 1d).

PCL-diol was functionalized according to an established synthesis to produce cross-linkable PCL-DA, which was then used to fabricated porous scaffolds via an established SCPL protocol.[69] Fused salt templates were prepared using 20 mL vials filled with 10.0 g of sieved salt and 7.5 wt % DI water; the templates were centrifuged (3,220 x g, 15 min) and then dried under vacuum overnight prior to use (30 in. Hg, RT). Macromer solution was prepared using 0.15 g of PCL-DA per mL of DCM with 15 vol % photoinitiator (10 wt % DMAP in NVP) and was added to cover each salt template (~5 mL). Centrifugation (1,260 x g, 10 min) was used to promote precursor solution diffusion throughout the fused templates, and then scaffolds were cured via exposure to UV-light (UV-Transilluminator, 6 mW cm^{-2}, 365 nm, 5 min). Following solvent evaporation, scaffolds were soaked in aqueous solution to extract all salt porogens, and dried scaffolds were finally annealed (30 in. Hg, 85°C, 1 h). The resulting porous scaffolds were then sliced to size using a vibratome (either 1 or 2 mm thick) and were finally biopsy punched to a diameter of 9 mm (**Figure 2-2**).

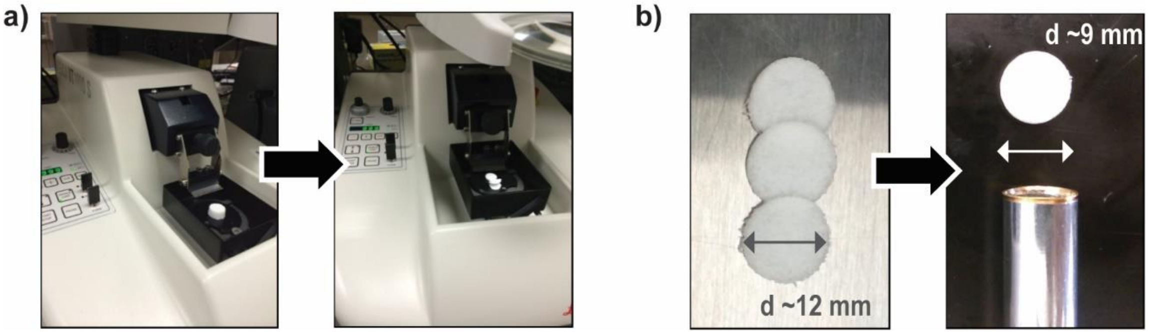

Figure 2-2. (a) Annealed scaffolds were sliced to desired thickness using a vibratome, and (b) were punched to desired diameter to prepare finalized specimens.

These PCL-DA scaffolds have been in development for over 5 years, and as such their material properties have been thoroughly characterized in numerous studies.[37, 69, 71, 137] In this work, the focus was on implantation *in vivo*, so several key scaffold properties were monitored before and after sterilization via gamma-irradiation (KLS Martin). Differential scanning calorimetry (DSC, TA Instruments Q100, N=3, 5 °C/min, RT to 200 °C) was used to determine PCL melting temperature ($T_{m,PCL}$ is related to scaffold T_{trans}), and the enthalpy of fusion was used to calculate % crystallinity.[71] TA Universal Analysis software was used to determine the T_m onset, T_m midpoint and PCL enthalpy of fusion (ΔH_m). Static compressive properties were determined using an Instron 3345 (N=3, 1.5 mm/min); modulus (E) and compressive strength (CS) at 85% strain (ε) were determined from the resultant stress-strain curves. Scaffold % porosity (N=3) was calculated via gravimetrically determining the density of porous scaffolds compared to analogous solid films (ρ =1.19 g/mL) according to Equation 1:

$$Porosity\ (\%) = \frac{\rho_{solid\ film} - \rho_{porous\ scaffold}}{\rho_{solid\ film}} * 100 \qquad (1)$$

Scaffold "self-fitting" or shape memory properties were also examined qualitatively using a plastic model calvarial defect (UHMWPE, d ~8 mm). While the SMP scaffolds have also been characterized in *in vitro* stem cell studies,[49] no cell work was performed and no biologics were added to the scaffold because this was a preclinical study intended to assess the scaffolds healing potential as an off-the-shelf (ie. biologic-free) device. Instead, the PCL scaffold was assessed biomechanically in the final animal group versus a poly(ether ether ketone) (PEEK) implant device. Slabs of PEEK were provided by KLS Martin and were milled to the desired thickness (t ~2 mm), and CNC was used to cut the

PEEK to the desired diameter (d ~7.5 mm). The PEEK samples were sterilized via ethylene oxide (Anderson Anproline Sterilisation Cabinet, AN-74i).

2.3.3. *In Vivo* Implantation

This study was approved by the Texas A&M University IACUC (AUP 2015-0240/2018-0403). SMPs were prepared as previously described (9 mm diameter x 1 mm height; 9 mm diameter x 2 mm height) and gamma sterilized prior to surgery (KLS Martin). Six-month-old New Zealand White rabbits (n=4 rabbits/treatment group) were anesthetized using 40 mg/kg ketamine, 5 mg/kg xylazine, and 0.05 mg/kg acepromazine administered intramuscularly. Following induction, 0.12 mg/kg buprenorphine sustained release (Simbadol™ Zoetis) and 2 mg/kg carprofen (Rimadyl® Zoetis) were administered subcutaneously for analgesia. Additionally, 5 mLs/kg Lactated Ringer's solution was administered subcutaneously. A surgical plane of anesthesia was maintained via isoflurane mask inhalation (1-3%, to effect). The hair coat of the dorsal aspect of the skull was clipped and removed and then aseptically prepared using alternating scrubs of 7.5% betadine and sterile saline solutions.

A 4 cm skin incision was created along the midline of the skull. The periosteum was carefully incised and elevated and retracted with Gelpi retractors. Bilateral calvarial defects were created in the parietal bones with an 8.0 mm diameter trephine burr (Ace Surgical Supply, Brockton, MA) under saline irrigation, with one defect positioned on either side of midline. To ensure proper placement, defects were created 1 to 2 mm from the sagittal and coronal sutures in all rabbits. The defects were treated with one of three treatment conditions: (1) untreated control, (2) PCL-DA, or (3) PEEK. PCL-DA SMPs or

PEEK samples were implanted into right calvarial defects. Left calvarial defects served as untreated controls. For the SMP implantation, individual SMPs were briefly placed in a sterile 55°C saline bath for 2-4 minutes during defect drilling. The PCL-DA SMPs were assessed manually to ensure a malleable state, followed by brief wicking of warm saline away from the SMP and placement into each defect. In some instances PCL-DA implants were adjusted using sterile cotton tip applicators until they cooled and locked into position. The surgical site was lavaged and routine closure of deep tissues was performed using 3-0 Monocryl in a simple continuous patterns. Skin was closed in a single layer using 4-0 Monocryl in an intradermal pattern. The 12 rabbits were divided into three treatment groups (4 rabbits/group). Group I rabbits received 9 mm x 1 mm PCL-DA SMPs and was terminated at 4 weeks. Group II rabbits received 9 mm x 2 mm PCL-DA SMPs and was terminated at 4 weeks. Group III rabbits received 9 mm x 2 mm PCL-DA (2 rabbits) or 8 mm x 2 mm PEEK implants (2 rabbits) and were terminated at 16 weeks. At termination, rabbits were first sedated using ketamine, xylazine, and acepromazine as described above, followed by euthanisia with 100 mg/kg pentobarbital sodium (Euthasol® Virbac, Carros, France). Decapitation was performed post-mortem and skulls were submerged in 10% neutral bufferered formalin at a minimum of 1:10 tissue to formalin ratio.

2.3.4. Gross Examination, Histology and microCT

Gross dissection, histology, and microCT was performed on a fee-for-service basis by the Cardiovascular Pathology (CVP) Laboratory at Texas A&M University. Prior to manipulation, calvaria were assessed via microCT. Samples for each group were scanned using the NSI X50 micro-CT (North Star Imaging, Rogers, MN). Calvarial defects and adjacent healthy calvaria were excised using a Mopec Stryker Saw (Oak Park, MI). Calvarial samples were decalcified in Formical-4 solution (Company, çity, state) and processed for histological evaluation by routine 5 micron thick sections and H&E or Masson's trichrome stains. Calvaria were assessed using qualitative and quantitative observations by a board-certified veterinary pathologist.

2.3.4.1. Quantification of Bone Volume and Surface Area

Upon completion of microCT, quantification of bone formation was performed using. Mimics 20.0 (Materialise, Plymouth, MI). Untreated control defects were used to optimize reconstruction parameters, and Hounsfield units (HU) were set between 24,518-34,952 HU for all reconstructions. New bone formation within the surgical defect was quantified by first generating a digital cylinder (8 mm diam.) within each defect. Tissue within each cylinder was thresholded using 24,518-34,952 HU to quantify bone volume (mm^3) and surface area (mm^2).

2.3.5. Biomechanical "Push-Out" Testing

A custom 3D printed clamp with 9.5 mm thru hole was affixed around the defect on the sample and centered under a flat-bottomed 7.5 mm diameter stainless steel push-out rod which was attached to the end of the linear actuator on the custom biomechanical testing system (**Figure 2-3**). Displacement was zeroed at 5 N compressive preload then advanced at a rate of 5 mm/min (0.0083 mm/s).[139] Force and displacement were measured with 100 lbf (444 N) load cell and 2 inch stroke linear variable differential transformer (LVDT), respectively. Failure load (N) and stiffness (N/mm) were calculated from the resulting load-extension curve, with stiffness defined as the slope of the linear regression obtained from the most linear portion of the load-extension curve.

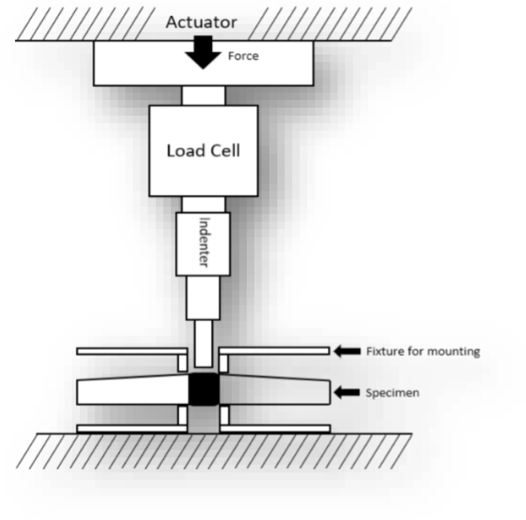

Figure 2-3. Custom biomechanical testing apparatus.

2.3.6. Statistical Analysis

For scaffold material characterization before and after sterilization, data were reported as the mean ± standard deviation. Values were compared using Student's *t*-test and a *p*-value $p<0.05$ was considered statistically significant. Bone quantification volume and surface area were reported as mean ± standard deviation. Bone healing data between untreated control defects and PCL-DA implants were analyzed within each group using GraphPad Prism using two-way ANOVA with Sidak's multiple comparisons post-hoc test. Significance was established at $p<0.05$. For the biomechanical push-out test, both load to failure and stiffness were assessed using a paired t-test and difference of means (μ) was reported; a *p*-value of $p<0.05$ was considered statistically significant.

2.4. Results and Discussion

2.4.1. Device Characterization

"Self-fitting" or SMP PCL-DA scaffolds were successfully prepared at the desired geometry (t ~1 mm, d ~9 mm). These were intended to be slightly larger than the defect (d ~8 mm, **Figure 2-4-a**), to allow shape recovery to fully drive the scaffold toward the defect edges. The scaffolds were then sterilized via γ-irradiation and basic scaffold properties were characterized before and after to ensure high maintenance of desired properties prior to implantation (**Table 2-1**). As shown, key scaffold properties were not significantly altered due to sterilization: PCL T_m ~52-58 °C & crystallinity ~60% (essential for "self-fitting" capabilities), robust mechanical properties E ~20 MPa and CS ~26 MPa, and ~70% porosity were all maintained. Scaffold SMP behavior was assessed qualitatively using a plastic model defect and was also not shown to be impacted by sterilization (**Figure 2-4-b**).

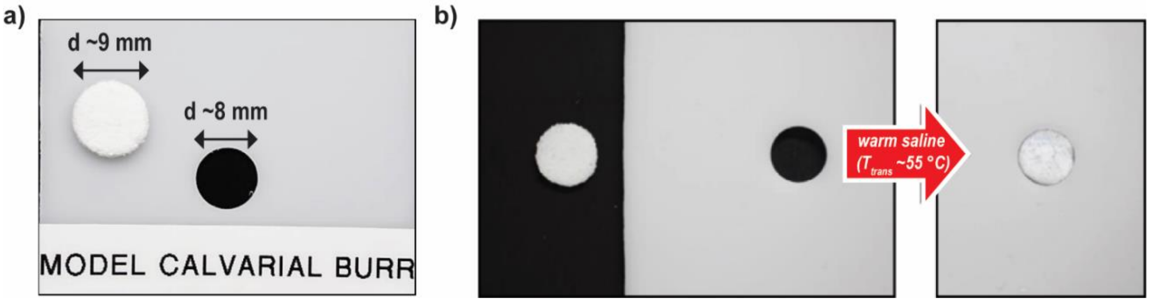

Figure 2-4. (a) Scaffold diameter was designed to be slightly larger than the defect, and (b) SMP or self-fitting properties were maintained after sterilization, as shown here using a plastic model defect.

Table 2-1. Scaffold properties were well-maintained following sterilization.

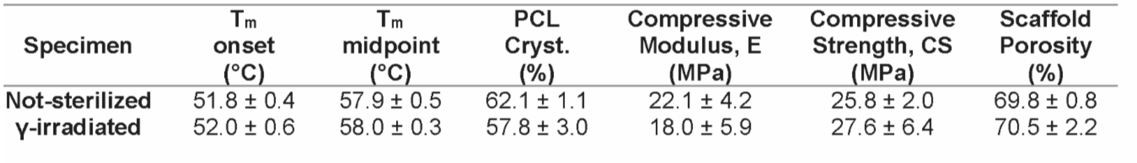

Specimen	T_m onset (°C)	T_m midpoint (°C)	PCL Cryst. (%)	Compressive Modulus, E (MPa)	Compressive Strength, CS (MPa)	Scaffold Porosity (%)
Not-sterilized	51.8 ± 0.4	57.9 ± 0.5	62.1 ± 1.1	22.1 ± 4.2	25.8 ± 2.0	69.8 ± 0.8
γ-irradiated	52.0 ± 0.6	58.0 ± 0.3	57.8 ± 3.0	18.0 ± 5.9	27.6 ± 6.4	70.5 ± 2.2

2.4.2. Surgical Implantation

Following thorough material characterization, scaffolds were successfully implanted into bilateral cranial defects (d ~ 8 mm) of New Zealand white rabbits (**Figure 2-5**). Overall, the scaffold implantation via "self-fitting" or SMP behavior was successful as porous scaffolds were able to be easily press-fitted into the calvarial defects following exposure to warm saline. Subjectively, SMP implants (need to decide on consistency throughout manuscript – sometimes call them PCL-DA's, then SMPs, then PCL-DA SMPs) exhibited excellent thermoresponsive behavior, handling, and were readily implanted into calvarial defects. As expected, PEEK implants were more difficult to fit due to their rigid, fixed nature.

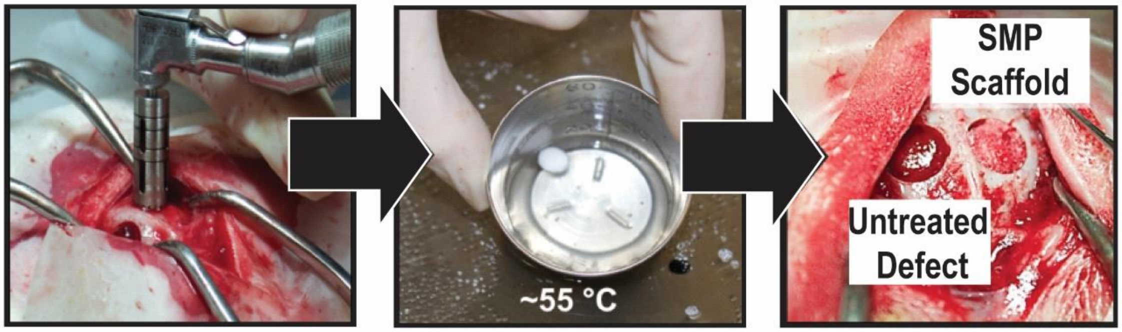

Figure 2-5. "Self-fitting" PCL-DA scaffolds were implanted via their thermoresponsive SMP property whereby warming to the T_{trans} permits scaffold softening allowing for facile press-fitting into the defect site.

2.4.3. Gross Examination and Histology

Gross examination of Group I specimens (**Figure 2-6-b**) showed no appreciable differences in cerebral tissue for the SMP scaffolds compared to the untreated defect control. Group I histology (**Figure 2-6-c**) revealed an expected amount of woven bone formation circumferentially around the defect controls. SMP scaffolds contained islands of woven bone circumferentially around each implant. There was evidence of scaffold bowing in Group I specimens. Scaffold thickness was adjusted from ~1 mm to ~2 mm for Groups II and III which was shown to have improved fitting in a plastic model defect (**Figure 2-7**).

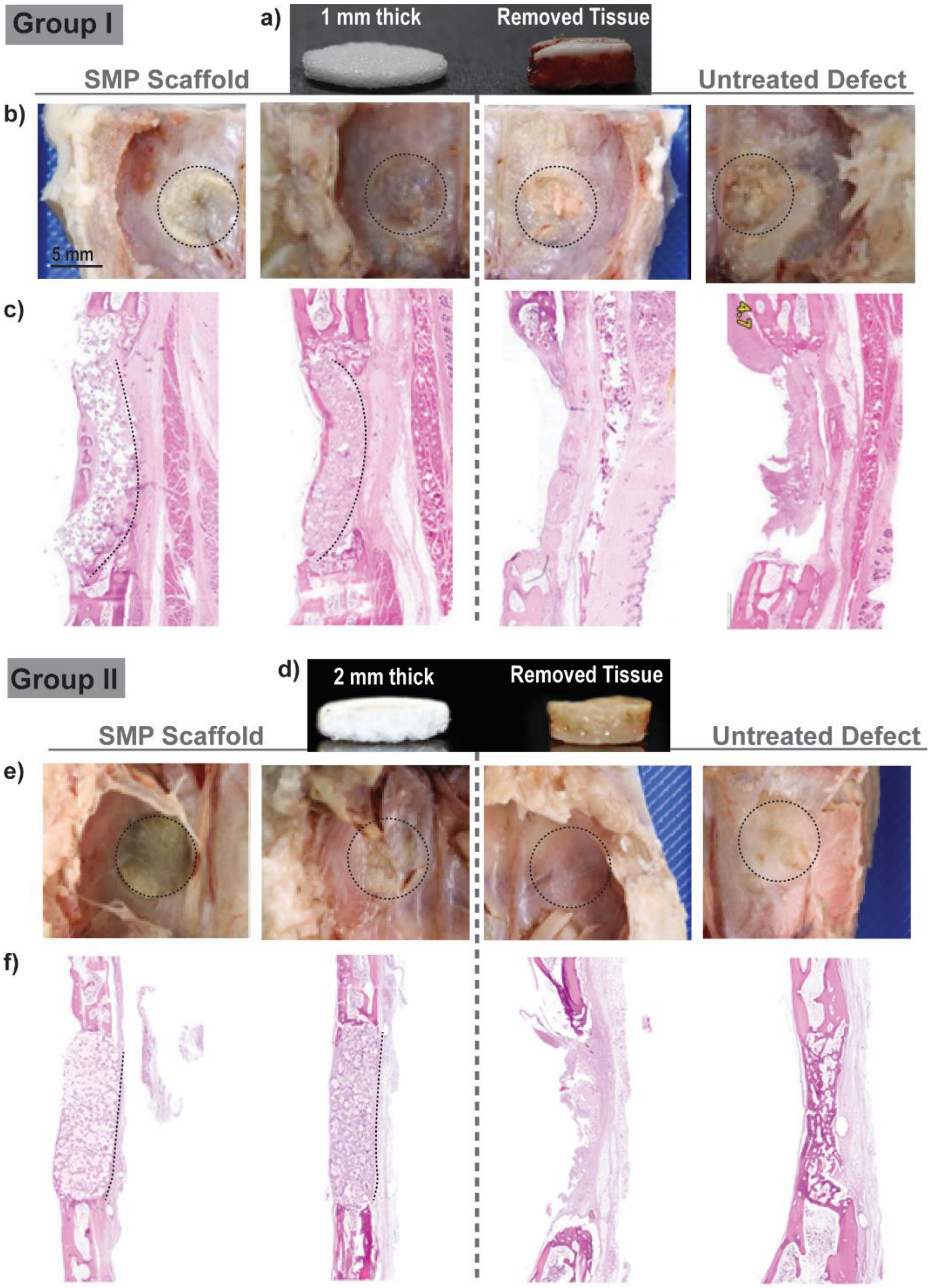

Figure 2-6. For Group I, scaffolds 1 mm thick were implanted and (b) gross examination did not show appreciable difference between the test article and untreated control. But (c) histology with H&E staining showed signs of scaffold bowing. Thus, (d) scaffold thickness was adjusted to 2 mm for Group II. (e) Gross examination and (f) histology were likewise performed. Each group used 4 test subject but two representatives were selected to be shown for each. Healing was assessed at 4 weeks, Black dashed lines were used to outline the defect site in gross examination photos and to demonstrate scaffold positioning in histology sections.

Gross examination of Group II specimens (**Figure 2-6-d**) revealed implants that more closely matched the geometry of adjacent bone. Similar to Group I, Group II gross examination (**Figure 2-6-e**) did not show appreciable differences in cerebral tissue for the test site compared to untreated controls. Group II histology revealed coalescing islands of eosinophilic to amphiphilic woven bone and complete bridging by new woven bone. For Group II SMP implantation sites, osteogenesis primarily occurred in the form of woven bone at the periphery of each scaffold, but a majority of the tissue intercalating and replacing the scaffold was non-ossified fibrous connective tissue. Red blood cells, implant detritus, and their clearing by phagocytic cells were also evident. This response is consistent with the expected healing response at 4 weeks. Notably, the implementation of thicker scaffolds improved the positioning of scaffolds and ability to adequately fill the defect as evident in their lack of bowing (**Figure 2-6-e**).

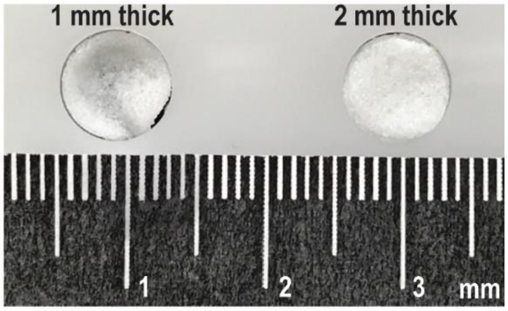

Figure 2-7. (a) Scaffold fitting properties were improved by the thickness modification as tested in a plastic model defect, and (b) thicker scaffold specimens were also successfully implanted.

For Group III, scaffold geometry was maintained at 2 mm thick and healing was assessed at a longer timepoint (16 weeks). The previous implantation scheme (ie. scaffold on left, untreated control on right) was maintained for two rabbits, resulting in two untreated control defects for Group III. In the remaining two rabbits, one defect received 8 mm x 2 mm PEEK implants and the contralateral defect received PCL-DA SMP implants. These two rabbits were used for biomechanical evaluation. For the two rabbits that were assessed via gross examination and histology (**Figure 2-8**), gross examination revealed smooth regular contours for the untreated control sites (expected for non-critical defects), while the test article sites showed evidence of a tan material (likely remaining, undegraded scaffold), some bulging on the ventral surface, and in one animal, tan bone discoloration in surrounding tissue. Histology revealed that the SMP scaffolds were biocompatible, or in other words, did not exhibit any long-term evidence of a protracted inflammatory response. Additionally, the SMP scaffolds exhibited tissue ingrowth, both of blood vessels and fibrous tissue, with modest evidence of bone ingrowth into pores, particularly near the periphery at the site of bone-implant contact. These areas were characterized by an orderly layer of woven bone with typical marrow spaces, covered by variable amounts of orderly skeletal muscle, adipose tissue, and fibrous connective tissue. Trichrome staining further confirmed a modest amount of collagen within the test site. While these findings were promising there was a lack of bone in the center of the implant, potentially impeded by the relatively slow degrading PCL-DA. Collectively, these results suggest that the SMP scaffolds were biocompatible at 4 and 16 weeks, and bone growth was present within scaffold pores, particularly at the scaffold/implant interface, which was quantified via microCT.

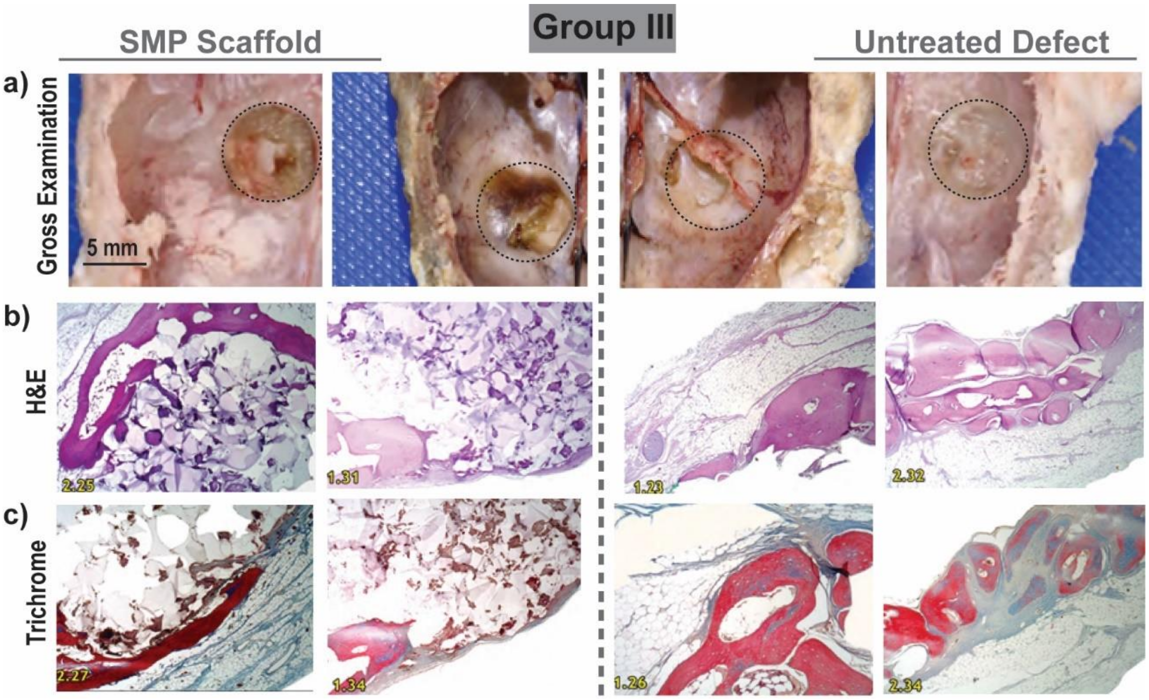

Figure 2-8. For Group III, healing was assessed at 16 weeks via (a) gross examination and (b) histology with H&E staining, and (c) histology with trichrome staining.

2.4.4. MicroCT and Bone Quantification

Three dimensional reconstructions were generated and are described in **Figure 2-9-a,b**. Subjectively, there was more bone in the center of untreated control defects as compared to the PCL-DA SMPs, which was expected in a non-critical defect model. However, there was no detectible difference in bone volume or surface area when assessed quantitatively (**Figure 2-10, Table B-1 and B-2**). These results suggest that the implanted SMP scaffolds allowed similar amounts of bone healing as compared to untreated defect control and as such the PCL-DA SMPs do not inhibit bone healing. These results are consistent with the histologic findings of substantial bone on-growth at the dorsal and ventral surfaces of the bone expected to promote greater implant stability, which will be further described using biomechanics.

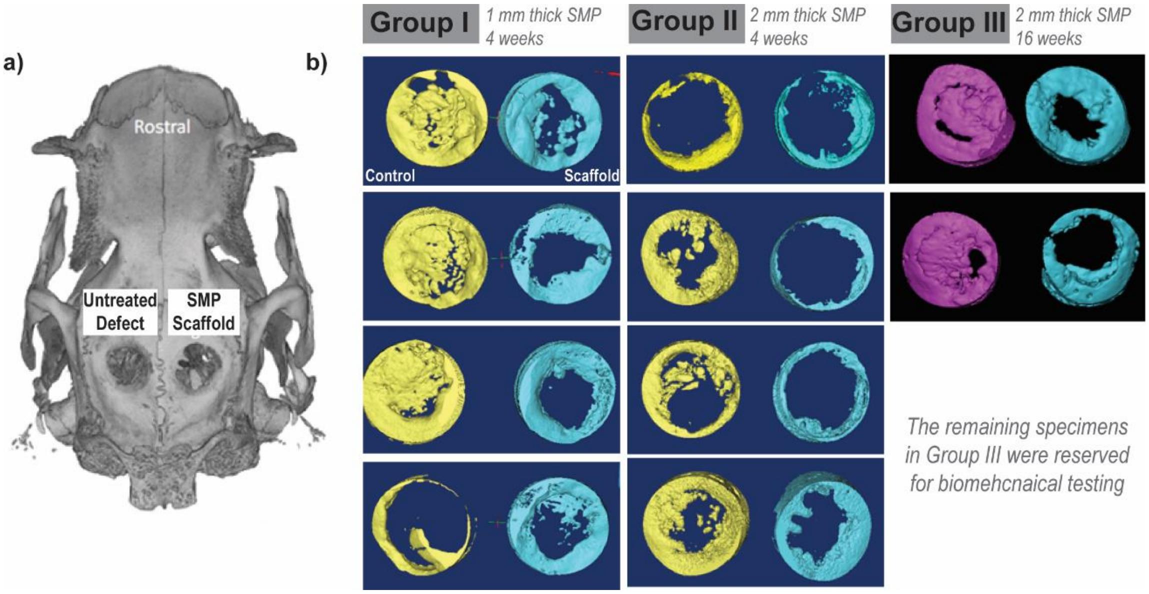

Figure 2-9. MicroCT was performed for all groups and (a) a representative full microCT labeled with the untreated control on the left and the SMP scaffold on the right is shown. (b) 3D reconstructions are shown for all specimens used for bone quantification.

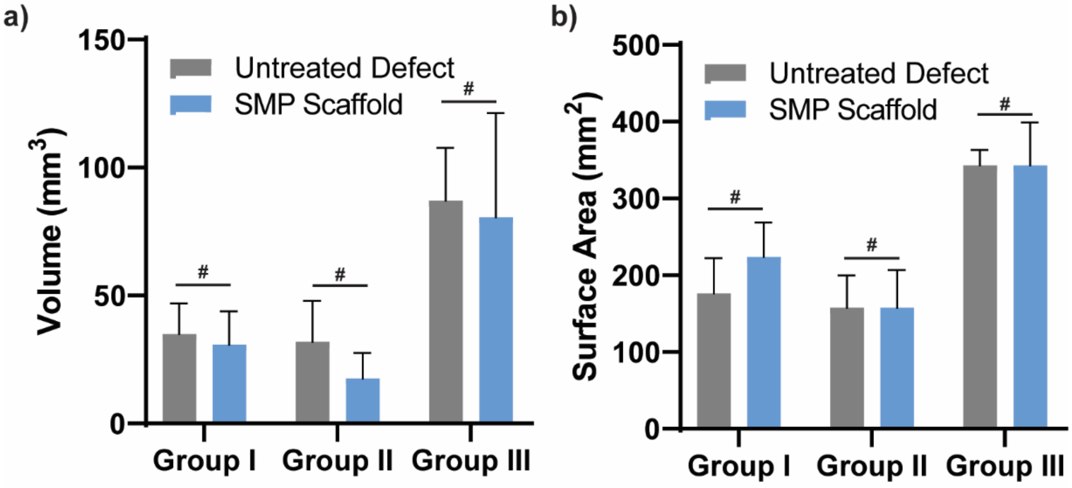

Figure 2-10. Bone ingrowth quantification based on microCT reconstructions for (a) volume and (b) surface area.

2.4.5. Biomechanical Testing

Despite the pre-implantation modulus of the PEEK implants being orders of magnitude higher than that of the SMP, after 16 weeks, the partially healed SMP filled defects were noticeably more resistant to pushout than the contralateral PEEK implants in terms of the maximum load required to cause implant failure. Differences in failure load and stiffness were calculated for each rabbit as the value of the SMP treatment minus the value of the PEEK treatment (Table SX). A Students paired t-test performed on both the failure load ($\mu = 85.7,\ \sigma = 2.90,\ p = .0152 < .05$) and the stiffness ($\mu = 85.3,\ \sigma = 5.94,\ p = .0313 < .05$) showed the measured differences to be statistically significant (**Figure 2-11, Table B-3 and B-4**). The porous SMP scaffolds likely surpassed the solid PEEK controls biomechanically due to tissue ingrowth especially at the scaffold edges, which is consistent with histology and microCT findings. Moreover, these findings support the notion that the "self-fitting" or SMP scaffold offer clinical advantages for treatment of CMF defects due to improved osseointegration.

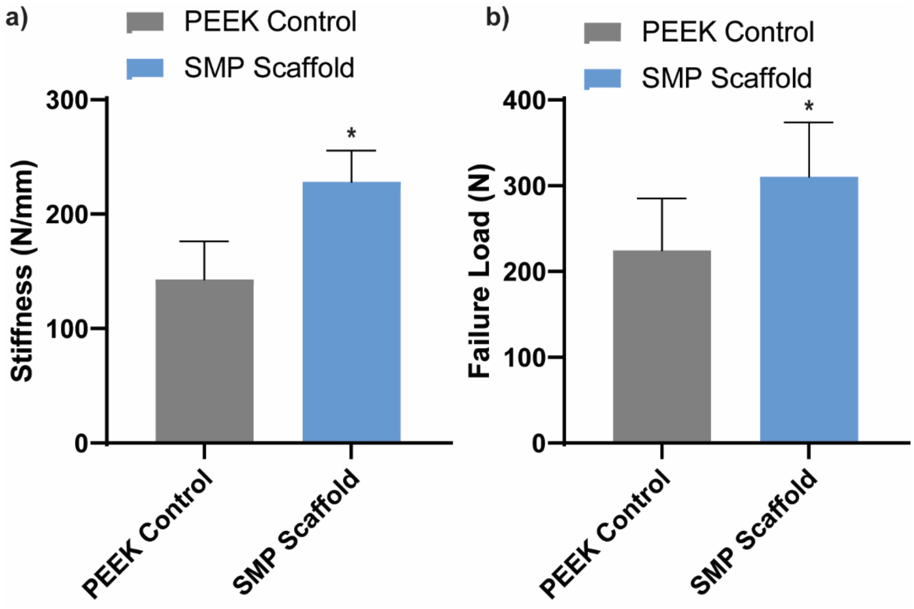

Figure 2-11. Bone ingrowth quantification based on microCT reconstructions for (a) volume and (b) surface area.

2.4.6. Conclusions

While this study was somewhat limited in scope, it served as an effective pilot study to demonstrate the potential advantages of using a porous SMP scaffold centered around its unique self-fitting capabilities. In general, the SMP scaffolds were shown to support woven bone formation particularly at the scaffold periphery, and to support bone ingrowth comparable to the untreated control via microCT at 4 and 16 weeks of healing. At 16 weeks, the SMP scaffold outperformed a PEEK control when assessed via push out test. While PEEK is well-known for its mechanical similarities to bone, the porous scaffold supports superior osseointegration and thus greater implant stability. The intention of this study was to focus on the clinical potential of the SMP scaffolds as simple mass-producible or off-the-shelf device. Considering the lack of additives, the 100% PCL-

DA SMP scaffolds performed well on their own demonstrating their inherent osteoconductivity. That said, future scaffold compositions and surgical iterations may focus on varied SMP composition, improved handling properties, and formulations that would facilitate growth factor inclusion should investigators wish to investigate combination therapies.

3. INTRINSIC OSTEOINDUCTIVITY OF PCL-DA/PLLA SEMI-IPN SHAPE MEMORY POLYMER SCAFFOLDS

3.1. Overview

Engineering osteoinductive, self-fitting scaffolds offers a potential treatment modality to repair irregularly shaped craniomaxillofacial bone defects. Recently, we innovated on osteoinductive poly(ε-caprolactone)-diacrylate (PCL-DA) shape memory polymers (SMPs) to incorporate poly-L-lactic acid (PLLA) in the PCL-DA network, forming a semi-interpenetrating network (semi-IPN). Scaffolds formed from these PCL-DA/PLLA semi-IPNs display stiffnesses within the range of trabecular bone and accelerated degradation relative to scaffolds formed from slowly degrading PCL-DA SMPs. Herein, we demonstrate for the first time that PCL-DA/PLLA semi-IPN SMP scaffolds show increased intrinsic osteoinductivity relative to PCL-DA. We also confirm that application of a bioinspired polydopamine (PD) coating further improves the osteoinductive capacity of these PCL-DA/PLLA semi-IPN SMPs. In the absence of osteogenic supplements, protein level assessment of human mesenchymal stem cells (h-MSCs) cultured in PCL-DA/PLLA scaffolds revealed an increase in expression of osteogenic markers osterix, bone morphogenetic protein-4 (BMP-4), and collagen 1 alpha 1 (COL1A1), relative to PCL-DA scaffolds and osteogenic medium controls. Likewise, the expression of runt-related transcription factor 2 (RUNX2) and BMP-4 was elevated in the presence of PD-coating. In contrast, the chondrogenic and adipogenic responses associated with the scaffolds matched or were reduced relative to osteogenic medium controls, indicating that the scaffolds display intrinsic osteoinductivity.

3.2. Introduction

Bone tissue engineering has emerged as a promising strategy for treating critical-sized craniomaxillofacial (CMF) defects.[113, 140-142] Traditionally, autografts, allografts and alloplastic materials have been used as treatment options for these defects.[143-145] However, they are limited due to restricted availability, donor site morbidity, and foreign body responses.[113, 145, 146] Due to the complex, irregular geometries of such defects, shaping the rigid grafts to tightly fit within the defects poses an additional limitation to current approaches.[146] Thus, several properties of tissue-engineered scaffolds are critical for successful CMF treatment: (1) biocompatibility and degradability of the scaffold into non-toxic products[5]; (2) conformity of the scaffold to the defect shape[145, 146]; (3) osteoconductivity and high porosity to permit cell infiltration into the scaffold,[21, 147, 148] (4) osteoinductivity to promote the differentiation of osteogenic cell populations,[21, 149, 150] and (5) bioactivity (i.e. induction of the formation of carbonated hydroxyapatite (HAp) to facilitate bonding to adjacent bone tissue).[150] While several approaches have been described to improve the osteoconductivity and osteoinductivity of tissue-engineered constructs,[150-153] the translational capacity of these constructs remains limited due to the restrictions necessitated by the irregular shapes of CMF defects.[154]

Our prior work has described the potential of thermoresponsive shape memory polymer (SMP) scaffolds for treating the irregularly-shaped CMF defects.[37] When cycled through their thermal transition temperature (T_{trans}), thermoresponsive SMPs become deformable and can then be molded into the desirable defect shape, which is retained upon cooling below $T_{trans.}$[155] Poly(ε-caprolactone)-diacrylate (PCL-DA; M_n = 10 kDa), a UV-crosslinkable, aliphatic polyester, was fabricated into three-dimensional (3D) porous scaffolds using a solvent-casting, particulate leaching (SCPL) method and examined.[37, 49, 156] The resulting biodegradable, 3D scaffolds displayed highly interconnected porous structures with ~70% porosity, high shape fixity, and compressive moduli greater than 10 MPa.[71] Moreover, relative to respective controls, we observed that these scaffolds may intrinsically induce osteogenic differentiation of human MSCs (h-MSCs), specifically, in the absence of significant chondrogenic or adipogenic effects.[49] The relatively long degradation time of PCL (+2 years), its relatively low stiffness and its lack of inherent bioactivity, however, may hinder bone regeneration thus limiting its therapeutic potential.[71, 157]

To address these limitations, we incorporated a thermoplastic poly-L-lactic acid (PLLA; M_n = 15 kDa) in the PCL-DA network (75:25 wt% ratio), forming a semi-interpenetrating network (semi-IPN).[71, 157, 158] This PCL-DA/PLLA semi-IPN scaffold maintained the crystallinity of PCL-DA scaffolds, essential for shape memory properties, while enhancing their degradation rate due to relative immiscibility and subsequent phase separation between PCL-DA and PLLA.[71, 159] Concurrently, due to the semi-crystallinity and rigidity of PLLA,[27,28] the compressive modulus of the PCL-DA/PLLA semi-IPN scaffold was increased to ~19 MPa, within the range of trabecular bone.[19,29] Although the degradability and stiffness of these SMP scaffolds was improved, it is unclear whether their bioactivity or osteoinductivity was altered versus that of PCL-DA scaffolds.

To improve the osteoinductivity and bioactivity of SMP PCL-DA scaffolds, we have previously investigated the use of a bioinspired polydopamine (PD) coating.[37, 49, 69] In contrast to conventional bioactive ceramic or glass fillers (e.g., calcium phosphates and HAp), PD coatings allow the scaffolds to maintain their malleability at T_{trans} – necessary for their shape memory behavior.[49] PD-coated materials have been demonstrated to be biocompatible *in vivo*[160-162] and cytocompatible *in vitro*,[163] as well as to promote carbonated HAp mineral deposition.[164, 165] With respect to applications relevant to bone repair, several reports by us and colleagues have demonstrated the ability of PD coatings to enhance the osteogenic differentiation of mesenchymal stem cells (MSCs) and promote mineral deposition.[49, 166-168]

The primary goal of this study is to compare the intrinsic capacity of PD-coated and -uncoated PCL-DA and PCL-DA/PLLA (75/25 wt%) scaffolds in promoting osteogenic differentiation of h-MSCs for potential application in CMF defect repair. Furthermore, we aim to compare mineral deposition on the above-mentioned scaffolds to examine changes in their bioactivity. Briefly, PCL-DA and PCL-DA/PLLA scaffolds were prepared using our previously reported SCPL fabrication method.[37, 69] The scaffolds were subsequently treated with dopamine hydrochloride solution to coat their surfaces with PD. Prior to any studies, the scaffold specimens (d ~ 9 mm) were press-fitted into a model CMF defect (d ~ 8 mm, i.e., the size of a critically sized rat calvarial defect).[120] We initially examined the scaffolds' bioactivity by soaking them in simulated body fluid (SBF) for a period of 14 days and evaluating ensuing mineral deposition. Following this, bone marrow-derived h-MSCs from three donors were pooled and cultured on both the PD-coated (PD-PCL-DA and PD-PCL-DA/PLLA) and -uncoated scaffolds (U-PCL-DA and U-PCL-DA/PLLA) in the absence of osteogenic supplements. We subsequently examined the differentiation of h-MSCs relative to osteogenic medium controls through protein level measurements of osteogenic, chondrogenic, and adipogenic markers following 14 days of culture on the scaffolds.

3.3. Materials and Methods

3.3.1. Materials

Poly(ε-caprolactone)-diol (PCL-diol, M_n = 10 kDa per manufacturer specifications), 4-(dimethylamino)pyridine (DMAP), trimethylamine (Et_3N), acryloyl chloride, potassium carbonate (K_2O_3), anhydrous magnesium sulfate ($MgSO_4$), (3S)-cis-3,6-dimethyl-1,4-dioxane-2,5-dione (L-lactide), tin(II) 2-ethylhexanoate [$Sn(Oct)_2$], ethylene glycol, sodium chloride (NaCl), 2,2-dimethoxy-2-phenyl acetophenone (DMP), 1-vinyl-2-pyrrolidinone (NVP), phosphate buffered saline (PBS), sodium bicarbonate, dopamine hydrochloride, calcium chloride, dibasic potassium phosphate, HCl (12 M), magnesium chloride hexahydrate, L-ascorbic acid 2-phosphate, dexamethasone, β-glycerophosphate, dithiothreitol, potassium chloride and common solvents were purchased from Sigma-Aldrich. Lithium chloride (LiCl), Tris hydrochloride (Tris-HCl), Tween 20, sodium azide (NaN_3), ethylenediaminetetraacetic acid (EDTA), lithium dodecyl sulfate (LiDS), bovine serum albumin solution (BSA; Fraction V), absolute ethanol (EtOH), TRIS buffer and 10% formalin solution were purchased from Fisher Scientific. Dulbecco's PBS (DPBS) was obtained from Corning. Acryloyl-PEG-succinimidyl valerate was obtained from Laysan Bio, Inc. Peptide RGDS was obtained from Bachem. All solvents and ethylene glycol were dried over 4 Å molecular sieves prior to use. All monomers and polymers were vacuum dried prior to use. Salt was sieved using an ASTM E-11 no.40 (425 µm) and no. 35 (500 µm) sieves; average salt size was shown to be 460 ± 70 µm using scanning electron microscopy (SEM) and ImageJ.

3.3.2. Macromer Syntheses

PCL-diol (M_n = 10 kDa) was end-functionalized using acryloyl chloride to prepare photo-sensitive PCL-diacrylate (PCL-DA) (>90% acrylation) as previously reported.[37, 69, 158, 159] Poly(L-lactic acid) (PLLA) (M_n =15 kDa) was synthesized via ring-opening of L-lactide using $Sn(Oct)_2$ as the catalyst and ethylene glycol as the initiator, with a monomer to initiator ratio of 104:1.[158, 159] ACRL-PEG-RGDS was synthesized by reacting RGDS, a cell adhesion peptide, with acryloyl-PEG-SVA (1:1 by mol.) in sodium bicarbonate buffer (50 mM, pH~8.5, 2 hr, 150 rpm). The resulting ACRL-PEG-RGDS was purified by dialysis, lyophilized, and stored at -20 °C under nitrogen (N_2).[49]

3.3.3. Fabrication and Characterization of SMP Scaffolds

3.3.3.1. Scaffold Fabrication and PD Coating

PCL-DA (100% PCL-DA) and PCL-DA/PLLA (75:25 wt%) porous scaffolds containing ACRL-PEG-RGDS were prepared via SCPL according to an adapted protocol.[37, 49, 69] Briefly, fused salt templates were prepared by adding water (7.5 wt. %) to NaCl particles (10.0 g, 460 ± 70 µm) in a 20 mL vial (I.D. ~25 mm) over four additions. The salt molds were centrifuged (15 min, 3,220 x g) and were vacuum dried overnight at room temperature (RT, 30 in. Hg). Macromer solutions for each composition were prepared (0.15 g polymer/mL DCM, 1 mM ACRL-PEG-RGDS) with 15 vol. %

photoinitiator solution (10 wt % DMAP in NVP). Enough macromer solution was added to cover each fused salt template (~5 mL) and they were then centrifuged (10 min, 1260 x g) followed by UV-curing for 5 min (UV-Transilluminator, 6 mW cm^{-2}, 365 nm). Scaffolds were air-dried overnight and were then soaked in a solution (1:1 by vol.) of water and ethanol. The scaffolds were removed from glass vials after at least 24 hr of soaking and were soaked in water for an additional 4 days with daily solution changes to leach all salt particles. Scaffolds were then removed and were air-dried overnight prior to heat-treatment (170 °C, 10 min, 30 in. Hg). Next, annealed porous scaffold cylinders were sliced to the final thickness (t ~2 mm) using a vibratome (Leica VT 1000 S). For the PD-coated groups, scaffold discs (d ~12 mm, t ~2 mm) were degassed using a syringe followed by submersion in a dopamine hydrochloride solution atop a rocker table (2 mg/mL in 10 mM Tris buffer, pH = 8.5, 16 hr, 150 rpm). PD-coated scaffold specimens were rinsed thoroughly with distilled water followed by vacuum drying overnight (RT, 30 in. Hg). All scaffolds were then punched to their final diameter (d ~9 mm).

The SMP scaffolds were designed to be slightly larger than a critical size rat calvarial defect (d ~8 mm)[120] and were press-fitted into a plastic model defect to best mimic scaffold geometry in an *in vivo* setting, as demonstrated in **Figure 3-1**. After brief exposure to warm saline (T ~55 °C, ~30 s), scaffolds became malleable and were press-fitted into the model defect (d ~8 mm, t ~2 mm) prepared within a plastic sheet (McMaster-Carr, UHMWPE) using a drill press (Grizzly G7948). After a ~2 min hold at RT, to permit shape fixity, the scaffolds were removed from the plastic model defect. The scaffolds were then sterilized using ethylene oxide (Andersen Sterilizers, Inc.; Model AN 74i Anprolene Gas Sterilization). All analyses were conducted with sterilized shape-fixed scaffold discs.

Figure 3-1. Fabricated scaffolds were warmed in saline (T ~55 °C, 30s) and were press-fitted into a plastic model defect. They were then held at RT for 2 min prior to removal from the model defect to allow for shape fixity. The resulting shape-fixed scaffold discs were used for material characterization and cell studies performed herein.

3.3.3.2. Pore Size and Porosity

Scanning electron microscopy (SEM, Tescan Vega 3, Au-Pt sputter coating, accelerating voltage ~10 kV) was performed to visualize pore morphology. Then, ImageJ software was used on SEM images to measure (n = 5 per image) pore diameter. Percent porosity (n = 3) of the SMP scaffolds was determined via:

$$Porosity\ (\%) = \frac{\rho_{solid\ film} - \rho_{porous\ scaffold}}{\rho_{solid\ film}} * 100$$

where $\rho_{porous\ scaffold}$ is the density of porous SMP scaffold specimens and $\rho_{solid\ films}$ is the density of analogous non-porous, solid films. Density of both the porous scaffolds and solid films was determined gravimetrically; note that for accuracy, these measurements were performed on non-press-fitted specimens.

3.3.3.3. Attenuated total reflectance-Fourier transform infrared spectroscopy (ATR-FTIR)

Following fabrication, ATR-FTIR (Bruker ALPHA-Platinum, n = 32) was performed on each scaffold composition. All spectra were normalized to the same scale for comparison. The incorporation of PLLA into the PCL-DA/PLLA semi-IPN scaffolds was confirmed by the presence of a PLLA carbonyl peak (1760 cm^{-1}) compared to the PCL carbonyl peak (1720 cm^{-1}).[169, 170]

3.3.3.4. Bioactivity

SBF was prepared according to an established protocol.[171] Scaffold discs were each placed into a 25 mL centrifuge vial with 10 mL of the prepared SBF and were vortexed to remove air bubbles until scaffolds were submerged. The tubes were likewise incubated at 37 °C and 60 rpm for 14 days. Then, scaffolds were removed, rinsed with distilled water and vacuum dried overnight (RT, 30 in. Hg). SEM was again performed to visualize mineralization. Then, energy dispersive X-ray spectroscopy (EDS, Oxford Instruments) was performed in conjunction with SEM (carbon-evaporation coating) to obtain the relative elemental composition of scaffold surfaces following exposure to SBF.

3.3.3.5. Hydrolytic Degradation: Water Uptake and Mass Loss

Scaffold discs were submerged in 10 mL of phosphate buffered saline (PBS, 1X, pH ~7.4) in sealed 20 mL glass vials. The samples were incubated (VWR, Model 1570) at 37 °C and 60 rpm. After 14 days, scaffolds were removed and rinsed thoroughly with distilled water. They were then blotted and massed for their wet weight. Lastly, scaffolds were dried, and their final dry mass was determined. Water uptake (%) and mass loss

(%), due to hydrolysis of the polyester-based scaffolds, was determined gravimetrically according to the following equations:

$$Water\ Uptake\ (\%) = \frac{m_{wet} - m_{final}}{m_{final}} * 100$$

$$Mass\ Loss\ (\%) = \frac{m_{final} - m_{initial}}{m_{final}} * 100$$

where $m_{initial}$ is the mass of the dry scaffold prior to exposure to PBS, m_{wet} is the mass of the wet scaffold immediately after removal from solution, and m_{final} is the mass of the removed scaffold after it has been thoroughly dried. Scaffolds were again visualized using SEM, according to the previously described procedure, to assess pore morphology following 14 days of hydrolysis.

3.3.4. Cell Culture

Cryopreserved bone marrow derived h-MSCs (Texas A&M Institute for Regenerative Medicine) from three different donors were thawed and expanded in Minimum Essential Medium-α (α-MEM, Gibco) supplemented with 16.5% MSC-qualified fetal bovine serum (FBS; Atlanta Biologicals), and 1% glutamine (Glutamax; Life Technologies) in a 37 °C-5% CO_2 jacketed incubator. Cells from the three h-MSC donors were harvested at passage 5-6 and pooled in equal parts for a final concentration of 3.5×10^6 cells/mL in growth medium: Dulbecco's Modified Essential Medium (DMEM; Corning) supplemented with 10% FBS and 1% antibiotic/antimycotic solution (10,000 IU/mL penicillin, 10,000 µg/mL streptomycin, and 25 µg/mL amphotericin; Life Technologies).

Uncoated-PCL-DA (U-PCL-DA; n = 7), PD-coated-PCL-DA (PD-PCL-DA; n = 5), U-PCL-DA/PLLA (n = 5) and PD-PCL-DA/PLLA (n = 5) scaffolds were placed in separate wells of a 24-well plate and wetted with a gradient solution of EtOH and DPBS, starting with 100% EtOH and ending with 100% DPBS. The scaffolds were then washed 4 times with DPBS to remove any residual EtOH solution. Following this, 50 μL of h-MSC cell suspension (3.5 x 10^6 cells/mL) were pipetted onto the upper surface of each scaffold and incubated for 20 min. To ensure homogenous cell seeding, the cell suspension was pipetted three times on the surface of the scaffolds. Thereafter, the scaffolds were gently flipped within each well, and an additional 50 μL of cell suspension was likewise seeded onto the other surface and incubated for 20 min. Following cell seeding, 1 mL of fresh growth medium was added to each well and the plate was incubated for 3 hr to allow for cell attachment. Subsequently, the cell-laden scaffolds were gently washed with DPBS to remove nonadherent cells, transferred to a new 24-well plate, and cultured in fresh growth medium. U-PCL-DA scaffolds (n = 3) in growth medium containing osteogenic media supplements (50 μg/mL L-ascorbic acid 2-phosphate, 0.1 μM dexamethasone, 10 mM β-glycerophosphate) were utilized as a control (U-PCL-DA OM) to illustrate the intrinsic osteoinductivity of these SMP scaffolds. Medium changes for all scaffolds were performed every 2 days. The scaffolds were harvested after 14 days in culture, washed in DPBS for 5 min, and divided into three sections: one for evaluating cell attachment and spreading, and two for homogenization for end-point analyses. The latter were placed in 1.7 mL microcentrifuge tubes, flash frozen in liquid N_2, and stored at -80 °C.

3.3.5. Cell Attachment and Spreading

After 14 days of culture, scaffold pieces were prepared for confocal imaging of cell attachment and spreading. After rinsing in DPBS, cell-laden scaffolds were fixed in 10% formalin solution, and subsequently stained with Alexa Fluor-646 phalloidin (Life Technologies) and SYBR green (Invitrogen). The scaffolds were imaged at 10X using confocal microscopy (Zeiss LSM 510 META).

3.3.6. Construct Harvest for End-Point Analysis

Protein was extracted from each of the scaffolds using a modified version of a previously described extraction protocol.[172] Briefly, flash-frozen scaffold sections were placed into contact with 300 µl of lysis buffer (100 mM Tris, 500 mM LiCl, 10 mM EDTA, 1% LiDS, 5 mM dithiothreitol, 1% phosphatase and protease inhibitor [Thermo Scientific], pH~7.8) and centrifuged for 5 min at 10,000 rpm to allow the lysis buffer to fully infiltrate the scaffolds. Following centrifugation, the scaffolds were incubated for 10 min at RT with mixing every 2.5 min. Thereafter, the scaffolds were placed in -80 °C for 7 min, then taken out and incubated in 37 °C water bath for 3 min. The scaffolds were then incubated for 3 min at RT with mixing every 1 min. Two additional freeze-thaw cycles were conducted for a total of 3 cycles, followed by centrifugation for 1 min at 10,000 rpm to isolate the supernatant. Supernatants from each sample’s two scaffold pieces were combined in a 1.7 mL microcentrifuge tube and frozen in -80 °C for subsequent protein analysis. Total DNA was measured by Quant-iT™ PicoGreen dsDNA assay (Life Technologies) per the manufacturer’s instructions. DNA levels were utilized for normalization of protein levels on a per cell basis.

3.3.6.1. MAGPIX Immunoassay Multiplexing

The protein levels of collagen 1 alpha 1 (COL1A1), bone morphogenetic protein-4 (BMP-4) and osteonectin were measured from supernatants using a human premixed magnetic bead analyte kit (R&D Systems) and a MAGPIX® immunoassay system (Luminex) per the manufacturer's protocol. Briefly, samples were loaded into a 96-well plate, after which magnetic bead suspensions, biotinylated detection antibodies, and streptavidin-phycoerythrin were added to sample wells. The concentrations of proteins of interest were obtained from measured median fluorescence intensities (MFI) relative to a standard curve. Results were normalized to the sample's DNA content and presented relative to U-PCL-DA OM.

3.3.6.2. Western Blot Analysis

Western blots were used to semi-quantitatively compare protein expression of extracellular matrix (ECM) proteins and transcription factors by h-MSCs cultured within uncoated and coated PCL-DA and PCL-DA/PLLA scaffolds. Sample supernatants corresponding to 400 ng of DNA were denatured by the addition of β-mercaptoethanol, heated at 95 ºC for 10 min and then loaded into either an 8% or a 12% sodium dodecyl sulfate polyacrylamide gel. Proteins were separated by electrophoresis and subsequently transferred to a nitrocellulose membrane (Thermo Scientific). Following this, the membrane was rinsed twice with distilled-deionized H_2O and then blocked with 5% BSA in TBST/NaN_3 (25 mM Tris-HCl, pH 7.5, 137 mM NaCl, 0.1% Tween 20, 0.05% NaN_3) for 1 hr at RT. Primary antibodies were diluted in a solution of 5% BSA in TBST/NaN_3

and applied to the membrane overnight at 4 ºC with constant shaking. Further details regarding the antibodies employed are given in **Table B-5**.

Bound primary antibodies were detected by applying the appropriate alkaline phosphatase-conjugated or horseradish peroxidase-conjugated secondary antibody (Jackson ImmunoResearch) for 1 hr at RT, followed by the application of Novex chemiluminescent substrate (Life Technologies) or Luminol chemiluminescent reagent (Santa Cruz Biotechnology), respectively. Chemiluminescence was detected using a ChemiDoc™ XRS$^+$ System equipped with ImageLab™ software (Bio-Rad Laboratories). Exposure times were set manually to prevent signal saturation. Band integrated optical density for each protein was quantified using Adobe Photoshop CS2 (Version 9.0) and normalized to the loaded DNA amount and to U-PCL-DA OM. Representative blot images are shown in **Figure 3-2**.

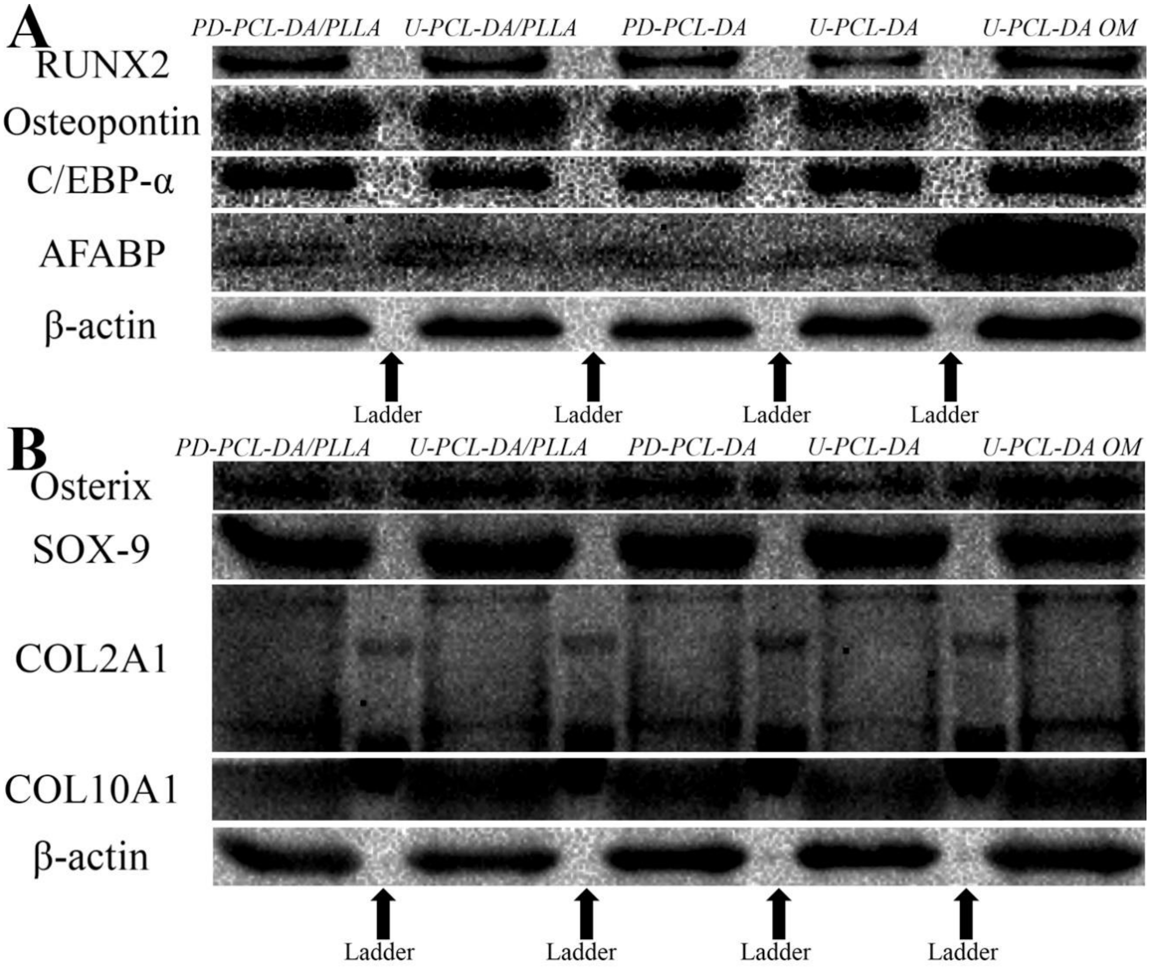

Figure 3-2. Representative images from western blot analysis of osteogenic, chondrogenic and adipogenic protein expression by h-MSCs cultured on PCL-DA-based SMP scaffolds. (A) RUNX2, osteopontin, C/EBP-α, AFABP and β-actin from 12% sodium dodecyl sulfate polyacrylamide gels (SDS-PAGE), and (B) osterix, SOX-9, COL2A1, COL10A1 and β-actin from 8% SDS-PAGE gels.

3.3.7. Statistical analysis

All data are reported as the mean ± standard error of mean. Statistical analyses were performed using SPSS software (Version 26.0). Comparison of means from experimental groups was done using two-way ANOVA. The use of this test is appropriate for experimental designs which seek to test the effects of two independent variables (the scaffold material type and the presence of PD coating).[173, 174] The two-way ANOVA was utilized to determine significance resulting from main effects of either independent variables or the significance resulting from the interaction between these two variables. A p-value < 0.05 was considered statistically significant.

3.4. Results

3.4.1. Structure of PCL-DA and PCL-DA/PLLA Scaffolds

Scaffolds were prepared with either PCL-DA only or a semi-IPN comprised of cross-linked PCL-DA and a PLLA thermoplastic (**Figure 3-3-A**). Prior to the onset of 3D cell culture studies, scaffold properties such as pore morphology were investigated following ‘press-fitting’ into a model defect (**Figure 3-3-B,C**). As can be seen from **Figure 3-3-D-G** relative to **Figure 3-4**, while the pores along the scaffold edge are deformed and compressed, they remained open following the ‘press-fitting’ process. Moreover, the scaffolds retained an interconnected porous structure. Pore diameter and porosity measures for each scaffold are summarized in **Table 3-1**. Pore size was maintained at ~200-210 µm for the U-PCL-DA and the U-PCL-DA/PLLA, and was slightly reduced to ~180-190 µm following the addition of a PD coating. All compositions maintained similar porosity of ~65%.

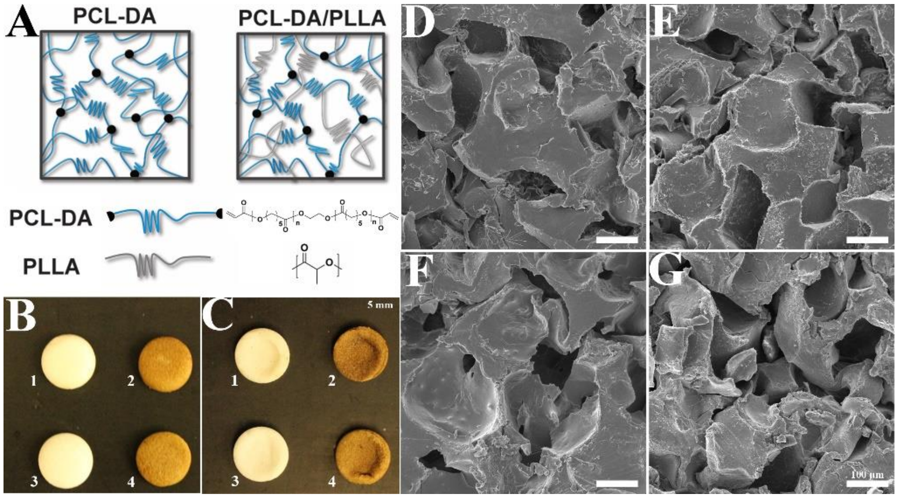

Figure 3-3. (A) Graphical illustration of the PCL-DA network and the PCL-DA/PLLA semi-IPN network comprising the scaffolds. Representative macroscopic images of the **(B)** top and **(C)** bottom sides of the 'press-fitted' PCL-DA-based SMP scaffolds. Brown coloration is indicative of a PD coating. 1, U-PCL-DA; 2, PD-PCL-DA; 3, U-PCL-DA/PLLA; 4, PD-PCL-DA/PLLA. Scale bar = 5 mm. Representative SEM images of the interconnected pore structure of **(D)** U-PCL-DA, **(E)** PD-PCL-DA, **(F)** U-PCL-DA/PLLA, and **(G)** PD-PCL-DA/PLLA scaffolds following press-fitting. Scale bar = 100 µm.

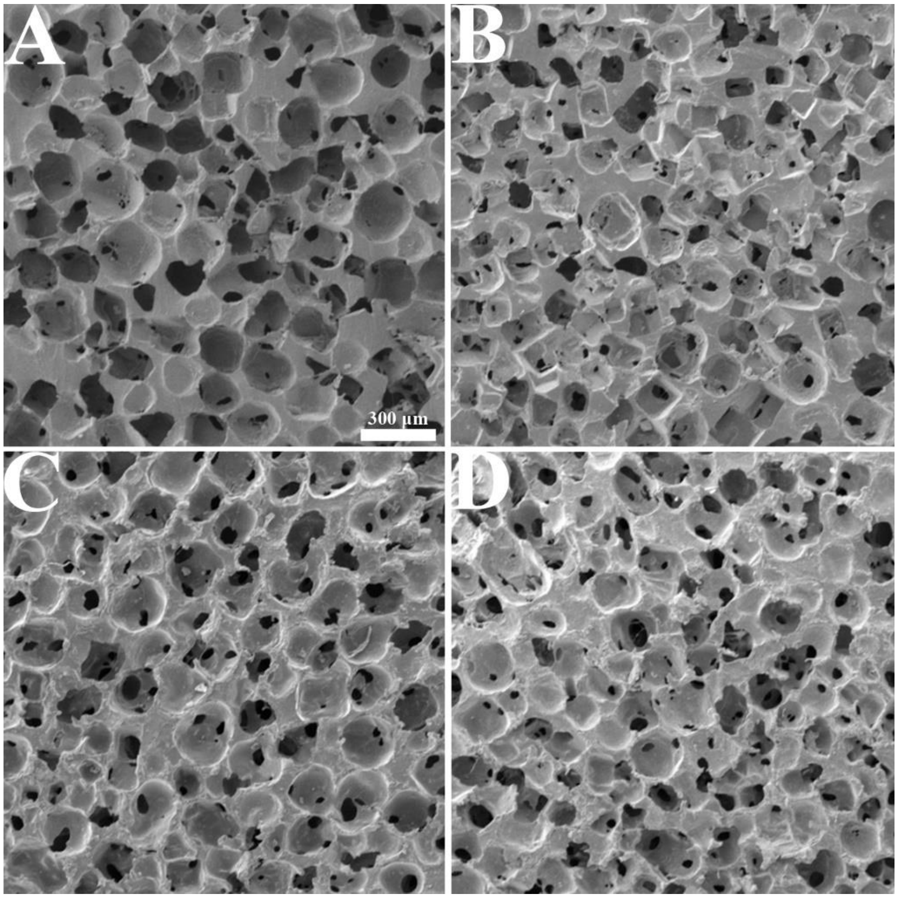

Figure 3-4. Representative scanning electron microscopy (SEM) images of the (A) U-PCL-DA, (B) PD-PCL-DA, (C) U-PCL-DA/PLLA, and (D) PD-PCL-DA/PLLA scaffolds used to evaluate pore diameter. Scale bar = 300 µm and applies to all images.

Table 3-1. Pore diameter (n = 10) and porosity (n = 3) measures for SMP scaffolds. Values are reported as mean ± standard error of the mean.

	U-PCL-DA	**PD-PCL-DA**	**U-PCL-DA/PLLA**	**PD-PCL-DA/PLLA**
Pore Diameter (µm)	202.47 ± 4.94	181.04 ± 7.25	208.64 ± 5.75	193.22 ± 6.70
% Porosity	64.97 ± 0.25	63.94 ± 0.32	65.67 ± 0.15	65.77 ± 0.12

ATR-FTIR was used to examine differences in chemistries of the scaffold compositions as shown in **Figure 3-5**. Spectra for PCL-DA/PLLA compositions showed an additional carbonyl peak at 1760 cm^{-1} indicating that thermoplastic PLLA was successfully incorporated. Analysis of PD-coated compositions was limited because the PD carbonyl peak (1723 cm^{-1}) overlaps with the PCL carbonyl peak (1720 cm^{-1}). However for PD-coated compositions, this peak showed a noticeable shoulder, which is consistent with previous reports on PD coatings.[175] PD-coated samples also showed a more pronounced hydroxyl peak (broad, 3400 cm^{-1}) indicative of increased hydrophilicity.

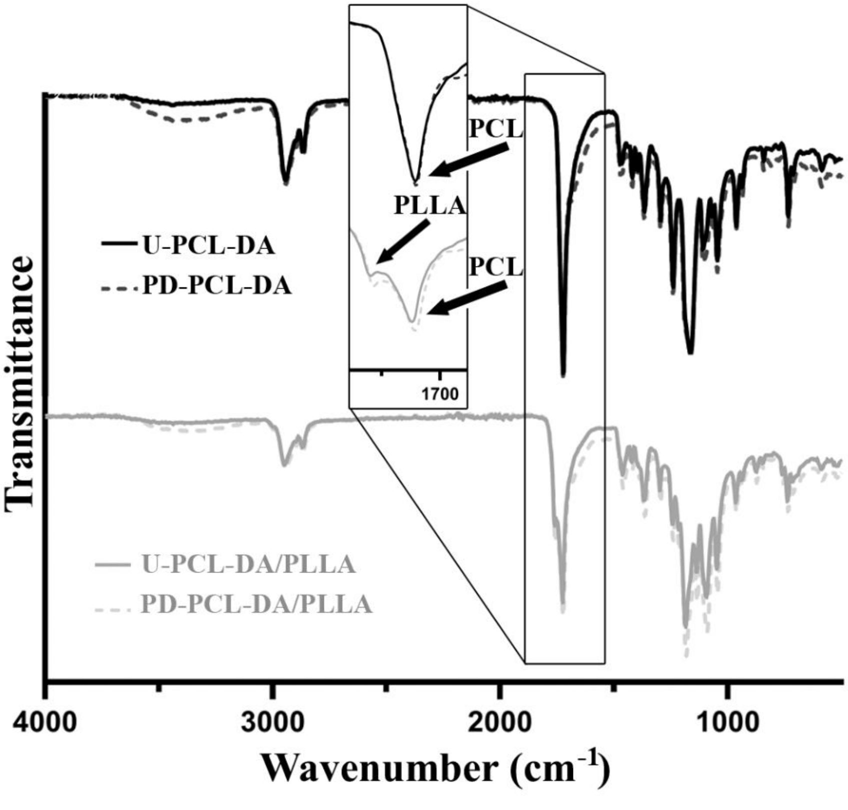

Figure 3-5. Representative ATR-FTIR spectra for U-PCL-DA, PD-PCL-DA, U-PCL-DA/PLLA, and PD-PCL-DA/PLLA.

3.4.2. Hydrolytic Degradation and Bioactivity of Scaffolds

Scaffolds are ideally designed to degrade at a similar rate to tissue regeneration for optimal healing. PCL-DA is known to degrade more slowly than bone, so PCL-DA/PLLA scaffolds are of considerable interest because they have shown to degrade at an accelerated rate relative to PCL-DA.[157] Previous PCL/PLLA scaffold degradation studies have been limited to base-catalyzed conditions, so herein, scaffolds were incubated in neutral PBS (1X, pH ~7.4) for 14 days. Water uptake (%) and mass loss (%) results are summarized in **Table B-6**. Water uptake ranged from ~98% for U-PCL-DA to ~106% for PD-PCL-DA, whereas for PCL-DA/PLLA compositions water uptake was ~118% regardless of the coating. Hydrolytic degradation as measured via day 14 gravimetric mass loss was ~2.5% for U-PCL-DA and PD-PCL-DA scaffolds versus ~3% for the PCL-DA/PLLA compositions. Degraded scaffolds were visualized using SEM as shown in **Figure 3-6**.

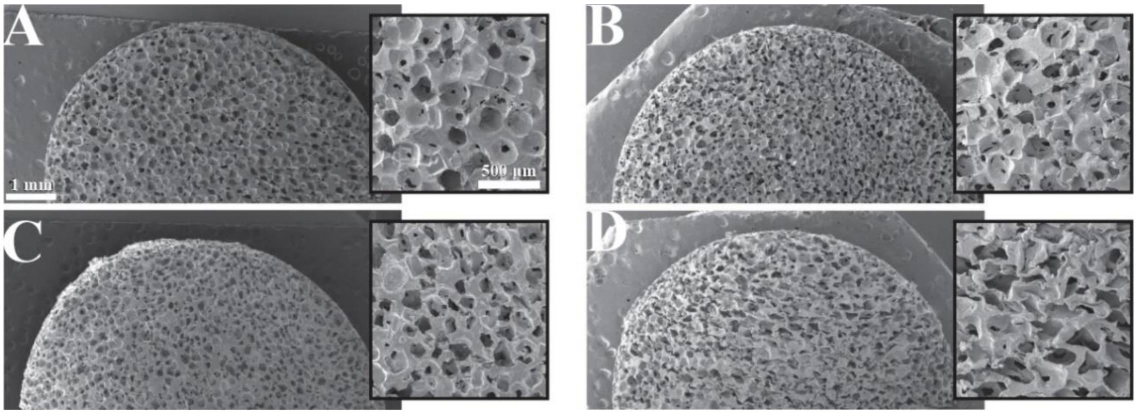

Figure 3-6. Representative SEM of degraded scaffold for (A) U-PCL-DA and (B) PD-PCL-DA, (C) U-PCL-DA/PLLA, and (D) PD-PCL-DA/PLLA following 14-day incubation at 37 °C in PBS.

In terms of bioactivity, our previous work demonstrated that PD coatings induced carbonated HAp deposition on PCL-DA SMP scaffolds.[37] To elucidate whether the addition of the relatively hydrophilic PLLA into the PCL-DA network altered mineral deposition on the resulting semi-IPN scaffolds, PD-coated and uncoated PCL-DA and PCL-DA/PLLA scaffolds were exposed to SBF (1X). Mineralization was observed exclusively on the PD-coated scaffolds, regardless of PLLA presence (**Figure 3-7**). HAp mineralization was further verified by EDS where spectra showed a phosphorous (P) and a calcium (Ca) peak for the PD-coated compositions (**Figure 3-8**). The ratio of Ca/P was found to be ~2 for both PD-coated compositions (**Table B-7**) which is higher than the theoretical Ca/P for HAp (Ca/P ~1.5-1.67),[176] yet is consistent with Ca/P in healthy bone.[177]

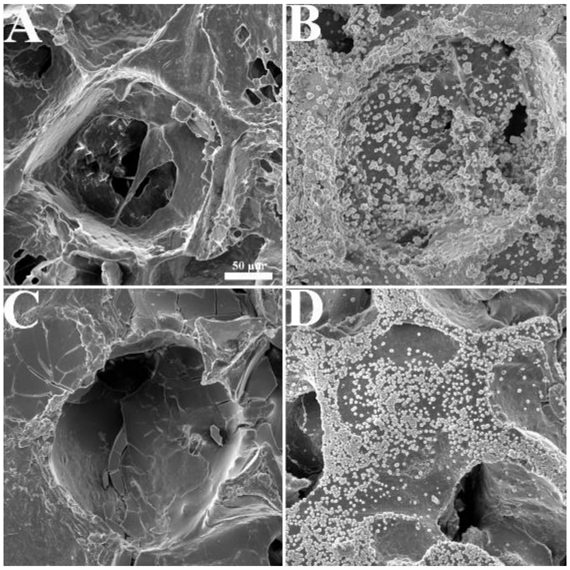

Figure 3-7. SEM images of the (A) U-PCL-DA, (B) PD-PCL-DA, (C) U-PCL-DA/PLLA, and (D) PD-PCL-DA/PLLA scaffolds displaying mineral deposition following soaking in SBF (1X) for 14 days at 37 °C. Scale bar = 50 μm and applies to all images.

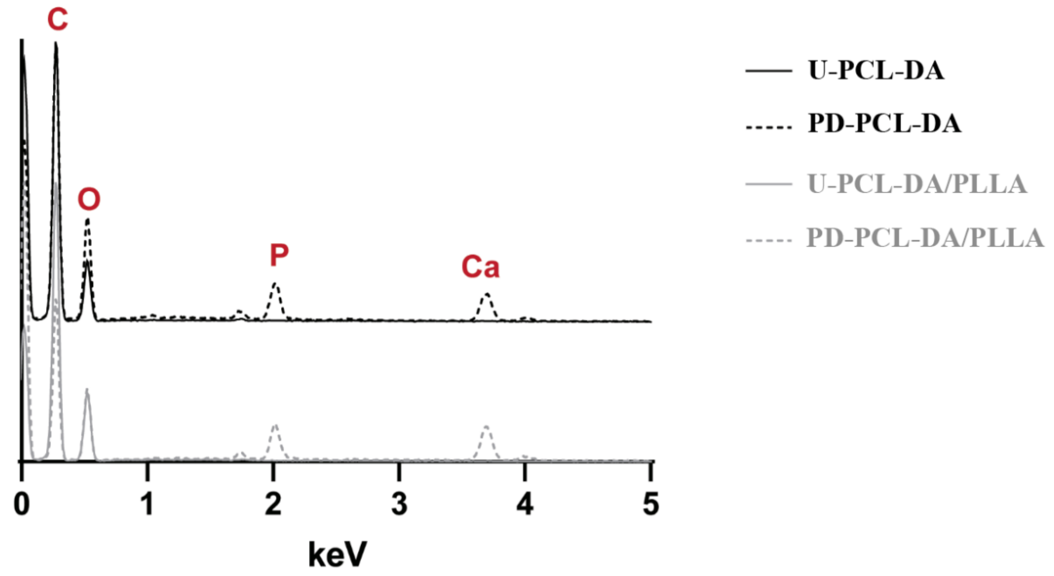

Figure 3-8. Representative EDS spectra for U-PCL-DA, PD-PCL-DA, U-PCL-DA/PLLA, and PD-PCL-DA/PLLA.

3.4.3. Cell Attachment and Spreading within Scaffold Pores

Following 14 days of culture, h-MSC attachment and spreading within the various scaffolds was investigated using confocal microscopy. As can be seen in **Figures 3-9-A-D**, both PCL-DA and PCL-DA/PLLA scaffolds were able to demonstrate robust cell adhesion, irrespective of the presence of PD coating. Additionally, we observed no statistically significant differences in relative DNA measures from sample homogenates (**Figure 3-9-E**). This suggests that there are minimal differences in cell attachment arising from different SMP scaffold compositions or the presence of a PD coating.

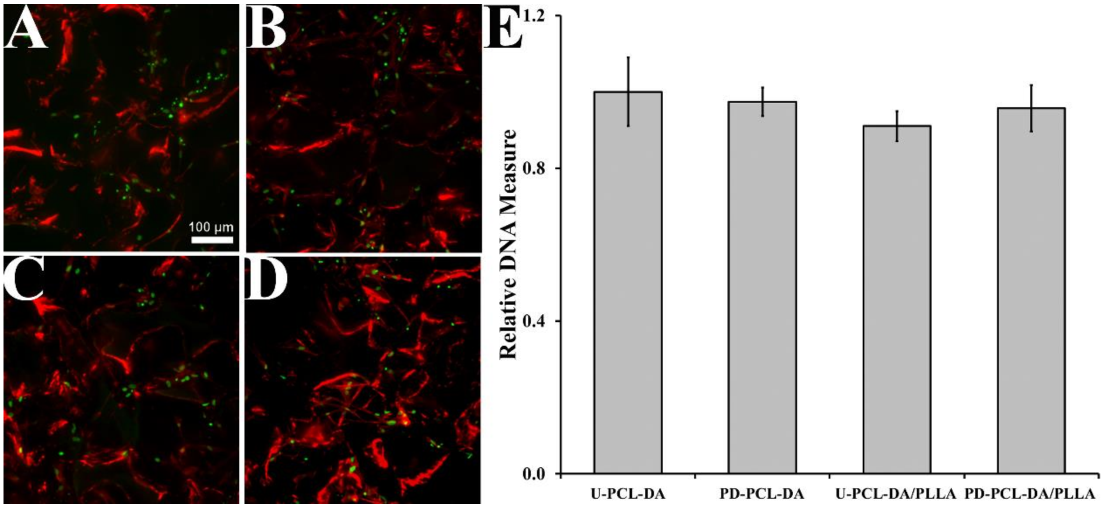

Figure 3-9. Representative stacked confocal images of h-MSCs stained with nuclear dye SYBRGreen (Green) and with the F-actin dye Phalloidin (Red) in transverse sections of (A) U-PCL-DA (B) PD-PCL-DA (C) U-PCL-DA/PLLA and (D) PD-PCL-DA/PLLA scaffolds. Scale bar = 100 µm and applies to all images. Please note the observed scaffold structure due to autofluorescence. (E) DNA measures from extracted cell lysates. Data are presented relative to U-PCL-DA. Error bars correspond to the standard error of the mean (n = 4-5 per scaffold type).

3.4.4. Assessment of Specific Osteogenic Differentiation of h-MSCs

The capacity of PD-coated and uncoated PCL-DA/PLLA and PCL-DA scaffolds to promote specific osteogenic lineage progression of h-MSCs was compared in the absence of osteogenic supplements. This was done to evaluate the intrinsic osteoinductivity of these scaffolds in the presence or absence of PD coating. Additionally, the extent of non-specific chondrogenic and adipogenic h-MSC differentiation was assessed across the four formulations. U-PCL-DA scaffolds exposed to osteogenic medium (U-PCL-DA OM) were used as controls.

3.4.4.1. Osteogenic Differentiation

Following 14 days of culture, the expression levels of key osteogenic markers (osterix, RUNX2, and BMP-4) were assessed. The incorporation of PLLA into the PCL-DA network resulted in a significant increase in expression of osterix ($p = 0.0020$) and BMP-4 ($p = 0.0023$) by h-MSCs relative to PCL-DA alone (**Figure 3-10-A**). Moreover, the expression levels of RUNX2 and BMP-4 were elevated following inclusion of PD coating in either scaffold type ($p = 0.0290$ and $p = 0.0373$, respectively). Although the expression of osterix displayed an increasing trend in the presence of the PD coating, the results fell below statistical significance ($p = 0.0505$).

We further assessed the expression of osteogenic ECM markers (COL1A1, osteopontin and osteonectin). The expression levels of COL1A1 and osteonectin by h-MSCs were elevated following 14-day culture on PCL-DA/PLLA semi-IPN scaffolds relative to PCL-DA scaffolds ($p = 0.0141$ and $p = 0.0004$, respectively; **Figure 3-10-B**), although these markers did not appear to be affected by the presence of PD coating.

Overall, our results demonstrate that the PCL-DA/PLLA semi-IPN scaffolds induced a greater osteogenic response relative to the PCL-DA scaffolds. Similar to our previous results,[21] the presence of PD coating enhanced the observed osteogenic response for both scaffold types. With the exception of osterix, the expression level of osteogenic markers on the PD-coated scaffolds as well as on U-PCL-DA/PLLA was equivalent to or exceeded that observed in U-PCL-DA OM osteogenic media controls. This lends support to the ability of these SMP scaffolds to intrinsically promote osteogenesis of h-MSCs.

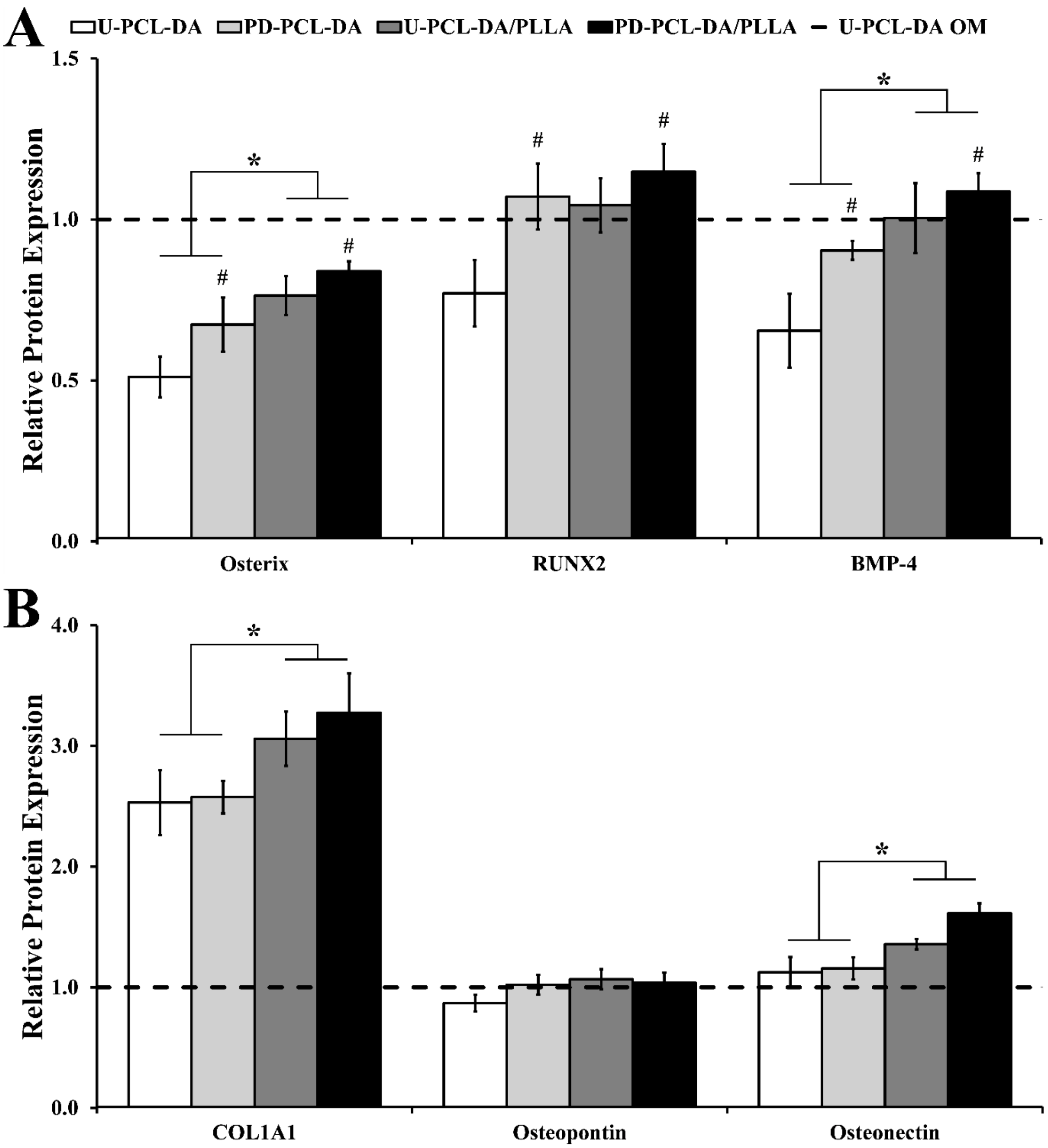

Figure 3-10. Relative protein expression of (A) Osterix, RUNX2 and BMP-4, and (B) and COL1A1, osteopontin and osteonectin associated with h-MSCs cultured on PCL-DA-based scaffolds. For each marker, the results are normalized to DNA and presented relative to U-PCL-DA OM osteogenic controls (dashed line). The asterisk (*) denotes a significant main effect resulting from PCL-DA/PLLA relative to PCL-DA scaffolds. The pound symbol (#) denotes a significant main effect resulting from PD coated scaffolds relative to uncoated scaffolds. Error bars correspond to the standard error of the mean. (n = 4-5 per scaffold type; $p < 0.05$).

3.4.4.2. Chondrogenic and Adipogenic Differentiation

Our initial work[49] illustrated no significant chondrogenic or adipogenic differentiation of h-MSCs following culture on PCL-DA porous scaffolds relative to adipogenic medium and chondrogenic medium controls. Herein, we sought to compare the expression of chondrogenic markers (SOX-9, collagen 2 alpha 1 [COL2A1] and collagen 10 alpha 1 [COL10A1]) by h-MSCs cultured on SMP scaffolds in the presence or absence of PD coating. As shown in **Figure 3-11**, the expression levels of SOX-9 displayed a statistically significant interaction effect between scaffold composition and PD-coating ($p = 0.0331$). This indicates that the effect of PD coating, if any, on SOX-9 expression is not the same for either SMP type. We, however, did not observe any statistically significant differences in SOX-9 or COL10A1 expression due to PD coating or SMP type individually. This suggests that their expression is not altered by either variable alone. Additionally, relative to h-MSCs on PCL-DA scaffolds, h-MSCs cultured on PCL-DA/PLLA scaffolds displayed an elevated COL2A1 expression ($p = 0.0158$). That said, the expression levels of these markers are consistent with levels observed for h-MSCs in U-PCL-DA OM controls, meaning that the scaffolds suppress chondrogenic differentiation to a similar extent as osteogenic media.

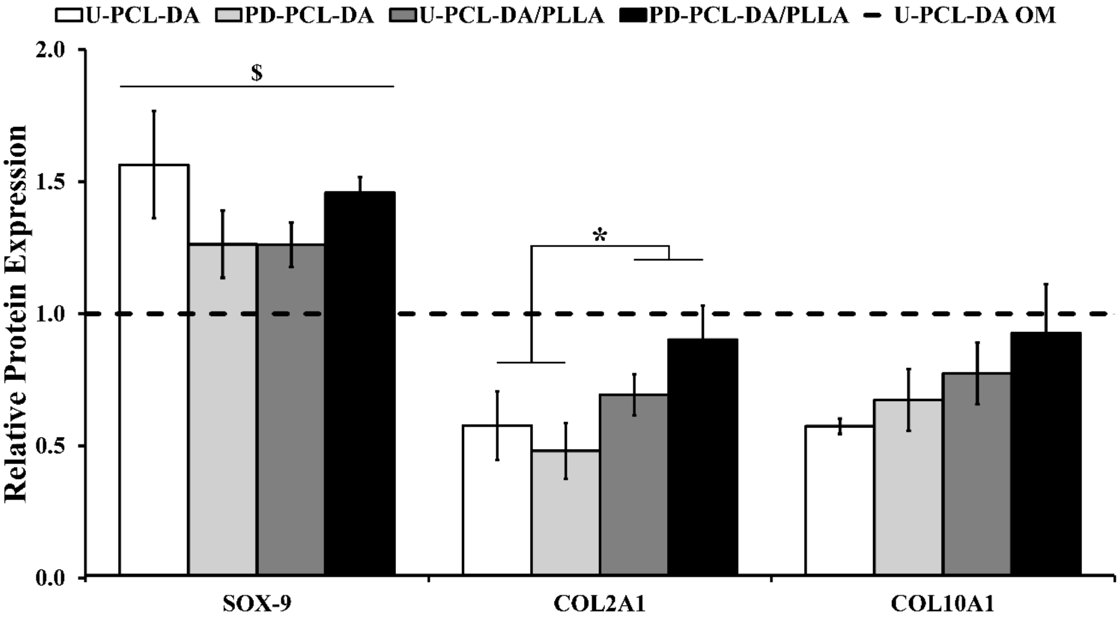

Figure 3-11. Relative protein expression of SOX-9, COL2A1 and COL10A1 associated with h-MSCs cultured on PCL-DA-based scaffolds. For each marker, the results are normalized to DNA and presented relative to U-PCL-DA OM osteogenic controls (dashed line). The asterisk (*) denotes a significant main effect resulting from PCL-DA/PLLA relative to PCL-DA scaffolds. The dollar sign ($) denotes a significant interaction effect between the SMP scaffold type and PD coating presence. Error bars correspond to the standard error of the mean. (n = 4-5 per scaffold type; $p < 0.05$).

As for assessing the adipogenic response of h-MSCs on PCL-DA and PCL-DA/PLLA scaffolds, we compared the expression of CCAAT/enhancer-binding protein alpha (C/EBP-α) and adipocyte fatty acid-binding protein (AFABP). Interestingly, cultures on PCL-DA/PLLA scaffolds displayed an increased expression of C/EBP-α relative to PCL-DA cultures (p = 0.0016; **Figure 3-12**). Further, analysis of AFABP expression revealed a statistically significant interaction effect (p = 0.0222) between the presence of PD coating and SMP type. However, the expression levels of these markers are below with levels observed for h-MSCs in U-PCL-DA OM controls, meaning that the scaffolds suppress adipogenic differentiation to a similar extent as osteogenic media.

Cumulatively, the adipogenic and chondrogenic responses of h-MSCs on PD-coated and -uncoated PCL-DA and PCL-DA/PLLA scaffolds indicate that the osteogenic response supported by these scaffolds is largely specific.

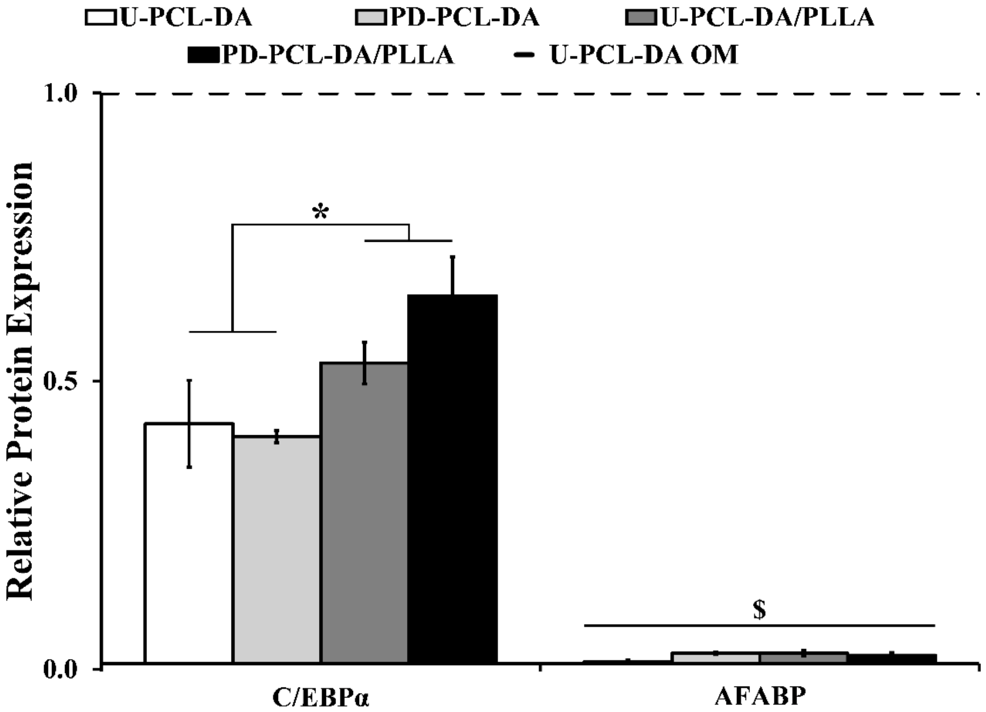

Figure 3-12. Relative protein expression of C/EBP-α and AFABP associated with h-MSCs cultured on PCL-DA-based scaffolds. For each marker, the results are normalized to DNA and presented relative to U-PCL-DA OM osteogenic control (dashed line). The asterisk (*) denotes a significant main effect resulting from PCL-DA/PLLA relative to PCL-DA scaffolds. The dollar sign ($) denotes a significant interaction effect between the SMP scaffold type and PD coating presence. Error bars correspond to the standard error of the mean. ($n = 4$-5 per scaffold type; $p < 0.05$).

3.5. Discussion

PCL-DA-based SMPs hold substantial promise for CMF repair applications primarily due to their capacity to conform to the irregular shapes of CMF defects, and their degradability.[37, 49] The semi-IPN design of PCL-DA/PLLA scaffolds enhanced the degradability of these SMPs as well as improved their mechanical stiffness to fall within range of trabecular bone.[157-159] In the present work, we compared the capacity of PD-coated and uncoated PCL-DA and PCL-DA/PLLA scaffolds in driving osteogenic differentiation of h-MSCs. We initially investigated the pore structure, neutral hydrolytic degradation (PBS) and bioactivity (SBF) of the scaffolds. Following this, we cultured h-MSCs pooled from 3 donors within these scaffolds and evaluated protein levels of osteogenic, chondrogenic, and adipogenic markers after 14 days of culture to gain insight into the intrinsic capacity of the various scaffolds to promote specific osteogenic differentiation of h-MSCs.

Previous work utilizing PD coatings has demonstrated their ability to enhance bioactivity and cell attachment.[37, 49] Consistent with what was previously reported, the presence of PD-coating on both PCL-DA and PCL-DA/PLLA scaffolds resulted in an enhanced HAp mineral deposition relative to the uncoated scaffolds. On the other hand, our reported equal DNA measures suggest equal cell numbers within the scaffolds. Conflicting investigation by Chuah *et al*.[178] demonstrated how PD coating on polydimethylsiloxane substrates enhanced h-MSC adhesion. Similarly, we also observed differences in cell-adhesion when culturing osteoblasts on PD-coated PCL-DA scaffolds.[18] The discrepancy between these previously reported results and our current observations may be explained due to the absence of any cell-adhesion peptides (e.g. RGDS) in both cases. This may suggest that the presence of cell-adhesion peptides in our scaffolds predominates any conferred augmentation to cell-adhesion arising from PD coating.

The combination of PD coating and PCL-DA/PLLA semi-IPN scaffold chemistry (i.e. PD-PCL-DA/PLLA) imparted the greatest increase in osteogenic protein expression by h-MSCs compared to the other scaffolds (i.e. PD-PCL-DA, U-PCL-DA, and U-PCL-DA/PLLA). It is important to note that in this investigation, the intrinsic capacity of the scaffolds was assessed in the absence of osteogenic supplements (L-ascorbic acid 2-phosphate, β-glycerophosphate, and dexamethasone). This allows reported enhancement in osteogenic differentiation of h-MSCs on PD-PCL-DA/PLLA scaffolds to be attributed to alterations in scaffold chemistry[179, 180] – which has previously been demonstrated to guide stem cell differentiation.[181-184] For instance, Yao *et al.*[185] investigated how modification of hydrophobic PCL substrates with the relatively hydrophilic PLA may enhance osteogenic differentiation of h-MSCs. Furthermore, PD – known for improving material hydrophilicity[186] – was reported by Xu *et al.*[187] and Deng *et al.*[188] to enhance osteogenic differentiation of MSCs coupled with changes in substrate chemistry on HAp/polyamide 66 and electrospun PCL substrates, respectively. Overall, these results indicate that incorporating PLLA, and PD coatings in PCL-DA-based SMPs may improve their osteoinductive properties through optimization of surface properties.

Recent studies have indicated alternate mechanisms to the osteogenic properties of PD coatings[189] through the dopaminergic activation of D1-like and D2-like receptors.[190-192] Specifically, Wang *et al.*[191] demonstrated how activation of D1 receptors, through dopamine or D1-agonist treatment, promoted osteogenesis of h-MSCs. Similarly, Lee *et al.*[192] showed that, in the absence of osteogenic media supplements, dopaminergic activation of D1-like and D2-like receptors increased the expression of *Osterix* and

RUNX2 genes in MC3T3-E1 osteoblasts. It is important to note that the work of Lee *et al*.[192] was emulating the leaching of dopamine from PD coatings, which is implicated in shaping PD's dopaminergic and subsequent osteogenic effects. As a result, this may provide additional explanation to the observed increase in osteogenic protein expression by h-MSCs cultured on PD-coated scaffolds.

In the absence of osteogenic supplements, protein level assessment of h-MSCs cultured on PCL-DA/PLLA semi-IPN scaffolds revealed an increase in expression of osteogenic markers osterix, BMP-4 and COL1A1, relative to PCL-DA. It is also important to note that the expression levels of osteogenic proteins by h-MSCs on these SMP scaffolds were – with the exception of osterix - equivalent to levels induced by osteogenic supplements. In contrast, expression levels of studied chondrogenic and adipogenic proteins were, respectively, comparable to and below those observed in U-PCL-DA OM controls. Cumulatively, the present results indicate the osteogenic response supported by these scaffolds is largely specific. To increase the specificity of the observed osteogenic response, future approaches utilizing PCL-DA/PLLA scaffolds may incorporate osteoinductive growth factors – such as BMPs[191] – or additional peptide sequences known to promote osteogenic differentiation.[193, 194]

3.6. Conclusions

The work herein compares the intrinsic capacity of PCL-DA and PCL-DA/PLLA semi-IPN SMP scaffolds, with and without a PD coating, in directing specific h-MSC osteogenic differentiation. Our results demonstrate that, in the absence of osteogenic supplements, the inclusion of thermoplastic PLLA into the PCL-DA network to form a semi-IPN promoted greater osteoinductive effects by h-MSCs when compared to PCL-DA. Furthermore, coating these scaffolds with the bioinspired PD elevated expression levels of proteins associated with osteogenic differentiation in h-MSCs, and induced HAp mineralization following SBF (1X) treatment. Furthermore, the osteogenic response associated with the scaffolds appeared to be largely specific. Overall, these SMP scaffolds could potentially serve as self-fitting, tissue-engineered constructs for treating irregular CMF defects through promoting osteoinduction of native progenitor cells and osteoconduction to facilitate bone ingrowth.

4. PCL-BASED SHAPE MEMORY POLYMER (SMP) SEMI-IPNS: THE ROLE OF MISCIBILITY IN TUNING THE DEGRADATION RATE*

4.1. Overview

The utility of poly(ε-caprolactone) (PCL) as a shape memory polymer (SMP) may be improved by accelerating its degradation. Recently, we reported novel semi-interpenetrating networks (semi-IPNs) comprised of crosslinked PCL diacrylate (PCL-DA) and thermoplastic poly(L-lactic acid) (PLLA) that exhibited SMP behavior, accelerated degradation and enhanced moduli versus the PCL-DA control. Herein, we systematically varied the thermoplastic component of the PCL-based semi-IPNs, incorporating homo- and copolymers based on lactic acid of different M_n, hydrophilicity and crystallinity. Specifically, semicrystalline PLLAs of different M_n (7.5 k, 15 k, 30 k and 120 k) were explored as the thermoplastic in the semi-IPNs. Additionally, to probe crystallinity and hydrophilicity, amorphous (or nearly amorphous) thermoplastics of different hydrophilicities (PDLLA and PLGAs 85:15, 70:30 and 50:50, L-lactide:glycolide wt% ratio) were employed. For all semi-IPNs, the wt% ratio of the crosslinked PCL-DA to thermoplastic was 75/25. The nature of the thermoplastics was linked to semi-IPN miscibility and the trends in accelerated degradation rates.

∗ Reprinted with permission from "PCL-Based Shape Memory Polymer (SMP) Semi-IPNs: The Role of Miscibility in Tuning the Degradation Rate" by Pfau, M.R., McKinzey, K.G., Roth, A.A., and Grunlan, M.A., 2020. *Biomacromolecules*, 21, 2493-2501, Copyright [2020] by American Chemical Society.

4.2. Introduction

Poly(ε-caprolactone) (PCL) is a thermoresponsive shape memory polymer (SMP) that has been explored as self-expanding stents,[195-197] self-tightening sutures,[4, 198, 199] and, recently by our group, as self-fitting scaffolds to treat irregularly-shaped bone defects.[37, 69, 71] The crystalline lamellae of PCL serve as "switching segments", actuated by a thermal melting temperature (T_m, ~55 °C). Thus, PCL solid films or porous scaffolds are able to hold a temporary shape following sequential heating ($T > T_m$), shaping and cooling ($T < T_m$) and are able to recover their original shape upon heating ($T > T_m$).[37, 69, 71] The slow degradation rate of PCL (> 24 months) is a major limitation in its utility and is attributed to its high crystallinity (~45%) and hydrophobicity.[200-202] In general, for aliphatic homopolyesters, increased rates of degradation are associated with greater hydrophilicity and lower crystallinity. For instance, compared to PCL, poly(glycolic acid) (PGA; ~45-65% crystalline) degrades more quickly (~6-12 months) as a result of its enhanced hydrophilicity. Attributed to its hydrophobicity and semi-crystallinity (~25-35%) poly(L-lactic acid) (PLLA) likewise degrades slowly (>24 months) whereas amorphous poly(D,L-lactic acid) (PDLLA) degrades more quickly (2-16 months).[201, 202] While a lack of crystallinity is often associated with a desirably faster degradation rate, it occurs with a reduction in rigidity and strength. Moreover, retention of PCL crystallinity is essential to its shape memory behavior.

A strategy to modify PCL that would accelerate the rate of degradation but also improve mechanical properties and without loss of shape memory behavior is highly desirable. To tailor rates of degradation, most often, two or more polyesters are combined as copolymers or as blends.[203-205] For instance, poly(L-lactic-*co*-glycolic acid) (PLGA) copolymers degrade faster than the parent homopolymers and rates may be tuned by the lactic to glycolic acid mol % ratio, from ~1-2 months (50:50) to ~5-6 months (85:15).[206, 207] However, since PLGA copolymers are generally amorphous, they exhibit reduced moduli values versus PGA or PLLA.[202, 206] Likewise, PCL has been copolymerized with D,L-lactide and glycolide, resulting in amorphous copolymers with faster rates of degradation but with a reduction in PCLs crystallinity.[208] PDLLA-PCL-PDLLA triblock copolymers degraded faster than the PCL homopolymer and exhibited a PCL T_m, but % crystallinity was not quantified nor were mechanical properties.[209] PCL has also been incorporated into blends, namely for the purpose of enhancing the ductility and toughness of PLLA.[210-212] By improving miscibility (i.e. reducing phase separation) with compatibilizers[213-215] or reactive mixing,[216, 217] the mechanical properties of PCL/PLLA blends can be improved. In contrast, the immiscibility of PCL/PLLA blends contributes to enhanced rates of degradation.[218] None of aforementioned strategies utilize cross-linked PCL network in combination with other polymers as a potential route to materials with a combination of shape memory behavior, accelerated degradation, and robust mechanical properties.

We have previously reported SMP PCL networks prepared from the photocrosslinking of semi-crystalline PCL-diacrylate (PCL-DA).[37, 69] Subsequently, semi-interpenetrating networks (semi-IPNs) were formed comprised of a crosslinked PCL-DA network and thermoplastic PLLA (M_n = 15 kDa).[71, 159] Due to the retention of PCL crystallinity the semi-IPNs retained their shape memory behavior. At a wt% ratio of 75/25

(PCL-DA/PLLA), semi-IPN scaffolds exhibited a superior modulus and strength but also an accelerated rate of degradation. Notably, the degradation of the semi-IPN was faster than that of the analogous blend. The accelerated degradation of the semi-IPNs was speculated to be related to phase separation.[157] The ability to accelerate the degradation of PCL via a semi-IPN design, without compromising shape memory or mechanical properties, holds potential to improve the performance of numerous bioresorbable devices.

Herein, the thermoplastic PLA within a PCL-based semi-IPN was systematically varied to examine the impact on semi-IPN degradation and mechanical properties (**Figure 4-1**). For ***Group A***, semi-crystalline PLLAs of varying M_ns were incorporated as the thermoplastic component to assess the impact of thermoplastic M_n on semi-IPN properties. For ***Group B***, semi-crystalline PLLA as well as amorphous PDLLA and various amorphous/nearly amorphous PLGAs (85:15, 70:30 and 50:50, L-lactide:glycolide) were incorporated as the thermoplastic (M_n maintained at ~15 kDa) to assess the impact of hydrophilicity on semi-IPN properties. For all semi-IPNs, the wt% ratio of PCL-DA to thermoplastic was maintained at 75/25. The extent of phase separation was evaluated via scanning electron microscopy (SEM). Additionally, the degradation rates and accompanying erosion behavior, shape memory behavior and mechanical properties were assessed. For select compositions, the impact of thermal annealing on miscibility and subsequent degradation rates and mechanical properties was also evaluated.

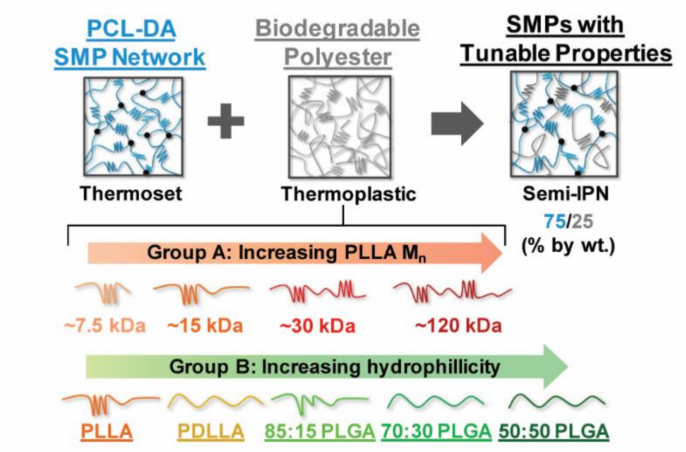

Figure 4-1. Semi-IPN compositions based on a PCL-DA network and varying PLA-based thermoplastics. *Group A*: semi-crystalline PLLA of varying M_ns and *Group B*: semi-crystalline PLLA (~15 kDa), amorphous PDLLA (~15 kDa) and amorphous/nearly amorphous PLGAs (85:15, 70:30 and 50:50, ~15 kDa). The semi-IPNs are designated by the thermoplastic component.

4.3. Experimental

4.3.1. Materials

PCL-diol (M_n = 10 kDa per manufacturer specifications), 4-(dimethylamino)pyridine (DMAP), trimethylamine (Et_3N), acryloyl chloride, potassium carbonate (K_2O_3), anhydrous magnesium sulfate ($MgSO_4$), (3S)-*cis*-3,6-dimethyl-1,4-dioxane-2,5-dione (L-lactide), 3,6-dimethyl-1,4-dioxane-2,5-dione (lactide), glycolide, tin(II) 2-ethylhexanoate [$Sn(Oct)_2$], ethylene glycol, PLLA (M_n ~120 kDa), 2,2-dimethoxy-2-phenyl acetophenone (DMP), 1-vinyl-2-pyrrolidinone (NVP), sodium hydroxide (NaOH) and common solvents were purchased from Sigma-Aldrich. All solvents and ethylene glycol were dried over 4 Å molecular sieves prior to use. All monomers and polymers were vacuum dried prior to use.

4.3.2. Syntheses

All reactions were run under a nitrogen (N_2) atmosphere with a Teflon-covered stir bar. Chemical structures (including % acrylation and M_n) were confirmed with ^{1}H NMR spectroscopy (Inova 500 MHz spectrometer operation in the FT-mode with $CDCl_3$ as the standard). The purified polymers' thermal properties were characterized using differential scanning calorimetry (DSC, TA Instruments Q100) as described below.

PCL-diol (M_n = 10 kDa; T_g = -65 ºC, T_m = 53 ºC, 46.5% crystallinity) was reacted with acryloyl chloride to prepare PCL-diacrylate (PCL-DA) as previously reported.[69] Briefly, PCL-diol (20.0 g, 2.0 mmol) was dissolved in CH_2Cl_2 (120 mL) with DMAP (6.6 mg) as the catalyst. After purging with N_2, triethylamine (4.0 mmol) and acryloyl chloride (8.0 mmol) were sequentially added to the flask via dropwise incorporation and the reaction was stirred at RT for 30 min. The crude polymer was purified to obtain PCL-DA (M_n confirmed ~10 kDa via ^{1}H NMR end group analysis, >90% acrylation, >80% yield).[69] PLLAs [7.5 kDa, 15 kDa and 30 kDa] were prepared via a ring opening polymerization (ROP) of L-lactide (6.0 g) using ethylene glycol as the initiator and $Sn(Oct)_2$ as the catalyst at 120 ºC overnight.[219] The M_n was controlled via molar equivalence ratio of monomer to initiator: [52:1] (7.5 kDa), [104:1] (15 kDa) and [208:1] (30 kDa). The crude products were each dissolved in a minimal amount of $CHCl_3$, precipitated in methanol, filtered and vacuum dried. The M_n of the purified products were verified by ^{1}H NMR end group analysis (C**H** δ = 5.2 ppm and C**H₃** δ = 1.5 ppm in repeat unit compared to terminal C**H₃** δ = 4.4 ppm). PLLA [120 kDa] was used without further purification. PLLAs exhibited the following thermal transitions: 7.5 kDa [T_g = 45 ºC, T_m = 153 ºC, 49.3% crystallinity], 15 kDa [T_g = 45 ºC, T_m = 155 ºC, 52.7% crystallinity], 30 kDa [T_g = 46 ºC, T_m = 159 ºC, 56.2% crystallinity] and 120 kDa [T_g = 50 ºC, T_m = 170 ºC, 20.0% crystallinity].

PDLLA [15 kDa] was prepared via ROP of D,L-lactide (6.0 g) as above and the M_n of the purified product likewise verified by ^{1}H NMR end group analysis. The PDLLA exhibited the following thermal transitions: T_g = -28 ºC, no T_m observed, 0% crystallinity.

PLGAs [15 kDa] were similarly prepared via ROP of different molar ratios of L-lactide to glycolide [85:15, 70:30, and 50:50, 6.0 g monomer total for all PLGA ROPs]. The M_n of the purified products were verified by ^{1}H NMR end group analysis (C**H** δ = 5.2 ppm and C**H₃** δ = 1.5 ppm in repeat unit compared to terminal C**H₃** δ = 4.4 ppm). The target ratios of L-lactide to glycolide were verified using ^{1}H NMR (C**H** δ = 5.2 ppm and C**H₃** δ = 1.5 ppm in the PLLA repeat unit compared to C**H₂** δ = 4.6-4.8 ppm in the PGA repeat unit). The PLGAs exhibited the following thermal transitions: 85:15 (T_g = 41 ºC, T_m = 137 ºC, 3.2% crystallinity), 70:30 (T_g = 37 ºC, no T_m observed, 0% crystallinity), and 50:50 (T_g = 21 ºC, no T_m observed, 0% crystallinity).

4.3.3. Film Fabrication

All semi-IPN films were prepared with a 75/25 wt% ratio of PCL-DA to the designated PLA thermoplastic. For ***Group A***, PLLAs of varying M_ns (7.5 kDa, 15 kDa, 30 kDa, and 120 kDa) were incorporated as the thermoplastic. For ***Group B***, PDLLA (15 kDa) and PLGAs (15 kDa) [85:15, 70:30, and 50:50 molar ratios of L-lactide to glycolide] were incorporated as the thermoplastic. The semi-IPNs are herein denoted according to their thermoplastic component (e.g. ***7.5k PLLA*** for the PCL-DA/7.5 kDa PLLA semi-IPN, PDLLA for the PCL-DA/PDLLA semi-IPN and ***85:15 PLGA*** for the PCL-DA/85:15

PLGA semi-IPN). A PCL-DA/PCL-diol semi-IPN control (***PCL-diol***) was prepared by incorporating PCL-diol (M_n ~10 kDa) as the thermoplastic component into the PCL-DA. A 100% PCL-DA only control (***100% PCL-DA***; i.e. no thermoplastic) was also prepared.

Semi-IPN films were prepared from polymer solutions with the designated polymer(s) (25 wt% total polymer in DCM) using 15 vol% photoinitiator solution (10 wt% DMP in NVP). The solution was transferred to a silicone mold (2 mm thickness; McMaster-Carr) secured between two glass slides and was exposed to UV light (UV-Transilluminator, 6 mW cm^{-2}, 365 nm) for 3 min per side. The solvent-swollen discs were sequentially air dried (RT, overnight), dried under vacuum (RT, 4 h, 30 in. Hg), soaked in EtOH on a shaker table (3 h, 150 rpm), air dried (RT, overnight) and lastly annealed (85 °C, 1 h, 30 in. Hg). In addition, select semi-IPN films [***15k PLLA***, ***PDLLA***, ***85:15 PLGA***] and the ***100% PCL-DA*** control were also fabricated as above but with a higher annealing temperature (170 °C, 1 h, 30 in. Hg). The final thickness of films was ~1.1 mm. Blend controls were prepared at a 75/25 wt% ratio of PCL-diol to a particular PLA thermoplastic (15k PLLA, PDLLA and 85:15 PLGA). These blends as well as the PCL-diol only control were prepared as films (5 mm x 1.1 mm, McMaster-Carr) via simple melt casting, where the polymer(s) were heated to just above any T_m of the polymer(s) and ~35 mg of polymer mixture was cast into a silicone mold (5 mm x 1.1 mm, McMaster-Carr) on top of a glass slide. Films were removed from heat after 3 min and were allowed to set at RT for > 24 h. All films were stored in a desiccator prior to use.

4.3.4. Thermal Transitions and % Crystallinity

Differential scanning calorimetry (DSC; TA Instruments Q100) was utilized to determine the thermal transitions (T_g and T_m) and % crystallinity of thermoplastic polymers as well as semi-IPN films. Specimens (~10 mg; *N* = 3) were sealed in hermetic pans were heated from RT to 200 °C at a heating rate of 5 °C min^{-1}. For thermoplastic polymer, values were taken from the second DSC cycle to remove any thermal history. For semi-IPN films, values were taken from the first DSC cycle to account for the thermal history endued by the fabrication. From the endothermic PCL and PLLA melting peaks, T_m and enthalpy change (ΔH_m) were measured. Percent crystallinity (% χ_c) of thermoplastic polymers was calculated via

$$\%\chi_c = \frac{\Delta H_m - \Delta H_c}{\Delta H_m^{\circ}} * 100$$

where ΔH_m is the enthalpy of fusion taken from the integral of the endothermic melt peak, ΔH_c is the enthalpy of crystallization from the exothermic cold crystallization peak, and ΔH_m° is the theoretical value for 100% crystalline PCL (139.5 J/g)[220] or PLLA (93.0 J/g).[221] For semi-IPN films, a correction factor was used to account for the weight percent of each polymer component:

$$\%\chi_c = \frac{\Delta H_m - \Delta H_c}{\Delta H_m^{\circ} * w} * 100$$

where w is the mass fraction of the given polymer component.

4.3.5. Thermal Gravimetric Analysis (TGA)

TGA (TA Instruments Q50) of semi-IPN films (~10 mg, *N* = 1) in platinum pan were run under N_2 from RT to 500 °C at a heating rate of 10 °C min^{-1}. The mass of the samples throughout heating was determined to quantify percent mass loss.

4.3.6. Sol Content

Discs (~5 mm x ~1.1 mm; *N* = 3) were immersed in 10 mL CH_2Cl_2 using one specimen per scintillation vial. Vials were maintained for 48 h at 150 rpm (VWR Mini Shaker). Swollen discs were then removed, air dried and dried *in vacuo* (30 in. Hg, RT, ~24 h), and the mass of dried discs was determined to quantify percent mass loss (i.e. sol content).

4.3.7. Degradation Behavior

Base-catalyzed accelerated degradation tests were performed in 1 M NaOH according to ASTM F1635. Film specimens (d ~5 mm, h ~1.1 mm) (*N* = 3 per time point) were immersed in 10 mL of the basic solution in a sealed glass vial and maintained at 37 °C at 60 rpm (VWR Benchtop Shaking Incubator Model 1570). At each designated time point (8, 24, 48, 72, 120 and 168 h), specimens were removed from the solution, thoroughly rinsed with DI water, blotted and dried under vacuum (RT, overnight, 30 in. Hg). For each specimen, the initial mass and mass at the designated time point were measured with an analytical balance. Specimens were utilized for a single time point only. Surface and cross-section images of select specimens (those with a mass loss of ~ 20%) were obtained for SEM. Films were subjected to Au-Pt sputter coating (~7 nm) and images were obtained with a Tescan Vega 3 SEM (accelerating voltage of 10 kV).

4.3.8. Phase Separation

SEM images of a film surfaces was likewise performed to assess differences in phase separation (i.e. miscibility).

4.3.9. Tensile Properties

Tensile properties of films were evaluated at RT with a tensile tester (Instron 5944). Rectangular specimens (l ~29 mm, w ~5 mm, t ~0.9 mm; $N = 8$) were secured with pneumatic clamps (gauge length of 7 mm) and subjected to a constant rate of strain (50 mm/min). From the resulting stress-strain curves, modulus (E) and tensile strength (TS) were determined.

4.3.10. Shape Memory Behavior

Rectangular specimens (l ~20 mm × w ~5 mm × t ~0.9 mm) were subjected to the following sequence: (1) after exposure to a water bath at 85 °C ($T > T_m$) for 1 min, deform the film strip into a coiled shape with a metal mandrel, (2) cool at RT for 3 min to fix this temporary shape, (3) place the fixed coil in the 85 °C water bath and observe recovery at t = 0 and 10 s.

4.3.11. Statistical Analyses

Data were reported as a mean ± standard deviation. Values were compared in GraphPad Prism via ANOVA followed by a t-test where a p-value of < 0.05 was considered statistically significant.

4.4. Results and Discussion

4.4.1. Synthesis of Thermoplastic Polymers

Prior to their incorporation into semi-IPN films, all thermoplastic polymers were extensively characterized in terms of their structure and M_n (by ^{1}H NMR) as well as their T_g, T_m and % crystallinity (by DSC) (**Figure A-1**). The targeted M_ns were achieved as were the ratios of L-lactide to glycolide for PLGA copolymers. For PLLAs, % crystallinity was generally similar (~49 to 56%) as the M_n increased (7.5 kDa to 30 kDa, respectively), but then decreased substantially for the 120k PLLA (~20%). This decreased % crystallinity for high M_n PLLA is consistent with prior reports.[222] While 70:30 and 50:50 PLGA copolymers were amorphous, the 85:15 PLGA (i.e. the highest L-lactide content) exhibited a very low level of PLLA % crystallinity (~3%), also in agreement with prior literature.[207, 223]

4.4.2. Semi-IPN Fabrication

Semi-IPNs comprised of crosslinked PCL-DA and a PLA-based thermoplastic were prepared to assess the resulting impact on material properties. For ***Group A***, semi-crystalline PLLAs of varying M_ns were incorporated as the thermoplastic component to assess the impact of thermoplastic M_n on semi-IPN properties. For ***Group B***, semi-crystalline PLLA, amorphous PDLLA and various amorphous/nearly amorphous PLGAs (85:15, 70:30 and 50:50, L-lactide:glycolide) were incorporated as the thermoplastic (M_n maintained at ~15 kDa) to assess the impact of hydrophilicity on semi-IPN properties. The comparison of PLLA (15k) and PDLLA (15k) permitted evaluation of effect of crystallinity. Additionally, comparison of PDLLA and PLGAs allowed assessment of hydrophilicity. PCL-DA/PCL-diol semi-IPN control (***PCL-diol***) was prepared by incorporating PCL-diol (M_n ~10 kDa) as the thermoplastic component into the PCL-DA.

The targeted 75/25 wt% ratio of PCL-DA to PLA thermoplastic (i.e. that of the precursor solutions) in the resulting semi-IPN films were confirmed with TGA experiments (**Figure 4-2-a**). The thermoplastic polymers underwent a distinct onset of thermal degradation at a temperature lower than that of the PCL-DA network (~250 ºC versus >400 ºC). All semi-IPNs showed ~25% mass loss at temperatures below 400 °C, indicating a 75:25 wt% ratio of PCL-DA to thermoplastic. Because the PCL-diol displayed thermal stability similar to the PCL-DA, its wt% ratio of the ***PCL-diol*** semi-IPN could not be likewise confirmed.

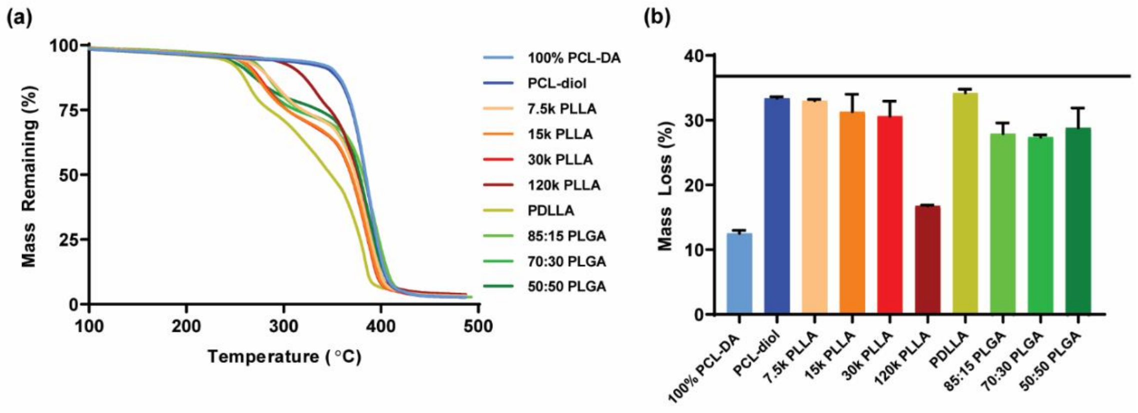

Figure 4-2. TGA results verifying ~25% thermoplastic in PCL-DA/PLA semi-IPNs (a) and sol content values demonstrating adequate cross-linking with an upper limit of ~37% mass loss [~12% 100% PCL-DA control + ~25% thermoplastic] for semi-IPN films (b).

Additionally, the sol content values of films were determined to confirm adequate cross-linking of the PCL-DA upon formation of the semi-IPNs (**Figure 4-2-b**). The ***100% PCL-DA*** control film (i.e. no thermoplastic) had a sol content value of ~12%. None of the semi-IPNs exceeded 37% sol content, a maximum value expected based on combined contributions of sol from the PCL-DA (~12%) and the thermoplastic polymer (~25%). The sol content of the ***120k PLLA*** (i.e. the semi-IPN comprised of PCL-DA and 120k PLLA) was particularly low (~15%) versus all other semi-IPNs which was attributed to the diminished capacity of this high M_n PLLA to be extracted. These sol content results confirm that PCL-DA (>95% acrylation) was able to undergo crosslinking in the presence of all PLA thermoplastics, effectively forming the designated PCL-DA/PLA semi-IPN compositions.

4.4.3. Degradation Behavior

PCL-DA/PLA semi-IPN degradation rates were affected by the PLA-based thermoplastic's M_n (***Group A***) and hydrophilicity as well as crystallinity (***Group B***) (**Figure 4-3**). For ***Group A*** semi-IPNs, the rates of degradation were distinctly faster when based on lower M_n semi-crystalline PLLAs (7.5k, 15k and 30k) versus the highest M_n semi-crystalline PLLA (120k). In fact, the degradation profile of the ***120k PLLA*** semi-IPN was similarly as slow as the ***100% PCL-DA*** and ***PCL-diol*** controls. The ***15k PLLA*** semi-IPN degraded faster than the other semi-IPNs in this group. For ***Group B*** semi-IPNs, the thermoplastic M_n was maintained at 15 kDa and were semi-crystalline (15k PLLA) or amorphous/nearly amorphous but varied in terms of hydrophilicity (i.e. PDLLA < 85:15 PLGA < 70:30 PLGA < 50:50 PLGA). For this group, the ***15k PLLA*** semi-IPN degraded most rapidly whereas the ***85:15 PLGA*** and ***PDLLA*** semi-IPNs degraded at fast but relatively intermediate rates and the ***70:30 PLGA*** and ***50:50 PLGA*** semi-IPNs degraded at slow rates similar to the controls. The ***15k PLLA*** semi-IPN degraded faster than the ***PDLLA*** semi-IPN and all other semi-IPNs in this group.

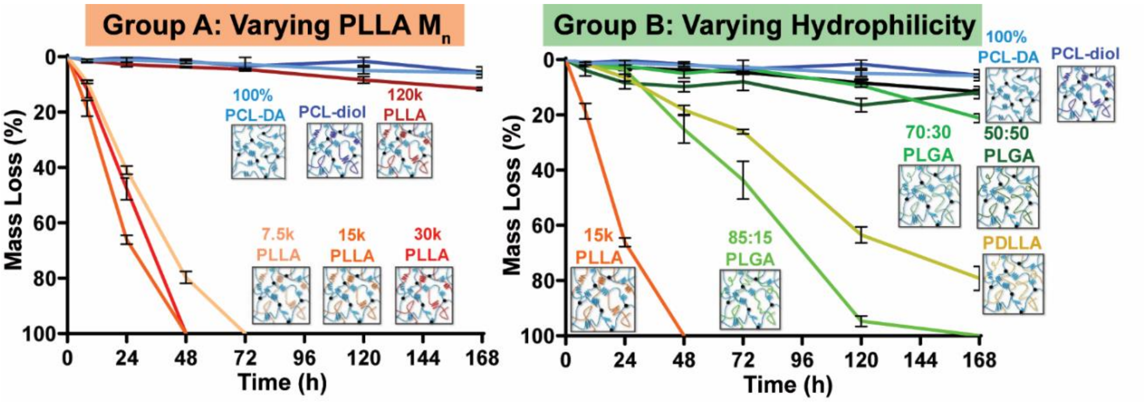

Figure 4-3. Mass loss under accelerated conditions (1 M NaOH, 37 °C, 60 rpm) for semi-IPNs and controls. The semi-IPNs are designated by the thermoplastic component.

The semi-IPNs and controls were subsequently grouped into two categories according to their relative degradation rates: “fast” (***15k PLLA*** > ***30k PLLA*** ≈ ***7.5k PLLA*** > ***PDLLA*** ≈ ***85:15 PLGA)*** and “slow” (***70:30 PLGA*** > ***120k PLLA***≈ ***50:50 PLGA*** > ***PCL-diol*** ≈ ***100% PCL-DA)*** (**Figure 4-4**). Mass loss as well as SEM of film surfaces were acquired at different time points (8 h, 48 h and 1 week) during degradation to reveal distinctions in degradation rates and the accompanied erosion behavior. At just 8 h, the “fast” degrading ***15k PLLA*** semi-IPN exhibited statistically greater mass loss (~20% mass loss) and visual evidence of erosion versus the ***7.5k PLLA*** and ***30k PLLA*** semi-IPNs (mass loss ~10%) (**Figure 4-4-a**). By 48 h, all three of these semi-IPNs had completed degraded (i.e. 100% mass loss). Amongst the next “fast” degrading semi-IPNs, substantial mass loss and erosion was apparent after 48 h, with the ***PDLLA*** and ***85:15 PLGA*** semi-IPNs exhibiting statistically similar mass loss (~20% mass loss) (**Figure 4-4-b**). At 1 week, nearly complete mass loss was observed for these two semi-IPNs. Finally, for "slow" degrading semi-IPNs, only at 1 week did these exhibit appreciable mass loss (**Figure 4-4-c**). Here, the ***70:30 PLGA*** semi-IPN (~20% mass loss) degraded faster versus the ***120k PLLA*** and ***50:50 PLGA*** semi-IPNs (~10% mass loss) whereas the ***PCL-diol*** semi-IPN control and ***100% PCL-DA*** controls degraded slowest (~5% mass loss). Corresponding SEM images of specimen cross-sections were obtained and likewise highlight the observed trends observed in the SEM images of film surfaces (**Figure 4-5**). The fastest degrading compositions exhibited signs of surface erosion but this may be attributed to the base-catalyzed conditions, which has been reported for the previously studied ***15k PLLA*** semi-IPN[157] and for various PLLA-based polyesters.[224]

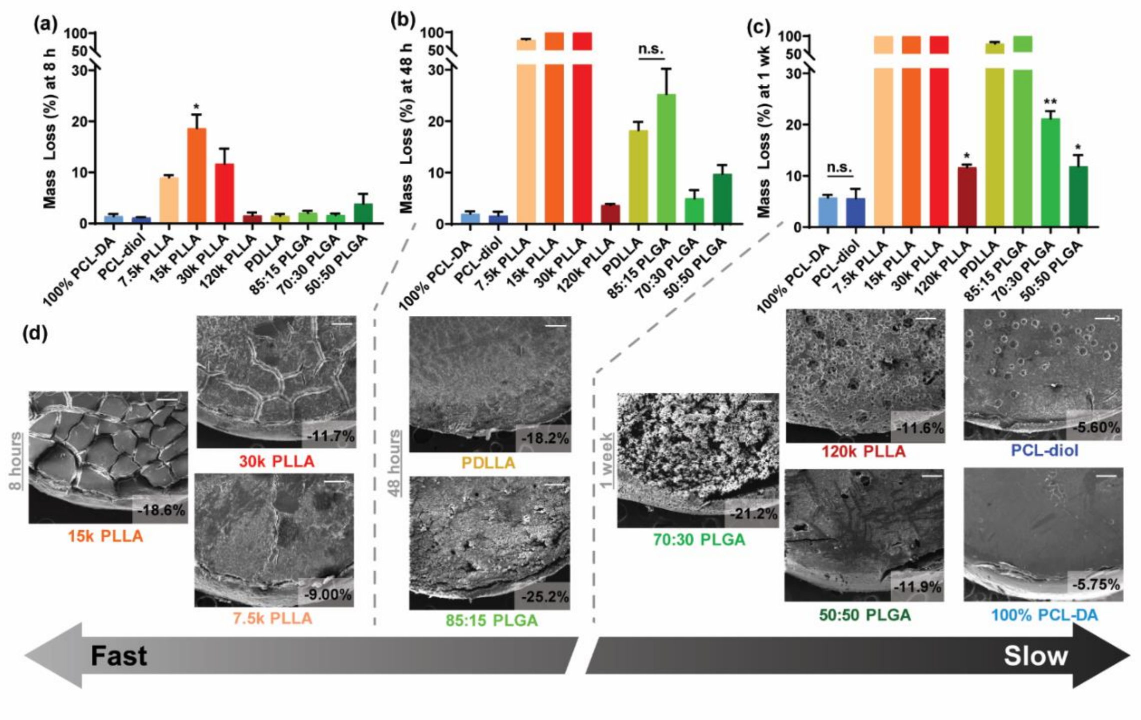

Figure 4-4. Mass loss under accelerated conditions (1 M NaOH, 37 °C, 60 rpm) for semi-IPNs and controls (a-c) and corresponding SEM images of film surfaces at the noted time points (d). Scale bars = 250 µm.

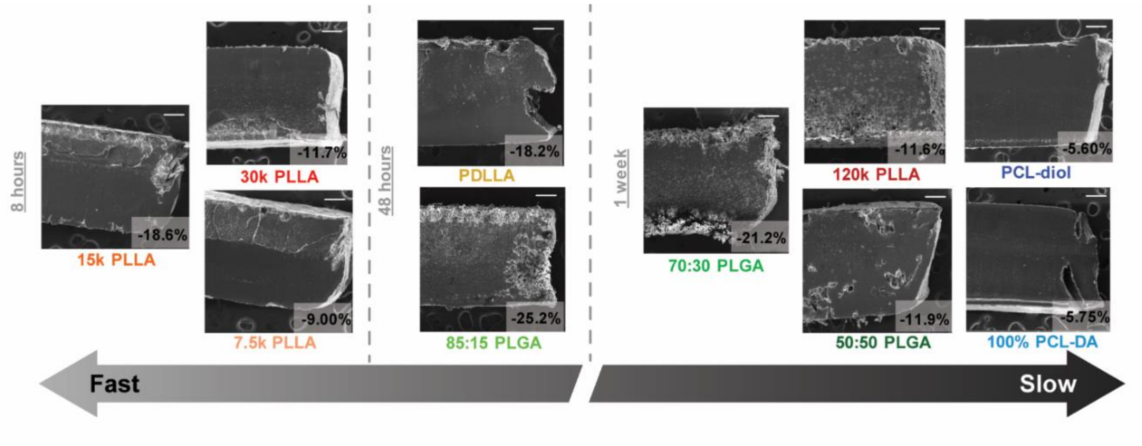

Figure 4-5. SEM of degraded film cross-sections at noted timepoints and ranking of PCL-DA/PLA semi-IPNs based on degradation rate. Average mass loss values are noted on the SEM images. Scale bars = 250 µm.

These differences in semi-IPN degradation rates were assessed based on the following considerations: PCL % crystallinity, PLLA % crystallinity, and finally, the extent of phase separation (i.e. immiscibility) observed in the semi-IPNs. First, PCL % crystallinity was considered since a reduction would be expected to produce accelerated degradation rates. However, this was statistically similar among all the semi-IPNs (~40%; corrected for relative mass percent of PCL-DA in the semi-IPN) (**Figure 4-6-a**). Next, the PLLA % crystallinity of semi-IPNs was assessed in cases where prepared with thermoplastics that were semi-crystalline (**Figure 4-6-b**). Among ***Group A***, the PLLA % crystallinity of the ***120k PLLA*** semi-IPN (~33%) was significantly reduced versus that of ***7.5k***, ***15k*** and ***30k PLLA*** semi-IPNs (~45%). The relative rates of hydrolytic degradation of PLLA homopolymers are known to increase with an increase in PLLA M_n, provided there is a concomitant decrease in % crystallinity which promotes water diffusion.[222] In this study, the ***120k PLLA*** semi-IPN degraded slowly despite it being the least crystalline of the PLLAs investigated. For ***Group B***, it was noted that 85:15 PLGA thermoplastic exhibited minor % crystallinity (~3%), but for the ***85:15 PLGA*** semi-IPN, the PLLA % crystallinity increased (~20%) (**Figure 4-6-b**). Interestingly, in this group, the ***15k PLLA*** semi-IPN degraded the most quickly followed by the ***85:15 PLGA*** and ***PDLLA*** semi-IPNs, while the degradation rates of the ***70:30 PLGA*** and ***50:50 PLGA*** semi-IPNs were slow, similar to the ***PCL-diol*** and ***PCL-DA*** controls. Thus, in these PCL-based semi-IPNs, the incorporation of relatively more crystalline and hydrophobic PLA-based polymers ultimately resulted in faster rates. This is contrary to the trends of hydrolysis rates of homo- or copolymers based on crystallinity and hydrophilicity. Therefore, the extent of phase separation (i.e. immiscibility) was finally considered to explain the relative degradation rates of the semi-IPNs.

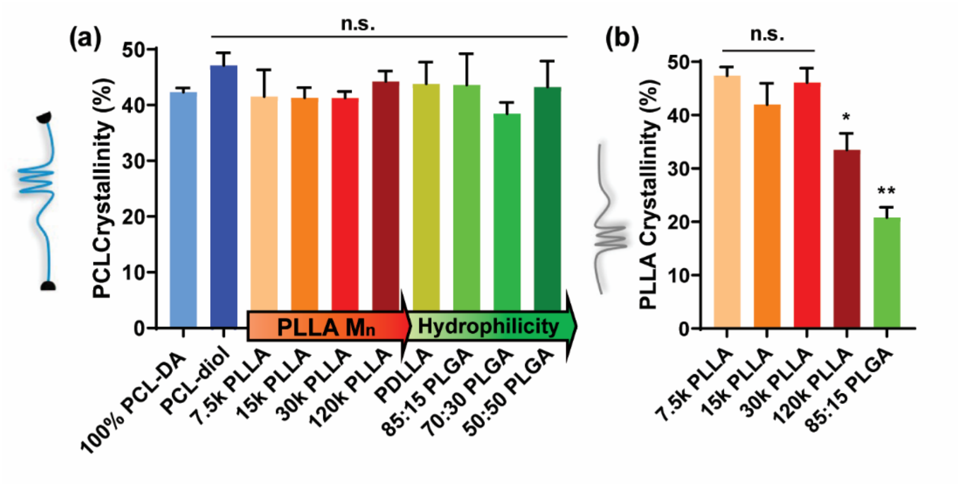

Figure 4-6. PCL % crystallinity of semi-IPNs was maintained at ~40% (corrected for relative mass percent of PCL-DA in the semi-IPN), *$p < 0.05$ versus *PCL-DA* (a). PLLA % crystallinity of the ***120k PLLA*** semi-IPN (~33%) was significantly reduced versus that of ***7.5k, 15k*** and ***30k PLLA*** semi-IPNs (~45%). PLLA % crystallinity of the ***85:15 PLGA*** semi-IPN increased to ~20% (versus ~3% for PLGA thermoplastic). *$p < 0.05$ and **$p < 0.01$ versus ***7.5k PLLA.***

It has been previously shown that the degree of phase separation in polymer blends can influence degradation as well as mechanical properties.[210, 211, 225] SEM imaging has been previously used to categorize the degree of immiscibility in polymer systems, where phase separation is marked by coalescence, or defined circular regions where one polymer has separated from the other.[226, 227] Prior to degradation, SEM images of the controls and semi-IPN film surfaces (**Figure 4-7**) and cross-sections (**Figure 4-8**) revealed distinct phase morphologies. Each composition was characterized as "miscible", "partially miscible" or "immiscible" and was noted as corresponding to "slow", "fast" or "slow" degradation rates, respectively. The ***PCL-diol*** semi-IPN and ***100% PCL-DA*** control, the slowest degrading films, exhibited the highest degree of miscibility as evidenced by their uniform morphologies. This was expected based on their chemical homogeneity. Slow degrading ***120k PLLA*** (***Group A***) and ***70:30 PLGA*** and ***50:50 PLGA*** (***Group B***) semi-IPNs exhibited the highest degree of immiscibility as evidenced by distinct domains indicative of polymer coalescence. Semi-IPNs ***15k PLLA***, ***7.5k PLLA,*** and ***30k PLLA*** (***Group A***) and ***PDLLA*** and ***85:15 PLGA*** (***Group B***) were deemed as being "partially miscible" based on their intermediate morphologies; these corresponded to the fastest degradation rates. In the case of the ***15k PLLA*, *7.5k PLLA*** and ***30k PLLA*** semi-IPNs, their partial miscibility (rather than immiscibility like that of the ***120k PLLA*** semi-IPN) could be attributed to the similar M_n of these PLLAs versus that of the PCL-DA (10 kDa). The partial miscibility of the ***PDLLA*** and ***85:15 PLGA*** semi-IPNs (versus the immiscibility of ***70:30 PLGA*** and ***50:50 PLGA*** semi-IPNs) could be attributed to their lack of hydrophilicity that renders them more similar to the hydrophobic PCL-DA. In total, the degree of phase separation of the semi-IPNs could be correlated to degradation rate. Partially miscibility led to the fastest rates of degradation, presumably by reducing barrier to water penetration. Immiscible semi-IPNs degraded more slowly due to domains of greater homogeneity that effectively acted like individual miscible phases, thereby slowing water penetration and subsequent degradation.

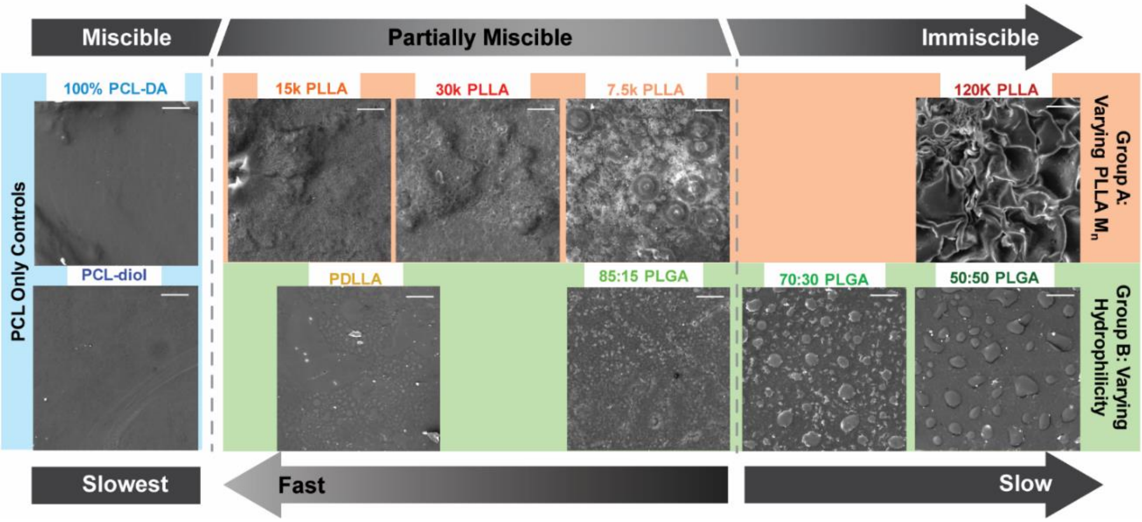

Figure 4-7. SEM images of semi-IPNs and controls film surfaces prior to degradation. Categorization of miscibility (“miscible”, “partially miscible” or “immiscible”) based on extent of phase separation and corresponding relative rate of degradation (“slow” or “fast”). Scale bars = 50 μm.

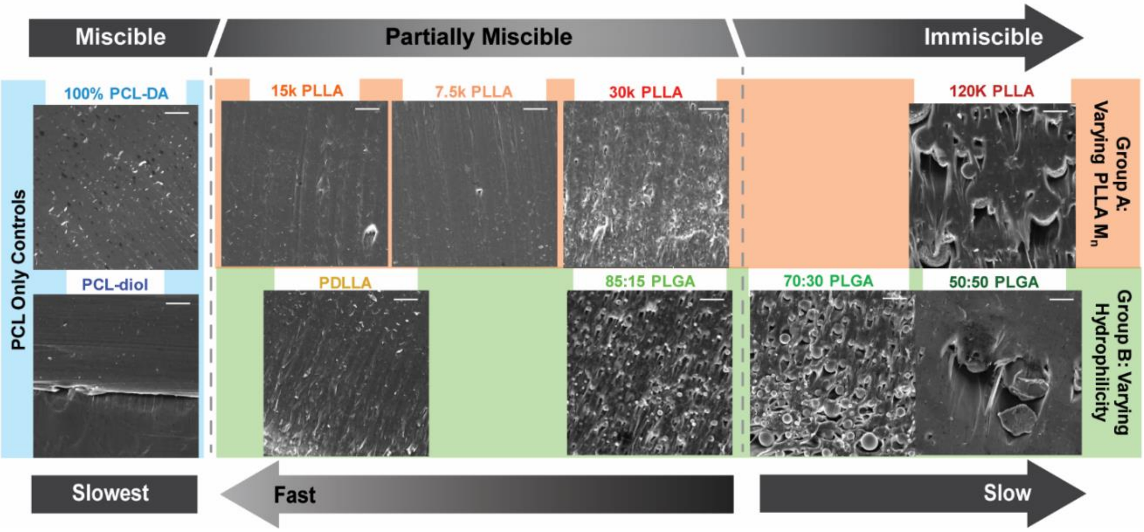

Figure 4-8. SEM images of semi-IPNs and controls film cross-sections prior to degradation. Categorization of miscibility ("miscible", "partially miscible" or "immiscible") based on extent of phase separation and corresponding relative rate of degradation ("slow" or "fast"). Scale bars = 50 µm.

4.4.4. Tensile Properties

Tensile testing was performed to determine modulus and TS values of the semi-IPNs and controls (**Figure 4-9**). The modulus values of all PLA-containing semi-IPNs were significantly improved compared to the ***100% PCL-DA*** as well as the ***PCL-diol*** semi-IPN controls. This is notable given that phase separation, observed to varying degrees for all semi-IPNs, is known to negatively impact mechanical properties such as modulus.[204, 211] While all semi-IPNs retained similar PCL % crystallinity versus the ***PCL-DA*** control (**Figure 4-6**), their increased moduli is also notable given the substitution of 25 wt% of crosslinked PCL-DA for a thermoplastic. Not unexpectedly, the greatest increases in modulus were for semi-IPNs based on PLLAs of greatest crystallinity (e.g. ***7.5k PLLA***, ***15k PLLA***, and ***30k PLLA***). The TS values of the PLA-containing semi-IPNs did not always surpass but did remain within 25% of that of the ***PCL-DA*** control. TS values were likewise the highest for semi-IPNs prepared from semi-crystalline thermoplastics.

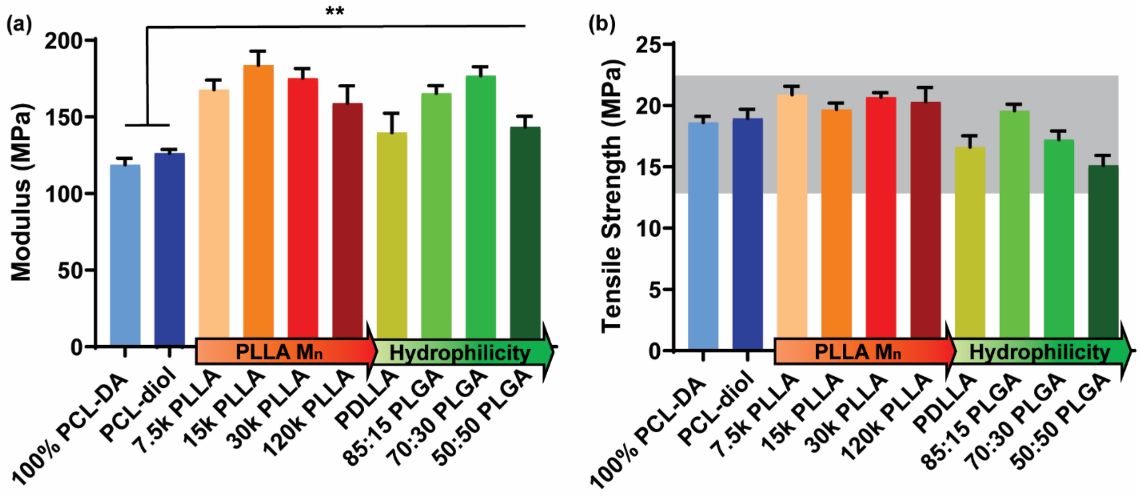

Figure 4-9. Tensile modulus of semi-IPNs and controls; $**p < 0.01$ versus the *PCL-DA* control. (a) Tensile strength of semi-IPNs and controls; Grey bar represents +/- 25% of the tensile strength of the PCL-DA. (b)

4.4.5. Shape Memory Properties

SMP properties of the semi-IPNs were analyzed qualitatively. Like the ***100% PCL-DA*** control, all compositions were able to fix (“hold”) a temporary coil shape following sequential heating, shaping and cooling (**Figure 4-10-a**). After exposure to water (85 °C), all compositions also recovered their original shape within 10 sec (**Figure 4-10-b**). This result was expected since the PCL lamellae serve as the switching segments and the PCL crystallinity was retained for all semi-IPNs (**Figure 4-6-a**).

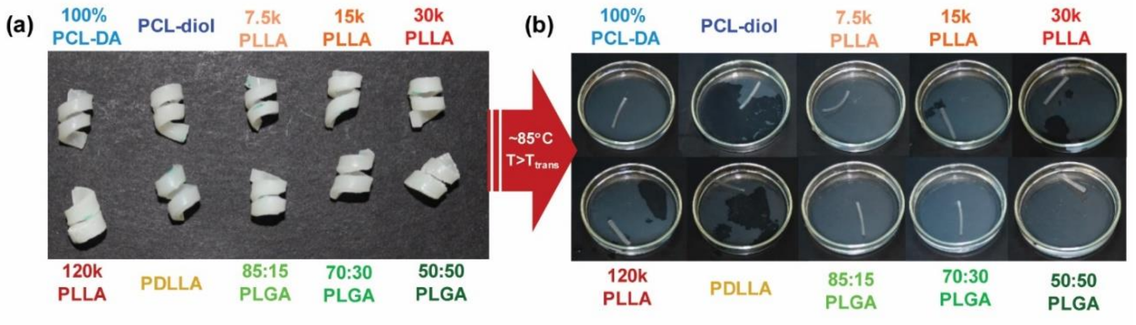

Figure 4-10. Qualitative shape memory testing was performed, and all compositions were able to effectively hold a temporary coil shape (a), and upon heating, all samples returned to their permanent rectangular shape in ~10 sec (b).

4.4.6. Effect of Increased Annealing Temperature

In the aforementioned experiments, the semi-IPNs were annealed at T_{anneal} = 85 °C (i.e. > $T_{m, PCL}$ ~55 °C) in the final step of their fabrication. In our previous work, ***15k PLLA*** was prepared as porous scaffolds using T_{anneal} = 85 °C as well as 170 °C (i.e. > $T_{m, PLLA}$ ~155 °C); the latter higher temperature induced greater shrinking and a concomitant reduction in pore size.[71] Herein, it was hypothesized that a higher anneal temperature would impact relative degradation rates. Thus, select semi-IPNs were chosen due to their "partial miscibility" and relatively fast rates of degradation (decreasing in order ***15k PLLA*** > ***PDLLA*** ≈ ***85:15 PLGA***) and their equivalent thermoplastic M_n (~15 kDa) (**Figure 4-11**). Analogous melt casted blends were also included to determine distinct degradation behaviors versus semi-IPNs.

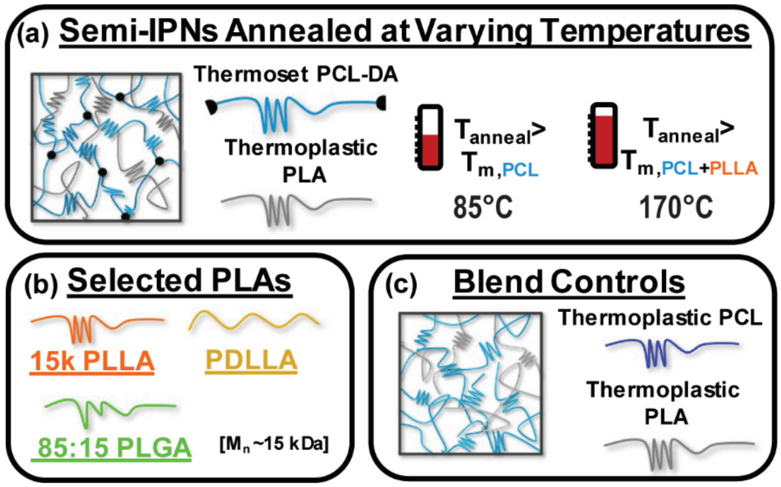

Figure 4-11. Schematic summarizing the study to assess the impact of increased annealing temperature for selected semi-IPNs (a), PLA thermoplastics used to form the semi-IPNs (b) and blend controls (c).

The relative degradation rates of the ***100% PCL-DA*** control was not substantially impacted by the annealing temperature attributed to its chemical homogeneity and miscibility (**Figure 4-12-a**). For the ***15k PLLA*** semi-IPNs, annealing at the higher temperature resulted in a decrease in the rate of degradation, with semi-IPNs annealed at 85 °C fully degrading within 72 hours while those annealed at 170 °C lasted beyond 1 week (**Figure 4-12-b**). For the ***PDLLA*** semi-IPNs, degradation also slowed when annealed at the higher temperature, but mass loss differences were not significant until the one-week time point (**Figure 4-12-c**). Finally, for the ***85:15 PLGA*** semi-IPNs, the higher annealing temperature dramatically reduced the rate of degradation and the blend degraded similarly slow (**Figure 4-12-d**). In the case of analogous blends, the 100% PCL-diol blend lost significantly less mass at 1 week versus the ***PCL-DA*** controls. Analogous blends of ***15k PLLA*** and ***85:15 PLGA*** semi-IPNs degraded more slowly. However, the blend analogue of the ***PDLLA*** semi-IPN degraded somewhat more quickly. PCL %

crystallinity was dramatically increased for blends by >50% for all compositions including the control (**Figure 4-13-a**). PLLA % crystallinity was somewhat similar or slightly lower (**Figure 4-13-b**). Despite the lack of crosslinking, the higher PCL % crystallinity of blends may contribute to their differing degradation profiles versus the corresponding semi-IPNs.

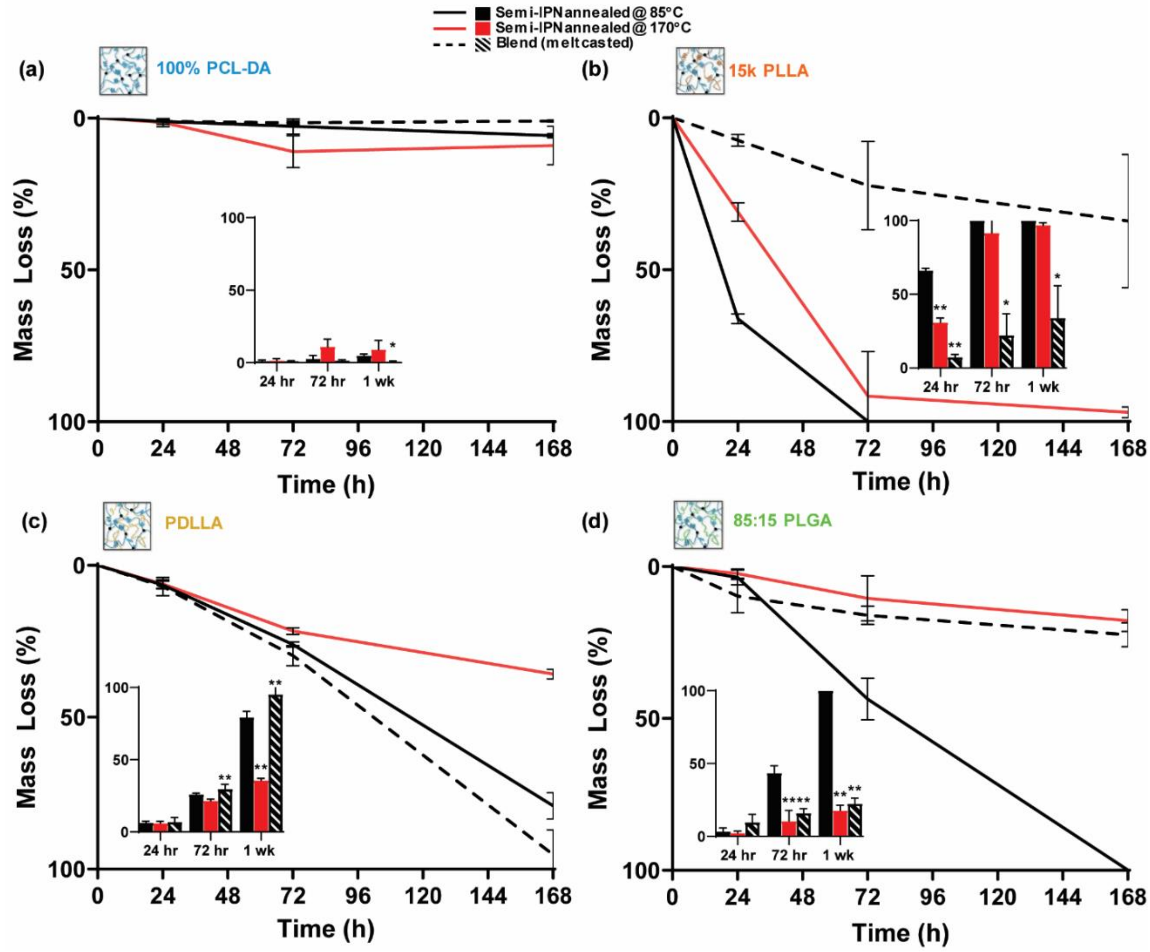

Figure 4-12. Mass loss under accelerated conditions (1 M NaOH, 37°C, 60 rpm) for compositions annealed at 85°C, at 170°C, and analogous melt-casted blends: *100% PCL-DA* control and 100% PCL-diol blend (a), *15k PLLA* semi-IPNs and blend (b), *PDLLA* semi-IPNs and blend (c), and *85:15 PLGA* semi-IPNs and blend (d). $^{*}p < 0.05$ and $^{**}p < 0.01$ versus the corresponding compositions annealed at 85°C.

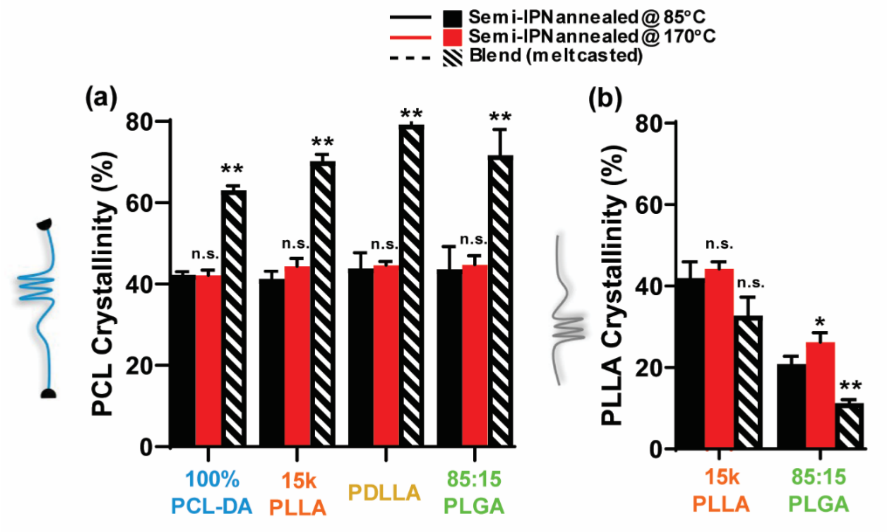

Figure 4-13. PCL % crystallinity (a) and PLLA % crystallinity (b) in PCL-DA/PLA semi-IPNs and controls annealed at 85°C and 170°C and analogous blend controls. Values were corrected for mass percent and PCL % crystallinity was maintained in semi-IPNs annealed at both temperatures but was significantly higher in all blends. $*p < 0.05$ and $**p < 0.01$ versus the corresponding control or semi-IPN annealed at 85 °C (a) and $*p < 0.05$ and $**p < 0.01$ versus the corresponding semi-IPN annealed at 85 °C (b).

Irrespective of annealing temperature, semi-IPNs exhibited similar PCL % crystallinity (**Figure 4-13-A**) and similar or a slight increase in PLLA % crystallinity (for ***15k PLLA*** and ***85:15 PLGA*** semi-IPNs, respectively) (**Figure 4-13-B**). Thus, % crystallinity does not appear to be a major factor in the relatively slower degradation rates of the semi-IPNs annealed at the higher temperature. So, for non-degraded films, phase separation of the surfaces (**Figure 4-14-a**) and cross-sections (**Figure 4-15**) was evaluated. For all semi-IPNs, the extent of phases separation was reduced when annealed at 170 ºC, which likely resulted in the observed slower rates of degradation.

As noted above, these selected PCL-DA/PLA semi-IPNs exhibited higher modulus values and maintained TS values versus the ***PCL-DA*** control when annealed at 85 °C

(**Figure 4-9**). To determine the impact of the higher annealing temperature, the semi-IPNs and control annealed at 170 °C were likewise evaluated (**Figure 4-14-b,c**). When annealed at this higher temperature, the semi-IPNs all exhibited higher modulus and TS values versus the ***PCL-DA*** controls. For ***PDLLA*** and ***85:15 PLGA*** semi-IPNs, the higher annealing temperature resulted in a statistically significant increase the modulus and TS values versus when annealed at the lower temperature. This may be attributed to their decreased phase separation. Moreover, when annealed at 170 °C, all of these semi-IPNs all exhibited significantly higher modulus and significantly higher TS values versus the ***100% PCL-DA*** controls. Finally, shape fixity and shape recovery were shown to be maintained for semi-IPNs annealed at 170°C, attributed to the maintenance of PCL % crystallinity (**Figure 4-16**).

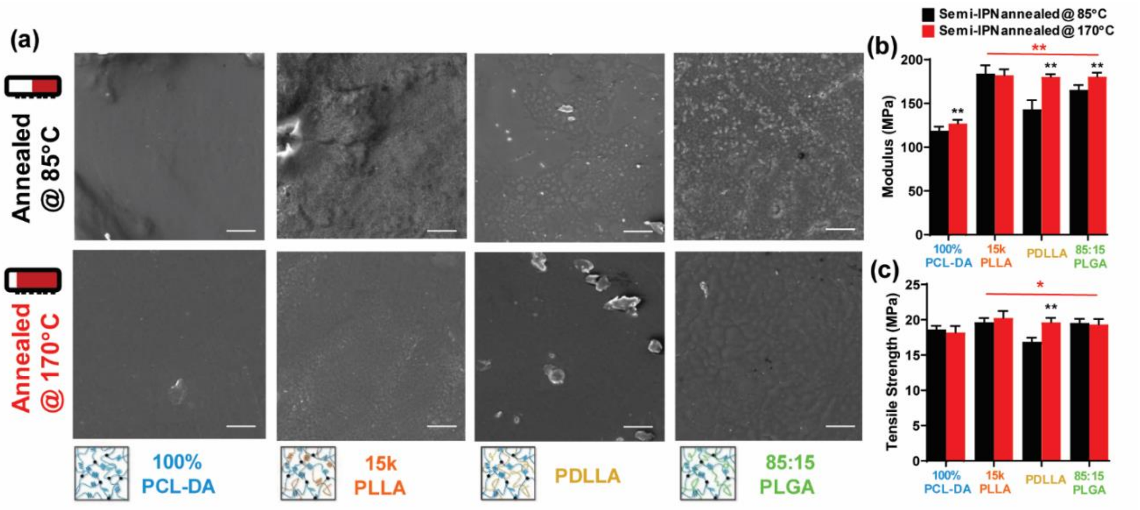

Figure 4-14. SEM of semi-IPN and control film surfaces (annealed at 85°C or 170°C) prior to degradation; scale bars = 50 μm (a), modulus (b) and TS (c). Statistics noted in "red" indicate comparisons between the semi-IPNs and *100% PCL-DA* control annealed at 170°C; statistics noted in "black" indicate comparisons between the designated film

annealed at 170°C versus the analogous film annealed at 85 °C. *$p < 0.05$ and **$p < 0.01$.

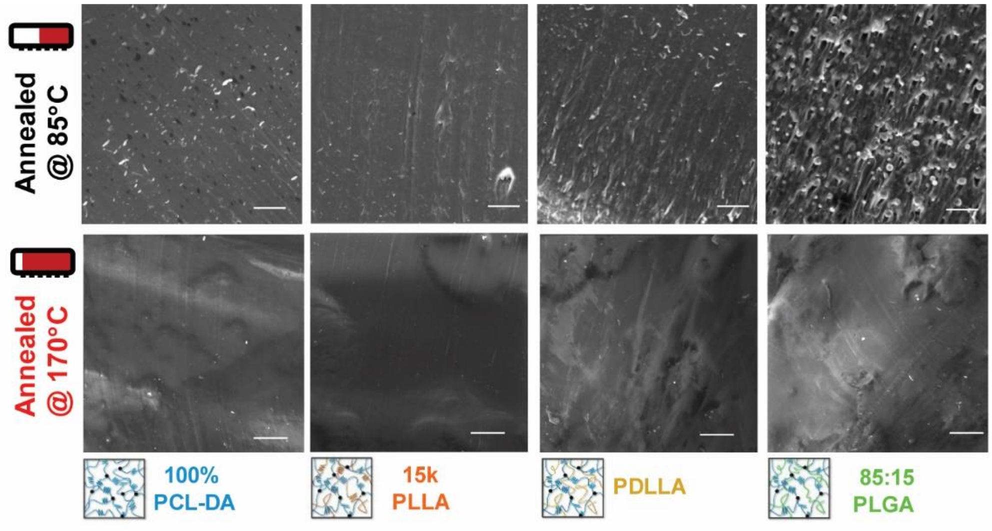

Figure 4-15. SEM of semi-IPN and control film cross-sections (annealed at 85 °C or 170 °C) prior to degradation. Annealing at the higher temperature reduced phase separation. Scale bars = 50 µm.

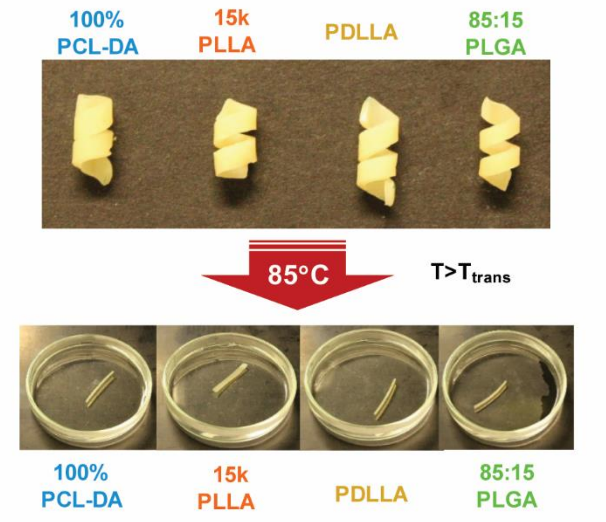

Figure 4-16. Shape memory properties were visualized qualitatively and all compositions annealed at 170 °C were shown to maintain shape fixity (a) and shape recovery (b).

4.5. Conclusions

This study demonstrated that the degradation rates of PCL-based SMPs can be accelerated and tuned with a semi-IPN design comprised of crosslinked PCL-DA and a PLA-based thermoplastic of varying M_n, crystallinity and hydrophilicity. It was shown that the extent of phase separation observed for the semi-IPNs was linked to the relative rates of degradation. PCL-DA/PLA semi-IPNs that resulted in partial miscibility exhibited relatively fast rates of degradation whereas greater immiscibility led to relatively slow rates of degradation (**Figure 4-17**). However, all semi-IPNs degraded faster than the PCL-DA control. Amongst partially miscible semi-IPNs, fabrication that included a higher annealing temperature resulted in increased miscibility and a slower rate of degradation. Due to their retention in PCL crystallinity, all semi-IPNs exhibited shape memory behavior. Finally, modulus was increased for all semi-IPNs versus the PCL-DA control. Annealing at higher temperatures can reduce phase separation, thereby reducing the rate of degradation and potentially improving mechanical properties. This work points to the utility of a semi-IPN design to create PCL-based semi-IPNs with tunable degradation rates and improved rigidity.

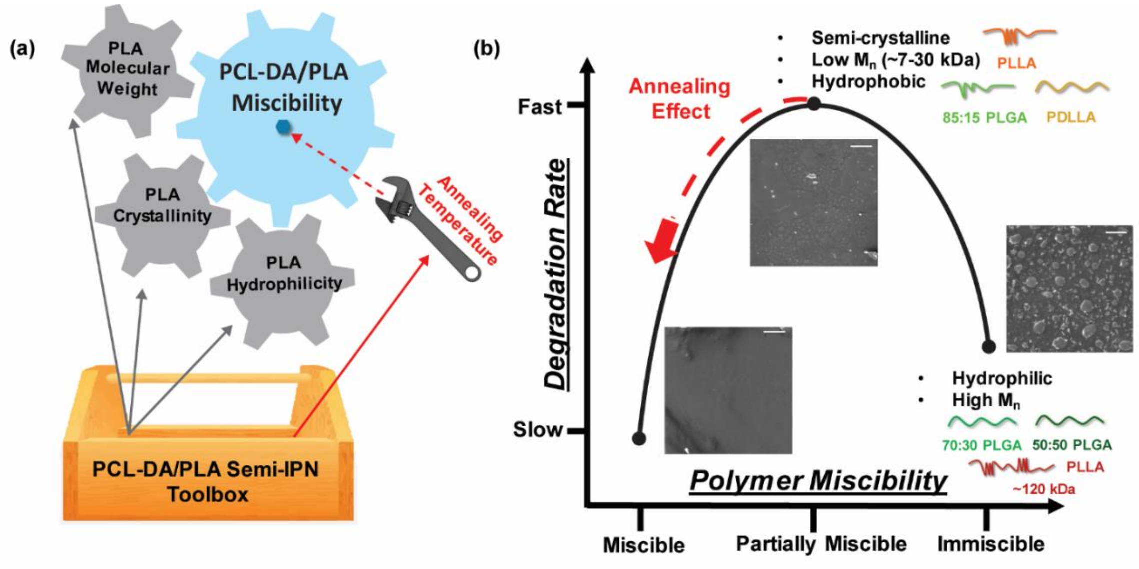

Figure 4-17. Key properties of PLA-based thermoplastics as well as annealing temperature may be considered in preparing PCL-DA/PLA semi-IPNs with accelerated rates of degradation (a). The relationship between degradation rates and miscibility observed for PCL-DA/PLA semi-IPNs; details about the PLA thermoplastic components are listed (b).

5. PCL-DA/PLA SEMI-IPN SCAFFOLDS WITH TUNABLE HYDROLYTIC DEGRADATION AND THE IMPACT OF ANNEALING PAREMETERS ON SCAFFOLD PROPERTIES

5.1. Background and Motivation

This study is a continuation of Chapter IV where PCL-DA/PLA semi-IPN films showed tunable degradation rates primarily linked to PCL/PLA miscibility; annealing temperature was also shown to impact miscibility and resulting construct properties.[158] Previous testing was limited to solid films and to hydrolytic degradation studies performed under base-catalyzed conditions. In this Chapter, we advance to porous scaffolds of the same PCL-DA/PLA compositions and explore their *in vitro* degradation under non-catalyzed conditions. Previously studied PCL-DA/PLA films were also subjected to the non-catalyzed degradation study to compare trends to base-catalyzed conditions, since polyester degradation via hydrolysis is known to be pH dependent.[224, 228, 229]

Catalyzed degradation conditions are frequently employed because the timescale is more convenient for obtaining results, but they often do not correspond to degradation behaviors observed under non-catalyzed or neutral conditions.[203] As these PCL-DA/PLA semi-IPNs are intended for use as self-fitting CMF bone scaffolds, their degradation and erosion profiles should be examined under physiologically relevant, neutral conditions. These *in vitro* non-catalyzed hydrolysis studies are expected to better predict PCL-DA/PLA scaffold degradation for future *in vivo* use. **Figure 5-1** shows the PCL-DA/PLA semi-IPN compositions that were studied herein; note that the compositions are the same chemistries as Chapter IV, but the highly phase separated compositions were not included.

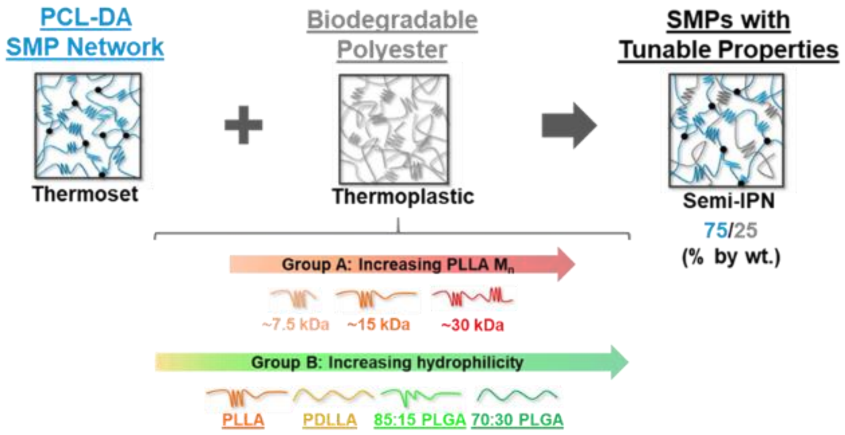

Figure 5-1. PCL-DA/PLA semi-IPNs studied under neutral degradation conditions as both solid films and porous scaffolds. *Group A*: semi-crystalline PLLA of varying M_ns and *Group B*: semi-crystalline PLLA (~15 kDa), amorphous PDLLA (~15 kDa) and amorphous/nearly amorphous PLGAs (85:15 and 70:30 ~15 kDa).

5.2. Experimental

5.2.1. Materials

PCL-diol (M_n = 10 kDa per manufacturer specifications), 4-(dimethylamino)pyridine (DMAP), trimethylamine (Et_3N), acryloyl chloride, potassium carbonate (K_2O_3), anhydrous magnesium sulfate ($MgSO_4$), (3S)-*cis*-3,6-dimethyl-1,4-dioxane-2,5-dione (L-lactide), 3,6-dimethyl-1,4-dioxane-2,5-dione (lactide), glycolide, tin(II) 2-ethylhexanoate [$Sn(Oct)_2$], ethylene glycol, 2,2-dimethoxy-2-phenyl acetophenone (DMP), 1-vinyl-2-pyrrolidinone (NVP), sodium hydroxide (NaOH) and common solvents were purchased from Sigma-Aldrich. All solvents and ethylene glycol were dried over 4 Å molecular sieves, all reagents were vacuum dried overnight (ON), and all glassware and stir bars were dried at 120 °C ON prior to use. Salt was sieved using an ASTM E-11 no.40 and no. 35 sieves with 425 μm and 500 μm openings respectively;

scanning electron microscopy (SEM) and ImageJ showed an average salt size of 460 ± 70 μm.

PCL-diol was functionalized to PCL-DA based on the established protocol in Chapter IV. All PLA thermoplastics including, semi-crystalline PLLA of varying M_n [7.5 kg/mol, 15 kg/mol, 30 kg/mol] and amorphous PDLLA, 85:15 PLGA, and 70:30 PLGA [all at 15 kg/mol] were also prepared as previously described.[158]

5.2.2. Fabrication

Semi-IPN compositions based on a PCL-DA network and varying PLA-based thermoplastics at 75/25 by wt. were studied herein. Semi-IPNs are designated by the thermoplastic component. *Group A*: ***7.5k PLLA***, ***15k PLLA***, and ***30k PLLA*** *Group B*: ***PDLLA***, ***85:15 PLGA***, and ***70:30 PLGA***. A ***100% PCL-DA*** control was also included.

5.2.2.1. Films

Films were prepared according to the same procedure used in Chapter 4.3.3, via UV curing of a PCL-DA/PLA macromer solution between two glass slides. Typical films were annealed at 85 °C (1 h, 30 in Hg.) referred to as low temperature (LT). Selected compositions were annealed at a higher temperature (HT, 170 °C, 1 h, 30 in. Hg) as shown in **Figure 5-2**. As in Chapter IV, the PCL-DA/PLA semi-IPNs selected for high annealing were chosen for their fast degradation under base-catalyzed conditions.

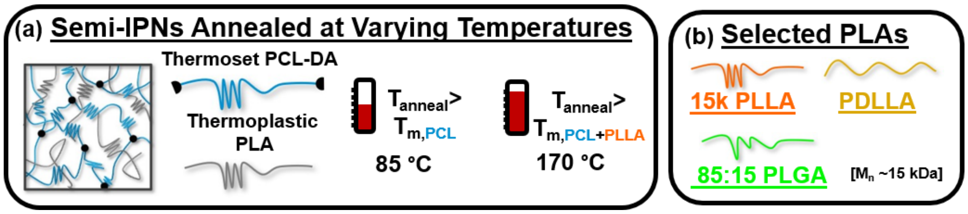

Figure 5-2. All semi-IPN compositions from Figure 5-1 were annealed at 85 °C (LT), and selected PCL-DA/PLA compositions were also annealed at 175 °C (HT).

5.2.2.2. Scaffolds

Porous scaffolds were also prepared according to an adapted protocol.[69] Scintillation vials were used to prepared fused salt molds with 10.0 g of sieved salt and 7.5% by wt. DI H_2O. The water was incorporated over 4 additions with manual stirring in between, and was finally centrifuged prior to drying *in vaco* (RT, ON, 30 in. Hg). The next day macromer solutions were prepared using a total concentration of 0.15 g macromer per mL of dichloromethane (DCM). PCL-DA/PLA semi-IPN compositions were prepared by incorporating a 75/25 mix in macromer solutions. Next, photoinitiator solution was added at 15 % by vol. (10% by wt. DMAP in NVP). Homogenized solutions were poured over salt molds (~5 mL each) followed by centrifugation for assisted macromer diffusion through the fused salt template, followed by UV curing. After sufficient solvent evaporation (48 h, fume hood), scaffolds were leached in a 1/1 mixture of H_2O to ethanol with daily solution changes over the course of 5 days to fully leach all salt porogens. Scaffolds were again dried prior to being subjected to annealing conditions. For scaffolds three different annealing conditions were used: high temperature (HT, 170 °C, 10 min, 30 in Hg), medium temperature (MT, 145 °C, 20 min, 30 in. Hg), and low temperature (LT, 85 °C, 30 min). Scaffold annealing designations are listed in **Figure 5-3**. These groups were selected based upon PLA T_m (or lack thereof), which dictated whether or not scaffolds could achieve a uniform pore size. For instance, semi-crystalline PLLAs (Tm ~153-159 °C depending on M_n) could not be annealed at LT or MT conditions because the macromers prevented shrinkage, and uniform pore formation, as previously shown for PCL-DA/PLLA compositions of varying wt %.[71]

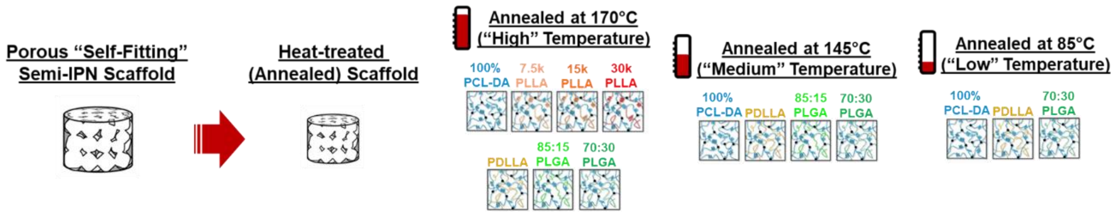

Figure 5-3. PCL-DA/PLA semi-IPN scaffolds were annealed under three different conditions (LT, MT or HT), and compositions were designated based on their ability to undergo shrinkage during annealing to yield uniform pore size and morphology.

5.2.2.3. Initial Scaffold Properties

5.2.2.3.1. Pore Size and Porosity

Pore size (N=2 scaffolds, 2 SEM images each) and porosity % (N=3) were determined based on the previously described protocol in *Chapter 3.3.3.2.*

5.2.2.3.2. Compressive Mechanical Properties

Scaffold samples (d ~6 mm x t ~2 mm; $N = 7$) were subjected to a constant strain (1.5 mm/min) up to 85% strain to determine compressive mechanical properties (Instron 5944) The compressive modulus (E) and strength (CS) were obtained from the resultant stress train curve using Bluehill software.

5.2.3. *In Vitro* Non-Catalyzed Hydrolytic Degradation

Non-catalyzed neutral degradation tests were performed in IX PBS (pH ~7.4) according to ASTM F1635, whereby specimens were utilized for a single time point only. Scaffold disks (d ~6 mm, h ~2 mm) (*N* = 3 per time point) were immersed in 10 mL of the PBS solution in a sealed glass vial and maintained at 37 °C at 60 rpm (VWR Benchtop Shaking Incubator Model 1570). At each designated time point (3, 6, 9, 12, and 15 mo.), specimens were removed from the solution, thoroughly rinsed with DI water, blotted and dried under vacuum (RT, overnight, 30 in. Hg). For each specimen, the initial mass and mass at the designated time point were measured with an analytical balance.

5.3. Results and Discussion

5.3.1. Film Degradation under Non-Catalyzed Conditions

New degradation data on PCL-DA/PLA semi-IPNs under neutral conditions was compared to the previous results under base catalyzed conditions for films annealed at LT and HT (**Figure 5-4**). The change in degradation study conditions yielded significant changes to degradation kinetics and compositional trends. Under non-catalyzed conditions none of the films fully degraded even after a total of 15 mo. of hydrolysis. In the base-catalyzed studies, the ***15k PLLA*** semi-IPN was thought to degrade the most quickly but under neutral conditions it was one of the slowest degrading compositions. Instead, the ***PDLLA***, ***85:15 PLGA*** and ***70:30 PLGA*** were the fastest degrading film compositions under neutral conditions, whereas in base-catalyzed studies they degraded at an intermediate rate. Thus, these results demonstrate the importance of screening biodegradable scaffold compositions under neutral hydrolytic conditions rather than using base catalysis. We expect these neutral degradation studies to give a better representation of how scaffolds will degrade as CMF bone scaffolds. A higher annealing temperature (HT) was previously shown to slow film degradation under base-catalyzed conditions. But herein increased annealing temperature was shown to accelerate degradation for the ***PDLLA*** and ***85:15 PLGA*** compositions (**Figure 5-5)**. We speculate that this is linked to PCL/PLA phase separation, but further work is required, so post-hydrolysis film characterization including imaging and spectroscopy are in progress to better elucidate degradation mechanisms.

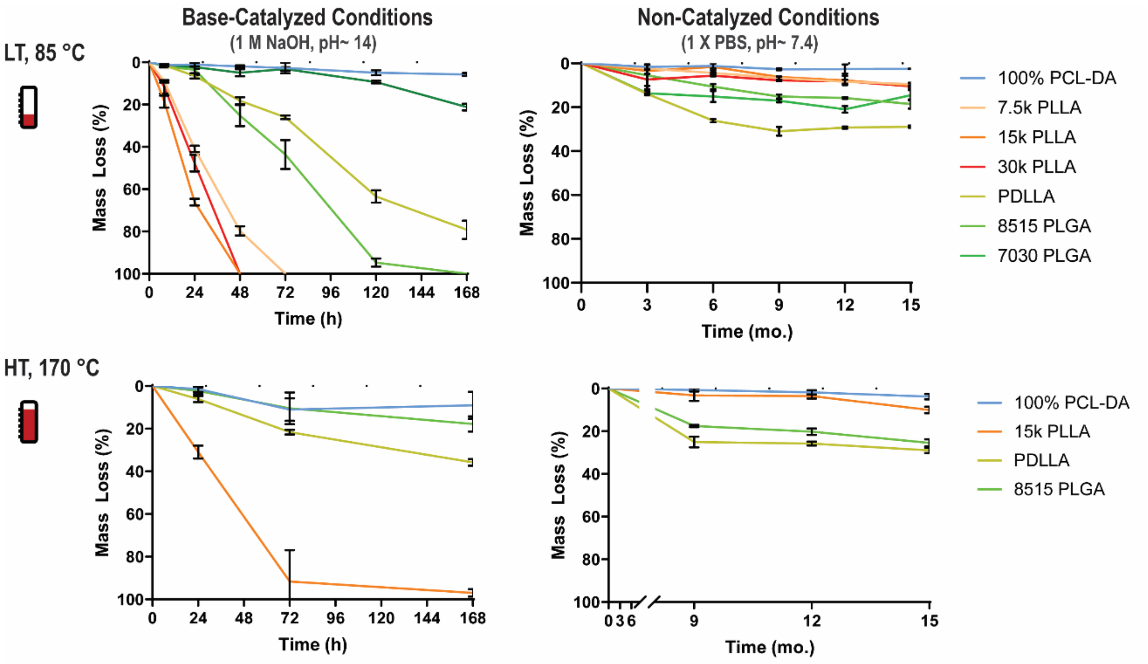

Figure 5-4. Degradation of PCL-DA/PLA semi-IPNs via hydrolysis under (left) base-catalyzed and (right) non-catalyzed conditions were examined for LT-annealed films (top) and for selected compositions of HT-annealed films (bottom).

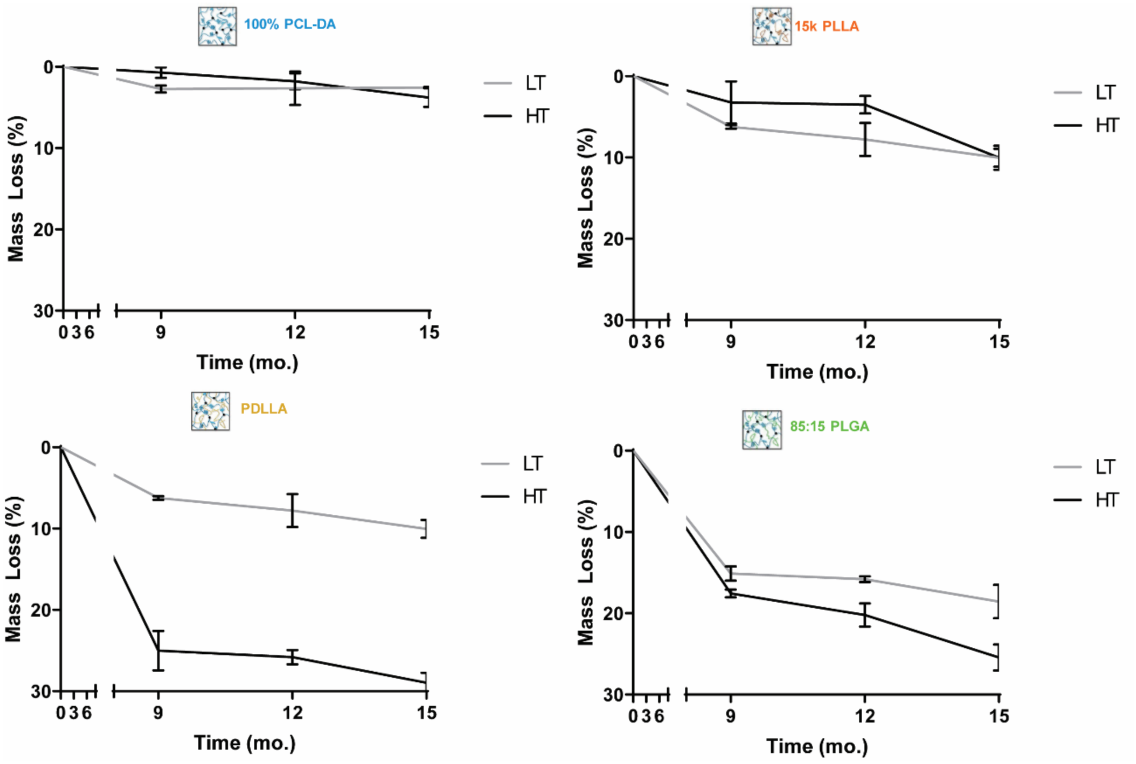

Figure 5-5. The impact of annealing temperature (LT or HT) on PCL-DA/PLA semi-IPN films was assessed for selected compositions.

5.3.2. Scaffold Characterization

5.3.2.1. Initial Properties

Pore size (**Figure 5-6**) and porosity % (**Figure 5-7**) were shown to be maintained for the PCL-DA/PLA semi-IPNs at their designated annealing conditions. This ensures that property trends observed are from changes to scaffold chemistry (ie. phase separation). Then, initial compressive mechanical properties were examined, and average modulus (E) and compressive strength (CS) were determined. Under high temperature (HT) annealing conditions, E and CS were significantly improved for all PCL-DA/PLA semi-IPN scaffolds compared to the 100% PCL-DA control (**Figure 5-8**). This was similar to previous trends shown for analogous solid films and their tensile properties.[158] Furthermore, the 100% PCL-DA controls showed compressive properties toward the low end of matching cancellous bone (E ~4-12 MPa, CS ~20-50 MPa),[206] but the implementation of PCL-DA/PLA semi-IPNs allowed for even more robust E and CS for optimized bone healing. In terms of annealing temperature dependence, E was shown to be most optimal under HT annealing conditions versus MT or LT, but CS was largely unchanged regardless of annealing conditions (**Figure 5-9**). Moreover, this result highlights the necessity in examining and optimizing scaffold fabrication parameters, such as annealing temperature, to best tune resultant scaffold properties for bone regeneration.

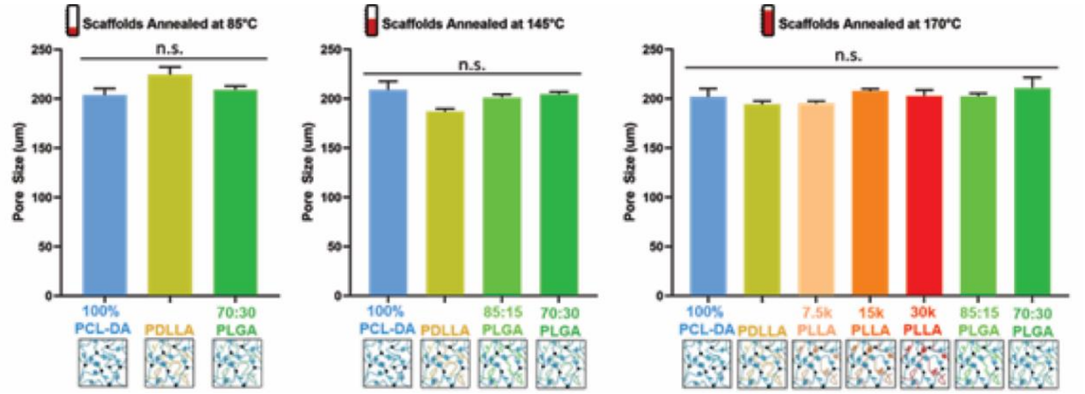

Figure 5-6. Pore size was shown to be maintained for all compositions annealed under the same conditions as each other.

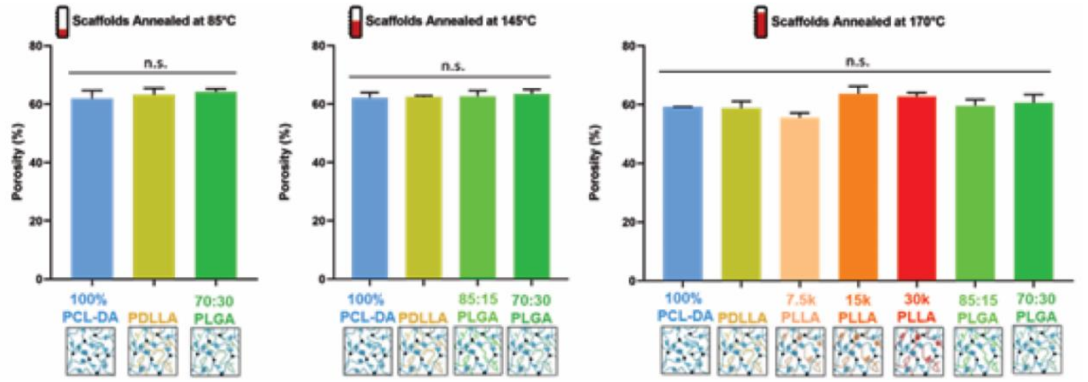

Figure 5-7. Porosity % was shown to be maintained for all compositions annealed under the same conditions as each other.

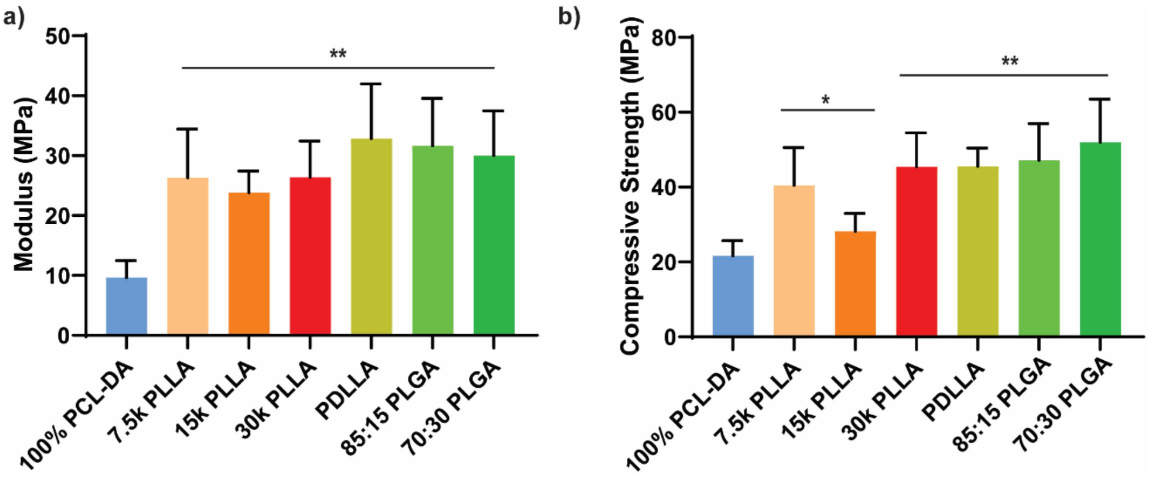

Figure 5-8. Compressive mechanical properties were compared including (a) E and (b) CS for all HT-annealed scaffolds; $*p < 0.05$ and $**p < 0.01$ compared to the 100% PCL-DA control.

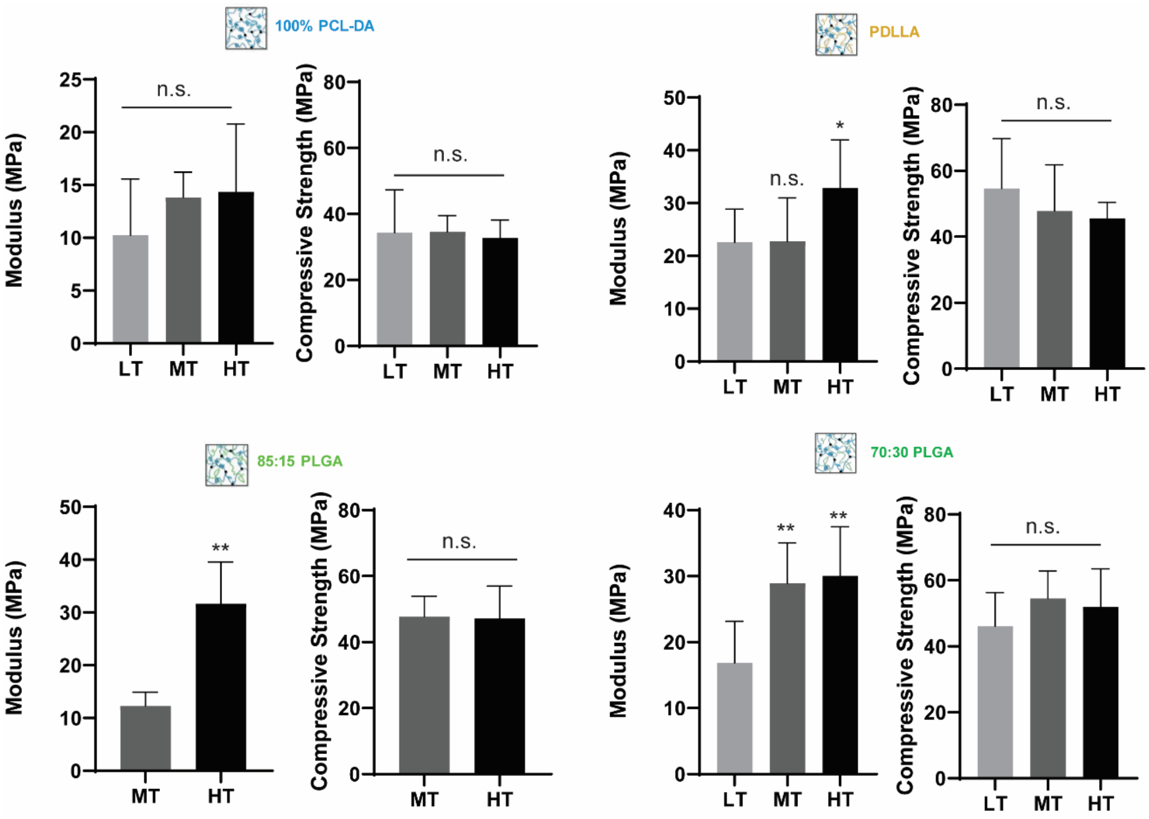

Figure 5-9. Compressive mechanical properties (E and CS) were compared for selected scaffold compositions after being subjected to varying annealing conditions (LT, MT or HT); *$p < 0.05$ and **$p < 0.01$.

5.3.2.2. *In Vitro* Hydrolysis Behavior

Neutral (PBS, 1X, pH ~7.4) hydrolytic behavior of PCL-DA/PLA semi-IPNs annealed at high temperature (HT) was monitored over 15 months (**Figure 5-11**). Varying the microstructure of the PLA component in PCL-DA/PLA semi-IPN scaffolds was shown to successfully yield accelerated scaffold degradation rates. The enhanced degradation rates of the semi-IPN scaffolds observed *in vitro* is expected to yield more favorable tissue ingrowth in future *in vivo* studies compared to the more slowly degrading 100% PCL-DA control. Degradation was also shown to be tunable for PCL-DA/PLA semi-IPNs depending on hydrophilicity and M_n of the PLA component. This has the potential to be useful in developing a line of bone tissue scaffolds that have different degradation rates to best suit a patient-specific needs (i.e. age, bone type, defect size). Moreover, the ***7.5k PLLA***, ***PDLLA***, ***85:15 PLGA***, and ***70:30 PLGA*** semi-IPN compositions were shown to degrade the most rapidly and would benefit most from advancing to future *in vivo* studies. Scaffold annealing temperature was also examined and did not appear to impact overall degradation rate (**Figure 5-12**). However, post-degradation analyses are still in progress to determine if it might have had an impact on hydrolysis mechanism, or on how the scaffold degrades over time.

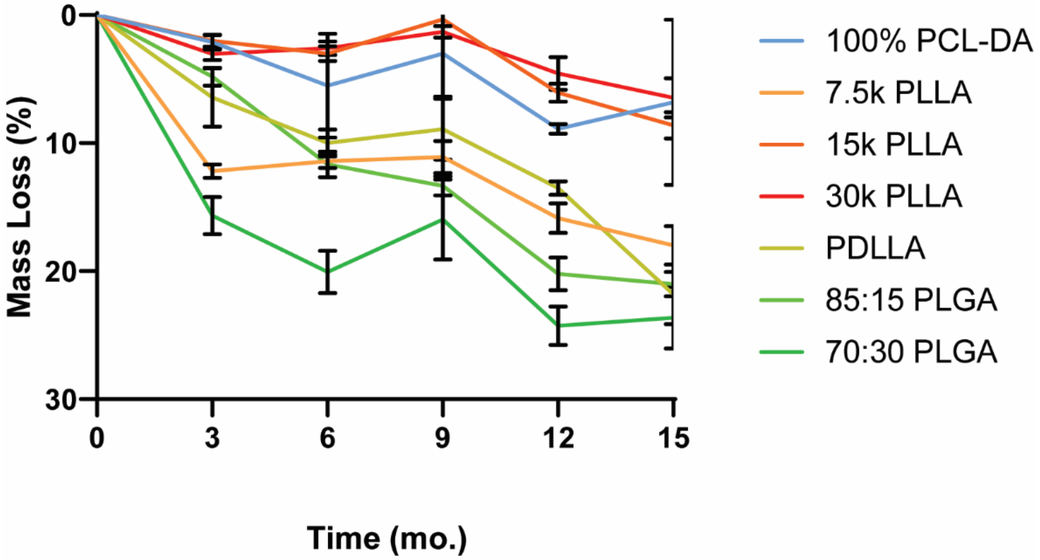

Figure 5-10. HT-annealed PCL-DA/PLA semi-IPN scaffold degradation under non-catalyzed conditions showed that low M_n, hydrophilicity, and amorphous microstructures in the PLA thermoplastic component accelerated scaffold degradation.

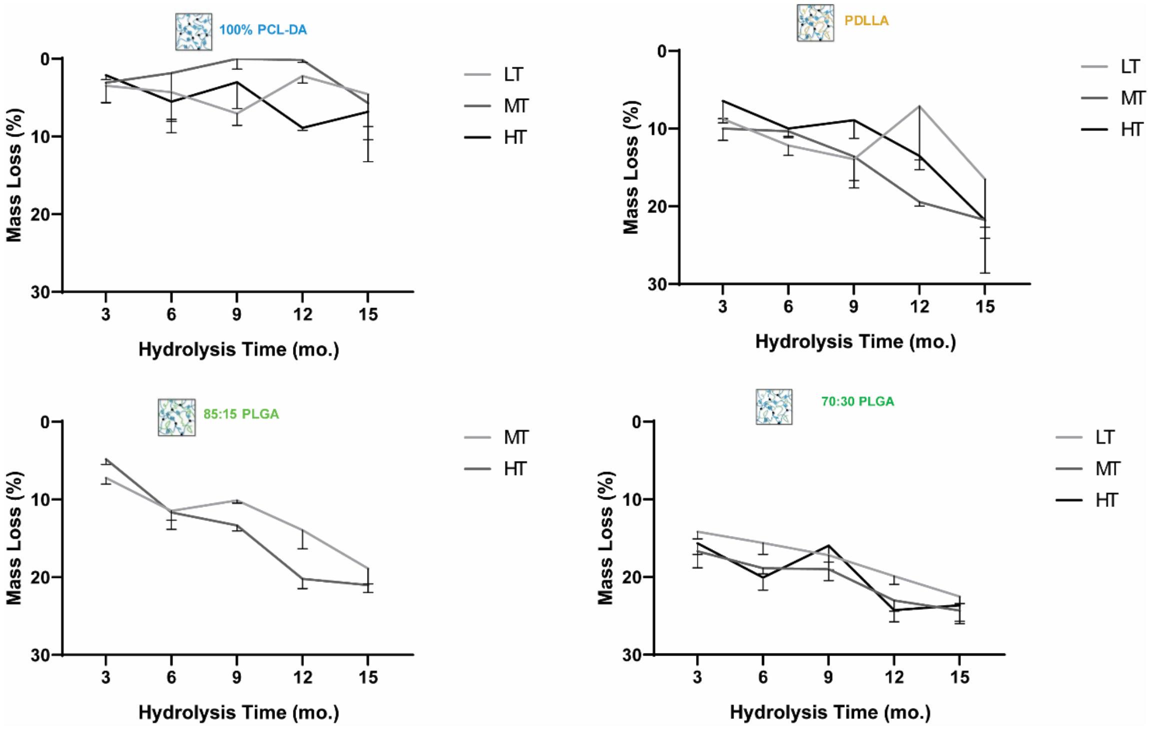

Figure 5-11. Annealing parameter (LT, MT or HT) did not appear to have an impact on overall scaffold degradation rate for selected compositions.

6. SHAPE MEMORY POLYMER (SMP) SCAFFOLDS WITH IMPROVED SELF-FITTING PROPERTIES*

6.1. Overview

"Self-fitting" shape memory polymer (SMP) scaffolds prepared as semi-interpenetrating networks (semi-IPNs) with crosslinked linear-poly(ε-caprolactone)-diacrylate (PCL-DA, Mn ~10 kg/mol) and linear-poly(L-lactic acid) (PLLA, M_n ~15 kg/mol) [75/25 wt%] exhibited robust mechanical properties and accelerated degradation rates versus a PCL-DA scaffold control. However, their potential to treat irregular craniomaxillofacial (CMF) bone defects is limited by their relatively high fitting temperature (T_{fit} ~55 °C; related to the T_m of PCL) required for shape recovery (i.e. expansion) and subsequent shape fixation during press fitting of the scaffold, which can be harmful to surrounding tissue. Additionally, the viscosity of the solvent-based precursor solutions, cast over a fused salt template during fabrication, can limit scaffold size. Thus, in this work, analogous semi-IPN SMP scaffolds were also formed with a 4-arm star-PCL-tetracryalate (star-PCL-TA) (M_n ~10 kg/mol) and star-PLLA (M_n ~15 kg/mol). To assess the impact of a star-polymer architecture, four semi-IPN compositions were prepared: linear-PCL-DA/linear-PLLA (***L/L***), linear-PCL-DA/star-PLLA (***L/S***), star-PCL-TA/linear-PLLA (***S/L***) and star-PCL-TA/star-PLLA (***S/S***). Two PCL controls were also prepared: ***LPCL*** (i.e. 100% linear-PCL-DA) and ***SPCL*** (i.e. 100% star-PCL-

---

* Reprinted with permission from "Shape Memory Polymer (SMP) Scaffolds with Improved Self-Fitting Properties" by Pfau, M.R., McKinzey, K.G., Roth, A.A., Graul, L.M., Maitland, D.J., and Grunlan, M.A., 2021. *J. Mater. Chem. B*, Copyright [2021] by Royal Society of Chemistry.

TA). The ***S/S*** semi-IPN scaffold exhibited particularly desirable properties. In addition to achieving a lower, tissue-safe T_{fit} (~45 °C), it exhibited the fastest rate of degradation which is anticipated to more favorably permit neotissue infiltration. The radial expansion pressure exerted by the ***S/S*** semi-IPN scaffold at T_{fit} was greater than that of ***LPCL*** which is expected to enhance osseointegration and mechanical stability. The intrinsic viscosity of the ***S/S*** semi-IPN macromer solution was also reduced such that larger scaffold specimens could be prepared.

6.2. Introduction

A major limitation of biologic and alloplastic grafts used to treat irregularly shaped cranio-maxillofacial (CMF) bone defects is the difficulty in achieving sufficient bone-to-graft contact, essential for osseointegration and healing.[230, 231] Autografting remains the clinical "gold standard", but in addition to the demands of surgical harvesting, bone graft rigidity contributes to poor shaping and tissue contact, ultimately leading to graft resorption.[113, 232, 233] Synthetic CMF bone graft substitutes, including ceramic injectables[33] and bone cements,[234] utilize *in situ* curing to achieve a defect-specific fit. However, they are limited by risks associated with brittle mechanical properties (leading to post-surgical fracture), exothermic curing (leading to tissue damage), and shrinkage post-cure (leading to poor bone-to-graft contact).[27-29] PEEK implants can be formed with patient- specific geometry via 3D printing, but are non-regenerative.[234, 235] Thus, an off-the-shelf regenerative scaffold material that can readily achieve conformal fit into irregular CMF bone defects is expected to improve healing outcomes.

We have previously reported "self-fitting" scaffolds based on thermoresponsive shape memory polymers (SMPs) as a regenerative approach to treat CMF bone defects.[37, 49, 69, 71, 137] Porous SMP scaffolds were prepared from *linear*-poly(ε-caprolactone) diacrylate (*linear*-PCL-DA, M_n ~10 kg/mol) by photocuring a solvent-based macromer solution over a fused salt template followed by aqueous extraction of the template (i.e. solvent-casting/particulate leaching, SCPL). For such PCL SMP scaffolds, covalent cross-links act as netpoints and PCL lamellae act as switching segments. In a surgical setting, the PCL scaffolds could be warmed in saline to their "fitting temperature" (T_{fit} ~55 °C, related to $T_{m,PCL}$), causing the PCL lamellae to begin to melt and the scaffold to subsequently soften. It could thus be readily press-fitted into the defect site as shape recovery would drive expansion of the scaffold to the perimeter. Then, as the scaffold would cool to body temperature ($T < T_{fit}$), the PCL lamellae would re-crystallize and return the scaffold to its relatively rigid state with the scaffold fixed into the shape of the defect. Importantly, the PCL SMP scaffolds displayed high shape fixity and recovery, non-brittle mechanical properties, and high pore interconnectivity.[37, 49, 69, 137] Increasing the rigidity of the PCL scaffolds would improve structural support in the early stages of healing and increasing the rate of degradation would promote osseointegration and regeneration.[19, 21, 236-238] Thus, thermoplastic *linear*-poly(L-lactic acid) (PLLA, ~15 kg/mol) was incorporated into thermoset *linear*-PCL-DA networks to yield *linear*-PCL-DA/*linear*-PLLA semi-interpenetrating network (semi-IPN) scaffolds.[71, 159] A semi-IPN scaffold prepared with 75/25 wt% PCL/PLLA maintained SMP behavior (T_{fit} ~55 °C), but demonstrated an increased modulus and accelerated degradation rate compared to the *linear*-PCL-DA control. The faster degradation of the *linear*-PCL-DA/*linear*-PLLA semi-IPNs was linked to polymer phase separation.[71, 157, 158] Likewise, phase separation has been known to impact mechanical and degradation properties of polyester blends.[210, 211, 218, 225]

Further improvements to mechanical and degradation properties of PCL-based SMP scaffolds, as well as reducing the T_{fit} (to avoid possible tissue damage) and reducing macromer solution viscosity (to aid in scaffold fabrication), would be a significant enhancement in their utility. Because of their unique thermal, degradative, mechanical, and rheological properties,[239-241] *star*-polymer analogues may offer distinct advantages to the PCL/PLLA semi-IPN scaffolds. T_m values of multi-arm polymers are typically reduced due in part to their more sterically hindered architectures.[242-244] Biodegradable star polyesters have also been employed to refine degradation behavior.[242, 245, 246] Additionally, *star*-polymers are associated with reduced hydrodynamic volumes which affects dispersion and interfacial macromolecular interactions.[247, 248] Thus, *star*-polymers have been used to improve miscibility and resulting toughness of blends and polymer nanocomposites.[249-252] Lastly, *star*-polymers are well known for having reduced dilute solution viscosities due to less chain entanglements relative to their linear counterparts.[253, 254] In the fabrication of SMP scaffolds, during solvent casting of the macromer solution over a fused salt template, this could aide in diffusion such that larger scaffold specimens could be readily prepared.

Herein, towards favorable tuning of semi-IPN scaffold properties, the impact of a crosslinkable 4-arm *star*-PCL analogue and thermoplastic 4-arm *star*-PLLA was assessed. Specifically, scaffold compositions were systematically made with combinations of *linear*-PCL-DA or *star*-PCL-tetracryalate (*star*-PCL-TA) and *linear*-PLLA or *star*-PLLA: *linear-PCL-DA/linear-PLLA (**L**/**L**)*, *linear-PCL-DA/star-PLLA* (***L***/***S***), *star*-PCL-TA/*linear-PLLA* (***S***/***L***) *and star*-PCL-TA/*star-PLLA* (**Figure 6-1a**). The ratio of PCL/PLLA was maintained at 75/25 wt%, that of the ***L/L*** semi-IPN previously shown to best enhance compressive modulus and degradation rate versus the *linear*-PCL-DA control (***LPCL***) (i.e. 100% PCL-DA).[71, 159] In addtion to the ***LPCL*** control, a *star*-PCL-TA control (***SPCL***) (i.e. 100% PCL-TA) was also prepared. All scafffolds were prepared with the same SCPL protocol to generate scaffolds with similar pore size and interconnectivity (**Figure 6-1b**). The resulting SMP scaffolds were assessed for their thermal, degradative, mechanical, and shape memory properties. The solution viscosity of macromer solutions used in the SCPL fabrication process was also examined and select compositions were used to fabricate scaffolds with larger dimensions.

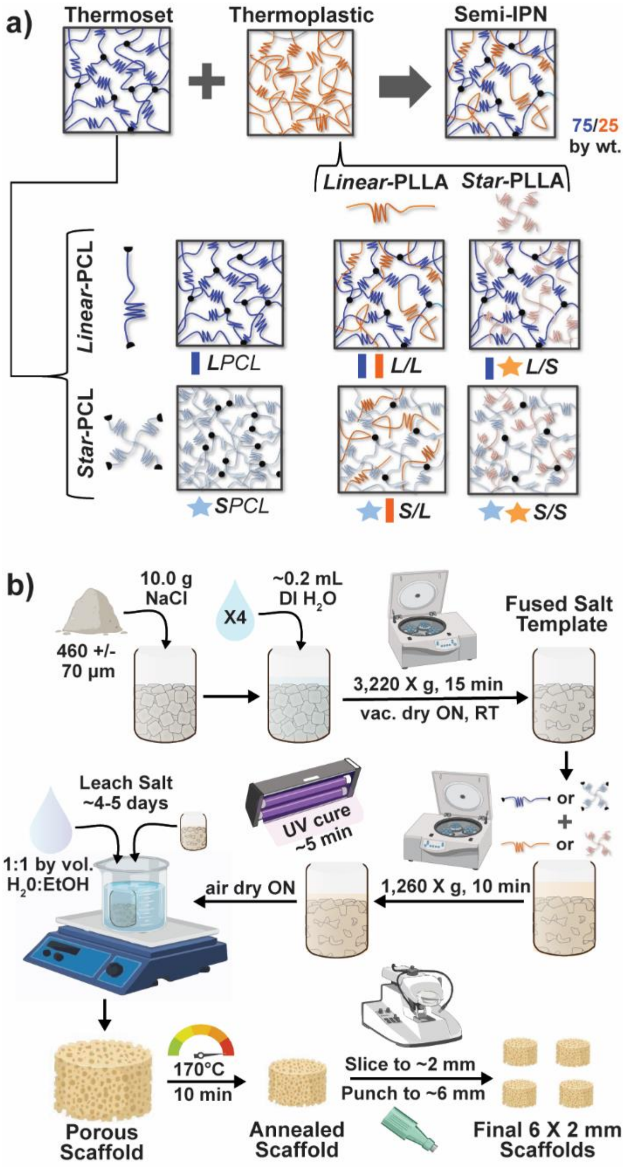

Figure 6-1. (a) Four semi-IPN SMP scaffolds were prepared with combinations of *linear*-PCL-DA or *star*-PCL-TA and *linear*-PLLA or *star*-PLLA (75/25 PCL/PLLA). Two 100% PCL controls were also prepared from *linear*-PCL-DA or *star*-PCL-TA. (b) All SMP scaffolds were prepared via solvent-casting/particulate leaching (SCPL) whereby a designated solvent-based macromer solution was sequentially cast over a fused salt template, UV-cured, and the template extracted to yield highly interconnected pores.

6.3. Experimental

6.3.1. Materials

Linear-PCL-diol (M_n = 10 kg/mol per manufacturer specifications), 4-(dimethylamino)pyridine (DMAP), triethylamine (Et_3N), acryloyl chloride, potassium carbonate (K_2CO_3), anhydrous magnesium sulfate ($MgSO_4$), sodium chloride (NaCl, salt), (3S)-*cis*-3,6-dimethyl-1,4-dioxane-2,5-dione (L-lactide), ε-caprolactone, pentaerythritol, tin(II) 2-ethylhexanoate ($Sn(Oct)_2$), ethylene glycol, 2,2-dimethoxy-2-phenyl acetophenone (DMP), 1-vinyl-2-pyrrolidinone (NVP), sodium hydroxide (NaOH), deuterated chloroform ($CDCl_3$), and solvents were purchased from Sigma-Aldrich. All solvents and ethylene glycol were dried over 4 Å molecular sieves, all reagents were vacuum dried overnight (ON), and all glassware and stir bars were dried at 120 °C ON prior to use. Salt was sieved using an ASTM E-11 no.40 and no. 35 sieves with 425 µm and 500 µm openings respectively; scanning electron microscopy (SEM) and ImageJ showed an average salt size of 460 ± 70 µm.

6.3.2. Syntheses

All reactions were run under a nitrogen (N_2) atmosphere with a Teflon-covered stir bar. Following purification, polymer structures (including % acrylation, architecture, and M_n) were confirmed with ^{1}H NMR spectroscopy (Inova 500 MHz spectrometer in FT-mode with $CDCl_3$ as the standard). Polymer thermal properties were determined using differential scanning calorimetry (DSC, TA Instruments Q100) as described below.

Thermoplastic *linear*- and *star*-PLLA (M_n ~15 kg/mol) were synthesized via ring opening polymerizations (ROPs) according to an established protocol.[219] L-lactide (6.0 g), alcohol initiator, and $Sn(Oct)_2$ catalyst were allowed to react ON at 120 °C. The alcohol initiator was varied from difunctional ethylene glycol to tetrafunctional pentaerythritol to achieve a *linear*- and *star*-PLLA architecture, respectively. M_n was controlled via molar equivalence of monomer to initiator (104:1, [M]:[I]). The crude products were dissolved in a minimal amount of chloroform and were precipitated into methanol. Final products were filtered and vacuum dried (RT, ON, 30 in. Hg) to obtain purified *linear*- and *star*-PLLA. Target M_n and architecture were verified using ^{1}H NMR end group analysis (C**H** δ = 5.2 ppm in repeat unit compared to terminal C**H** δ = 3.7 ppm). The following thermal transitions were observed for *linear*-PLLA [T_g = 45 °C, T_m = 155 °C, 50% crystallinity] and *star*-PLLA [T_g = 49 °C, T_m = 152 °C, 15% crystallinity] (Figure S1).

Star-PCL-tetrol was synthesized via ROP (analogous to that described above) with a target M_n of ~10 kg/mol to match that of *linear*-PCL-diol (M_n = 10 kg/mol; Sigma-Aldrich). The ε-caprolactone (25.0 g), pentaerythritol (88:1, [M]:[I]) and $Sn(Oct)_2$ were combined and were allowed to react ON at 120 °C. The crude product was re-dissolved and precipitated as described above to yield purified *star*-PCL-tetrol. The target M_n and architecture were verified via ^{1}H NMR end group analysis (C$\mathbf{H_2}$ δ = 4.1 ppm in repeat unit compared to terminal C$\mathbf{H_2}$ δ = 3.7 ppm). Thermal transitions were determined for both the *linear*-PCL-diol [T_g = -65 °C, T_m = 53 °C, 48% crystallinity] and the *star*-PCL-tetrol [T_g = -63 °C, T_m = 50 °C, 45% crystallinity] (Figure S2).

Linear-PCL-diol and *star*-PCL-tetrol were acrylated to form photo-crosslinkable *linear*-PCL-DA and *star*-PCL-TA macromers, respectively, using established acrylation protocols.[69] Briefly, *linear*-PCL-diol (20.0 g, 2.0 mmol) was combined with DMAP (6.6

mg) serving as the catalyst and they were dissolved in dichloromethane (DCM, 0.17 g/mL). After purging with N_2, triethylamine (4.0 mmol) and acryloyl chloride (8.0 mmol) were added to the flask and the reaction was left to stir at RT for 30 min. An analogous procedure was followed for the *star*-PCL-tetrol but molar ratios were doubled to account for the 4 end groups [DMAP = 13.2 mg, triethylamine = 8.0 mmol, acryloyl chloride = 16.0 mmol]. Established work-up procedures were followed to obtain *linear*-PCL-DA and *star*-PCL-TA.[69] Percent acrylation was confirmed via ^{1}H NMR end group analysis (C$\mathbf{H_2}$ $\delta = 4.1$ ppm in repeat unit, compared to acrylate protons C$\mathbf{H}$=C$\mathbf{H_2}$ $\delta = 5.6$, 6.1 and 6.4 ppm) to be > 85% for both *linear*-PCL-DA and *star*-PCL-TA (Figure S3).

6.3.3. Fabrication

6.3.3.1. Scaffolds

Porous scaffolds were prepared via SCPL, based on a previous report,[69] employing a fused salt template for pore interconnectivity. Sieved NaCl (10.0 g, 460 ± 70 μm) was placed in a 20 mL scintillation vial (I.D. = 25 mm) and DI water (7.5 wt%) was added in four portions followed by manual stirring with a spatula after each addition. The wet salt was pressed with a glass rod and the vials were centrifuged (15 min, 3220 x g). The opened vials were air dried for ~ 1 hr and were subsequently vacuum dried (RT, ON, 30 in. Hg).

Next, macromer solutions were prepared by dissolving a designated macromer or combination of two macromers (75/25 wt% ratio) in DCM (0.15 g total per mL DCM). Photoinitiator solution (10 wt % DMP in NVP) was then added at 15 vol%. To each salt template ~5 mL of macromer solution was added and the vials were centrifuged (10 min, 1260 x g) to promote macromer solution diffusion throughout the template. To crosslink acrylated macromers, opened vials were then exposed to UV light for 5 min (UV-Transilluminator, 6 mW cm^{-2}, 365 nm) followed by air drying in a fume hood ON. To remove the salt template, vials were then placed in a solution of water and ethanol (1:1 by vol.) for ~5 days with daily solution changes. Resulting porous scaffolds were air dried ON, and finally heat treated (170 °C, 10 min, 30 in. Hg). The dried scaffolds (d ~12 mm) were sliced into three specimens (t ~2 mm) (Vibratome, Leica VT 1000 S) and were biopsy punched (Integra Miltex, 6 mm). Final specimen dimensions were d ~6 mm x t ~ 2mm.

6.3.3.2. Solid films

Analogous solid films of each scaffold composition were prepared for % porosity calculations and to evaluate polymer miscibility in film cross-sections. A macromer solution (25 wt% total polymer in DCM), combined with the aforementioned photoinitiator solution (15 vol%), was added to a circular silicone mold (d ~45 mm x t ~2 mm; McMaster-Carr) secured between 2 glass slides. The mold was then exposed to UV-light (UV Transilluminator, 6 mW cm^{-2}, 365 nm) for 3 min on each side. The swollen films were air dried ON followed by vacuum drying (RT, 4 hr, 30 in. Hg), soaking in ethanol while placed atop a shaker table (150 rpm, 3 hr), air drying ON, and finally, heat treated (170 °C, 30 min, 30 in. Hg). Films were punched to form disc specimens (d ~5 mm x t ~1.1 mm) used for testing.

6.3.4. Scaffold Characterization

6.3.4.1. Scaffold Sol Content

Scaffolds (d ~6 mm x t ~2 mm; *N* = 3) were each submerged in 10 mL of DCM in a scintillation vial. Sealed vials were placed atop a shaker table (150 rpm, 48 hr) and scaffolds were subsequently rinsed with DCM, air dried, and dried under vacuum (RT, ON, 30 in. Hg). Initial and final mass values were used to calculate % sol content.

6.3.4.2. Thermal Gravimetric Analysis (TGA)

TGA (TA Instruments Q50) of scaffolds (~10 mg; *N* = 1) was performed under N_2 from RT to 500 °C (heating rate = 10 °C/min) using platinum pans.

6.3.4.3. % Porosity

The percent porosity of scaffolds (*N* = 3) was determined gravimetrically using Equation 1:

$$Porosity\ (\%) = \frac{\rho_{solid\ film} - \rho_{porous\ scaffold}}{\rho_{solid\ film}} * 100 \qquad (1)$$

where $\rho_{porous\ scaffold}$ is the density of the final scaffold specimens and $\rho_{solid\ films}$ is the density of analogous solid film samples.

6.3.4.4. Pore Size

Scaffold pore interconnectivity and pore size were evaluated with SEM (JEOL JCM-5000 Neoscope, accelerating voltage ~10 kV) following coating with Au-Pt (~4 nm). Scaffold images (n = 4) were analyzed using image analysis software (Image J); measurements (*N* = 30) were taken from pores along the diagonal midline to determine average pore size.

6.3.4.5. Thermal Transitions and % Crystallinity

Differential scanning calorimetry (DSC; TA Instruments Q100) was used to determine T_g, T_m, and % crystallinity of PCL and PLLA polymers prior to scaffold fabrication. Specimens (~10 mg; *N* = 3) were sealed in hermetic pans and heated at a rate of 10 °C/min, and values were taken from the second cycle to erase thermal history. The onset and midpoint of $T_{m,PCL}$ and $T_{m,PLLA}$ was determined using TA Universal Analysis software from the onset and the maximum of the endothermic melt peak, respectively. Percent crystallinity was determined with Equation 2:

$$\%\chi_c = \frac{\Delta H_m - \Delta H_c}{\Delta H_m^{\circ}} * 100 \tag{2}$$

where ΔH_m is the enthalpy of fusion taken from the integral of the endothermic melt peak, ΔH_c is the enthalpy of crystallization from the exothermic cold crystallization peak and ΔH_m° is the theoretical value for 100% crystalline PCL (139.5 J/g)[220] or PLLA (93.0 J/g).[221] Scaffolds (*N* = 3) were likewise examined but using a heating rate of 5 °C/min and using the first cycle to examine the impact of fabrication. For semi-IPNs (PCL/PLLA 75/25 wt%), a correction factor to account for polymer wt% was included in % crystallinity calculations according to Equation 3:

$$\%\chi_c = \frac{\Delta H_m - \Delta H_c}{\Delta H_m^{\circ} * w} * 100 \tag{3}$$

where w is the mass fraction of the designated polymer species (i.e. $w = 0.75$ for PCL and $w = 0.25$ for PLLA in semi-IPN compositions).

6.3.4.6. Degradation

Degradation tests were performed under base-catalyzed conditions (0.2 M NaOH) according to ASTM F1635. Scaffold specimens (d ~6 mm x t ~2mm; *N* = 3 per time point) were each submerged in 10 mL of the basic solution in a sealed glass vial and maintained in an incubator (VWR Benchtop Shaking Incubator Model 1570) at 37 °C and 60 rpm. At each of the five designated time points (24, 48, 72, 120, and 168 h), samples were removed, thoroughly rinsed with DI water, blotted, and finally dried under vacuum (RT, ON, 30 in. Hg). Specimen mass was measured to examine gravimetric mass loss.

6.3.4.7. Compressive Mechanical Properties

Scaffold specimens (d ~6 mm x t ~2 mm; *N* = 8) underwent static compression testing (Instron 5944) at RT. Specimens were subjected to a constant strain (1.5 mm/min) up to 85% strain. Due to their non-brittle nature, no specimen fractured. The average compressive modulus (E), strength (CS), and toughness were reported: E was determined from the initial linear region ($\leq$ 10% ε). CS was determined from the stress at 85% strain. Toughness values were calculated from the area of the stress-strain curves up to 85% strain.

6.3.4.8. Shape Memory Properties

6.3.4.8.1. Self-Fitting Behavior in Model Defect

Scaffold specimens (d ~6 mm x t ~2 mm; *N* = 3) were evaluated for their "self-fitting" ability using a model defect representative a rat calvarial defect.[255, 256] From an ultra-high-molecular-weight polyethylene (UHMWPE) sheet (McMaster-Carr, t ~2 mm), a circular defect (d ~5 mm) was created with a drill press (Grizzly G7948). A "fitting temperature" (T_{fit}) was determined as the saline temperature that, after 1 min of submersion, consistently produced a scaffold that was malleable to the touch. A hot plate equipped with a digital temperature probe (Heidolph, MR HEI-TEC) was used to the warm saline in 1 °C intervals within a given scaffold's onset to midpoint $T_{m,PCL}$ range (i.e. 50-56 °C for *linear*-PCL-based and 42-50 °C for *star*-PCL-based scaffolds). T_{fit} was determined to be ~55 °C (for *linear*-PCL-based scaffolds) and ~45 °C (for *star*-PCL-based scaffolds). Next, each scaffold specimen was subjected to the following protocol: (1) submerged into saline previously heated to the designated T_{fit} and maintained for 1 min; (2) removed and immediately press-fitted into a model defect (at RT); (3) maintained in the model defect for 2 min to fix the new temporary shape; (4) removed from the defect (pushing out by hand), allowed to sit for 2 min; (5) re-submerged into the saline bath at T_{fit} for 1 min to elicit shape recovery, removed, allowed to cool at RT for 2 min. At key points during this sequence, the scaffold diameter was measured using electronic calipers to quantify scaffold strain (ε). Steps 1-5 were repeated to determine shape fixity (R_f) and shape recovery (R_r) over a second cycle. From this process, the R_f and shape recovery R_r for the first (N = 1) and second (N = 2) cycles were calculated, according to Equations 4 and 5, respectively:

$$R_f(N) = \frac{\varepsilon_u\,(N)}{\varepsilon_m} \tag{4}$$

$$R_r(N) = \frac{\varepsilon_m - \varepsilon_p\,(N)}{\varepsilon_m - \varepsilon_p\,(N-1)} \tag{5}$$

where ε_m is the maximum strain following step 2, $\varepsilon_u (N)$ is the strain in the stress-free state following step 3, and ε_p is the final recovered strain following step 4. Strain values were determined via electronic caliper measurements.

6.3.4.8.2. Radial Pressure During Shape Recovery

Scaffold discs (d ~6 mm x t ~2 mm; *N* = 5) were subjected to radial mechanical testing (Instron 5965 equipped with a Blockwise RJA62 J-Crimp Radial Compression Station), to determine the radial pressure exerted during shape recovery at a scaffold's T_{fit} (***L**PCL*, ***L/L***, ***L/S*** at 55 °C and ***S**PCL*, ***S/L***, ***S/S*** at 45 °C). This was intended to mimic shape recovery during self-fitting of the scaffold specimen into a d ~ 5 mm defect. Specimens were loaded into the bore set to an initial d ~6.5 mm at RT. The temperature was then increased to the designated T_{fit} and maintained for 3 min. Next, the bore diameter was reduced from 6.5 mm to 5 mm at a rate of 1 mm/min. Force was monitored throughout the procedure, and total radial force (TRF) was calculated and converted to radial pressure based on exact scaffold dimensions.[257]

6.3.4.9. Solution Viscosity and Scaffold Scale-up

6.3.4.9.1. Solution Viscosity

The complex viscosity [η*] of each scaffold macromer precursor solutions (*N* = 3) was measured as a function of frequency (100 Hz to 0.1 Hz, Anton Parr MCR 301). Macromer solutions (0.15 g per mL of DCM) were comprised of *linear*-PCL-diol or *star*-PCL-tetrol (i.e. non-acrylated) and no photoinitiator solution to avoid cross-linking during the test. To determine the intrinsic viscosity, the η* data was extrapolated to a theoretical zero shear rate (0 Hz).

6.3.4.9.2. Solution Diffusion through Salt Template

Select macromer solutions (***L/L*** and ***S/S***), containing dye, were used to assess differences in the rate of diffusion through a salt template. To aide inspection of diffusion, salt templates with a somewhat higher heights were prepared as above but with 15.0 g of sieved salt. Macromer solutions (~7.5 mL) were prepared with designated macromers (i.e. *linear*-PCL-DA and *linear*-PLLA or *star*-PCL-TA and *sta*r-PLLA), 15 vol% photoinitiator solution, and a few drops of food coloring. With two salt templates placed side-by-side, each macromer solution was gently poured over the template simultaneously and diffusion captured via video. The process was repeated in triplicate.

6.3.4.9.3. Scaled-up Scaffold Fabrication

The ***L/L*** and ***S/S*** compositions were again selected to fabricate larger scaffolds due to their lowered solution viscosities. A 5 mm hole (diamond core drill bit, Marshalltown) was drilled into the bottom of a 100 mL beaker (I.D. = 43.6 mm) to aid in macromer solution diffusion. Each 100 mL beaker was filled with 50.0 g of salt and 7.5 wt% water was incorporated over 4 additions with mechanical mixing following each addition. A smaller beaker was used to manually push the wet salt down and the salt molds were vacuum dried (RT, 30 in. Hg., ON). Macromer solutions were prepared (~15 mL) according to that described above for fabrication of smaller scaffolds. Once mixed, macromer solution was poured on top of the fused salt mold and was allowed to sit for ~3 min to permit diffusion; aluminum foil covered the beaker to prevent premature UV curing and solvent evaporation. Following UV-cure (IntelliRay 400, 50% intensity) for 10 min, specimens were allowed to dry in a fume hood (48 hr) and were then soaked in a 1:1 DI water:ethanol solution with daily solution changes. Dried scaffolds were then annealed and sliced into 2 mm specimens, as described above for the smaller scaffolds. Note, both types of scaffolds were maintained at their full diameter for size comparisons (ie. no biopsy punch was used). Photos were taken throughout the procedure and low magnification optical microscopy (Leica DM 6B; 5X) was performed on scaffold specimens to broadly examine pore morphology. The procedure was performed in triplicate and scaffolds were measured with electronic calipers to quantify dimensional changes. SEM (JEOL JCM-5000 Neoscope, accelerating voltage ~10 kV, Au-Pt coating ~4 nm) with energy dispersive X-ray spectroscopy (EDS, Oxford Instruments) elemental mapping was also performed for to confirm full porogen leaching of larger constructs.

6.3.5. Statistical Analyses

All data was reported as the average ± standard deviation. ANOVA tests were performed and if there was a statistical difference, t-tests were performed against the ***LPCL*** control. T-tests were also used to make direct comparisons between compositions of interest, which will be specified for each result discussed. For mechanical testing, interquartile range tests were performed and values that were determined as being outliers were removed from the data (final $N \geq 5$). For rheology data, linear regression was used to extrapolate complex viscosity to zero shear. Regression analyses were only performed up to 1 Hz to achieve $R^2 > 0.5$ and zero shear viscosities were reported as averages ± the standard error.

6.4. Results and Discussion

6.4.1. Macromer Synthesis

Linear- and *star*-PLLA (M_n ~ 15 kg/mol) (**Figure A-2**) as well as *linear*-PCL-diol and *star*-PCL-tetrol (M_n ~10 kg/mol) (**Figure A-3**) were characterized. Star macromer M_n was selected to match previously studied linear macromers in order to rule out M_n as a variable. As described above, ^{1}H NMR end group analysis was used to determine M_n and confirm architecture (i.e. terminal group protons were approximately doubled for star precursors). DSC was used to determine thermal transitions and % crystallinity, with differences in thermal properties used to further validate precursor architecture. The T_g and T_m values as well as % crystallinity varied for the *linear*-PLLA (T_g ~45 °C, T_m ~155 °C, ~50%) versus the *star*-PLLA (T_g ~49 °C, T_m ~152 °C, ~15%). Likewise, differences were observed for the T_g, T_m, and % crystallinity values of the *linear*-PCL diol (T_g ~ -65 °C, T_m ~53 °C, ~48%) and the *star*-PCL tetrol (T_g ~ -63 °C, T_m ~50 °C, ~45%). Subsequently, the *linear*-PCL diol and *star*-PCL tetrol were successfully acrylated (>85%) to yield *linear*-PCL-DA and *star*-PCL-TA, respectively (**Figure A-4**).

6.4.2. Scaffold Fabrication

Fabricated scaffolds were characterized in various ways to ensure effective cross-linking (sol content), to confirm the targeted PCL/PLLA wt% ratio of 75/25 (TGA), and to quantify pore size and % porosity (SEM and density calculations, respectively). Sol content values for 100% PCL controls [***LPCL*** and ***SPCL***] was just 2-4 %, further indicating successful cross-linking (i.e. > 95%) (**Figure 6-2**). All semi-IPN scaffolds displayed sol content values < 29%, similar to the controls when the thermoplastic PLLA (incorporated at 25 wt%) was considered. Additionally, the TGA thermograms of semi-IPNs all showed ~25 wt% mass loss from 250-350 °C that corresponded to the 25 wt% PLLA contained (**Figure 6-3**). Thus, the PLLA did not diminish *linear*-PCL-DA or *star*-PCL-TA cross-linking and the targeted 75/25 wt% ratio of PCL:PLLA was maintained. Finally, SEM imaging and analysis confirmed the targeted pore interconnectivity and ~220 µm average pore size (**Figure 6-4-a**), within the range associated with osteogenesis.[258] Porosity calculations revealed that all scaffolds were similarly ~60% (**Figure 6-4-b**).

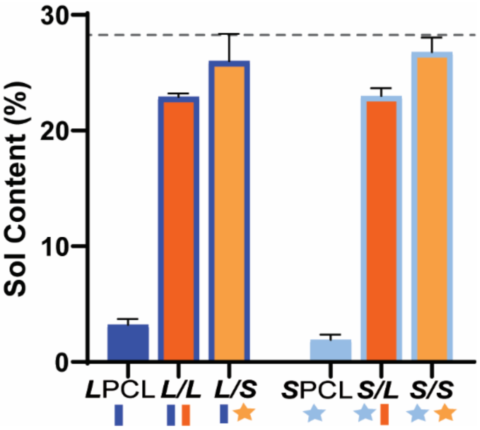

Figure 6-2. Sol content values of scaffolds demonstrating adequate cross-linking with an upper limit of ~29% mass loss [~2-4% for ***LPCL*** and ***SPCL*** controls + ~25% thermoplastic PLLA] for semi-IPN films.

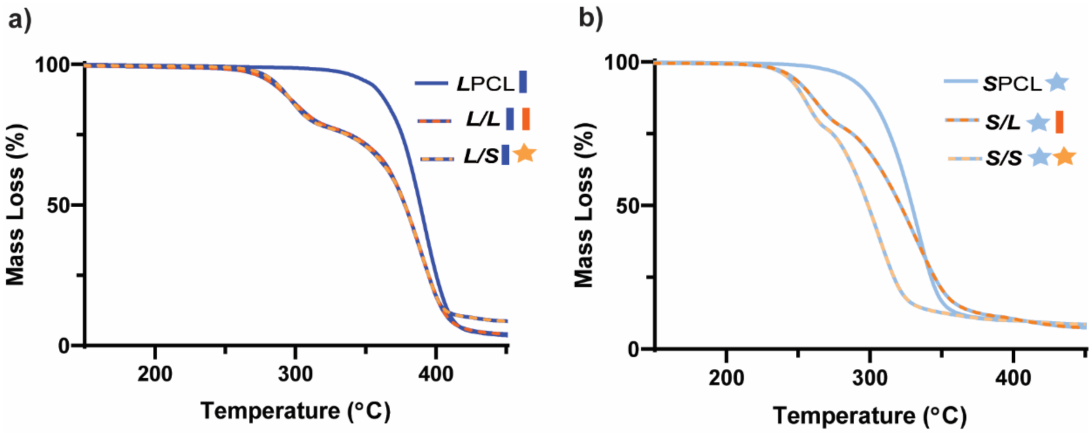

Figure 6-3. TGA of scaffolds verifying ~25% thermoplastic in PCL/PLLA semi-IPNs (a) for *linear*-PCL-DA based compositions, and (b) for *star*-PCL-TA based compositions.

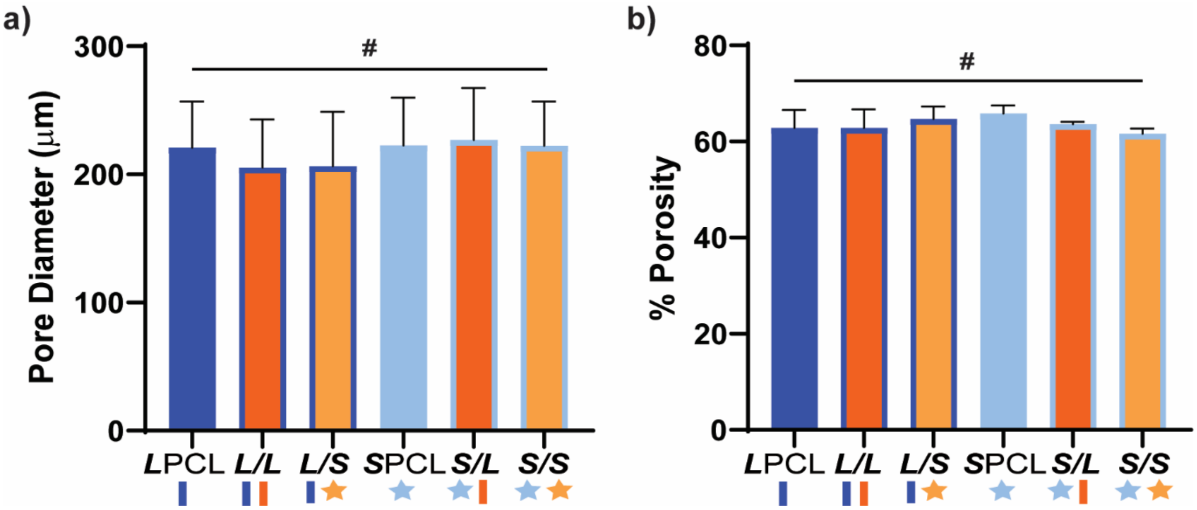

Figure 6-4. (a) Pore size was maintained at ~220 μm for all scaffolds, and (b) all scaffolds exhibited similar ~60% porosity ($^{\#}p > 0.05$).

6.4.3. Scaffold Thermal Properties

6.4.3.1. PCL T_m

The midpoint melting temperature of PCL ($T_{m,PCL}$) represents the temperature to which the scaffold must be heated to confer *maximum* shape recovery, key to self-fitting into the bone defect. The T_m values were quantified for all scaffold compositions (**Figure 6-5-a, Table B-8**). Notably, the midpoint $T_{m,PCL}$ values were significantly reduced (~6 °C) for *star*-PCL-based versus *linear*-PCL-based scaffolds. The ***LPCL*** scaffold had a $T_{m,PCL}$ ~56 °C (midpoint) that was maintained following incorporation of *linear*- or *star*-PLLA to form ***L/L*** and ***L/S*** semi-IPN scaffolds, respectively. In contrast, for the ***SPCL*** scaffold, the $T_{m,PCL}$ (midpoint) was significantly reduced to ~50 °C. These values were maintained with the incorporation of *linear*- or *star*-PLLA to form ***S/L*** and ***S/S*** semi-IPNS, respectively. As is discussed later, *star*-PCL-based scaffolds begin to soften and undergo self-fitting in model defects at temperatures below $T_{m,PCL}$ ~50 °C (midpoint), due to the fact that the onset melting temperature of PCL is just ~42 °C (**Figure 6-5-b, Table B-8**). This presents a unique way to afford a tunable $T_{m,PCL}$ in a chemically cross-linked PCL scaffold, considering that our group has previously tuned PCL M_n (~10 kg/mol to ~5 kg/mol) but this did not yield appreciable differences in scaffold $T_{m,PCL}$ (56.2 ± 0.4 to 54.4 ± 0.6 °C, respectively).[71] In this way, *star*-PCL-based compositions are expected to improve tissue safety during self-fitting into bone defects.

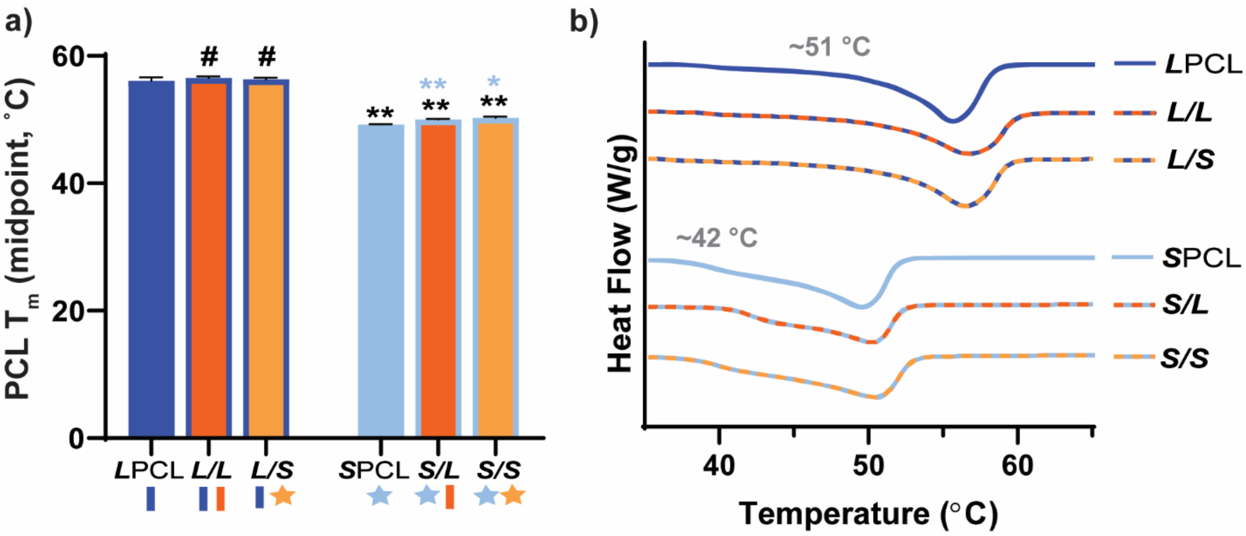

Figure 6-5. (a) Midpoint T_m of PCL of scaffolds; $*p < 0.05$, $**p < 0.01$, $\#p > 0.05$. Note: The "black color-coded statistics" are comparisons to ***LPCL*** and "blue color-coded statistics" are comparisons to ***SPCL***. (b) Representative thermogram for each scaffold composition.

6.4.3.2. PCL Crystallinity

PCL crystalline lamellae are the origin of shape memory behavior and thus self-fitting behavior and further have a significant impact on degradation and mechanical properties. Thus, scaffold PCL % crystallinity was quantified from DSC (**Figure 6-6-a, Table B-8**). For ***LPCL***, PCL % crystallinity was ~42%. When corrected for weight % in semi-IPN compositions (PCL/PLLA, 75/25 wt%), PCL % crystallinity was maintained for *linear*-PCL-based semi-IPNs (i.e. ***L/L*** and ***L/S***). In the case of ***SPCL***, PCL crystallinity was significantly reduced to ~30%. As described later, the PCL % crystallinity of all scaffolds was sufficient to retain similarly shape recovery and shape fixity. However, the addition of *linear*- or *star*-PLLA to form ***S/L*** and ***S/S*** semi-IPNs resulted in increased PCL crystallinity of ~34% and ~39% (with ***S/S*** similar to the ***LPCL*** control), respectively.

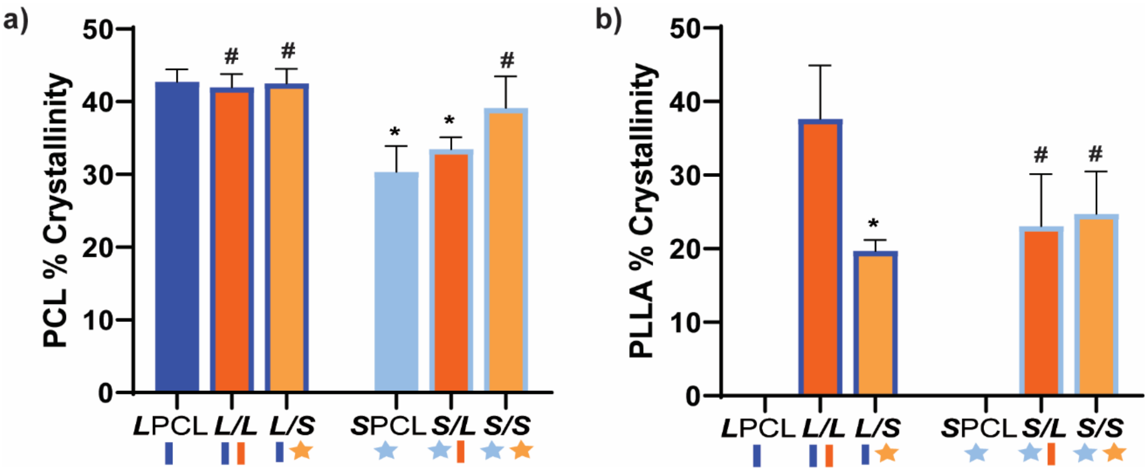

Figure 6-6. Scaffold (a) PCL % crystallinity; *p < 0.05 and #p > 0.05 versus ***LPCL*** and (b) PLLA % crystallinity; *p < 0.05 and #p > 0.05 versus ***L/L***.

6.4.3.3. PLLA Crystallinity

PLLA crystallinity will impact scaffold degradation and mechanical properties. The previously reported ***L/L*** semi-IPN scaffold exhibited PLLA crystallinity (~38%) and $T_{m,PLLA}$ (midpoint) (164 °C) (**Table B-8, Figure 6-6-b**). When *star*-PLLA was incorporated into the *linear*-PCL-DA network, the resulting ***S/L*** semi-IPN scaffold exhibited significantly decreased PLLA crystallinity (~20%, ~158 °C). For *star*-PCL-based semi-IPNs, the PLLA crystallinity was somewhat intermediate: ***S/L*** (~23%, ~160 °C) and ***S/S*** (~25%, ~157 °C), but was not statistically significant compared to the ***L/L***. Thus, versus the ***L/L*** semi-IPN scaffolds, the ***S/L***, ***S/L***, and ***S/S*** had somewhat diminished PLLA crystallinity and is considered in analysis of degradation and mechanical properties.

6.4.4. Degradation Behavior

Previously, we reported that the ***L***/***L*** semi-IPN scaffold degraded significantly faster than the ***LPCL*** control.[71, 157, 159] Further acceleration of degradation is anticipated to favorably allow neotissue formation as well as osteogenesis.[19, 236-238] This present study revealed that the ***L/S*** semi-IPN degraded faster than the ***L/L*** semi-IPN (**Figure 6-7-a**). In the case of *star*-PCL-based compositions, the ***SPCL*** scaffold degraded slowly, similar to ***LPCL*** (**Figure 6-7-b**). However, the ***S/L*** and ***S/S*** semi-IPNs degraded faster and generally similar to each other. By examining mass loss at the 72 hr timepoint (**Figure 6-7-c**) as well as images of specimens at increasing time points (**Figure 6-7-d**), it is clear that ***S/L*** and ***S/S*** exhibited the most rapid rate of mass loss, even faster than ***L/S***. Notably, mass loss at earlier timepoints (48 hr) was greater for ***S/S*** versus ***S/L***. The origin of the accelerated degradation of the semi-IPNs was considered. While reduced levels of PCL and/or PLLA % crystallinity of semi-IPNs (**Table B-8, Figure 6-6**) would be predicted to increase their rate of degradation, these properties were not always correlative. For instance, the ***L/S*** and ***S/S*** showed similar PCL % crystallinity (~40%), and the ***L/S*** showed a lower PLLA % crystallinity (~20% compared to 25%), but the ***S/S*** degraded significantly faster than the ***L/S***. Thus, PCL/PLLA phase separation was considered, as this has been known to contribute to accelerated degradation of blends[218, 225] and semi-IPNs.[71, 157, 158] SEM of analagous solid films demonstrated distinct morphologies for each composition (**Figure 6-8**). Both 100% PCL controls [***LPCL*** and ***SPCL***] showed a uniform morphology as expected based on their chemical homogeneity. The ***L***/***L*** (i.e. slowest degrading semi-IPN) also showed minimal signs of phase separation but all other semi-IPNs [***L***/***S***, ***S***/***L*** and ***S***/***S***] showed greater evidence of coalescence, known to indicate greater phase separation or immiscibility.[158, 226, 227] Further, these new semi-IPNs demonstrate the potential to both tune and accelerate scaffold degradation driven by phase separation. However, current results are limited to base-catalyzed conditions which have been known to impact polyester degradation kinetics,[224] but these scaffolds would benefit from moving forward to long-term neutral hydrolysis and *in vivo* degradation studies. PCL alone has been known to degrade *in vivo* over the course of ~2 years,[200, 201] but these faster degrading scaffolds demonstrate potential to more closely mimic the timescale of CMF bone regeneration (3 to 6 months).[238] Moreover, tunability observed may allow for scaffolds with patient-specific degradation rates (ie. age, defect size, etc.) to further optimize CMF bone regeneration.[259]

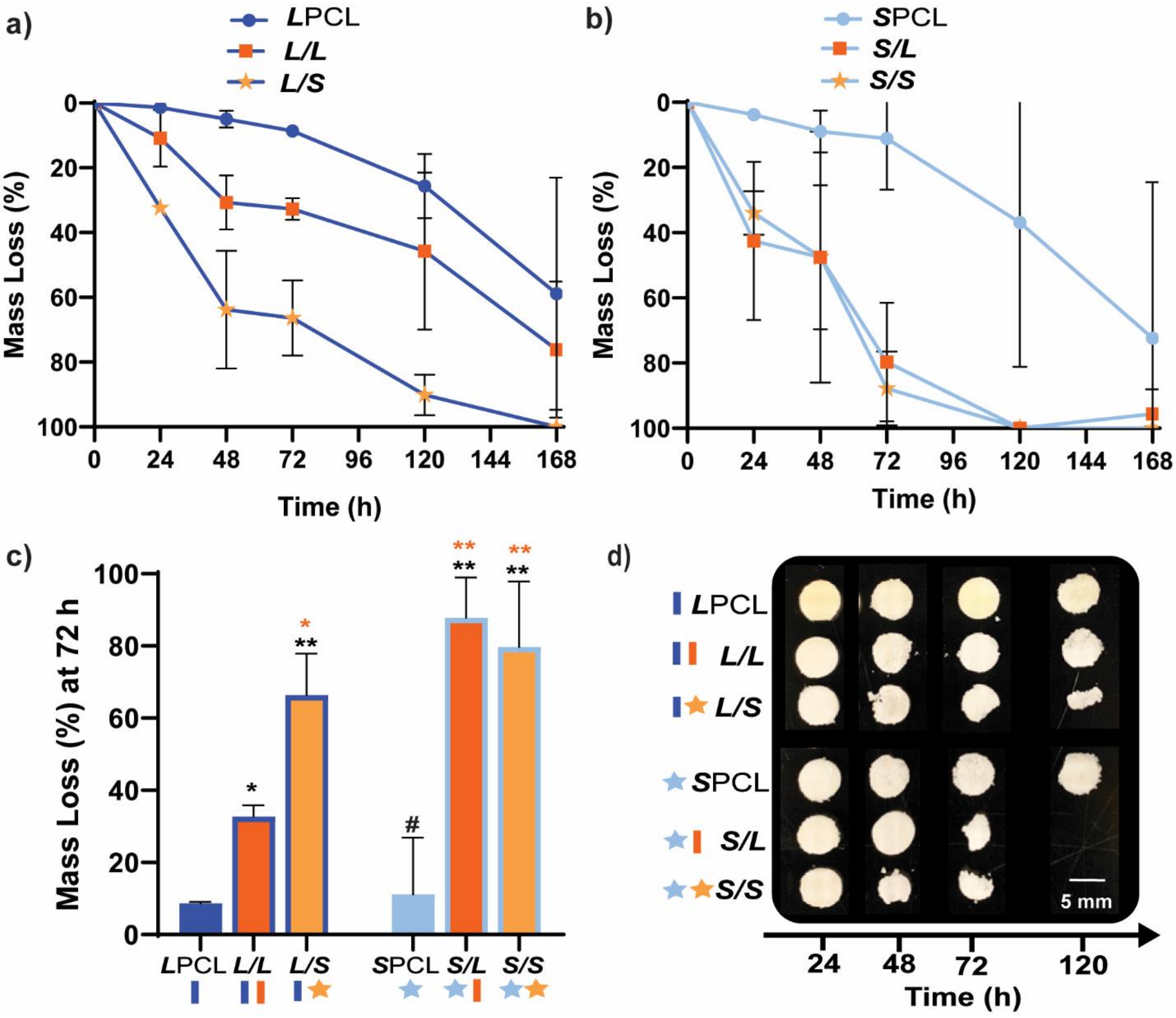

Figure 6-7. Gravimetric mass loss over time for base-catalyzed degradation studies (0.2 M NaOH, 37 °C, 60 rpm) for (a) *linear*-PCL-based and (b) *star*-PCL-based scaffolds. (c) Mass loss at 72 hr was compared for all scaffold compositions; $*p < 0.05$, $**p < 0.01$, $^{\#}p > 0.05$. *Note:* The "black color-coded statistics" were compared to *LPCL* control while "orange color-coded statistics" were compared to the *L*/*L* composition. (d) Representative photos of specimens at different timepoints during degradation study.

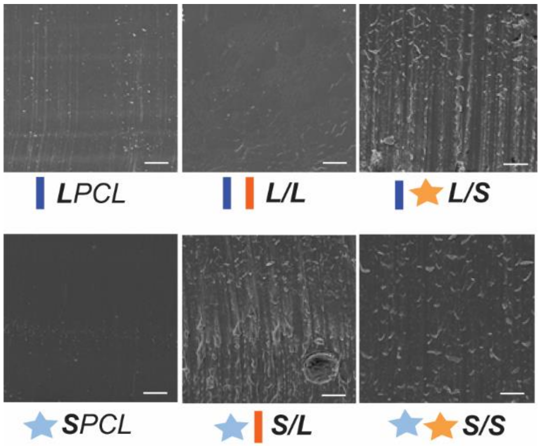

Figure 6-8. SEM images of solid film cross-sections of analogous compositions to scaffolds to examine relative miscibility or phase separation. Scale bars = 50 μm.

6.4.5. Mechanical, Shape Memory, and Radial Expansion Pressure Properties

6.4.5.1. Mechanical Properties

Mechanically robust SMP scaffolds are expected to afford superior outcomes in the treatment of bone defects. Static compressive testing was performed to assess the compressive mechanical properties of the SMP scaffolds. For *linear*-PCL-based compositions, versus the ***LPCL*** control (~9.65 MPa), the modulus (E) was significantly increased for both the ***L***/***L*** (~23.8 MPa) and ***L***/***S*** (~17.4 MPa) semi-IPNs (**Figure 6-9-a, Table B-9**). In terms of *star*-PCL-based compositions, for the ***SPCL*** control (~3.57 MPa), E was significantly lower than the ***LPCL***. This was attributed to the former's reduced PCL % crystallinity, in spite of having a higher relative cross-link density. However, versus the ***SPCL***, E was increased for the ***S***/***L*** (~11.9 MPa) and ***S***/***S*** (~11.3 MPa) semi-IPNs, similar to the ***LPCL*** control. All semi-IPNS exhibited higher E values versus the 100% PCL controls, but the E values of ***L/L*** and ***L/S*** were higher than that of ***S/L*** and ***S/S***. Similar trends generally emerged for compressive strength (CS) (**Figure 6-9-b**) as well as for toughness (**Figure 6-9-c**). No scaffold fractured during the test (i.e. withstood 85% strain), indicative of their non-brittle behavior that is desirable in the intended application of CMF bone defect treatment. Moreover, all scaffold compositions demonstrated robust mechanical properties for handling and press-fitting. Further if the reduced E and CS of the ***S**PCL* compositions is a concern, the PLLA semi-IPNs offer a strategy to recuperate the mechanical properties of the ***L**PCL* control while affording lowered $T_{m,PCL}$ and accelerated degradation. Of all compositions, the ***L/S*** semi-IPN exhibited the greatest CS and toughness, while the ***S/L*** semi-IPN exhibited enhanced CS and toughness versus the ***S**PCL* control. Thus, a *star*-architecture affords certain semi-IPNs (**L/S** and ***S/L***) with particularly notable mechanical properties.

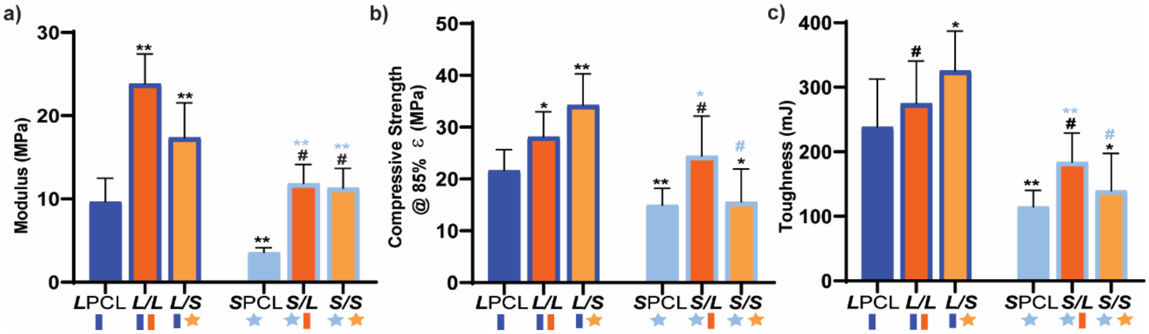

Figure 6-9. Compressive mechanical properties were compared including (a) E, (b) CS, and (c) toughness; $*p < 0.05$, $**p < 0.01$, $^{\#}p > 0.05$. *Note:* The "black color-coded statistics" are compared to the ***L**PCL* and "light blue color-coded statistics" are compared to ***S**PCL*.

6.4.5.2. Self-fitting Properties

Scaffold specimens (d ~6 mm x t ~2 mm) were press-fitted into a plastic model defect (d ~5 mm x t ~2 mm). This defect represented a rat bilateral calvarial defect model of the same dimensions, typically used as an entry-level model for bone defect healing studies.[256, 260] A slighter larger scaffold diameter was selected to promote contact along the defect perimeter. Herein, scaffolds were fitted in the same fashion envisioned a clinical setting (**Figure 6-10-a,b**). A T_{fit} was the minimum saline bath temperature that in just 1 minute produced a softened, malleable scaffold: ~55 °C for *linear*-PCL-based and ~45 °C for *star*-PCL-based scaffolds. A sequence of steps was used to assess self-fitting and ultimately quantify R_f and R_r (Fi**gure 6-10-c, Figure 6-11**). Following submersion in saline at T_{fit} for 1 minute [step 1], all scaffolds were successfully press-fitted into defects (i.e. expanded via shape recovery to fill the defect) [step 2]. After just 2 minutes within the defect, scaffolds returned to their relatively rigid state (i.e. underwent shape fixation in new shape within the defect) [step 3]. Next, scaffolds were removed from the defect and allowed to sit for 2 min (to determine shape fixity) [step 4] and reheated at T_{fit} in saline for 1 minute (to determine shape recovery) [step 5]. For both cycles, these values were consistently at or near 100% for all scaffolds. These results further validate that the semi-IPN design, based on any combination of *linear*-PCL-DA or *star*-PCL-TA and both *linear*-PLLA or *star*-PLLA, does not compromise shape memory behavior. However, as osteonecrosis begins to occur with exposure to temperatures ≥50 °C, the lower T_{fit} of *star*-PCL-based scaffolds (i.e. ***SPCL***, ***S/L***, and ***S/S***) is more "tissue-safe". Furthermore, their observed T_{fit} of 45 °C may be considered ideal for this application of self-fitting CMF bone scaffolds, as T_{fit} is still sufficiently above T_{body} to maintain fixed scaffolds in their rigid state to support CMF bone healing. Future work may allow for further lowering of SMP scaffold T_{fit} toward T_{body} that would provide new opportunities for use in self-expanding or self-deploying TE applications.

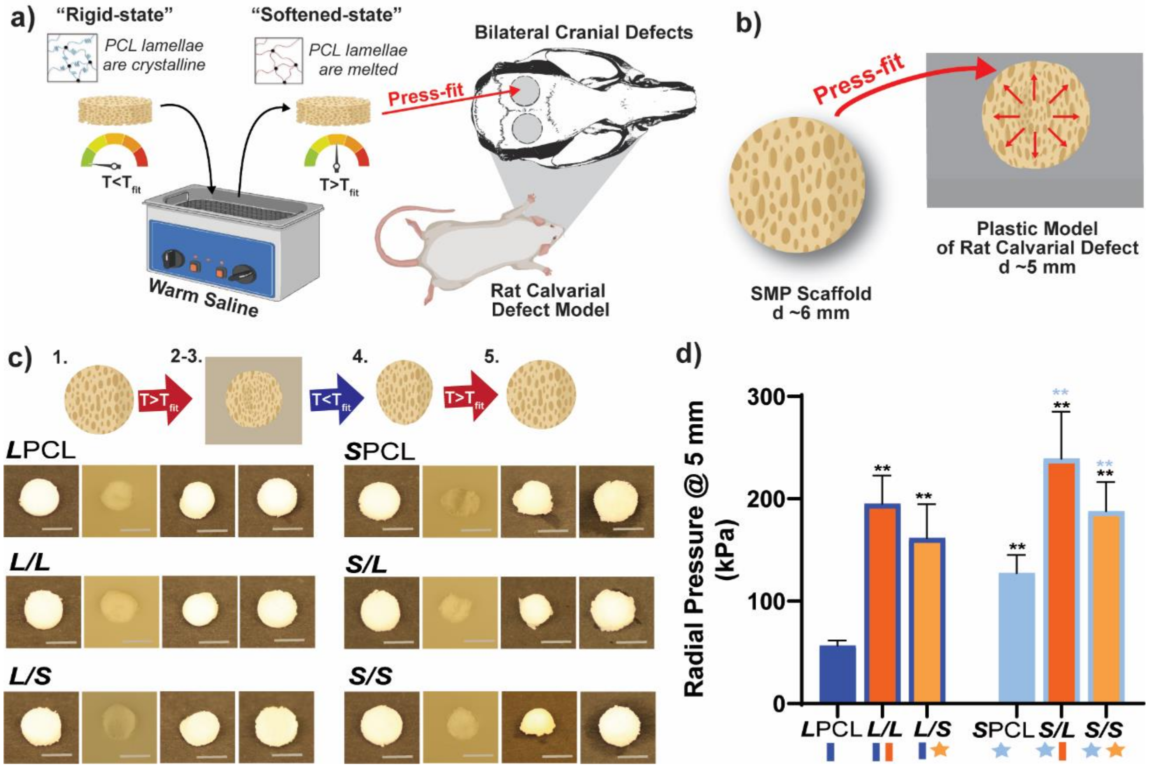

Figure 6-10. (a) Shape memory testing was performed to mimic a bilateral rat calvarial defect model *in vivo* study. (b) Scaffolds were designed to be slightly larger than the cranial defect, so the warm scaffold will exert a force on the defect edges, as shown in the schematic. (c) All compositions were able to be press-fitted into a plastic model defect and demonstrated excellent shape fixity/recovery. (d) Radial expansion pressure tested at T_{fit}; *$p < 0.05$, **$p < 0.01$. *Note:* "black color-coded" statistics are compared to *LPCL* and "blue color-coded statistics" are compared to *SPCL*.

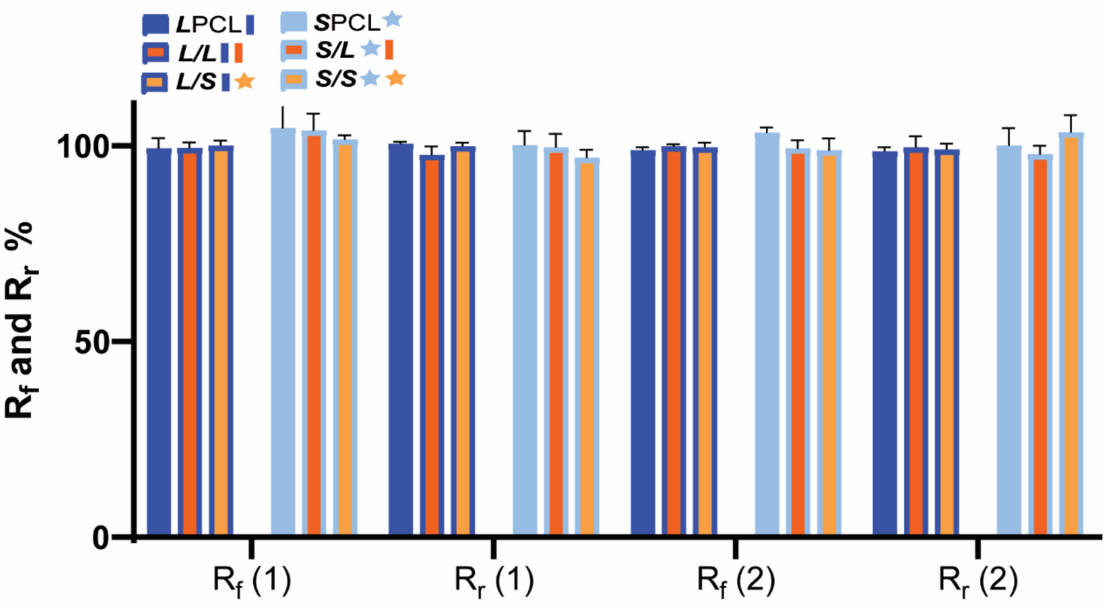

Figure 6-11. Quantitative shape fixity (R_f) and shape recovery (R_r) over 2 cycles; #p > 0.05.

6.4.5.3. Radial Pressure

For the first time, we report the radial pressures exerted by the SMP scaffolds during self-fitting at their T_{fit} to quantify the force exerted by the scaffold against the defect edges, driven by shape recovery (**Figure 6-10-d**). Enhanced radial pressures are anticipated to promote implant stability and osseointegration. The pressure was monitored while a scaffold (d ~ 6mm x t ~2 mm), initially loaded into a bore (d ~6.5 mm) at RT, was heated to its T_{fit} and the bore diameter then reduced to that of a calvarial defect (d ~5 mm). Versus the ***LPCL*** control (~57 kPa), radial pressure significantly increased for the ***L/L*** (~195 kPa) and ***L/S*** (~162 kPa) semi-IPNs, attributed to the rigid PLLA. The radial pressure of the ***SPCL*** (~127 kPa) was also much higher than the ***LPCL***, which may be attributed to its higher crosslink density. A further substantial increase in radial pressure was noted for the ***S/L*** (~239 kPa) and ***S/S*** (~188 kPa) versus the ***SPCL***, again stemming from the rigid PLLA. Thus, the substantial gains in radial pressure (versus the ***LPCL*** control) observed for the ***SPCL*** and all semi-IPNs affords improved scaffold expansion toward defect edges during self-fitting, which is anticipated to promote osseointegration and overall implant stability in future *in vivo* studies.

6.4.6. Solution Viscosity and Scaffold Scale-up

In the aforementioned analyses, SMP scaffolds were prepared with a diameter of ~6 mm (biopsy punch of a scaffold with d ~12 mm); this size is appropriate for bilateral rat calvarial defect studies. However, larger scaffolds are necessary for critically-sized defects in animal models (up to d ~22 mm)[120] and eventually for human patients. While centrifugation to drive diffusion is permissible for small scaffolds that are prepared in scintillation vials, this is not the case for larger scaffolds. Because *star*-polymers are known to have a lowered solution viscosity,[253, 254] we expected that SMP scaffolds prepared with such would more readily permit the preparation of larger specimens. First, the complex viscosity [η*] of scaffold precursor solutions were determined over a frequency sweep (**Figure 6-12-a**) and the intrinsic viscosity calculated by extrapolation to a zero-shear rate (**Figure 6-12-b**). Both 100% PCL controls (***LPCL*** and ***SPCL***), exhibited a relatively high intrinsic viscosity (~9 kPa*s). For semi-IPN macromer solutions containing *linear*-PCL, intrinsic viscosity was reduced with *star*-PLLA (***L/S***; ~1 kPa*s) versus with *linear*-PLLA (***L/L***; ~6 kPa*s). Semi-IPN macromer solutions based on *star*-PCL were likewise reduced, particularly with *star*-PLLA (***S/S***; ~1 kPa*s) versus with *linear*-PLLA (***S/L***; ~6 kPa*s). Because of their relatively high and low intrinsic viscosities, respectively, ***L/L*** and ***S/S*** semi-IPN macromer solutions were selected to prepare larger scaffold specimens. First, using fused salt templates prepared in scintillation vials, diffusion of the precursor solutions containing food coloring was monitored (**Figure 6-12-c**, **Video S1**). Owing to its lower intrinsic viscosity, the ***S/S*** solution diffused more quickly to the bottom of the template (~90 s) versus the ***L/L*** solution (>120 s). Next, ***L/L*** and ***S/S*** were prepared as actual scaled-up, "larger" scaffolds, using 100 mL beakers (50 g salt) in place of the 20 mL vials (10 g salt). Analogous "regular" scaffolds were prepared in the 20 mL vials (10.0 g salt), but the diameter was not reduced from ~12 mm using a biopsy punch. Thus, the "larger" scaffolds had a diameter and volume that was 2X and 5X, respectively, that of the "regular" scaffolds (**Figure 6-13-a,b**). For the "large" ***S/S*** scaffolds, a total of four 2 mm thick specimens (i.e. slices) could be harvested versus just three 2 mm thick slices for the "larger" ***L/L*** scaffolds (**Figure 6-14**). This stemmed from a lack of diffusion, wherein the ***L/L*** macromer solution did not reach the bottom of the mold, rendering the bottom portion deficient. While density did not change according to gravimetric analysis (**Figure 6-13-c**), low magnification optical microscopy revealed that ***S/S*** demonstrated superior uniformity of pores throughout versus the ***L/L***. Full porogen leaching has been previously noted as a limitation in SCPL fabrication;[261] however, herein the NaCl porogen used in fabrication was shown to be fully removed even from "larger" scaffolds, likely owing to the use of a fused salt template resulting in interconnected pores. This was validated via SEM and EDS mapping to show that the scaffolds did not contain any appreciable amount of Na or Cl (**Figure 6-15**). Lastly, as a further indicator of their utility as a surgical product to treat bone defects, the ***S/S*** scaffold was able to be trimmed with a scissor and also sutured (**Figure 6-16-a**).

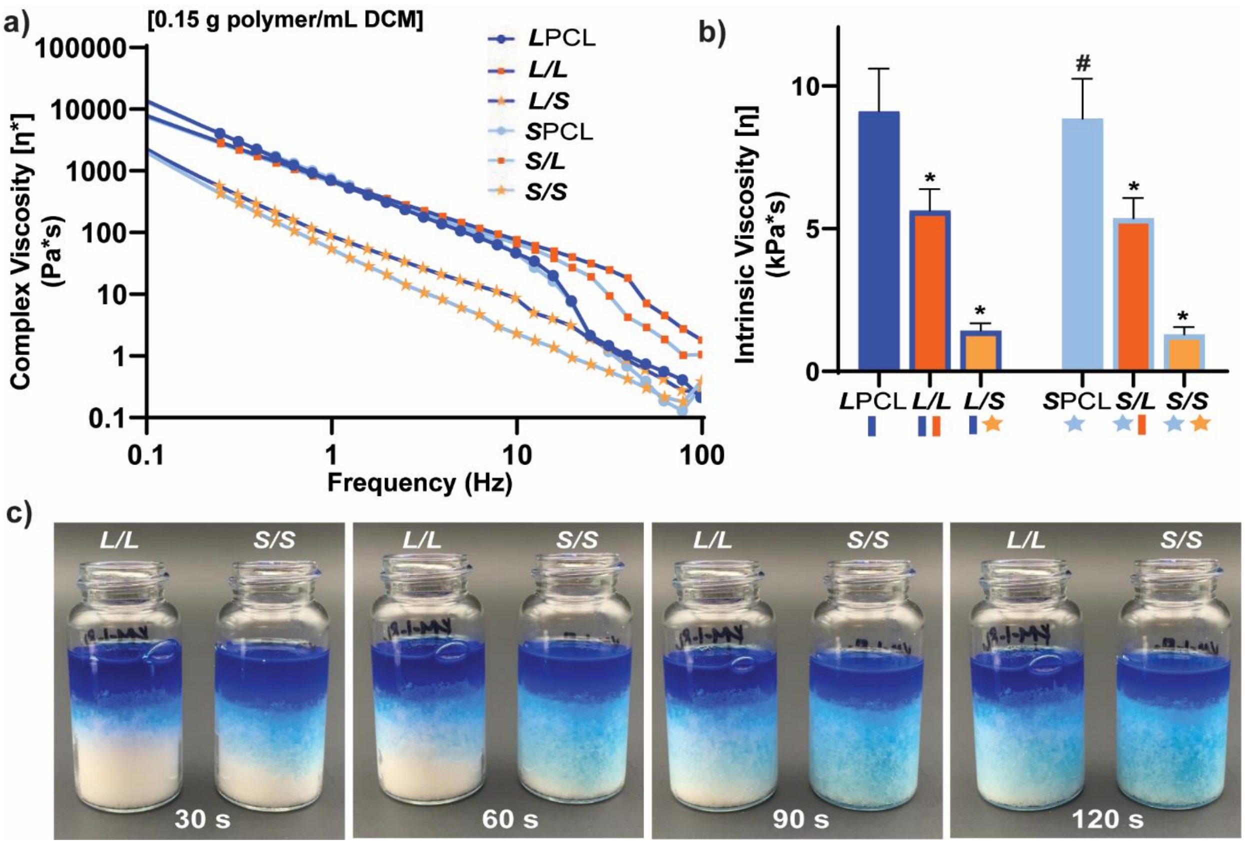

Figure 6-12. For scaffold precursor solutions: (a) complex viscosity [η*] versus frequency, (b) intrinsic viscosity (*$p < 0.05$, **$p < 0.01$ compared to ***LPCL***). (c) ***L/L*** and ***S/S*** semi-IPN macromer solution diffusion through a template using 15.0 g salt in a scintillation vial.

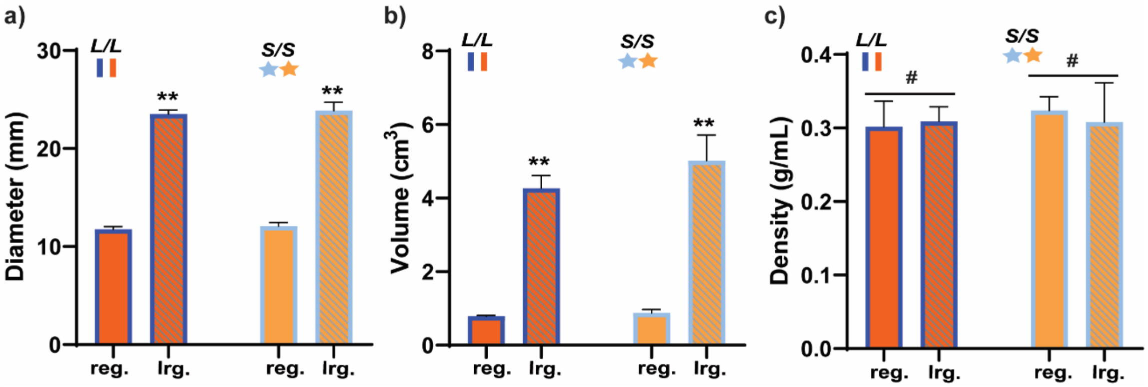

Figure 6-13. The scaled-up, larger, scaffolds ("lrg.") compared to smaller, regular scaffolds ("reg") having: (a) 2X the diameter, (b) 5X the volume, and (c) constant density (***p* <0.01, # *p* >0.05 versus "reg.").

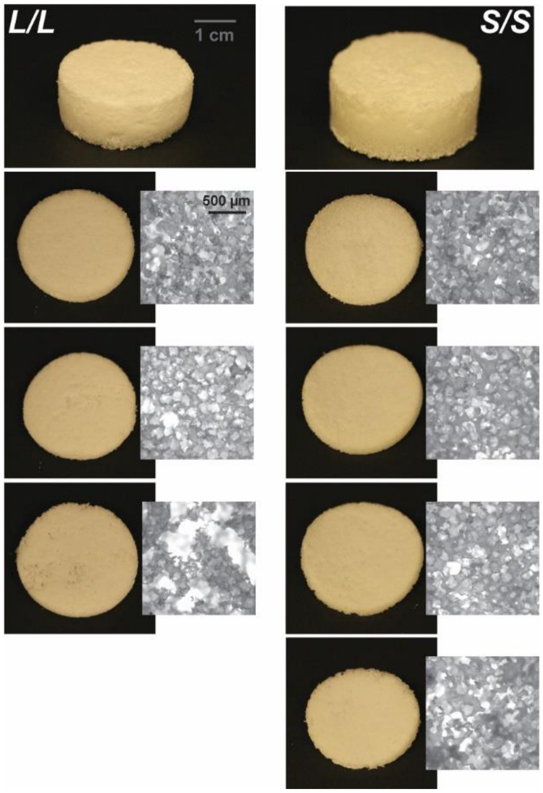

Figure 6-14. Photos and optical microscopy (5X) of scaled-up, "large" ***L/L*** and ***S/S*** scaffolds (d ~24 mm) demonstrating superior macromer diffusion, and more uniform pores, for the ***S/S*** composition.

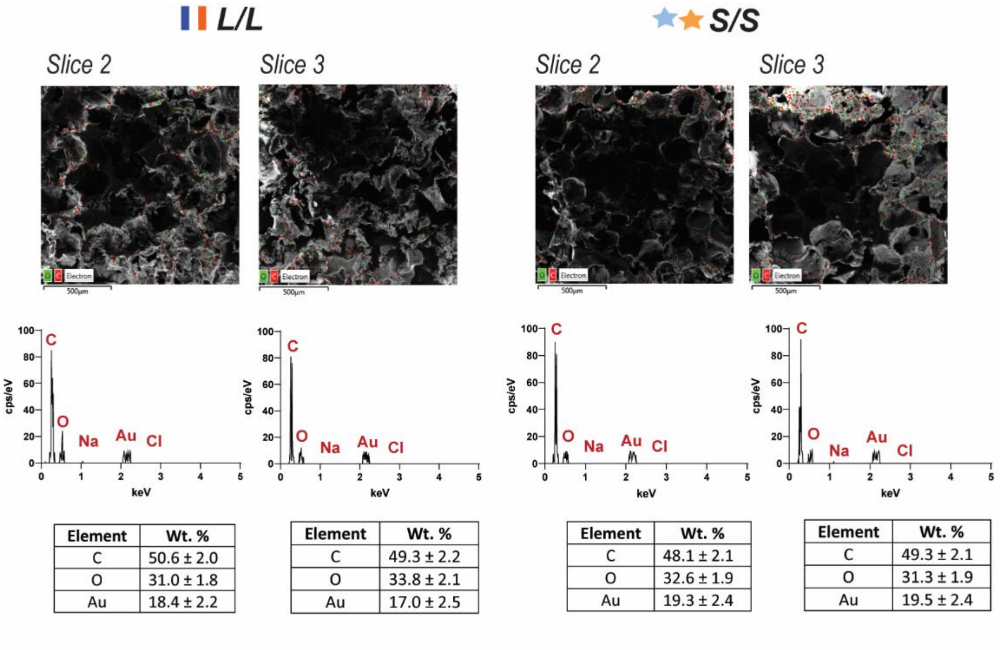

Element	Wt. %
C	50.6 ± 2.0
O	31.0 ± 1.8
Au	18.4 ± 2.2

Element	Wt. %
C	49.3 ± 2.2
O	33.8 ± 2.1
Au	17.0 ± 2.5

Element	Wt. %
C	48.1 ± 2.1
O	32.6 ± 1.9
Au	19.3 ± 2.4

Element	Wt. %
C	49.3 ± 2.1
O	31.3 ± 1.9
Au	19.5 ± 2.4

Figure 6-15. “Larger” scaffold slices were subjected to SEM EDS elemental mapping to confirm full porogen (NaCl) leaching. As shown, no Na or Cl was detected indicating that scaffolds were free from residual porogens.

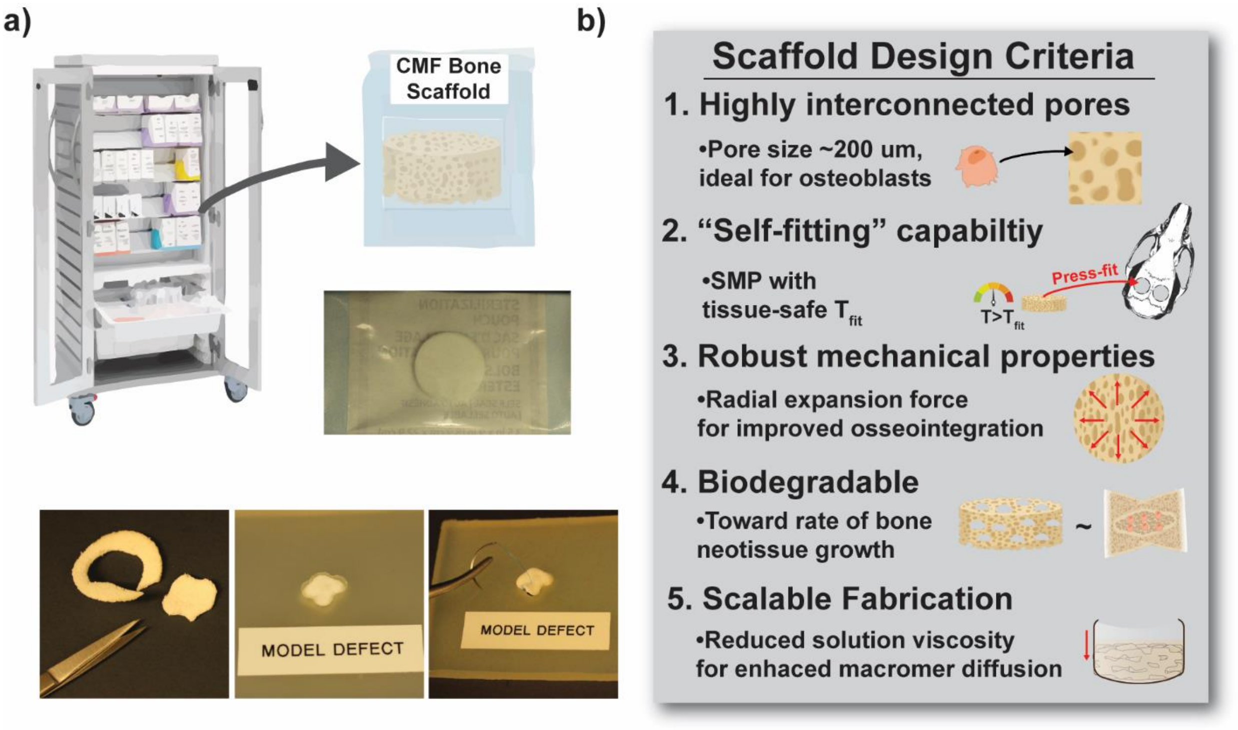

Figure 6-16. (a) The scaled-up, larger scaffold specimens (d ~24 mm x t ~2 mm) were able to be easily cut to custom defect geometries with scissors and could hold a suture. (b) The ***S/S*** semi-IPN (i.e. comprised of *star*-PCL-TA and *star*-PLLA) achieved five scaffold design criteria intended for an off-the-shelf surgical product to heal bone defects.

6.5. Conclusions

Towards improving the utility of "self-fitting" SMP scaffolds, semi-IPN compositions were prepared with *star*-polymer architectures. Originally prepared from *linear*-PCL-DA and *linear*-PLLA (75/25 wt%), the ***L/L*** semi-IPN exhibited improved rigidity and accelerated degradation versus *linear*-PCL-DA (***LPCL***). In this work, the semi-IPN based on *star*-PCL-TA and *star*-PLLA (***S/S***) (75/25 wt%) exhibted distinct advantages and fulfilled key criteria as a surgical product to treat CMF bone defects (**Figure 6-16-b**). The pore size (~200 µm) and pore interconnectivity, to promote osteogenesis and favorably allow for neotissue infiltration, was maintained using the

SCPL fabrication protocol. While this study was limited to *in* vitro material characterization, the ***LPCL*** control scaffolds have been previously shown to support osteogenesis that can be improved with the addition of cell adhesion motifs and bioactive coatings. New scaffold compositions are likewise expected to yield favorable results in future cell studies that may be further improved due to unique properties endued by incorporation of star architecture macromers. Importantly, self-fitting of the ***S/S*** semi-IPN scaffold could be performed at a more tissue-safe, lower T_{fit} (~45 °C) versus for the ***L/L*** semi-IPN scaffold (~55 °C). The ***S/S*** semi-IPN exhibited similar rigidity versus the original ***LPCL***, although it was somewhat less rigid and strong versus the ***L/L*** semi-IPN. Despite this, radial pressure during shape recovery at T_{fit} for the ***S/S*** semi-IPN was shown to be significantly improved versus for the ***LPCL*** and was similar to that of the ***L/L*** semi-IPN. This is expected to promote scaffold contact with the defect edges during self-fitting, improving mechanical stability as well as osseointegration. This ability to expand with greater force toward the defect edges during self-fitting is expected to improve scaffold anchoring as well as osseointegration. Additionally, the ***S/S*** semi-IPN exhibited even faster degradation versus the ***L/L*** semi-IPN, and so is expected to better promote neotissue infiltration. Finally, the reduced intrinsic viscosity of ***S/S*** semi-IPN precursor solution improved its diffusion through the salt template (in the absence of centrifiguation), permitting larger scafffolds to be prepared. Thus, *star*-polymer architectures were successfully leveraged to create “self-fitting” SMP scaffolds with properties better suited for treatment of CMF bone defects.

7. COMPATIBILIZED POLY(PROPYLENE FUMARATE) INCORPORATED INTO POLY(CAPROLACTONE) SMP NETWORKS FOR SCAFFOLDS WITH TUNABLE HYDRATION

7.1. Overview

Poly(propylene fumarate) (PPF) is an unsaturated polyester of interest in bone tissue engineering (TE) as it has been known to biodegrade on a relevant time scale for healing without sacrificing mechanical properties. We successfully incorporated PPF into poly(ε-caprolactone)-diacrylate (PCL-DA) shape memory polymer (SMP) bone tissue scaffolds via compatibilization. PCL and poly(D,L-lactic acid) (PDLLA) were selected for compatibilization and were prepared as macroinitiators (M_n ~3 kg/mol) resulting in diblock PCL-PPF and PDLLA-PPF (M_n ~10 kg/mol); homopolymer PPF was also prepared. These PPF-based polymers were incorporated with PCL-DA at 10 and 25 % by wt, and solvent casting particulate leaching (SCPL) was used to prepare porous scaffolds. Notably, compatibilized PPF diblock copolymers demonstrated facile incorporation with no required changes to existing macromer solutions used in scaffold fabrication. Resulting PCL-DA/PPF scaffolds demonstrated tunable pore size, porosity (%), and mechanical/thermal properties. Importantly, all compositions effectively maintained SMP or self-fitting behavior in a plastic model bone defect, with fitting temperature (T_{fit}) reduced to ~44 °C for PPF containing compositions. In a 4 month *in vitro* non-catalyzed hydrolysis study, all scaffolds showed minimal erosion but did show microstructural signs of hydrolysis including increasing PCL crystallinity % and mechanical properties over time. Moreover, mechanical properties were not shown to be diminished over 4 months, necessary for structural integrity during initial bone healing. PPF containing compositions displayed reduced mechanical properties compared to the 100% PCL-DA control but all values were still robust, in the MPa range, and interestingly, the PPF scaffolds showed tunable hydration with equilibrium water uptake as high as 1200%. These hydrogel-like properties were unexpected but could prove beneficial in bone TE, and future studies will focus on characterization in their hydrated state.

7.2. Introduction

Poly(ε-caprolactone)-diacrylate (PCL-DA) thermoresponsive shape memory polymer (SMP) networks have been developed as self-fitting scaffolds to treat craniomaxillofacial (CMF) bone defects. Existing CMF bone treatments (ie. autografts, metal fixation plates, etc.) are typically limited particularly in their ability to achieve good bone to implant contact at the defect interface, essential for osseointegration and subsequent healing. PCL-DAs SMP behavior affords scaffolds with self-fitting capabilities whereby they can be warmed in saline to their fitting temperature (T_{fit}) and can be easily press-fitted into CMF bone defects. As the warm scaffold is implanted, shape recovery drives the scaffold toward the defect edge, and once cooled to T_{body}, the scaffold will lock into its temporary shape in the precise configuration of the defect. This conformal fitting ability has been shown to improve tissue integration without inhibiting bone healing in an *in vivo* rabbit calvarial defect study as shown in Chapter II. The PCL-DA scaffolds show promise for improved CMF bone tissue engineering (TE); however, some existing construct properties may be further optimized for bone regeneration.

In the field of TE, scaffolds should be designed to biodegrade on a timescale that matches target tissue healing, so as not to impede neotissue ingrowth.[262, 263] While the 100% PCL-DA scaffolds were shown to support tissue integration, PCL is known to degrade relatively slowly *in vivo* (~1-2 years)[200, 201] and in the previous *in* vivo study bone ingrowth was only observed at the scaffold periphery. To accelerate scaffold degradation and promote bone ingrowth, poly(L-lactic acid) (PLLA) was incorporated as a thermoplastic to prepare PCL-DA/PLLA semi-IPNs with varying PCL/PLLA ratios.[159] The 75/25 PCL-DA/PLLA composition showed the most enhanced compressive modulus, and accelerated degradation compared to the 100% PCL-DA control.[71] Initial studies hypothesized that the observed degradation behavior may be linked to PCL/PLLA phase separation.[157] Thus, in follow-up studies, PLA-based thermoplastics with varying microstructures (M_n, crystallinity, hydrophilicity) were substituted into the PCL-DA/PLLA semi-IPNs and degradation rate was successfully tuned and further shown to be linked to PCL/PLA miscibility.[158] Whereas previous scaffold degradation tests had been limited to base-catalyzed conditions, these new PCL-DA/PLA semi-IPN scaffolds were examined in an *in vitro* non-catalyzed (ie. neutral) hydrolysis study. Under neutral degradation conditions, the previously studied PCL-DA/PLLA scaffolds did not degrade much more rapidly than the 100% PCL-DA control, likely due to semi-crystallinity of PLLA. But, the poly(D,L-lactic acid) (PDLLA) semi-IPN (PCL-DA/PDLLA, 75/25 by wt.) was shown to undergo accelerated degradation with ~22% mass loss over 15 months compared to just 7% for the 100% PCL-DA. The PCL-DA/PDLLA semi-IPN also showed improved mechanical properties (E ~32.8 MPa, CS ~38.6 MPa) with well-maintained self-fitting properties. Furthermore, the newly developed PCL-DA/PDLLA semi-IPN afforded the self-fitting scaffolds with improved degradative and mechanical properties, linked to favorable miscibility of PCL and PDLLA.

Poly(propylene fumarate) (PPF) has presented itself as a unique biodegradable polyester for use in bone TE due to unsaturated bonds in the repeat unit allowing for tunable cross-linking for network formation. This structural property affords PPF constructs with highly tunable mechanical and degradation properties.[264-267] As a result, PPF has been explored for a number of devices including orthopedic implants,[268, 269] bone cement,[270-272] and porous tissue scaffolds.[273-275] Accordingly, PPF incorporation would likely yield unique and tunable properties for the self-fitting PCL-DA bone scaffolds, but miscibility of PPF and PCL should be considered. PPF is relatively hydrophilic compared to PCL, and has been used in combination with poly(ethylene glycol) (PEG) to prepare hydrogels for cartilage regeneration.[276, 277] Additionally, PPF-PLLA scaffolds have been fabricated via phase separation of PPF and PLLA where varying degrees of immiscibility can tune scaffold properties.[278] PCL and PPF have been successfully combine as copolymers developed for nerve regeneration;[68, 279, 280] however, copolymerization could compromise PCL crystallinity, necessary for self-fitting behavior in the PCL-DA bone scaffolds. Therefore, we can instead take inspiration from polymer blends where a wide array of techniques have been used to “compatibilize” or improve the miscibility of two otherwise immiscible polymers to incorporate PPF into the existing PCL-DA network.[281-283]

In this study, we aim to use compatibilization inspired techniques to successfully incorporate PPF into PCL-DA, to prepare self-fitting PCL-DA/PPF co-network scaffolds with tunable properties. A popular technique in blend compatibilization is the utilization of short block copolymers with a segment corresponding to each of the immiscible polymers.[214, 215] Our design utilizes a compatibilizer block attached to the PPF intended for incorporation into the PCL-DA networks. PDLLA was selected as a compatibilizer based on our previous studies where PCL-DA/PDLLA semi-IPN showed accelerated degradation behavior. PCL was also selected as a compatibilizer to match the PCL-DA network. Along with the compatibilized deblocks: PPF-PCL (F-C) and PPF-PDLLA (F-D), PPF homopolymers were also synthesized and attempted to be incorporated into PCL-DA networks to determine necessity and efficacy of PPF compatibilization. As summarized in **Figure 7-1**, PPF-based macromers were incorporated at either 10 or 25 wt %, and to prepare a total of six PCL-DA/PPF co-networks: F-C-10, F-C-25, F-D-10, F-D-25, PPF-10, and PPF-25. A 100% PCL-DA control was included as well as the previously studied PCL-DA/PDLLA and PCL-DA/PLLA (75/25 by wt.) semi-IPNs [“PDLLA S-I” and “PLLA S-I”]. Herein, scaffolds were subjected to a 4 month *in vitro* non-catalyzed hydrolysis study and mechanical properties were monitored throughout the course of degradation.

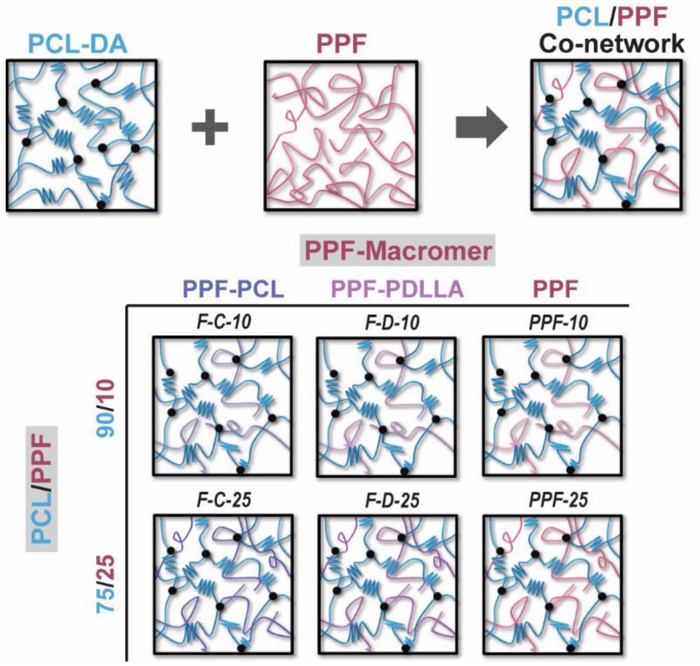

Figure 7-1. PCL-DA was combined with three different PPF macromers: PPF-PCL, PPF-PDLLA, and PPF homopolymer at two different PCL-DA/PPF ratios (by wt.): 90/10 and 75/25. This resulted in six different PCL-DA/PPF co-networks as shown.

7.3. Materials and Methods

7.3.1. Materials

PCL-diol (M_n = 10 kg/mol per manufacturer specifications), 4-(dimethyl-amino)pyridine (DMAP), triethylamine (Et_3N), acryloyl chloride, potassium carbonate (K_2CO_3), anhydrous magnesium sulfate ($MgSO_4$), sodium chloride (NaCl, salt), (3S)-*cis*-3,6-dimethyl-1,4-dioxane-2,5-dione (L-lactide), 3,6-dimethyl-1,4-dioxane-2,5-dione (lactide), ε-caprolactone, pentaerythritol, tin(II) 2-ethylhexanoate ($Sn(Oct)_2$), ethylene glycol, dodecanol, propylene oxide (PO), maleic anhydride (MAn), magnesium ethoxide ($Mg(OEt)_2$), hydroquinone, diethylamine (Et_2NH), 2,2-dimethoxy-2-phenyl acetophenone (DMP), 1-vinyl-2-pyrrolidinone (NVP), sodium hydroxide (NaOH), deuterated chloroform ($CDCl_3$), and solvents were purchased from Sigma-Aldrich. All solvents and ethylene glycol were dried over 4 Å molecular sieves, all reagents were vacuum dried overnight (ON), and all glassware and stir bars were dried at 120 °C ON prior to use. Salt was sieved using an ASTM E-11 no.40 and no. 35 sieves with 425 μm and 500 μm openings respectively; scanning electron microscopy (SEM) and ImageJ showed an average salt size of 460 ± 70 μm.

7.3.2. Methods

7.3.3. Syntheses

All syntheses were performed under nitrogen (N_2) atmosphere and were stirred using Teflon-covered stir bars. The obtained purified macromers were first examined for their properties prior to use in fabrication. ^{1}H NMR spectroscopy (Inova 500 MHz Spectrometer in FT-mode) was used to verify targeted macromer structure, M_n, and % acrylation of PCL, and thermal properties were determined using differential scanning calorimetry (DSC, TA Instruments Q100).

PCL-DA was prepared via end functionalization of PCL-diol and PLA thermoplastics was prepared from lactide monomer according to our previously established protocols.[69, 158]

7.3.3.1. Compatibilizers

PCL and PDLLA were selected a target M_n ~ 3 kg/mol based on preliminary studies, to be synthesized as a PPF compatibilizer (ie. macroinitiator). Ring opening polymerizations (ROPs) were performed using ε-caprolactone or lactide (6.0 g) as the monomer, with dodecanol as the initiator, and $Sn(Oct)_2$ as the catalyst. Reactions took place ON at 120 °C and monomer to initiator molar ratios were used to control compatibilizer M_n (PCL: [M]/[I] = 26.3, PDLLA: [M]/[I] = 20.8). Macroinitiators were re-dissolved in a minimal amount of chloroform and were precipitated into methanol followed by filtration and vacuum drying (ON, RT, 30 in. Hg). ^1H NMR was used to confirm chemical structures and target M_n for PCL ($CH_2C\mathbf{H_2}CH_2$ $\delta = 1.3$ ppm, $C\mathbf{H_2}CH_2C\mathbf{H_2}$ $\delta = 1.6$ ppm, $CH_2C\mathbf{H_2}C{=}O$ $\delta = 2.3$ ppm and $OC\mathbf{H_2}CH_2$ $\delta = 4.0$ ppm in repeat unit) and PDLLA ($C\mathbf{H}$ $\delta = 5.2$ ppm and $C\mathbf{H_3}$ $\delta = 1.5$ ppm in repeat unit). Comparison to terminal $C\mathbf{H_3}$ $\delta = 0.8$ ppm in dodecanol was used to perform end-group analysis and calculate M_n. Thermal properties were also determined for PCL [T_g = -63.0 ºC, T_m = 49.2 ºC, 55.0% crystallinity], and PDLLA [T_g = 30.6 ºC, T_m = -- ºC].

7.3.3.2. PPF Syntheses

The PPF protocol chosen is based on a newer synthetic route developed based on ROP with advantages over older techniques, including scalability and controllable molar mass/distribution.[284, 285] Two compatibilized PPF diblock copolymers [PPF-PCL and PPF-PDLLA] and PPF homopolymer were synthesized via a chain-growth mechanism. Maleic anhydride (MAn) and propylene oxide (PO) were combined (molar ratio MAn:PO 1:1) with PCL (M_n ~3 kg/mol) or PDLLA (M_n ~3 kg/mol) macroinitiator compatibilizers [molar ratio monomer:compatibilizer 40:1]. Reactions were performed in acetone with magnesium ethoxide ($Mg(OEt)_2$) [molar ratio monomer:catalyst 120:1] as the catalyst. Reactions were allowed to proceed over 48 h at RT to prepare poly(propylene maleate) (PPM) blocks with a target M_n of ~7 kg/mol. PPM copolymers were purified via washing with dilute HCl and were then precipitated into hexane. The resulting PPM-PCL and PPM-

PDLLA were dissolved in acetone and isomerization was carried out using diethylamine (Et_2NH); the reaction was allowed to proceed at 55 °C for 16 h. A minimal amount of hydroquinone was also added to prevent premature cross-linking. The resulting PPF copolymers were washed using phosphate buffer saline solution (0.5 M, pH = 4.0) and were precipitated into hexane to obtain purified PPF-PCL and PPF-PDLLA. ^{1}H NMR was used to confirm chemical structures and target M_n for PPF blocks ($C\mathbf{H_3}$ $\delta = 1.4$ ppm, $CH_2C\mathbf{H}CH_3$ $\delta = 5.2$ ppm, $OC\mathbf{H_2}C\mathbf{H}$ $\delta = 4.2$ ppm and $\mathbf{H}C{=}C\mathbf{H}$ $\delta = 6.3$ ppm in PPF block repeat unit), compared to terminal $C\mathbf{H_3}$ $\delta = 0.8$ ppm from dodecanol. Thermal properties were also determined for PPF-PCL [T_g = -51.7 ºC, T_m = 42.1 ºC, 38.7% crystallinity], and PPF-PDLLA [T_g = -28.7 ºC, T_g = 6.16 ºC, T_m = -- ºC].

A PPF homopolymer was also added into the study and followed the same synthetic procedure but without a macroinitiator. PPF was not soluble in $CDCl_3$ like the other macromers, so NMR could not be performed at this time. But thermal properties were determined for PPF [T_g = 52.3 ºC, T_m = -- ºC].

7.3.4. Fabrication

Scaffolds were prepared according to an adapted SCPL protocol with minor adjustments to ensure successful PPF incorporation and cross-linking. Based on the previously reported protocol, 10.0 g fused salt templates were prepared in 20 mL scintillation vials. For compatibilized PPF copolymers and control compositions macromer solutions were prepared at 0.15 g/mL in dichloromethane (DCM); weight % ratios were controlled at this step. Then, following centrifugation for macromer diffusion, scaffolds were cure for 5 minutes in a UV cure box (Intelliray 400, 50% intensity).

Notably, the PPF homopolymers could not be successfully incorporated with these minor adjustments, so for the PPF-10 and PPF-25 compositions, solvent mixes based on DCM/acetone were used to prepare macromer solutions and UV cure time was increased to 10 minutes. Once cured, all scaffolds were fully dried (2 days in fume hood) prior to leaching in a 50/50 solution of water/ethanol. Scaffolds were leached for ~5 days with daily solution changes to remove all salt porogens. Scaffolds were again adequately dried prior to heat treatment (85 °C, 1 h, 30 in Hg). Note that the PLLA S-I was subjected to a different heat treatment protocol (175 °C, 10 min, 30 in. Hg), due to the presence of semi-crystalline PLLA (T_m ~ 155 °C). Scaffolds were sliced (Leica VT 1000 S) and punched (Integra Miltex) to final dimensions (h ~ 2 mm, d ~ 6 mm)

7.3.5. Pore Size and Porosity %

Scaffold pore morphology was examined qualitatively using a scanning electron microscope (SEM, Tescan Vega 3, accelerating voltage ~10 kV, Au-Pt sputter coating ~7 nm). For each composition one scaffold was imaged and two photos were taken. For each photo, ImageJ was used to quantify pore diameter; all pores along the midline in each photo were measured.

Solid films analogous to the scaffold compositions studied herein were prepared according to an established protocol,[158] with updates mimicking the scaffold protocol (ie. using UV cure box for 5 minutes and using solvent mixes for PPF homopolymer compositions). Then, porosity % (N=3) was determined gravimetrically according to Equation 1:

$$Porosity\ (\%) = \frac{\rho_{solid\ film} - \rho_{porous\ scaffold}}{\rho_{solid\ film}} * 100 \tag{1}$$

where $\rho_{porous\ scaffold}$ is the density of the final scaffold specimens and $\rho_{solid\ films}$ is the density of analogous solid film samples.

7.3.5.1. Thermal Properties

Differential scanning calorimetry (DSC; TA Instruments Q100) was used to determine thermal properties (T_g, T_m, and % crystallinity) of macromers and scaffolds. Macromer samples (~5 mg, $N = 3$) were sealed in hermetic pans and heated at a rate of 10 °C/min, and values were taken from the second cycle to erase thermal history. Scaffold samples were tested in a similar fashion (~10 mg, N=3) but at a rate of 5 °C/min, and values were taken from the first cycle to include impacts from fabrication. TA Universal Analysis software was used to determine thermal transition values. Percent crystallinity was determined with Equation 2:

$$\%\chi_c = \frac{\Delta H_m - \Delta H_c}{\Delta H_m^{\circ}} * 100 \tag{2}$$

where ΔH_m is the enthalpy of fusion taken from the integral of the endothermic melt peak, ΔH_c is the enthalpy of crystallization from the exothermic cold crystallization peak and ΔH_m° is the theoretical value for 100% crystalline PCL (139.5 J/g).

7.3.6. Self-fitting Behavior

The self-fitting or shape memory behavior of the scaffolds was qualitatively observed and quantified (N=3) using a plastic model CMF bone defect as previously described in Chapter VI. Preliminary T_{fit} testing was performed using a hot plate with a digital probe (Heidolph, MR HEI-TEC), so that saline could be warmed in 2 °C increments to examine at which temperature scaffolds became malleable after 1 min of submersion. Scaffolds were subjected to the following procedure at their respective T_{fit}: (1) submerge in warm saline for 1 min, (2) press-fit into model defect and let cool to RT for 2 min, (3) remove from mold and hold at RT for 2 min, and (4) re-submerge in warm saline for 1 min followed by cooling to RT for 2 min. Representative photos were taken throughout the procedure.

7.3.7. Compressive Mechanical Properties

Static compression testing (Instron 5944) was performed on scaffold specimens (d ~6 mm x t ~2 mm; *N* = 8) at RT at a rate of 1.5 mm/min to 85% strain. The compressive modulus (E) and strength (CS) were determined using Bluehill software on resultant stress-strain curves.

7.3.8. *In Vitro* Degradation via Hydrolysis

A brief 4-month long *in* vitro degradation study performed under non-catalyzed conditions (1X PBS, pH ~7.4) according to ASTM F1635. Scaffold specimens (d ~6 mm x t ~2mm; N = 11 per time point) were each submerged in 10 mL of PBS solution in a sealed glass vial and maintained in an incubator (VWR Benchtop Shaking Incubator Model 1570) at 37 °C and 60 rpm. Timepoints were designated at one-month intervals at which point samples were removed, thoroughly rinsed with DI water, blotted, and massed and measured with calipers for dimensional changes. From these measurements water uptake and volume change were determined. Then samples were dried in vacuo (RT, ON, 30 in. Hg), and were massed and measured again to obtain information about mass loss and volume decrease over time.

A large number of samples were used for each composition at each given timepoint (N=11), such that post-degradation studies could be performed. SEM (N=1), DSC (N=3), and Instron testing (N=7) was performed for degraded scaffolds so that pore morphology, thermal and mechanical properties could be evaluated over 4 months of hydrolysis.

7.3.9. Statistical Analyses

All data was reported as the average ± standard deviation. ANOVA tests were performed and if there was a statistical difference, t-tests were performed compared to the 100% PCL-DA control.

7.4. Results and Discussion

7.4.1. Macromer Syntheses

PCL and PDLLA macroinitiators were successfully prepared at their target M_n of ~3 kg/mol and the reaction schemes are summarized in **Figure A-5-a.** PPF diblock copolymers, PPF-PCL and PPF-PDLLA, were also both successfully prepared near their target M_n ~10 kg/mol and reaction schemes are summarized in **Figure A-5-b,c** with relevant ^{1}H NMR spectra. A PPF homopolymer was also successfully prepared, but was not able to be dissolved in $CDCl_3$, and as such M_n could not be verified using this method. PCL-DA and PDLLA were also successfully prepared for use herein, and their properties have been previously well-characterized.[158]

7.4.2. Scaffold Fabrication and Initial Properties

The incorporation of compatibilized PPFs was successful and showed a marked improvement when compared with PPF homopolymers. PPF-PCL and PPF-PDLLA were able to be incorporated using the existing macromer solution parameter (0.15 g/mL in DCM), and resultant scaffolds were cured all the way through the scaffold after curing for the same amount of time as control scaffolds (5 min). PPF homopolymers were not able to be incorporated under the existing protocol and macromer solutions had to be made with a mix of DCM/acetone in order to achieve dissolution. Additionally, they required a higher curing time of 10 min, and even after these adjustments were made the PPF-25 still did not achieve successful curing throughout the scaffold. Moreover, compatibilization yielded facile fabrication of four new scaffold compositions: F-C-10, F-C-25, F-D-10, and F-D-25. While the PPF-10 and PPF-25 were not as successful, they were still sliced and punched into final scaffold specimens and were still subjected to degradation and post-degradation testing to continue assessing the impact on properties from PPF compatibilization.

Pore size and porosity % are summarized in **Figure 7-2**. In general, pore size and porosity % increased for PPF-containing compositions with respect to the 100% PCL-DA control. Considering that PPF is an unsaturated macromer capable of cross-linking within the network, this result was expected. During heat-treatment scaffolds shrink to their final geometry, but PPF incorporation yields increased cross-linking, which inhibits the mobility of chains between cross-links thereby limiting scaffold shrinkage. Pore sizes observed (~200-400 μm) are all within the acceptable range for osteoblasts,[148, 286] and a higher porosity could be conducive to a greater degree of cell seeding and nutrient/waste transport.[287]

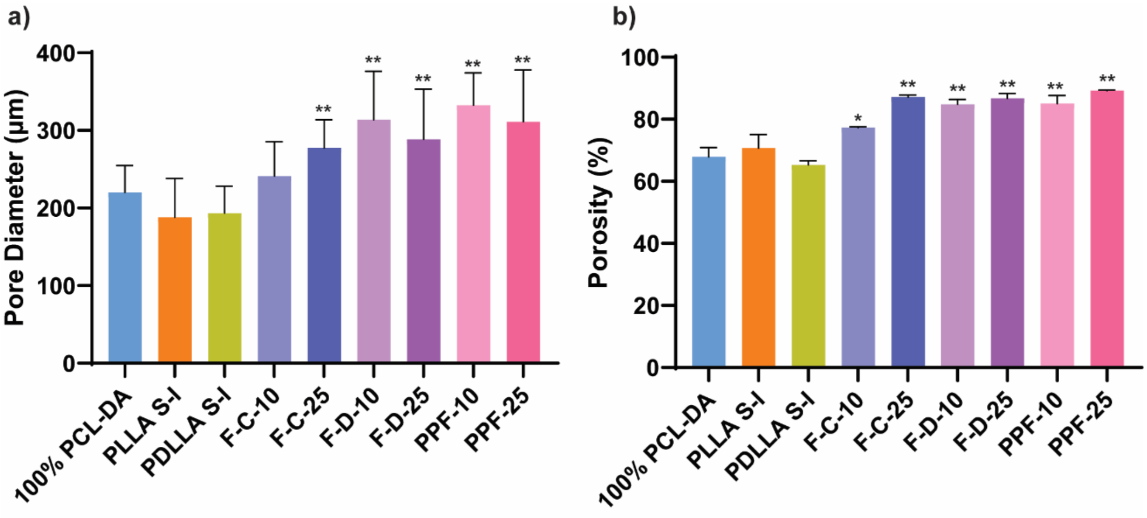

Figure 7-2. (a) Pore diameter and (b) porosity % were quantified for all scaffold compositions studies herein. Results were compared to the 100% PCL-DA control, *p<0.05 and **p<0.01.

Next, initial thermal properties were characterized with a focus on PCL T_m and % crystallinity because these have the most impact on self-fitting capabilities. At this stage, PCL crystallinity (**Figure 7-3**) is relative, in that, it has not yet been corrected for PCL/PLLA weight percent. When taking, this into consideration, we can see that PCL crystallinity decreased based on the compositions weight percent (ie. 75/25 have the lowest PCL crystallinity due to 25% non-PCL component). For all compositions, PCL crystallinity was at least 30%, which is expected to be sufficient for maintaining self-fitting properties. PCL T_m onset and midpoint were both analyzed as the T_{fit} is known to be within this range as shown in **Figure 7-4**. The PCL T_m midpoint was statistically lowered for all PPF-containing compositions compared to the 100% PCL-DA control, however most differences in values were marginal. Larger reductions in PCL T_m onset, compared to the 100% PCL-DA control, were observed with F-C-25 showing the largest reduction of 10 °C.

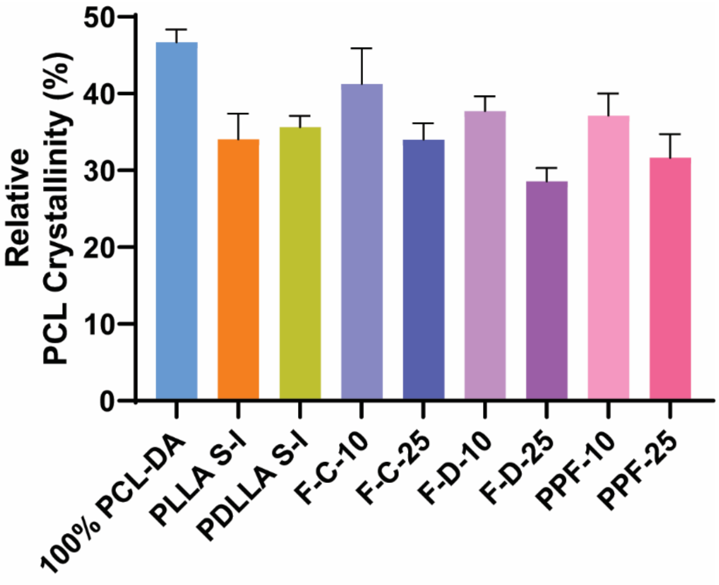

Figure 7-3. Relative PCL crystallinity was determined via DSC and was shown to correlate to the relative weight percent of corresponding compositions. All compositions were observed to have PCL with crystallinity of at least 30%.

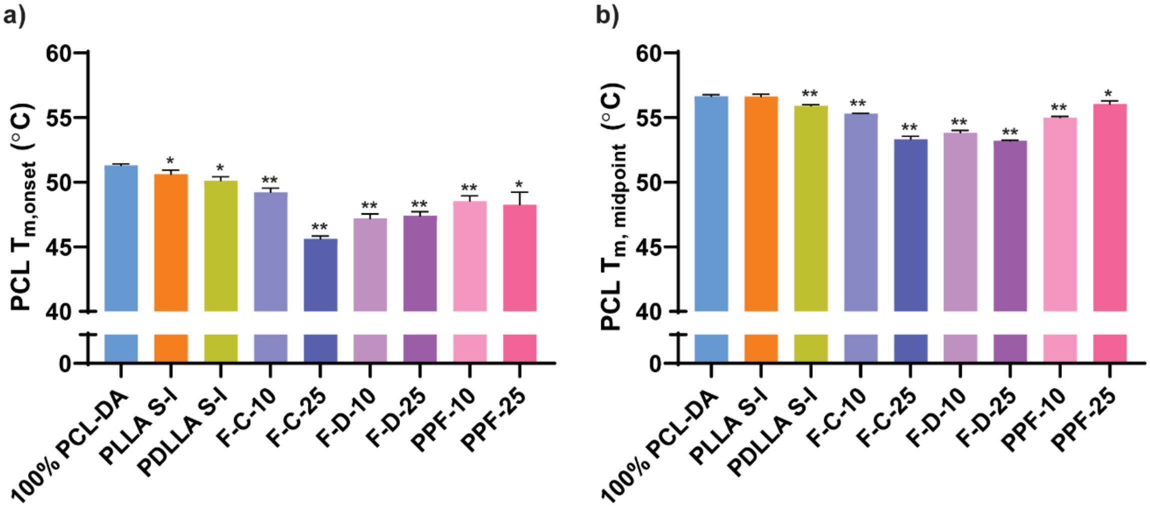

Figure 7-4. PCL T_m (a) onset and (b) midpoint were both shown to be significantly lowered for all PPF-containing compositions compared to the 100% PCL-DA control, *p<0.05 and **p<0.01.

Initial scaffold mechanical properties were also assessed, and average modulus (E) and compressive strength (CS) are shown in **Figure 7-5**. All results significantly differed from the 100% PCL-DA control, but whereas the PLA semi-IPNs reinforced mechanical properties, PPF co-networks showed reduced values. This was reasonable considering that relative PCL crystallinity was reduced and pore size was increased for these compositions, thus resulting in weaker mechanical properties. But significantly, PCL-DA/PPF co-networks E and CS values remained within the MPa range and demonstrated robust properties to withstand typical handling required for press-fitting.

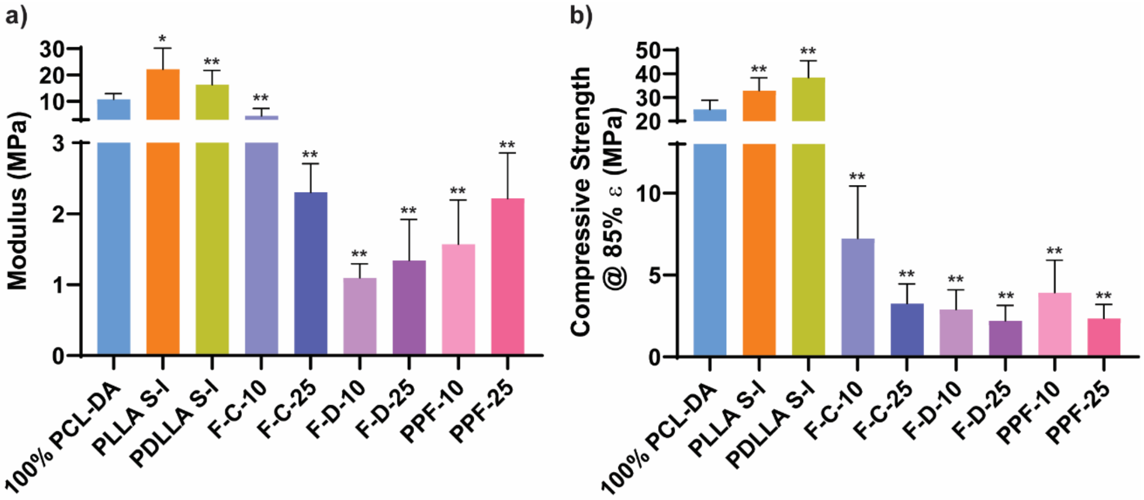

Figure 7-5. Scaffold mechanical properties (a) modulus and (b) compressive strength, *p<0.05 and **p<0.01 compared to the 100% PCL-DA control.

Lastly, scaffold self-fitting properties were examined in a plastic model defect and were not shown to be diminished for any of the PCL-DA/PPF co-network scaffolds. Photos were taken throughout the press-fitting sequence, and results are summarized in **Figure 7-6**. The controls [100% PCL-DA, PDLLA S-I, and PLLA S-I] have all been shown to have a T_{fit} of ~55 °C, but for all PCL-DA/PPF co-network scaffolds the T_{fit} was reduced to ~44 °C. This was even lower than expected based on PCL T_m onset results, and is likely driven by PPF hydration, which can lead to plasticization and lowering of thermal transitions.

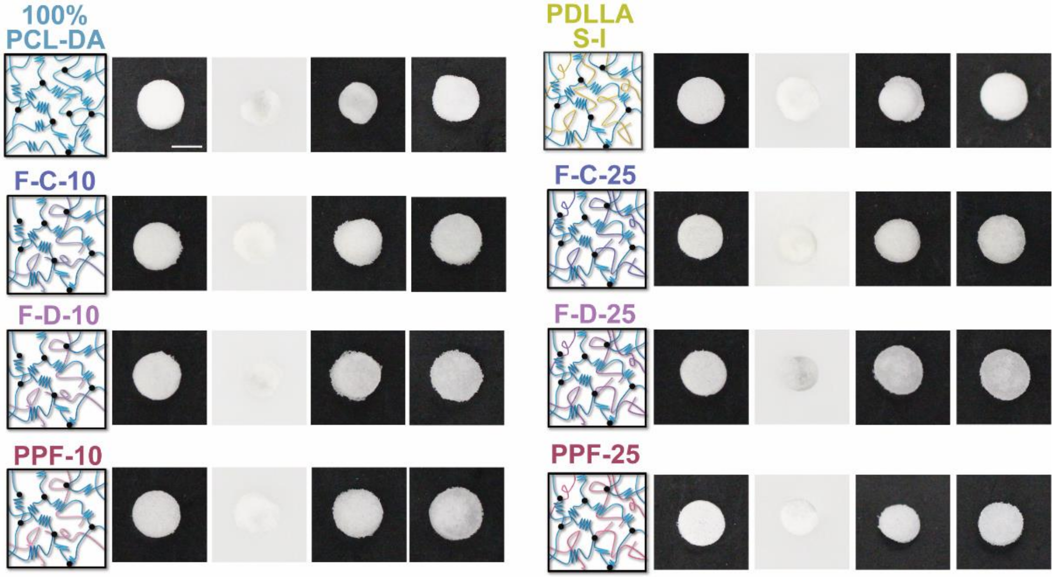

Figure 7-6. Scaffolds were subjected to thermoresponsive (T_{fit} ~ 55 °C for controls and ~44 °C for PCL-DA/PPF co-networks) press-fitting in a plastic model defect and representative photos were taken throughout to demonstrate shape fixity and recovery. Scale bar is = 5 mm and is representative for all images.

7.4.3. *In Vitro Degradation*

In general, initial scaffold properties observed for the newly developed PCL-DA/PPF co-networks showed promise as potential self-fitting CMF bone scaffolds. Therefore, we moved forward to studying the scaffolds and their basic properties throughout the course of a short *in vitro* non-catalyzed hydrolysis study. A 4-month study was selected as this is the general timescale that on-the-market resorbable bone implants retain strength, in order to support early bone healing.[288] Gravimetric mass loss over time yielded unexpected results as scaffolds exhibited minimal mass loss over time, and in some cases, showed mass increases with high errors (**Figure 7-7-a**). We speculate that this may be due to ion chelation of components in the PBS solution by the porous scaffolds as they degrade, but further testing such as EDS elemental mapping is required. Scaffold volume was shown to decrease with hydrolysis time, particularly for the F-D-25 composition (**Figure 7-7-b**). This reduction in volume with degradation may allow for greater tissue infiltration during initial bone healing.

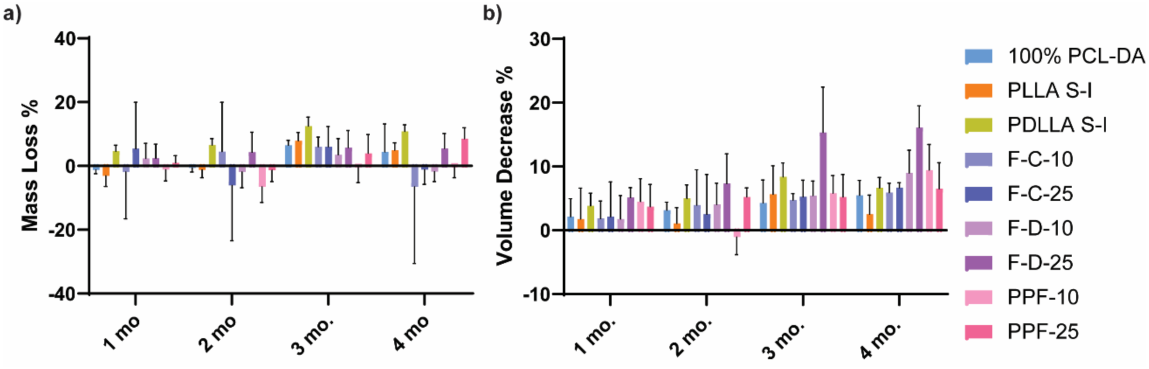

Figure 7-7. Scaffold (a) mass loss % and (b) volume decrease % are shown for all scaffold compositions over the course of 4-months.

Following scaffold removal at each timepoint, the samples were examined in their hydrated-state and water uptake % and volume increase % were monitored as shown in **Figure 7-8**. All the PCL-DA/PPF co-networks, except for the F-C-10, showed substantial swelling and significant levels of water uptake reaching as high as 150% volume increase and 1200% water uptake for the F-D-25 composition. At the 4-month timepoint, representative hydrated samples of each composition were photographed to show their swelling behavior (**Figure 7-9**). Moreover, the newly prepared PCL-DA/PPF co-network scaffolds displayed unique and tunable hydration, which could prove highly advantageous in TE.

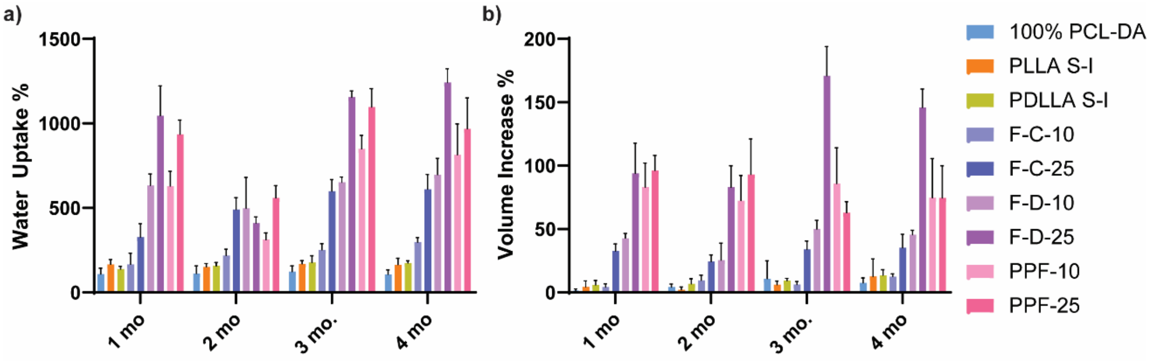

Figure 7-8. Scaffold (a) water uptake % and (b) volume increase % were monitored when scaffolds were removed from PBS solution at their monthly timepoint to assess hydration properties.

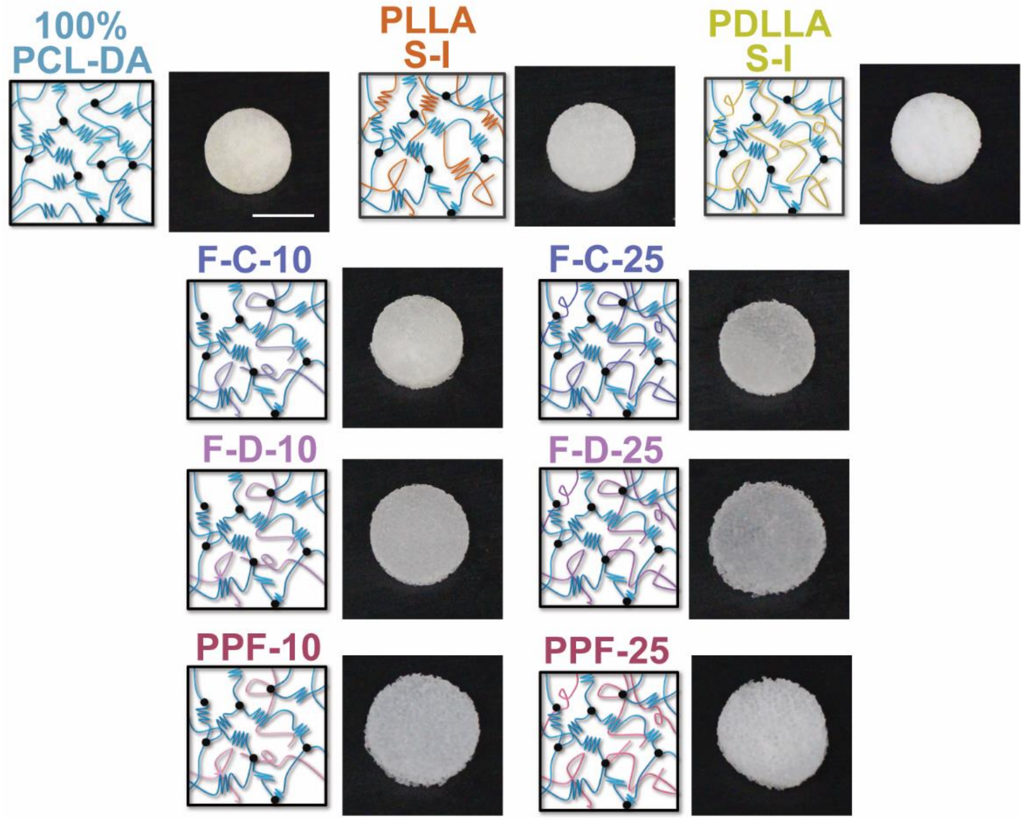

Figure 7-9. At the 4-month hydrolysis timepoint, photos were taken of the scaffolds while in their hydrated-state. Scale bar = 5 mm and is representative for all images.

7.4.3.1. Post-Degradation Characterization

The hydrogel-like properties observed for most of the PCL-DA/PPF co-network scaffolds were unexpected, so at this stage, the post-degradation testing was performed on dry compositions but may still yield pertinent information regarding degradation. There were no obvious signs of scaffold erosion over the 4-month duration of the study, so degraded scaffolds were further visualized via SEM and results are summarized in **Figure 7-11**. All compositions showed changes in pore morphology with hydrolysis, but in most compositions the changes were not obvious, and in general, porous structures were maintained over the course of 4-months. Notably, the PDLLA S-I showed significant changes in scaffold morphology likely associated with rapid degradation of PDLLA out of the system as discussed in Chapter V.

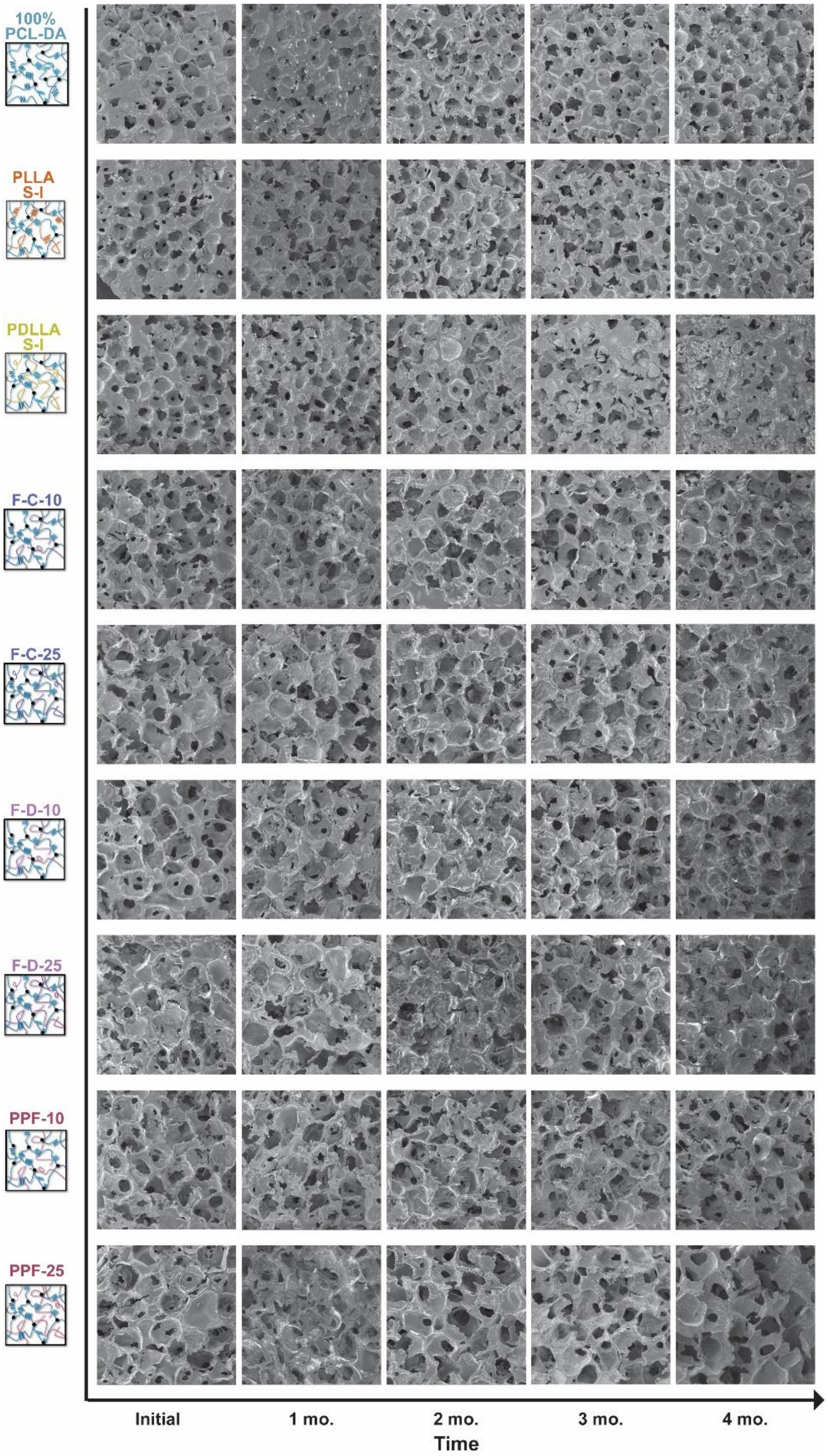

Figure 7-10. SEM was performed on scaffolds to monitor pore morphology with degradation.

7.4.3.1.1. Thermal Properties

DSC analyses was performed on post-degraded samples and PCL T_m midpoint and PCL % crystallinity were both shown to initially increase with degradation (**Figure 7-12**). This is consistent with reports on biodegradable polymers whereby amorphous regions degrade first thereby leaving behind more crystalline domains.[289, 290] For some compositions like the F-D-25, PCL crystallinity % was then shown to decrease beginning at the 3-month timepoint. Overall, the thermal properties changes over time are consistent with early stages of polymer biodegradation.

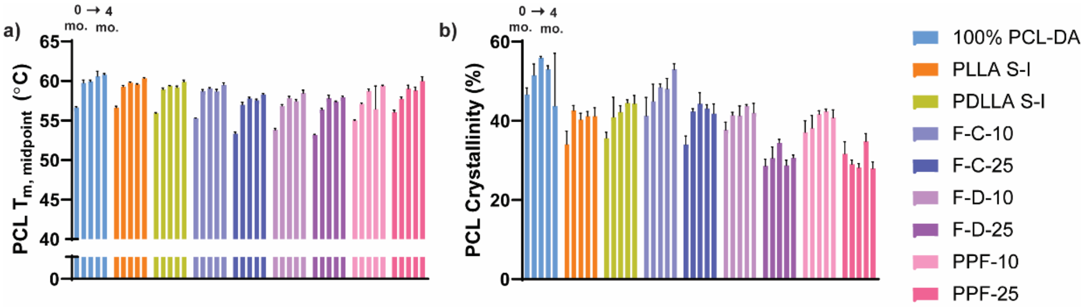

Figure 7-11. (a) PCL $T_{m,\ \text{midpoint}}$ and (b) PCL crystallinity % were determined for scaffold samples post-degradation. From left to right the bars for each composition indicate 0 to 4 months of *in vitro* hydrolysis.

7.4.3.1.2. Mechanical Properties

Post-degradation mechanical property trends tended to follow along with thermal property trends as shown in **Figure 7-13**. The E and CS of scaffolds were generally shown to increase over the 4-month non-catalyzed hydrolysis studies. This is consistent with the increases in PCL crystallinity with hydrolysis time that were also observed. Significantly, none of the compositions showed diminished mechanical properties over the 4-months *in* *vitro*, indicating these scaffolds have the required strength retention to support initial bone healing in bone defects.

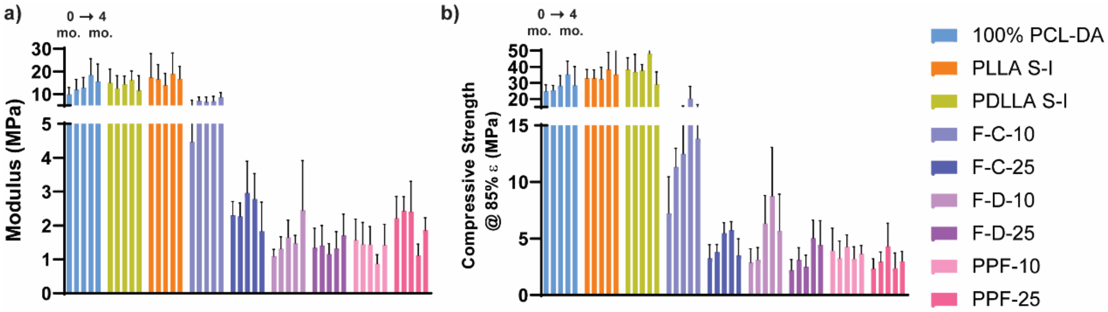

Figure 7-12. Scaffold (a) modulus and (b) compressive strength were monitored for samples throughout degradation. From left to right the bars for each composition indicate 0 to 4 months of *in vitro* hydrolysis.

7.5. Conclusions

Compatibilized diblock PPF-based copolymers prepared with PCL and PDLLA compatibilizers were successfully incorporated into PCL-DA networks at varying wt ratios, with only minor adjustments to the SCPL protocol. PPF homopolymers could not be likewise incorporated and even with further fabrication adjustments scaffold curing was incomplete. The PCL-DA/PPF co-network scaffolds generally displayed larger pore diameters and higher porosity % due to PPF cross-linking into the network, but these compositions still displayed robust mechanical properties for handling. Using a plastic model defect, all scaffolds were shown to maintain their self-fitting behavior and PCL-DA/PPF co-networks showed a significantly reduce T_{fit} of ~44 °C, with the potential to be more tissue-safe than the PCL control. After a 4-month non-catalyzed hydrolysis study, post-degradation characterization showed evidence of macromer chain scission in the form of increasing crystallinity and increasing E and CS over time. Notably the PCL-

DA/PPF co-networks displayed hydrogel-like properties due to hydration of PPF, which also resulted in the lowered T_{fit}. Future studies will further examine these scaffold iterations in their swollen state. Overall, this study further demonstrated importance of miscibility in tailoring scaffold properties, and compatibilization allowed for production of unique self-fitting scaffolds with tunable hydration.

8. CONCLUSIONS & FUTURE WORK

8.1. Conclusions

Shape memory PCL-DA scaffolds offer clinical advantages associated with self-fitting for improved osseointegration and healing of confined cranial and CMF bone defects. Furthermore, the SCPL fabrication platform allows for facile modification to design new scaffold compositions with highly tunable properties. In Chapter I, recent advances in the field of smart scaffolds based on SMPs were discussed. Studies that highlight the utility of smart scaffolds to regenerate various tissues were discussed as were the types of SMPs and fabrication techniques employed. In Chapter II, a previously developed and well-characterized 100% PCL-DA scaffold (T_{trans} = $T_{m,PCL}$ ~55 ºC) was prepared for use in a non-critical sized rabbit calvarial defect model (bilateral, diameter ~ 8 mm). After 16 weeks, the 100% PCL-DA scaffolds did not significantly differ in terms of bone volume or surface area, versus the untreated defect, demonstrating that the scaffold did not impede natural bone healing. Furthermore, in push-out tests versus a PEEK implant control, the PCL-DA scaffold enhanced stiffness and failure load, indicating enhanced tissue integration, stemming from self-fitting capabilities. This pilot study demonstrated that self-fitting PCL-DA scaffolds have excellent potential for treating CMF bone defects.

In Chapter III, osteogenesis of cultured hMSCs *in vitro* was for PCL-DA versus PCL/PLLA (75/25 wt%) semi-IPN scaffolds, both with and without a bioactive polydopamine (PD) coating known to induce HAp mineralization. The PCL-DA/PLLA semi-IPN was selected for its relatively accelerated degradation rate, towards improve neotissue infiltration, and enhanced compressive modulus for improved mechanical support in early stages of healing. Each type of scaffold (T_{trans} = $T_{m,PCL}$ ~54 ºC) (diameter ~ 9 mm) were press-fitted into a plastic model defect (diameter ~ 8 mm), representing a rat calvarial defect. These shape fixed scaffolds were removed from their defects and subjected to subsequent studies. Both types of PD-coated scaffolds were shown to induce HAp mineralization *in vitro* (1X SBF, 1 month), as confirmed by SEM EDS. hMSCs were cultured on scaffolds for 14 days in the absence of osteogenic supplements. The PD-coated PCL-DA/PLLA semi-IPNs exhibited the greatest osteogenic protein expression, indicating a synergistic effect of PLLA incorporation and PD-coating. The relatively more hydrophilic PLLA may impart unique surface properties favorable to osteoinductivity, while the PD-coating imparts osteoconductivity. Based on these favorable results, PD-coated PCL-DA/PLLA semi-IPN scaffolds was identified to progress to *in vivo* studies with a rat calvarial defect model and are currently in progress. PCL-DA/PLLA semi-IPN (75/25) SMP scaffolds have been shown to have beneficial properties pertinent to CMF bone TE, so in Chapter IV we continue to investigate semi-IPN properties. The existing 15 kg/mol semi-crystalline PLLA was exchanged for PLLA of varying M_n (7.5, 15, 30, and 120 kg/mol) and for generally amorphous macromers including PDLLA, 85:15 PLGA, 70:30 PLGA, and 50:50 PLGA (all maintained at 15 kg/mol). Initial base-catalyzed degradation studies on solid, non-porous, films showed that degradation rate was primarily linked to PCL/PLA phase separation rather than PLA thermoplastic properties. Additionally, all PCL-DA/PLA semi-IPN compositions degraded more quickly than the 100% PCL-DA control and various rates were achieved demonstrating that varying PLA microstructure can be used to tune degradation rate. In addition to tunable degradation rate, PCL-DA/PLA semi-IPNs also afforded improved mechanical properties imparted by the preservation of the PCL networks crystallinity in the semi-IPN design. Films were typically annealed at 85 °C, sufficiently above PCLs T_m (~55 °C), but a higher annealing temperature of 175 °C was implemented to also be above PLLAs T_m (~155 °C). The degradation rate of PCL-DA/PLA semi-IPNs annealed at 175 °C was reduced compared to films annealed at 85 °C and was linked to a reduction in PCL/PLA phase separation, or an improvement in their miscibility. Tensile properties were also further enhanced for compositions annealed at 175 °C compared to original films annealed at 85 °C. Notably, PCL crystallinity and resulting SMP behavior was well preserved for all compositions at both annealing temperatures. Thus, this study demonstrated how varying the PLA component in PCL/PLA semi-IPNs and varying annealing conditions can be used as tools to customize construct degradative and mechanical properties with high maintenance of SMP behavior.

Chapter V is closely linked to Chapter IV, in that, many of the same PCL-DA/PLA semi-IPN compositions were explored, but here, we moved on to porous scaffolds and to non-catalyzed *in* vitro hydrolysis studies. Solid films were also studied again but under non-catalyzed degradation conditions, where they showed quite different kinetics compared to the base-catalyzed studies. In Chapter IV, semi-IPNs containing semi-crystalline PLLA were shown to degrade the most quickly but under non-catalyzed conditions, these compositions degraded more slowly, but still significantly faster than 100% PCL-DA controls. Under neutral conditions the PDLLA, 85:15 PLGA, and 70:30

PLGA semi-IPN films degraded the most quickly. When a higher 175 °C annealing temperature was implemented, PDLLA and 85:15 PLGA semi-IPNs degraded significantly faster. While trends differed from the initial base-catalyzed studies, varying the PLA component and the annealing temperature still proved to tune degradation rate. Further, the differences in degradation profiles under different conditions demonstrated the importance of performing non-catalyzed long-term hydrolysis studies to more accurately predict how constructs will biodegrade *in vivo*. Therefore, scaffolds of the same PCL-DA/PLA semi-IPN compositions were prepared and were annealed at the high 175 °C temperature; several compositions were also annealed at a medium 145 °C and low 85 °C temperatures where selection was based on achieving similar pore size. The 7.5k PLLA, PDLLA, 85:15 PLGA, and 70:30 PLGA semi-IPN scaffolds degraded significantly faster than 100% PCL-DA control scaffolds while the 15k PLLA and 30k PLLA semi-IPNs degraded slowly, at a rate similar to the control. Under neutral conditions, PLA thermoplastic traits such as low M_n, lack of crystallinity, and hydrophilicity promoted faster degradation. Semi-IPN scaffolds generally degraded via the thermoplastic PLA degrading and eroding out of the system first, with some degradation but minimal erosion of the PCL component. Annealing temperature had a minimal effect on overall degradation rate but was shown to impact degradation profile particularly related to the PLA degrading out first versus degrading with the PCL-DA. But the impact of annealing temperature on degradation profile was highly dependent on composition and should be optimized for specific scaffold selections moving forwards. In general, a higher annealing temperature also further improved compressive modulus. In total, Chapter V demonstrated the importance of neutral or non-catalyzed degradation studies due to changes in scaffold degradation mechanism/kinetics under base-catalyzed conditions. Further, it verified the notions of Chapter IV that PCL-DA/PLA semi-IPNs annealed at varying temperatures can be used to tune the degradation and mechanical properties of self-fitting scaffolds.

Previous work and chapters herein established that phase separation can have a significant impact on PCL-DA/PLA semi-IPN construct properties, so in Chapter VI we examine macromers of differing architectures. Cross-linkable PCL and thermoplastic PLLA macromers of 4-arm star architecture were substituted in the existing semi-IPN design, previously based on linear macromers. *Linear*-PCL-DA, *linear*-PLLA, *star*-PCL-tetracrylate (*star*-PCL-TA), and *star*-PLLA were combined to prepare 4 semi-IPNs with alternating architectures [***L/L***, ***L/S***, ***S/L***, and ***S/S***] and two 100% PCL control [***L****PCL* and ***S****PCL*] were prepared as porous scaffolds. In base-catalyzed degradation studies, all semi-IPNs degraded faster than controls, and the ***L/S***, ***S/L*** and ***S/S*** all degraded faster than the previously studied ***L/L*** composition. This was linked to increased phase separation observed in analogous solid films of the fastest degrading compositions, but as explained in Chapter V, these compositions should be further evaluated under non-catalyzed conditions. Compressive properties were reduced for the ***S****PCL* compared to the ***L****PCL* control, but all semi-IPNs showed improved properties compared to their respective 100% PCL control. Significantly, the use of a 4-arm star PCL-TA network allowed the SMP T_{trans} or T_{fit} to be reduced by 10 °C from 55 °C to 45 °C, which has the potential to improve tissue-safety during implantation. Self-fitting or SMP properties were examined in a plastic model defect and shape fixity/recovery was ~100% for all compositions over two cycles. Radial force was tested for the first time, and all compositions studied herein had significantly higher radial pressure than the original ***LPCL***, which has potential to benefit implant stability and further enhance osseointegration. The star macromers were also shown to have a reduced solution viscosity allowing for fabrication without the need for centrifugation to assist macromer diffusion. As such, fabrication was scaled up using larger-sized containers and scaffolds with 5X the volume were successfully fabricated with uniform pore morphology for the ***S/S*** composition. Overall, this study showed that self-fitting thermoresponsive behavior may be tuned via implementing star macromer architecture, which was also shown to enhance radial force and to allow for greater fabrication utility.

In Chapter VII, previous results indicating the significance of miscibility inspired successful incorporation of PPF into PCL-DA networks via compatibilization to prepare PCL-DA/PPF co-networks with tunable properties. Short blocks of PCL and PDLLA were prepared as macroinitiators to produce two diblock copolymers: PCL-PPF and PDLLA-PPF, which allowed for incorporation at 10 and 25 wt. % using typical macromer solutions for scaffold fabrication. Compositions of the same wt. % were prepared using PPF homopolymers, but they could not be dissolved in the typical solvent, and even when a solvent mix was employed there were issues with scaffolds not fully UV-curing. This demonstrated the necessity and efficacy of using PCL and PDLLA compatibilizers. Due to PPF macromers ability to cross-link into the PCL-DA network, pore size and porosity were increased compared to the 100% PCL-DA control but this could be advantageous for cell proliferation. The PCL-DA/PPF co-networks were additionally shown to have reduced T_{fit} (~44 °C) with well-maintained self-fitting properties in a plastic model defect. Compressive properties were reduced for PPF containing constructs, but properties were still within the MPa range and were sufficiently robust for handling and press-fitting. Then, these PCL-DA/PPF co-network scaffolds were examined in a 4-month non-catalyzed *in vitro* hydrolysis study. Over the course of 4 months, minimal gravimetric mass loss was observed, however PCL crystallinity and mechanical properties tended to increase with hydrolysis time, consistent with early phases of polymer degradation. Interestingly, the PPF containing compositions all displayed hydrogel-like properties but to varying degrees depending on the compatibilizer and PPF wt %. These PCL-DA/PPF co-networks show excellent potential for use in future studies as they show early signs of degradation over 4 months, but without diminishing mechanical properties necessary to supporting early bone healing. Moreover, compatibilization of PPF proved to be a successful way to achieve incorporation in PCL-DA networks resulting in self-fitting PCL-DA/PPF co-network scaffolds with unique tunable hydration properties.

All in all, this work clearly illustrates the following: 1) Self-fitting scaffolds based on PCL-DA networks supported tissue integration and allowed for bone neotissue ingrowth when examined at 16-weeks in a rabbit calvarial defect model. 2) PCL-DA/PLLA semi-IPN scaffolds with a bioactive PD-coating showed enhanced *in vitro* hMSC osteogenic differentiation compared to an uncoated 100% PCL-DA control, 3) Substitution of PLAs with varying microstructure into PCL-DA/PLA semi-IPNs yielded tunable mechanical and degradative properties primarily linked to PCL/PLA miscibility, 4) Degradation of various PCL-DA/PLA semi-IPN scaffolds under non-catalyzed conditions yielded several fast degrading compositions that tended to degrade via erosion of the PLA component first; these degradation profiles and mechanical properties were also tunable with annealing temperature. 5) Exchanging linear PCL-DA and PLLA architecture for 4-arm star analogues showed improved scaffold properties including a reduced T_{fit}, enhanced radial force and improved fabrication capabilities. 6) PPF was successfully incorporated to PCL-DA networks via compatibilization to yield new PCL-DA/PPF co-networks with tunable hydration properties and with mechanical property retention over 4-months of *in vitro* hydrolysis. Moreover, existing scaffold compositions that had been previously developed were advanced towards *in vitro* hMSC and *in vivo* studies, while new compositions in the form of PCL-DA/PLA semi-IPNs and PCL-DA/PPF co-networks were developed and well-characterized for future use in cell and *in vivo* studies.

8.2. Future Work

As shown in **Figure 8-1**, the work performed in Chapters II-VII is interconnected via a self-fitting CMF bone scaffold development workflow, from benchtop to *in vivo* models. The newly developed compositions with properties of interest should be selected to progress through the scaffold development as follows: 1) From Chapter III, the PCL-DA/PLLA semi-IPN with the bioactive PD-coating should move forward to small animal *in vivo* studies based on favorable hMSC osteogenesis results compared to PD-coated and uncoated 100% PCL-DA controls. Beginning with a small animal model will allow for greater power in studies and is more practical at this stage when we are still assessing which chemistry compositions, and resulting scaffold properties, perform the best in a clinical setting. 2) From Chapters IV and V, the PCL-DA/PLA (75/25 by wt.) semi-IPNs prepared with PDLLA thermoplastic should be selected to progress to *in vitro* hMSC studies as this composition showed the fastest under neutral degradation, as well as improved compressive properties compared to the 100% PCL-DA control. PCL-DA/PDLLA scaffold properties were shown to be tunable via annealing conditions in Chapter IV and V; then, in Chapter VII, a version of the PCL-DA/PDLLA scaffold was included as a control for the PCL-DA/PPF co-network study but was subjected to that study's adapted fabrication protocol. The recommendation is to move forward based on the updated protocol from Chapter VII, as the non-catalyzed degradation results showed scaffolds maintained mechanical properties over 4-months was the most informative. This updated protocol using a UV cure box (as opposed to the previously used plate) is also beneficial for future use in preparing larger scaffolds and is recommended for future SCPL scaffold protocols. 3) In Chapter VI, the ***S/S***, composed of 4-arm star PCL and 4-arm star PLLA, was shown to have the best properties in terms of lowered T_{fit}, improved radial pressure, and scalable fabrication. Characterization on the ***S/S*** was limited to base catalyzed degradation conditions, so the next step is to examine their hydrolysis under neutral non-catalyzed conditions. Additionally, a stem cell study examining cell proliferation through the press-fitting sequence would be advantageous to prove that the ***S/S*** with a lowered T_{fit} of 45 °C improves cell viability compared to the 100% linear PCL-DA control with a T_{fit} of 55 °C. 4) In Chapter VII, brand new PCL-DA/PPF co-networks were designed and were immediately studied under non-catalyzed degradation conditions. These types of brief non-catalyzed hydrolysis studies are recommended for future scaffold testing rather than doing base-catalyzed testing which did not accurately predict degradation rates under neutral conditions. The compositions compatibilized with PDLLA: F-D-10 and F-D-25 (PCL-DA/PDLLA-co-PPF, 10 or 25 wt. %) showed the most interesting hydration properties and would benefit from moving forward to stem cell studies, especially since hydration was linked to improved osteogenesis of hMSCs in Chapter III. However, there are some other advanced materials characterization techniques to consider now that it has been established that these compositions behave as hydrogels. Thus far, mechanical testing has been performed on dried samples at room temperature, but the F-D-10 and F-D-25 will be in a swollen state when hydrated and at body temperature so it would be ideal to perform compressive and radial testing in an aqueous immersion chamber heated to 37 °C.

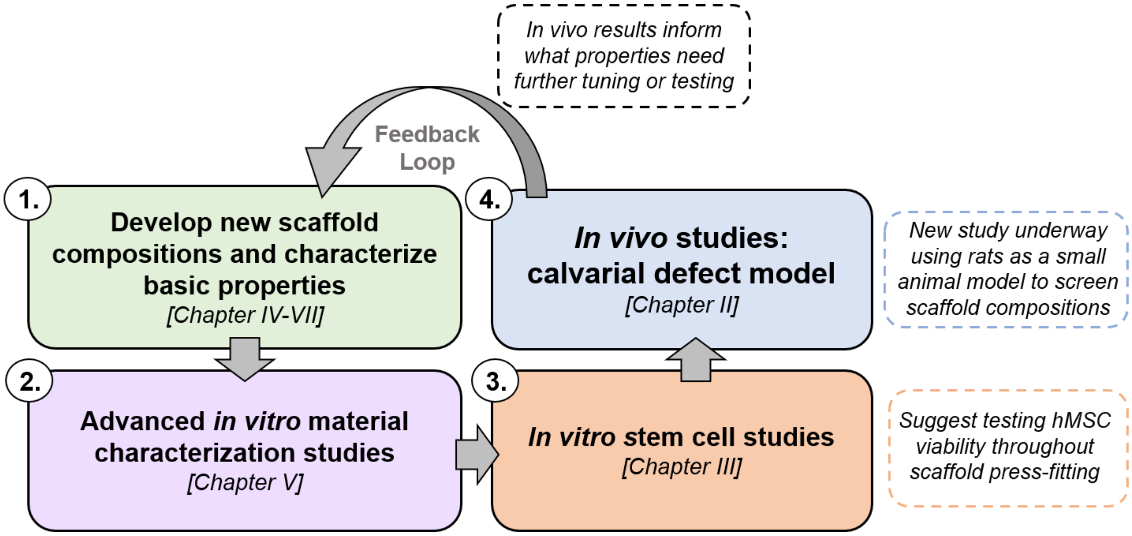

Figure 8-1. Flow chart demonstrating how new scaffold compositions of interest may progress through future development stages. Corresponding chapters are also noted to show how each tie into the overall process of designing self-fitting CMF bone scaffolds with optimal properties.

As mentioned above, the PD-coated PCL-DA/PLLA semi-IPN scaffolds that supported osteogenesis of hMSCs are currently being studied in a rat calvarial defect model. The study began using bilateral non-critical size calvarial defects (d~ 5 mm) performed with microCT, histology, and biomechanical testing akin to the work done in the rabbit study in Chapter II. The choice to use a small animal model with bilateral defects allows for greater power in statistical analyses while using less animals (more ethical and less costly) as we screen various scaffold compositions.[291] The next step is to perform similar testing but on a unilateral critical sized defect (d ~8 mm) in a rat model to see how well self-fitting scaffolds can support regeneration when endogenous healing is more limited.[120] From there larger animal models may be explored to examine the potential of self-fitting scaffolds in larger defects toward eventual use for treatment in humans. Common larger animal models for calvarial defects include rabbits (15 mm), canines (20 mm), and sheep (22 mm).[120] Another option to consider is changing from a regular circular defect to a more “irregular” shape. One such example is the 8-shaped defect that has been used to assess 3-D printed scaffolds in rabbits and can be produced using two connected circular burr-holes.[292, 293] The use of irregular shaped defects may have more translational relevance and could also better demonstrates the advantages associated with scaffold self-fitting capabilities.

In terms of further self-fitting scaffold development, we foresee utilizing synthetic macromer reaction techniques like those used in the compatibilization of PPF, but for adding new functionality to the self-fitting devices. For compatibilization, macro-initiators based on short chains of PCL or PDLLA were used to prepare PPF copolymers that allowed for facile incorporation into the PCL-DA network compared to PPF homopolymers. There is much further exploration of compatibilizers that could take place in terms of varying macro-initiator microstructure (M_n, copolymerize, architecture, etc.) to affect phase separation and fine-tune macroscopic properties. But there may be a desire to have a more profound impact on scaffold functionality rather than continuing to fine-tune degradation or mechanical profiles. Thus, the use of functionally-initiated macromers is suggested as summarized in **Figure 8-2**.

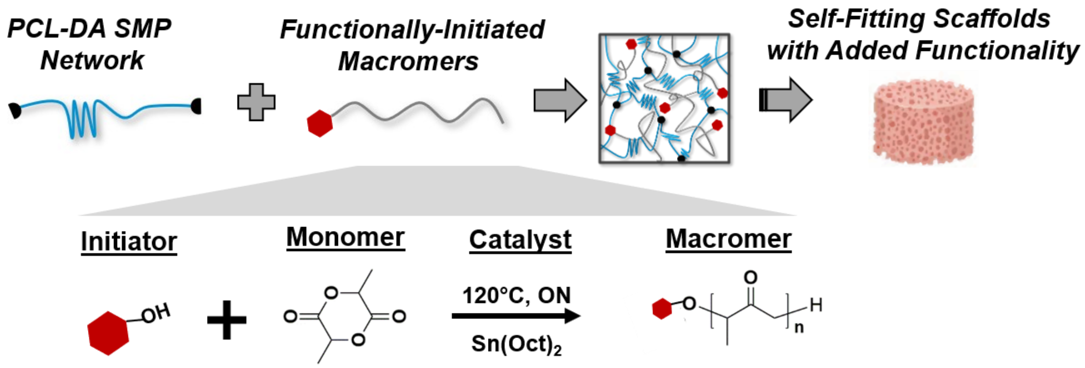

Figure 8-2. Schematic demonstrating how functional molecules with alcohol moieties may be used to initiate synthesis of biodegradable macromers via ROP. These may then be incorporated into PCL-DA networks to yield self-fitting scaffolds with additional capabilities.

Functional-initiators should have some established biologically relevant functionality and should have at least one alcohol moiety to initiate typical polyester ROP synthetic routes performed in this work. Three functional-initiators are proposed: menthol, graphene oxide (GO) and cholesterol, as summarized in **Figure 8-3**. The first suggestion for a potential functional-initiator is menthol which is a naturally derived aromatic compound known to have antibacterial activity against both gram-positive and gram-negative bacteria.[294] Menthol contains a chiral alcohol and has been successfully used to initiate successful ROPs with PLA monomers.[295, 296] Antibacterial activity of the menthol-PLAs was not reported, but macromer biodegradation is expected to lead to menthol release over time. This would add localized infection-fighting functionality to the scaffold and could benefit treatment of cranial bone defects where up to 60% of surgeries result in infection.[120] Typical gold standards for infection treatment include use of antibiotics such as rifampicin and vancomycin, which can be administered orally or via IV, but both are associated with high rates of antibiotic resistance.[297, 298] Thus, the use of a natural antibacterial, not susceptible to antibiotic resistance, could be highly advantageous to the self-fitting CMF bone scaffolds.

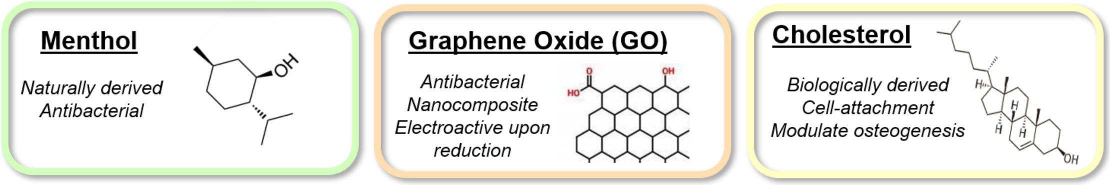

Figure 8-3. A summary of the proposed functional-initiators, their chemical structure and their potential advantages are listed.

Next, GO has also been shown to have antibacterial activity against gram-positive and gram-negative bacteria,[299] and has even been shown to be effective against multidrug resistant "superbug" strains.[300] GO has been successfully used as an initiator for ROP of PLLA to prepare GO-*graft*-PLLA that was electrospun into nanofibrous meshes that maintained antibacterial activity against *S. aureus and E. coli*.[301] GO, and reduced GO have also been widely used in polymeric nanocomposites and are well known to impart improved mechanical properties, and electrical activity.[302, 303] Therefore, GO could serve well as a potential functional-initiator for potentially adding infection-fighting, enhanced mechanics, and electrical activity to self-fitting scaffolds. Lastly, cholesterol is a well-known biologic molecule that contains an alcohol moiety and has been shown to enhance cell attachment.[304] Cholesterol has been used to initiate synthesis of PLLA copolymers, and has been linked to homeostasis and modulation of osteogenesis. This technique could offer advantages over the previously used ACR-PEG-RGD cell-binding modifier used in Chapter III, because the new functional-initiator route would ensure no effect on the PCL-DA network. This proposed technique is reminiscent of polymer-conjugation strategies, but those may rely on complicated synthetic routes whereas using functional-initiators with robust ROPs can provide a facile strategy for preparing the next generation of functional self-fitting CMF bone scaffolds.

REFERENCES

1. Behl, M.; Lendlein, A., Shape-memory polymers. *Mater. Today* **2007,** *10* (4), 20-28.
2. Behl, M.; Lendlein, A., Actively moving polymers. *Soft Matter* **2007,** *3* (1), 58-67.
3. Lendlein, A., Progress in actively moving polymers. *J. Mater. Chem.* **2010,** *20* (17), 3332-3334.
4. Lendlein, A.; Langer, R., Biodegradable, Elastic Shape-Memory Polymers for Potential Biomedical Applications. *Science* **2002,** *296* (5573), 1673.
5. Delaey, J.; Dubruel, P.; Van Vlierberghe, S., Shape-Memory Polymers for Biomedical Applications. *Adv. Funct. Mater.* **2020,** *30* (44), 1909047.
6. Lendlein, A.; Behl, M.; Hiebl, B.; Wischke, C., Shape-memory polymers as a technology platform for biomedical applications. *Expert Rev. Med. Devices* **2010,** *7* (3), 357-79.
7. Hasan, S. M.; Nash, L. D.; Maitland, D. J., Porous shape memory polymers: Design and applications. *J. Polym. Sci. B Polym. Phys.* **2016,** *54* (14), 1300-1318.
8. Small, I. V. W.; Singhal, P.; Wilson, T. S.; Maitland, D. J., Biomedical applications of thermally activated shape memory polymers. *J. Mater. Chem.* **2010,** *20* (17), 3356-3366.
9. Yakacki, C. M.; Gall, K., Shape-Memory Polymers for Biomedical Applications. In *Shape-Memory Polymers*, Lendlein, A., Ed. Springer Berlin Heidelberg: Berlin, Heidelberg, 2010; pp 147-175.
10. Wang, K.; Strandman, S.; Zhu, X. X., A mini review: Shape memory polymers for biomedical applications. *Front. Chem. Sci. Eng.* **2017,** *11* (2), 143-153.
11. Chen, H.-M.; Wang, L.; Zhou, S.-B., Recent Progress in Shape Memory Polymers for Biomedical Applications. *Chinese J. Polym. Sci.* **2018,** *36* (8), 905-917.
12. Vernon, L.; Vernon, H. Process of manufacturing articles of thermoplastic synthetic resins. 2234993, 1941.
13. Metz, R. M.; Kaar, S. G., Arthroscopic Bankart Repair With Remplissage: Indications and Technique. *Oper. Tech. Orthop.* **2020,** *30* (3), 100818.
14. Christensen, J.; Fischer, B.; Nute, M.; Rizza, R., Fixation strength of polyetheretherketone sheath-and-bullet device for soft tissue repair in the foot and ankle. *J. Foot Ankle Surg.* **2018,** *57* (1), 60-64.
15. Berg-Johansen, B.; Lovald, S.; Altiok, E.; Kurtz, S. M., Chapter 17 - Applications of Polyetheretherketone in Arthroscopy. In *PEEK Biomaterials Handbook (Second Edition)*, Kurtz, S. M., Ed. William Andrew Publishing: 2019; pp 291-300.
16. Morgan, R. A.; Loftus, I.; Ratnam, L.; Das, R.; Mailli, L.; Hamady, M.; Lobotesis, K., Clinical Experience With a Shape Memory Polymer Peripheral Vascular Embolisation Plug: A Case Series. *CVIR Endovasc.* **2021,** *4* (29).
17. Jansen, A.-J. S.; van Schaik, P. M.; Martens, J. M.; Reijnen, M. M., Embolization of the false lumen using IMPEDE-FX embolization plugs as part of treatment of an infrarenal post-dissection aneurysm: a case report. *CVIR Endovasc.* **2020,** *3* (1), 1-5.

18. Zhang, K.; Wang, S.; Zhou, C.; Cheng, L.; Gao, X.; Xie, X.; Sun, J.; Wang, H.; Weir, M. D.; Reynolds, M. A.; Zhang, N.; Bai, Y.; Xu, H. H. K., Advanced smart biomaterials and constructs for hard tissue engineering and regeneration. *Bone Res.* **2018,** *6* (1), 31.
19. Dhandayuthapani, B.; Yoshida, Y.; Maekawa, T.; Kumar, D. S., Polymeric Scaffolds in Tissue Engineering Application: A Review. *Int. J. Polym. Sci.* **2011,** *2011*, 290602.
20. Qu, H.; Fu, H.; Han, Z.; Sun, Y., Biomaterials for bone tissue engineering scaffolds: a review. *RSC Adv.* **2019,** *9* (45), 26252-26262.
21. Hollister, S. J., Porous scaffold design for tissue engineering. *Nat. Mater.* **2005,** *4* (7), 518-24.
22. Leng, J.; Lan, X.; Liu, Y.; Du, S., Shape-memory polymers and their composites: Stimulus methods and applications. *Prog. Mater. Sci.* **2011,** *56* (7), 1077-1135.
23. Liu, Y.; Lv, H.; Lan, X.; Leng, J.; Du, S., Review of electro-active shape-memory polymer composite. *Compos. Sci. Technol.* **2009,** *69* (13), 2064-2068.
24. Shang, J.; Le, X.; Zhang, J.; Chen, T.; Theato, P., Trends in polymeric shape memory hydrogels and hydrogel actuators. *Polym. Chem.* **2019,** *10* (9), 1036-1055.
25. Jang, L. K.; Fletcher, G. K.; Monroe, M. B. B.; Maitland, D. J., Biodegradable shape memory polymer foams with appropriate thermal properties for hemostatic applications. *J. Biomed. Mater. Res. A* **2020,** *108* (6), 1281-1294.
26. Cai, S.; Sun, Y.-C.; Ren, J.; Naguib, H. E., Toward the low actuation temperature of flexible shape memory polymer composites with room temperature deformability via induced plasticizing effect. *J. Mater. Chem. B* **2017,** *5* (44), 8845-8853.
27. Lennon, A. B.; Prendergast, P. J., Residual stress due to curing can initiate damage in porous bone cement: experimental and theoretical evidence. *J. Biomech.* **2002,** *35* (3), 311-321.
28. Lobb, D. C.; DeGeorge, B. R.; Chhabra, A. B., Bone Graft Substitutes: Current Concepts and Future Expectations. *Hand Surg.* **2019,** *44* (6), 497-505.e2.
29. Orr, J. F.; Dunne, N. J.; Quinn, J. C., Shrinkage stresses in bone cement. *Biomaterials* **2003,** *24* (17), 2933-2940.
30. Hou, Q.; De Bank, P. A.; Shakesheff, K. M., Injectable scaffolds for tissue regeneration. *J. Mater. Chem.* **2004,** *14* (13), 1915-1923.
31. Migliaresi, C.; Motta, A.; DiBenedetto, A. T., Injectable Scaffolds for Bone and Cartilage Regeneration. In *Engineering of Functional Skeletal Tissues*, Bronner, F.; Farach-Carson, M. C.; Mikos, A. G., Eds. Springer London: London, 2007; pp 95-109.
32. Van der Stok, J.; Van Lieshout, E. M.; El-Massoudi, Y.; Van Kralingen, G. H.; Patka, P., Bone substitutes in the Netherlands - a systematic literature review. *Acta Biomater.* **2011,** *7* (2), 739-50.
33. Low, K. L.; Tan, S. H.; Zein, S. H.; Roether, J. A.; Mouriño, V.; Boccaccini, A. R., Calcium phosphate-based composites as injectable bone substitute materials. *J. Biomed. Mater. Res. B Appl. Biomater.* **2010,** *94* (1), 273-86.

34. Spierings, P., Properties of Bone Cement: Testing and Performance of Bone Cements In *The Well-Cemented Total Hip Arthroplasty*; Breusch S, Malchau H, Eds. Springer: Germany: 2005.
35. Serbetci, K.; Korkusuz, F.; Hasirci, N., Thermal and mechanical properties of hydroxyapatite impregnated acrylic bone cements. *Polym. Test.* **2004,** *23* (2), 145-155.
36. Wang, J.; Li, X.; Song, Y.; Su, Q.; Xiaohalati, X.; Yang, W.; Xu, L.; Cai, B.; Wang, G.; Wang, Z.; Wang, L., Injectable silk sericin scaffolds with programmable shape-memory property and neuro-differentiation-promoting activity for individualized brain repair of severe ischemic stroke. *Bioact. Mater.* **2021,** *6* (7), 1988-1999.
37. Zhang, D.; George, O. J.; Petersen, K. M.; Jimenez-Vergara, A. C.; Hahn, M. S.; Grunlan, M. A., A bioactive “self-fitting” shape memory polymer scaffold with potential to treat cranio-maxillo facial bone defects. *Acta Biomater.* **2014,** *10* (11), 4597-4605.
38. Zhao, W.; Zhang, F.; Leng, J.; Liu, Y., Personalized 4D printing of bioinspired tracheal scaffold concept based on magnetic stimulated shape memory composites. *Compos. Sci. Technol.* **2019,** *184,* 107866.
39. Wang, L.; Cao, L.; Shansky, J.; Wang, Z.; Mooney, D.; Vandenburgh, H., Minimally invasive approach to the repair of injured skeletal muscle with a shape-memory scaffold. *Mol. Ther.* **2014,** *22* (8), 1441-1449.
40. Montgomery, M.; Ahadian, S.; Davenport Huyer, L.; Lo Rito, M.; Civitarese, R. A.; Vanderlaan, R. D.; Wu, J.; Reis, L. A.; Momen, A.; Akbari, S.; Pahnke, A.; Li, R.-K.; Caldarone, C. A.; Radisic, M., Flexible shape-memory scaffold for minimally invasive delivery of functional tissues. *Nat. Mater.* **2017,** *16* (10), 1038-1046.
41. Guillaume, O.; Daly, A.; Lennon, K.; Gansau, J.; Buckley, S. F.; Buckley, C. T., Shape-memory porous alginate scaffolds for regeneration of the annulus fibrosus: Effect of TGF-β3 supplementation and oxygen culture conditions. *Acta Biomater.* **2014,** *10* (5), 1985-1995.
42. Liu, D.; Xiang, T.; Gong, T.; Tian, T.; Liu, X.; Zhou, S., Bioinspired 3D Multilayered Shape Memory Scaffold with a Hierarchically Changeable Micropatterned Surface for Efficient Vascularization. *ACS Appl. Mater. Interfaces* **2017,** *9* (23), 19725-19735.
43. Baker, R. M.; Tseng, L.-F.; Iannolo, M. T.; Oest, M. E.; Henderson, J. H., Self-deploying shape memory polymer scaffolds for grafting and stabilizing complex bone defects: A mouse femoral segmental defect study. *Biomaterials* **2016,** *76*, 388-398.
44. Jiang, L. B.; Su, D. H.; Liu, P.; Ma, Y. Q.; Shao, Z. Z.; Dong, J., Shape-memory collagen scaffold for enhanced cartilage regeneration: native collagen versus denatured collagen. *Osteoarthr. Cartil.* **2018,** *26* (10), 1389-1399.
45. Wang, Y.-J.; Jeng, U. S.; Hsu, S.-h., Biodegradable Water-Based Polyurethane Shape Memory Elastomers for Bone Tissue Engineering. *ACS Biomater. Sci. Eng.* **2018,** *4* (4), 1397-1406.
46. Xie, M.; Wang, L.; Ge, J.; Guo, B.; Ma, P. X., Strong Electroactive Biodegradable Shape Memory Polymer Networks Based on Star-Shaped Polylactide and Aniline Trimer for Bone Tissue Engineering. *ACS Appl. Mater. Interfaces* **2015,** *7* (12), 6772-6781.

47. Neuss, S.; Blomenkamp, I.; Stainforth, R.; Boltersdorf, D.; Jansen, M.; Butz, N.; Perez-Bouza, A.; Knüchel, R., The use of a shape-memory poly(epsilon-caprolactone)dimethacrylate network as a tissue engineering scaffold. *Biomaterials* **2009,** *30* (9), 1697-705.
48. Huang, K.; Yang, M.-s.; Tang, Y.-j.; Ling, S.-Y.; Pan, F.; Liu, X.-d.; Chen, J., Porous shape memory scaffold of dextran and hydroxyapatite for minimum invasive implantation for bone tissue engineering applications. *J. Biomater. Appl.* **2020**, 0885328220950062.
49. Erndt-Marino, J. D.; Munoz-Pinto, D. J.; Samavedi, S.; Jimenez-Vergara, A. C.; Diaz-Rodriguez, P.; Woodard, L.; Zhang, D.; Grunlan, M. A.; Hahn, M. S., Evaluation of the osteoinductive capacity of polydopamine-coated poly(ε-caprolactone) diacrylate shape memory foams. *ACS Biomater. Sci. Eng.* **2015,** *1* (12), 1220-1230.
50. Xie, R.; Hu, J.; Hoffmann, O.; Zhang, Y.; Ng, F.; Qin, T.; Guo, X., Self-fitting shape memory polymer foam inducing bone regeneration: A rabbit femoral defect study. *Biochim. Biophys. Acta Gen. Subj.* **2018,** *1862* (4), 936-945.
51. Almeida, H. V.; Sathy, B. N.; Dudurych, I.; Buckley, C. T.; O'Brien, F. J.; Kelly, D. J., Anisotropic Shape-Memory Alginate Scaffolds Functionalized with Either Type I or Type II Collagen for Cartilage Tissue Engineering. *Tissue Eng. Part A* **2016,** *23* (1-2), 55-68.
52. Uto, S.; Hikita, A.; Sakamoto, T.; Mori, D.; Yano, F.; Ohba, S.; Saito, T.; Takato, T.; Hoshi, K., Ear Cartilage Reconstruction Combining Induced Pluripotent Stem Cell-Derived Cartilage and Three-Dimensional Shape-Memory Scaffold. *Tissue Eng. Part A* **2020**.
53. Miao, S.; Zhu, W.; Castro, N. J.; Nowicki, M.; Zhou, X.; Cui, H.; Fisher, J. P.; Zhang, L. G., 4D printing smart biomedical scaffolds with novel soybean oil epoxidized acrylate. *Sci. Rep.* **2016,** *6* (1), 27226.
54. Zhang, C.; Cai, D.; Liao, P.; Su, J.-W.; Deng, H.; Vardhanabhuti, B.; Ulery, B. D.; Chen, S.-Y.; Lin, J., 4D Printing of shape-memory polymeric scaffolds for adaptive biomedical implantation. *Acta Biomater.* **2021,** *122*, 101-110.
55. Boire, T. C.; Himmel, L. E.; Yu, F.; Guth, C. M.; Dollinger, B. R.; Werfel, T. A.; Balikov, D. A.; Duvall, C. L., Effect of pore size and spacing on neovascularization of a biodegradble shape memory polymer perivascular wrap. *J. Biomed. Mater. Res. A* **2021,** *109* (3), 272-288.
56. Ahmed, J.; Varshney, S. K., Polylactides—chemistry, properties and green packaging technology: a review. *Int. J. Food Prop.* **2011,** *14* (1), 37-58.
57. Bao, M.; Lou, X.; Zhou, Q.; Dong, W.; Yuan, H.; Zhang, Y., Electrospun Biomimetic Fibrous Scaffold from Shape Memory Polymer of PDLLA-co-TMC for Bone Tissue Engineering. *ACS Appl. Mater. Interfaces* **2014,** *6* (4), 2611-2621.
58. Chen, M.; Li, L.; Xia, L.; Zhang, F.; Jiang, S.; Hu, H.; Li, X.; Wang, H., Temperature Responsive Shape-Memory Scaffolds with Circumferentially Aligned Nanofibers for Guiding Smooth Muscle Cell Behavior. *Macromol. Biosci.* **2020,** *20* (2), 1900312.

59. Qi, X.; Yang, G.; Jing, M.; Fu, Q.; Chiu, F.-C., Microfibrillated cellulose-reinforced bio-based poly(propylene carbonate) with dual shape memory and self-healing properties. *J. Mater. Chem. A* **2014,** *2* (47), 20393-20401.
60. Pandey, A.; Singh, G.; Singh, S.; Jha, K.; Prakash, C., 3D printed biodegradable functional temperature-stimuli shape memory polymer for customized scaffoldings. *J Mech Behav Biomed Mater* **2020,** *108*, 103781.
61. Sabzi, M.; Babaahmadi, M.; Rahnama, M., Thermally and Electrically Triggered Triple-Shape Memory Behavior of Poly(vinyl acetate)/Poly(lactic acid) Due to Graphene-Induced Phase Separation. *ACS Appl. Mater. Interfaces* **2017,** *9* (28), 24061-24070.
62. Navarro-Baena, I.; Sessini, V.; Dominici, F.; Torre, L.; Kenny, J. M.; Peponi, L., Design of biodegradable blends based on PLA and PCL: From morphological, thermal and mechanical studies to shape memory behavior. *Polym. Degrad. Stab.* **2016,** *132*, 97-108.
63. Peponi, L.; Sessini, V.; Arrieta, M. P.; Navarro-Baena, I.; Sonseca, A.; Dominici, F.; Gimenez, E.; Torre, L.; Tercjak, A.; López, D.; Kenny, J. M., Thermally-activated shape memory effect on biodegradable nanocomposites based on PLA/PCL blend reinforced with hydroxyapatite. *Polym. Degrad. Stab.* **2018,** *151*, 36-51.
64. Wang, X.; Yan, H.; Zhou, Y.; Lou, X.; Zhang, Y., Fabrication of fibrous PLLA/PHBV scaffolds with shape memory capability. *J. Control. Release* **2017,** *259*, e144-e145.
65. Wang, X.; Yan, H.; Shen, Y.; Tang, H.; Yi, B.; Qin, C.; Zhang, Y., Shape Memory and Osteogenesis Capabilities of the Electrospun Poly(3-Hydroxybutyrate-co-3-Hydroxyvalerate) Modified Poly(l-Lactide) Fibrous Mats. *Tissue Eng. Part A* **2020,** *27* (1-2), 142-152.
66. Samuel, C.; Barrau, S.; Lefebvre, J.-M.; Raquez, J.-M.; Dubois, P., Designing Multiple-Shape Memory Polymers with Miscible Polymer Blends: Evidence and Origins of a Triple-Shape Memory Effect for Miscible PLLA/PMMA Blends. *Macromolecules* **2014,** *47* (19), 6791-6803.
67. Amini, M.; Wu, S., Designing a polymer blend nanocomposite with triple shape memory effects. *Compos. Commun.* **2021,** *23*, 100564.
68. Wang, S.; Lu, L.; Gruetzmacher, J. A.; Currier, B. L.; Yaszemski, M. J., Synthesis and characterizations of biodegradable and crosslinkable poly(ε-caprolactone fumarate), poly(ethylene glycol fumarate), and their amphiphilic copolymer. *Biomaterials* **2006,** *27* (6), 832-841.
69. Nail, L. N.; Zhang, D.; Reinhard, J. L.; Grunlan, M. A., Fabrication of a Bioactive, PCL-based "Self-fitting" Shape Memory Polymer Scaffold. *JoVE* **2015,** (104), e52981.
70. Beltran, F. O.; Houk, C. J.; Grunlan, M. A., Bioactive Siloxane-Containing Shape-Memory Polymer (SMP) Scaffolds with Tunable Degradation Rates. *ACS Biomater. Sci. Eng.* **2021**.
71. Woodard, L. N.; Kmetz, K. T.; Roth, A. A.; Page, V. M.; Grunlan, M. A., Porous Poly(ε-caprolactone)–Poly(l-lactic acid) Semi-Interpenetrating Networks as

Superior, Defect-Specific Scaffolds with Potential for Cranial Bone Defect Repair. *Biomacromolecules* **2017,** *18* (12), 4075-4083.

72. Antony, G. J. M.; Jarali, C. S.; Aruna, S. T.; Raja, S., Tailored poly(ethylene) glycol dimethacrylate based shape memory polymer for orthopedic applications. *J Mech Behav Biomed Mater* **2017,** *65*, 857-865.

73. Nöchel, U.; Reddy, C. S.; Uttamchand, N. K.; Kratz, K.; Behl, M.; Lendlein, A., Shape-memory properties of hydrogels having a poly(ε-caprolactone) crosslinker and switching segment in an aqueous environment. *Eur. Polym. J.* **2013,** *49* (9), 2457-2466.

74. Zhang, X.; Geven, M. A.; Grijpma, D. W.; Peijs, T.; Gautrot, J. E., Tunable and processable shape memory composites based on degradable polymers. *Polymer* **2017,** *122*, 323-331.

75. Sharifi, S.; van Kooten, T. G.; Kranenburg, H.-J. C.; Meij, B. P.; Behl, M.; Lendlein, A.; Grijpma, D. W., An annulus fibrosus closure device based on a biodegradable shape-memory polymer network. *Biomaterials* **2013,** *34* (33), 8105-8113.

76. Boire, T. C.; Gupta, M. K.; Zachman, A. L.; Lee, S. H.; Balikov, D. A.; Kim, K.; Bellan, L. M.; Sung, H.-J., Reprint of: Pendant allyl crosslinking as a tunable shape memory actuator for vascular applications. *Acta Biomater.* **2016,** *34*, 73-83.

77. Xie, Y.; Lei, D.; Wang, S.; Liu, Z.; Sun, L.; Zhang, J.; Qing, F.-L.; He, C.; You, Z., A Biocompatible, Biodegradable, and Functionalizable Copolyester and Its Application in Water-Responsive Shape Memory Scaffold. *ACS Biomater. Sci. Eng.* **2019,** *5* (4), 1668-1676.

78. Le Fer, G.; Becker, M. L., 4D Printing of Resorbable Complex Shape-Memory Poly(propylene fumarate) Star Scaffolds. *ACS Appl. Mater. Interfaces* **2020,** *12* (20), 22444-22452.

79. Yang, L.-Q.; He, B.; Meng, S.; Zhang, J.-Z.; Li, M.; Guo, J.; Guan, Y.-M.; Li, J.-X.; Gu, Z.-W., Biodegradable cross-linked poly(trimethylene carbonate) networks for implant applications: Synthesis and properties. *Polymer* **2013,** *54* (11), 2668-2675.

80. Baker, R. M.; Henderson, J. H.; Mather, P. T., Shape memory poly(ε-caprolactone)-co-poly(ethylene glycol) foams with body temperature triggering and two-way actuation. *J. Mater. Chem. B* **2013,** *1* (38), 4916-4920.

81. Wang, L.; Shansky, J.; Borselli, C.; Mooney, D.; Vandenburgh, H., Design and Fabrication of a Biodegradable, Covalently Crosslinked Shape-Memory Alginate Scaffold for Cell and Growth Factor Delivery. *Tissue Eng. Part A* **2012,** *18* (19-20), 2000-2007.

82. Zhang, X.; Liu, K.; Liu, J.; Ding, Y.; Li, W.; Zhang, A., Thermoresponsive cryogels from dendronized interpenetrating polymer network showing dual-shape memory. *Eur. Polym. J.* **2020,** *141*, 110092.

83. Touchet, T. J.; Cosgriff-Hernandez, E. M., 1 - Hierarchal structure–property relationships of segmented polyurethanes. In *Advances in Polyurethane Biomaterials*, Cooper, S. L.; Guan, J., Eds. Woodhead Publishing: 2016; pp 3-22.

84. Matsumoto, H.; Ishiguro, T.; Konosu, Y.; Minagawa, M.; Tanioka, A.; Richau, K.; Kratz, K.; Lendlein, A., Shape-memory properties of electrospun non-woven fabrics prepared from degradable polyesterurethanes containing poly(ω-pentadecalactone) hard segments. *Eur. Polym. J.* **2012,** *48* (11), 1866-1874.

85. Kai, D.; Prabhakaran, M. P.; Chan, B. Q. Y.; Liow, S. S.; Ramakrishna, S.; Xu, F.; Loh, X. J., Elastic poly (ε-caprolactone)-polydimethylsiloxane copolymer fibers with shape memory effect for bone tissue engineering. *Biomed. Mater.* **2016,** *11* (1), 015007.

86. Song, J. J.; Chang, H. H.; Naguib, H. E., Biocompatible shape memory polymer actuators with high force capabilities. *Eur. Polym. J.* **2015,** *67*, 186-198.

87. Gu, S.-Y.; Liu, L.-L.; Gao, X.-F., Triple-shape memory properties of polyurethane/polylactide–polytetramethylene ether blends. *Polym. Int.* **2015,** *64* (9), 1155-1162.

88. Shao, L.-n.; Dai, J.; Zhang, Z.-x.; Yang, J.-h.; Zhang, N.; Huang, T.; Wang, Y., Thermal and electroactive shape memory behaviors of poly(l-lactide)/thermoplastic polyurethane blend induced by carbon nanotubes. *RSC Adv.* **2015,** *5* (123), 101455-101465.

89. Yu, J.; Xia, H.; Teramoto, A.; Ni, Q.-Q., The effect of hydroxyapatite nanoparticles on mechanical behavior and biological performance of porous shape memory polyurethane scaffolds. *J. Biomed. Mater. Res. A* **2018,** *106* (1), 244-254.

90. Yan, B.; Gu, S.; Zhang, Y., Polylactide-based thermoplastic shape memory polymer nanocomposites. *Eur. Polym. J.* **2013,** *49* (2), 366-378.

91. Sambasivam, M.; White, R.; Cutting, K., 12 - Exploring the role of polyurethane and polyvinyl alcohol foams in wound care. In *Wound Healing Biomaterials*, Ågren, M. S., Ed. Woodhead Publishing: 2016; pp 251-260.

92. Ashida, K.; Iwasaki, K., Thermosetting Foams. In *Handbook of Plastic Foams*, Landrock, A. H., Ed. William Andrew Publishing: Park Ridge, NJ, 1995; pp 11-220.

93. Singhal, P.; Rodriguez, J. N.; Small, W.; Eagleston, S.; Van de Water, J.; Maitland, D. J.; Wilson, T. S., Ultra low density and highly crosslinked biocompatible shape memory polyurethane foams. *J. Polym. Sci. B Polym. Phys.* **2012,** *50* (10), 724-737.

94. Singhal, P.; Small, W.; Cosgriff-Hernandez, E.; Maitland, D. J.; Wilson, T. S., Low density biodegradable shape memory polyurethane foams for embolic biomedical applications. *Acta Biomater.* **2014,** *10* (1), 67-76.

95. Hasan, S. M.; Harmon, G.; Zhou, F.; Raymond, J. E.; Gustafson, T. P.; Wilson, T. S.; Maitland, D. J., Tungsten-loaded SMP foam nanocomposites with inherent radiopacity and tunable thermo-mechanical properties. *Polym. Adv. Technol.* **2016,** *27* (2), 195-203.

96. Cai, Y.; Jiang, J.-S.; Liu, Z.-W.; Zeng, Y.; Zhang, W.-G., Magnetically-sensitive shape memory polyurethane composites crosslinked with multi-walled carbon nanotubes. *Compos. Part A Appl. Sci. Manuf.* **2013,** *53*, 16-23.

97. Xu, J.; Song, J., High performance shape memory polymer networks based on rigid nanoparticle cores. *PNAS* **2010,** *107* (17), 7652.

98. Bothe, M.; Mya, K. Y.; Jie Lin, E. M.; Yeo, C. C.; Lu, X.; He, C.; Pretsch, T., Triple-shape properties of star-shaped POSS-polycaprolactone polyurethane networks. *Soft Matter* **2012,** *8* (4), 965-972.

99. Montgomery, M.; Davenport Huyer, L.; Bannerman, D.; Mohammadi, M. H.; Conant, G.; Radisic, M., Method for the fabrication of elastomeric polyester scaffolds

for tissue engineering and minimally invasive delivery. *ACS Biomater. Sci. Eng.* **2018,** *4* (11), 3691-3703.
100. Liu, Y.; Fang, N.; Liu, B.; Song, L.; Wen, B.; Yang, D., Aligned porous chitosan/graphene oxide scaffold for bone tissue engineering. *Mater. Lett.* **2018,** *233*, 78-81.
101. Gao, H.-L.; Lu, Y.; Mao, L.-B.; An, D.; Xu, L.; Gu, J.-T.; Long, F.; Yu, S.-H., A shape-memory scaffold for macroscale assembly of functional nanoscale building blocks. *Mater. Horiz.* **2014,** *1* (1), 69-73.
102. Yan, K.; Xu, F.; Li, S.; Li, Y.; Chen, Y.; Wang, D., Ice-templating of chitosan/agarose porous composite hydrogel with adjustable water-sensitive shape memory property and multi-staged degradation performance. *Colloid Surface B* **2020,** *190*, 110907.
103. Lendlein, A.; Balk, M.; Tarazona, N. A.; Gould, O. E. C., Bioperspectives for Shape-Memory Polymers as Shape Programmable, Active Materials. *Biomacromolecules* **2019,** *20* (10), 3627-3640.
104. Wang, J.; Quach, A.; Brasch, M. E.; Turner, C. E.; Henderson, J. H., On-command on/off switching of progenitor cell and cancer cell polarized motility and aligned morphology via a cytocompatible shape memory polymer scaffold. *Biomaterials* **2017,** *140*, 150-161.
105. Tseng, L.-F.; Mather, P. T.; Henderson, J. H., Shape-memory-actuated change in scaffold fiber alignment directs stem cell morphology. *Acta Biomater.* **2013,** *9* (11), 8790-8801.
106. Yang, P.; Baker, R. M.; Henderson, J. H.; Mather, P. T., In vitro wrinkle formation via shape memory dynamically aligns adherent cells. *Soft Matter* **2013,** *9* (18), 4705-4714.
107. Haug, R. H.; Morgan, J. P., Etiology, Distribution, and Classification of Traumatic Craniomaxillofacial Deformities and Defects. In *Craniomaxillofacial Reconstructive and Corrective Bone Surgery*, Greenberg, A. M.; Schmelzeisen, R., Eds. Springer New York: New York, NY, 2019; pp 45-51.
108. Allareddy, V.; Allareddy, V.; Nalliah, R. P., Epidemiology of facial fracture injuries. *J. Oral Maxillofac. Surg.* **2011,** *69* (10), 2613-8.
109. Cleft Lip & Palate. https://www.nidcr.nih.gov/health-info/cleft-lip-palate (accessed April 2, 2021).
110. Ugalmugle, S. S., Rupali *Craniomaxillofacial Devices Market Size, Share & Trends Analysis Report* GMI532; Jan. 2021, 2020; pp 1-128.
111. Greenwald, A. S.; Boden, S. D.; Goldberg, V. M.; Khan, Y.; Laurencin, C. T.; Rosier, R. N., Bone-graft substitutes: facts, fictions, and applications. *J. Bone Jt. Surg. Am.* **2001,** *83*, 98-103.
112. Elsalanty, M. E.; Genecov, D. G., Bone grafts in craniofacial surgery. *Craniomaxillofac. Trauma Reconstr.* **2009,** *2*, 125-134.
113. Neovius, E.; Engstrand, T., Craniofacial reconstruction with bone and biomaterials: review over the last 11 years. *J. Plast. Reconstr. Aesthet. Surg.* **2010,** *63* (10), 1615-23.

114. Song, T.; Qiu, Z.-Y.; Cui, F.-Z., Biomaterials for reconstruction of cranial defects. *Front. Mater. Sci.* **2015,** *9*, 346-354.
115. Betz, R. R.; Lavelle, W. F.; Samdani, A. F., Bone grafting options in children. *Spine (Phila Pa 1976)* **2010,** *35* (17), 1648-54.
116. Tessier, P.; Kawamoto, H.; Matthews, D.; Posnick, J.; Raulo, Y.; Tulasne, J. F.; Wolfe, S. A., Autogenous bone grafts and bone substitutes—tools and techniques: I. A 20,000-case experience in maxillofacial and craniofacial surgery. *Plast. Reconstr. Surg.* **2005,** *116* (5), 6S-24S.
117. Lee, S. H.; Yoo, C. J.; Lee, U.; Park, C. W.; Lee, S. G.; Kim, W. K., Resorption of autogenous bone graft in cranioplasty: Resorption and reintegration failure. *Korean J. Neurotrauma* **2014,** *10*, 10-14.
118. Moreira-Gonzalez, A. J., I. T.; Miyawaki, T.; Barakat, K.; DiNick, V. , Clinical outcome in cranioplasty: critical review in longterm follow-up. *J. Craniofac. Surg.* **2003,** *14*, 144-153.
119. Grant, G. A.; Jolley, M.; Ellenbogen, R. G.; Roberts, T. S.; Gruss, J. R.; Loeser, J. D., Failure of autologous bone—assisted cranioplasty following decompressive craniectomy in children and adolescents. *J. Neurosurg. Pediatrics* **2004,** *100*, 163-168.
120. Szpalski, C.; Barr, J.; Wetterau, M.; Saadeh, P. B.; Warren, S. M., Cranial bone defects: current and future strategies. *Neurosurg. Focus* **2010,** *29* (6), E8.
121. Pryor, L. S.; Gage, E.; Langevin, C.-J.; Herrera, F.; Breithaupt, A. D.; Gordon, C. R.; Afifi, A. M.; Zins, J. E.; Meltzer, H.; Gosman, A.; Cohen, S. R.; Holmes, R., Review of bone substitutes. *Craniomaxillofac. Trauma Reconstr.* **2009,** *2* (3), 151-160.
122. Arora, M.; Chan, E. K.; Gupta, S.; Diwan, A. D., Polymethylmethacrylate bone cements and additives: A review of the literature. *World J. Orthop.* **2013,** *4*, 67-74.
123. Kenny, S. M.; Buggy, M., Bone cements and fillers: A review. *J. Mater. Sci. Mater. Med.* **2003,** *14*, 923-938.
124. Magnan, B.; Bondi, M.; Maluta, T.; Samaila, E.; Schirru, L.; Dall'Oca, C., Acrylic bone cement: current concept review. *Musculoskelet. Surg.* **2013,** *97* (2), 93-100.
125. Giannoudis, P. V.; Dinopoulos, H.; Tsiridis, E., Bone substitutes: An update. *Injury* **2005,** *36S*, S20-S27.
126. Rammos, C. K.; Cayci, C.; Castro-Garcia, J. A.; Feiz-Erfan, I.; Lettieri, S. C., Patient-specific polyetheretherketone implants for repair of craniofacial defects. *J. Craniofac. Surg.* **2015,** *26* (3), 631-633.
127. Zegers, T.; ter Laak-Poort, M.; Koper, D.; Lethaus, B.; Kessler, P., The therapeutic effect of patient-specific implants in cranioplasty. *J. Craniomaxillofac. Surg* **2017,** *45* (1), 82-86.
128. Alonso-Rodriguez, E.; Cebrián, J. L.; Nieto, M. J.; Del Castillo, J. L.; Hernández-Godoy, J.; Burgueño, M., Polyetheretherketone custom-made implants for craniofacial defects: Report of 14 cases and review of the literature. *J. Craniomaxillofac. Surg* **2015,** *43* (7), 1232-1238.

129. Bonda, D. J.; Manjila, S.; Selman, W. R.; Dean, D., The recent revolution in the design and manufacture of cranial implants: Modern advancements and future directions. *Neurosurgery* **2015,** *77* (5), 814-824.

130. Guevara-Rojas, G.; Figl, M.; Schicho, K.; Seemann, R.; Traxler, H.; Vacariu, A.; Carbon, C.-C.; Ewers, R.; Watzinger, F., Patient-specific polyetheretherketone facial implants in a computer-aided planning workflow. *J. Oral Maxillofac. Surg.* **2014,** *72* (9), 1801-1812.

131. Alsberg, E.; Hill, E. E.; Mooney, D. J., Craniofacial tissue engineering. *Crit. Rev. Oral Biol. Med.* **2001,** *12*, 64-75.

132. Petrovic, V.; Zivkovic, P.; Petrovic, D.; Stefanovi, V., Craniofacial bone tissue engineering. *Oral Surg. Oral Med. Oral Pathol. Oral Radiol.* **2012,** *114* (3).

133. Abdulghani, S.; Mitchell, G. R., Biomaterials for *in situ* tissue regeneration: A review. *Biomolecules* **2019,** *9*, 750

134. Dias, J. R.; Ribeiro, N.; Baptista-Silva, S.; Costa-Pinto, A. R.; Alves, N.; Oliveira, A. L., *In situ* enabling approaches for tissue regeneration: Current challenges and new developments. *Front. Bioeng. Biotechnol.* **2020,** *8*, 85.

135. Grunlan, M. A.; Zhang, D.; Schoener, C. A.; Saunders, W. B. Shape memory polymer scaffolds for tissue defects. US 9925297, March 27, 2018.

136. Bružauskaitė, I.; Bironaitė, D.; Bagdonas, E.; Bernotienė, E., Scaffolds and cells for tissue regeneration: different scaffold pore sizes different cell effects. *Cytotechnology* **2016,** *68*, 355-369.

137. Zhang, D.; Petersen, K. M.; Grunlan, M. A., Inorganic–Organic Shape Memory Polymer (SMP) Foams with Highly Tunable Properties. *ACS Appl. Mater. Interfaces* **2013,** *5* (1), 186-191.

138. Liu, N.; Lyu, X.; Fan, H.; Shi, J.; Hu, J.; Luo, E., Animal models for craniofacial reconstruction by stem/stromal cells. *Curr. Stem Cell Res. Ther.* **2014,** *9*, 174-186.

139. Spicer, P. P.; Kretlow, J. D.; Young, S.; Jansen, J. A.; Kasper, F. K.; Mikos, A. G., Evaluation of bone regeneration using the rat critical size calvarial defect. *Nat. Protoc.* **2012,** *7* (10), 1918-29.

140. Elsalanty, M. E.; Genecov, D. G., Bone grafts in craniofacial surgery. *Craniomaxillofac. Trauma Reconstr.* **2009,** *2* (3), 125-134.

141. Shang, Q.; Wang, Z.; Liu, W.; Shi, Y.; Cui, L.; Cao, Y., Tissue-engineered bone repair of sheep cranial defects with autologous bone marrow stromal cells. *J. Craniofac. Surg.* **2001,** *12* (6), 586-93; discussion 594-5.

142. He, Y.; Zhang, Z.-Y.; Zhu, H.-G.; Qiu, W.; Jiang, X.; Guo, W., Experimental study on reconstruction of segmental mandible defects using tissue engineered bone combined bone marrow stromal cells with three-dimensional tricalcium phosphate. *J. Craniofac. Surg.* **2007,** *18* (4), 800-805.

143. Fröhlich, M.; Grayson, W. L.; Wan, L. Q.; Marolt, D.; Drobnic, M.; Vunjak-Novakovic, G., Tissue engineered bone grafts: biological requirements, tissue culture and clinical relevance. *Curr. Stem Cell Res. Ther.* **2008,** *3* (4), 254-64.

144. O'Keefe, R. J.; Mao, J., Bone tissue engineering and regeneration: from discovery to the clinic--an overview. *Tissue Eng. Part B Rev.* **2011,** *17* (6), 389-92.

145. Henkel, J.; Woodruff, M. A.; Epari, D. R.; Steck, R.; Glatt, V.; Dickinson, I. C.; Choong, P. F.; Schuetz, M. A.; Hutmacher, D. W., Bone Regeneration Based on Tissue Engineering Conceptions - A 21st Century Perspective. *Bone Res.* **2013,** *1* (3), 216-48.
146. Kinoshita, Y.; Maeda, H., Recent Developments of Functional Scaffolds for Craniomaxillofacial Bone Tissue Engineering Applications. *Sci. World J.* **2013,** *2013*, 863157.
147. Fröhlich, M.; Grayson, W. L.; Wan, L. Q.; Marolt, D.; Drobnic, M.; Vunjak-Novakovic, G., Tissue engineered bone grafts: biological requirements, tissue culture and clinical relevance. *Curr. Stem Cell Res. Ther.* **2008,** *3* (4), 254-64.
148. Karageorgiou, V.; Kaplan, D., Porosity of 3D biomaterial scaffolds and osteogenesis. *Biomaterials* **2005,** *26* (27), 5474-91.
149. Shin, H.; Jo, S.; Mikos, A. G., Biomimetic materials for tissue engineering. *Biomaterials* **2003,** *24* (24), 4353-64.
150. Amini, A. R.; Laurencin, C. T.; Nukavarapu, S. P., Bone tissue engineering: recent advances and challenges. *Crit. Rev. Biomed. Eng.* **2012,** *40* (5), 363-408.
151. Roseti, L.; Parisi, V.; Petretta, M.; Cavallo, C.; Desando, G.; Bartolotti, I.; Grigolo, B., Scaffolds for Bone Tissue Engineering: State of the art and new perspectives. *Mater. Sci. Eng. C Mater. Biol. Appl.* **2017,** *78*, 1246-1262.
152. Polo-Corrales, L.; Latorre-Esteves, M.; Ramirez-Vick, J. E., Scaffold design for bone regeneration. *J. Nanosci. Nanotechnol.* **2014,** *14* (1), 15-56.
153. García-Gareta, E.; Coathup, M. J.; Blunn, G. W., Osteoinduction of bone grafting materials for bone repair and regeneration. *Bone* **2015,** *81*, 112-121.
154. Gaihre, B.; Uswatta, S.; Jayasuriya, A. C., Reconstruction of Craniomaxillofacial Bone Defects Using Tissue-Engineering Strategies with Injectable and Non-Injectable Scaffolds. *J. Funct. Biomater.* **2017,** *8* (4), 49.
155. Lendlein, A.; Schmidt, A. M.; Schroeter, M.; Langer, R., Shape-memory polymer networks from oligo(ϵ-caprolactone)dimethacrylates. *J. Polym. Sci. A Polym. Chem.* **2005,** *43* (7), 1369-1381.
156. Zhang, D.; Burkes, W. L.; Schoener, C. A.; Grunlan, M. A., Porous inorganic-organic shape memory polymers. *Polymer (Guildf)* **2012,** *53* (14), 2935-2941.
157. Woodard, L. N.; Grunlan, M. A., Hydrolytic Degradation of PCL–PLLA Semi-IPNs Exhibiting Rapid, Tunable Degradation. *ACS Biomater. Sci. Eng.* **2019,** *5* (2), 498-508.
158. Pfau, M. R.; McKinzey, K. G.; Roth, A. A.; Grunlan, M. A., PCL-Based Shape Memory Polymer Semi-IPNs: The Role of Miscibility in Tuning the Degradation Rate. *Biomacromolecules* **2020,** *21* (6), 2493-2501.
159. Woodard, L. N.; Page, V. M.; Kmetz, K. T.; Grunlan, M. A., PCL–PLLA Semi-IPN Shape Memory Polymers (SMPs): Degradation and Mechanical Properties. *Macromol. Rapid Commun.* **2016,** *37* (23), 1972-1977.
160. Lee, J. H.; Lee, Y. J.; Cho, H. J.; Shin, H., Guidance of in vitro migration of human mesenchymal stem cells and in vivo guided bone regeneration using aligned electrospun fibers. *Tissue Eng. Part A* **2014,** *20* (15-16), 2031-42.

161. Xu, M.; Zhai, D.; Xia, L.; Li, H.; Chen, S.; Fang, B.; Chang, J.; Wu, C., Hierarchical bioceramic scaffolds with 3D-plotted macropores and mussel-inspired surface nanolayers for stimulating osteogenesis. *Nanoscale* **2016,** *8* (28), 13790-13803.
162. Li, Y.; Yang, W.; Li, X.; Zhang, X.; Wang, C.; Meng, X.; Pei, Y.; Fan, X.; Lan, P.; Wang, C.; Li, X.; Guo, Z., Improving Osteointegration and Osteogenesis of Three-Dimensional Porous Ti6Al4V Scaffolds by Polydopamine-Assisted Biomimetic Hydroxyapatite Coating. *ACS Appl. Mater. Interfaces* **2015,** *7* (10), 5715-5724.
163. Hong, S.; Kim, K. Y.; Wook, H. J.; Park, S. Y.; Lee, K. D.; Lee, D. Y.; Lee, H., Attenuation of the in vivo toxicity of biomaterials by polydopamine surface modification. *Nanomedicine (Lond)* **2011,** *6* (5), 793-801.
164. Ryu, J.; Ku, S. H.; Lee, H.; Park, C. B., Mussel-Inspired Polydopamine Coating as a Universal Route to Hydroxyapatite Crystallization. *Adv. Funct. Mater.* **2010,** *20* (13), 2132-2139.
165. Wu, C.; Han, P.; Liu, X.; Xu, M.; Tian, T.; Chang, J.; Xiao, Y., Mussel-inspired bioceramics with self-assembled Ca-P/polydopamine composite nanolayer: preparation, formation mechanism, improved cellular bioactivity and osteogenic differentiation of bone marrow stromal cells. *Acta Biomater.* **2014,** *10* (1), 428-38.
166. Lee, D. J.; Lee, Y.-T.; Zou, R.; Daniel, R.; Ko, C.-C., Polydopamine-Laced Biomimetic Material Stimulation of Bone Marrow Derived Mesenchymal Stem Cells to Promote Osteogenic Effects. *Sci. Rep.* **2017,** *7* (1), 12984.
167. Rim, N. G.; Kim, S. J.; Shin, Y. M.; Jun, I.; Lim, D. W.; Park, J. H.; Shin, H., Mussel-inspired surface modification of poly(L-lactide) electrospun fibers for modulation of osteogenic differentiation of human mesenchymal stem cells. *Colloids Surf. B Biointerfaces* **2012,** *91*, 189-97.
168. Sharma, D.; Jia, W.; Long, F.; Pati, S.; Chen, Q.; Qyang, Y.; Lee, B.; Choi, C. K.; Zhao, F., Polydopamine and collagen coated micro-grated polydimethylsiloxane for human mesenchymal stem cell culture. *Bioact. Mater.* **2019,** *4*, 142-150.
169. Gonçalves, C. M. B.; Coutinho, J. o. A. P.; Marrucho, I. M., Optical Properties. In *Poly(Lactic Acid)*, 2010; pp 97-112.
170. Elzein, T.; Nasser-Eddine, M.; Delaite, C.; Bistac, S.; Dumas, P., FTIR study of polycaprolactone chain organization at interfaces. *J. Colloid Interface Sci.* **2004,** *273* (2), 381-7.
171. Kokubo, T.; Takadama, H., How useful is SBF in predicting in vivo bone bioactivity? *Biomaterials* **2006,** *27* (15), 2907-2915.
172. Gharat, T. P.; Diaz-Rodriguez, P.; Erndt-Marino, J. D.; Jimenez Vergara, A. C.; Munoz Pinto, D. J.; Bearden, R. N.; Huggins, S. S.; Grunlan, M.; Saunders, W. B.; Hahn, M. S., A canine in vitro model for evaluation of marrow-derived mesenchymal stromal cell-based bone scaffolds. *J. Biomed. Mater. Res. A* **2018,** *106* (9), 2382-2393.
173. Chen, H.; Erndt-Marino, J.; Diaz-Rodriguez, P.; Kulwatno, J.; Jimenez-Vergara, A. C.; Thibeault, S. L.; Hahn, M. S., In vitro evaluation of anti-fibrotic effects of select cytokines for vocal fold scar treatment. *J. Biomed. Mater. Res. Part B Appl. Biomater.* **2019,** *107* (4), 1056-1067.

174. Diaz-Rodriguez, P.; Chen, H.; Erndt-Marino, J. D.; Liu, F.; Totsingan, F.; Gross, R. A.; Hahn, M. S., Impact of Select Sophorolipid Derivatives on Macrophage Polarization and Viability. *ACS Appl. Bio Mater.* **2019,** *2* (1), 601-612.

175. Zangmeister, R. A.; Morris, T. A.; Tarlov, M. J., Characterization of Polydopamine Thin Films Deposited at Short Times by Autoxidation of Dopamine. *Langmuir* **2013,** *29* (27), 8619-8628.

176. Raynaud, S.; Champion, E.; Bernache-Assollant, D.; Laval, J.-P., Determination of Calcium/Phosphorus Atomic Ratio of Calcium Phosphate Apatites Using X-ray Diffractometry. *J. Am. Ceram. Soc.* **2001,** *84* (2), 359-66.

177. Kourkoumelis, N.; Balatsoukas, I.; Tzaphlidou, M., Ca/P concentration ratio at different sites of normal and osteoporotic rabbit bones evaluated by Auger and energy dispersive X-ray spectroscopy. *J. Biol. Phys.* **2012,** *38* (2), 279-291.

178. Chuah, Y. J.; Koh, Y. T.; Lim, K.; Menon, N. V.; Wu, Y.; Kang, Y., Simple surface engineering of polydimethylsiloxane with polydopamine for stabilized mesenchymal stem cell adhesion and multipotency. *Sci. Rep.* **2015,** *5* (1), 18162.

179. Dwivedi, R.; Kumar, S.; Pandey, R.; Mahajan, A.; Nandana, D.; Katti, D. S.; Mehrotra, D., Polycaprolactone as biomaterial for bone scaffolds: Review of literature. *JOBCR* **2020,** *10* (1), 381-388.

180. Boyan, B. D.; Lotz, E. M.; Schwartz, Z., Roughness and Hydrophilicity as Osteogenic Biomimetic Surface Properties. *Tissue Eng. Part A* **2017,** *23* (23-24), 1479-1489.

181. Benoit, D. S. W.; Schwartz, M. P.; Durney, A. R.; Anseth, K. S., Small functional groups for controlled differentiation of hydrogel-encapsulated human mesenchymal stem cells. *Nat. Mater.* **2008,** *7* (10), 816-823.

182. Arabiyat, A. S.; Diaz-Rodriguez, P.; Erndt-Marino, J. D.; Totsingan, F.; Mekala, S.; Gross, R. A.; Hahn, M. S., Effect of Poly(sophorolipid) Functionalization on Human Mesenchymal Stem Cell Osteogenesis and Immunomodulation. *ACS Appl. Bio Mater.* **2019,** *2* (1), 118-126.

183. Curran, J. M.; Chen, R.; Hunt, J. A., The guidance of human mesenchymal stem cell differentiation in vitro by controlled modifications to the cell substrate. *Biomaterials* **2006,** *27* (27), 4783-4793.

184. Frassica, M. T.; Jones, S. K.; Suriboot, J.; Arabiyat, A. S.; Ramirez, E. M.; Culibrk, R. A.; Hahn, M. S.; Grunlan, M. A., Enhanced Osteogenic Potential of Phosphonated-Siloxane Hydrogel Scaffolds. *Biomacromolecules* **2020,** *21* (12), 5189-5199.

185. Yao, Q.; Cosme, J. G. L.; Xu, T.; Miszuk, J. M.; Picciani, P. H. S.; Fong, H.; Sun, H., Three dimensional electrospun PCL/PLA blend nanofibrous scaffolds with significantly improved stem cells osteogenic differentiation and cranial bone formation. *Biomaterials* **2017,** *115*, 115-127.

186. Liu, C.; Li, Y.; Wang, J.; Liu, C.; Liu, W.; Jian, X., Improving Hydrophilicity and Inducing Bone-Like Apatite Formation on PPBES by Polydopamine Coating for Biomedical Application. *Molecules* **2018,** *23* (7).

187. Xu, Y.; Li, H.; Wu, J.; Yang, Q.; Jiang, D.; Qiao, B., Polydopamine-induced hydroxyapatite coating facilitates hydroxyapatite/polyamide 66 implant osteogenesis: an in vitro and in vivo evaluation. *Int. J. Nanomedicine* **2018,** *13,* 8179-8193.
188. Deng, Y.; Yang, W.-Z.; Shi, D.; Wu, M.; Xiong, X.-L.; Chen, Z.-G.; Wei, S.-C., Bioinspired and osteopromotive polydopamine nanoparticle-incorporated fibrous membranes for robust bone regeneration. *NPG Asia Materials* **2019,** *11* (1), 39.
189. Lee, J. S.; Yi, J. K.; An, S. Y.; Heo, J. S., Increased Osteogenic Differentiation of Periodontal Ligament Stem Cells on Polydopamine Film Occurs via Activation of Integrin and PI3K Signaling Pathways. *Cell. Physiol. Biochem.* **2014,** *34* (5), 1824-1834.
190. Chen, S.; Bai, B.; Lee, D. J.; Diachina, S.; Li, Y.; Wong, S. W.; Wang, Z.; Tseng, H. C.; Ko, C.-C., Dopaminergic enhancement of cellular adhesion in bone marrow derived mesenchymal stem cells (MSCs). *Stem Cell Res. Ther.* **2017,** *7* (8), 395.
191. Wang, C.-X.; Ge, X.-Y.; Wang, M.-Y.; Ma, T.; Zhang, Y.; Lin, Y., Dopamine D1 receptor-mediated activation of the ERK signaling pathway is involved in the osteogenic differentiation of bone mesenchymal stem cells. *Stem Cell Res. Ther.* **2020,** *11* (1), 12.
192. Lee, D. J.; Tseng, H. C.; Wong, S. W.; Wang, Z.; Deng, M.; Ko, C.-C., Dopaminergic effects on in vitro osteogenesis. *Bone Res.* **2015,** *3* (1), 15020.
193. Kim, H. K.; Lee, J. S.; Kim, J. H.; Seon, J. K.; Park, K. S.; Jeong, M. H.; Yoon, T. R., Bone-forming peptide-2 derived from BMP-7 enhances osteoblast differentiation from multipotent bone marrow stromal cells and bone formation. *Exp. Mol. Med.* **2017,** *49* (5), e328-e328.
194. Kim, H. K.; Kim, J. H.; Park, D. S.; Park, K. S.; Kang, S. S.; Lee, J. S.; Jeong, M. H.; Yoon, T. R., Osteogenesis induced by a bone forming peptide from the prodomain region of BMP-7. *Biomaterials* **2012,** *33* (29), 7057-7063.
195. Ansari, M.; Golzar, M.; Baghani, M.; Soleimani, M., Shape memory characterization of poly(ε-caprolactone) (PCL)/polyurethane (PU) in combined torsion-tension loading with potential applications in cardiovascular stent. *Polym. Test.* **2018,** *68,* 424-432.
196. Yang, C.-S.; Wu, H.-C.; Sun, J.-S.; Hsiao, H.-M.; Wang, T.-W., Thermo-Induced Shape-Memory PEG-PCL Copolymer as a Dual-Drug-Eluting Biodegradable Stent. *ACS Appl. Mater. Interfaces* **2013,** *5* (21), 10985-10994.
197. Xue, L.; Dai, S.; Li, Z., Biodegradable shape-memory block co-polymers for fast self-expandable stents. *Biomaterials* **2010,** *31* (32), 8132-8140.
198. Jing, X.; Mi, H.-Y.; Huang, H.-X.; Turng, L.-S., Shape memory thermoplastic polyurethane (TPU)/poly(ε-caprolactone) (PCL) blends as self-knotting sutures. *J Mech Behav Biomed Mater* **2016,** *64*, 94-103.
199. Duarah, R.; Singh, Y. P.; Gupta, P.; Mandal, B. B.; Karak, N., Smart self-tightening surgical suture from a tough bio-based hyperbranched polyurethane/reduced carbon dot nanocomposite. *Biomed. Mater.* **2018,** *13* (4), 045004.
200. Sun, H.; Mei, L.; Song, C.; Cui, X.; Wang, P., The in vivo degradation, absorption and excretion of PCL-based implant. *Biomaterials* **2006,** *27* (9), 1735-1740.
201. Doppalapudi, S.; Jain, A.; Khan, W.; Domb, A. J., Biodegradable polymers—an overview. *Polym. Adv. Technol.* **2014,** *25* (5), 427-435.

202. Gunatillake, P.; Mayadunne, R.; Adhikari, R., Recent developments in biodegradable synthetic polymers. *Biotechnol. Annu. Rev.* **2006,** *12*, 301-347.
203. Woodard, L. N.; Grunlan, M. A., Hydrolytic Degradation and Erosion of Polyester Biomaterials. *ACS Macro Lett.* **2018,** *7* (8), 976-982.
204. Imre, B.; Pukánszky, B., Compatibilization in bio-based and biodegradable polymer blends. *Eur. Polym. J.* **2013,** *49* (6), 1215-1233.
205. Luckachan, G. E.; Pillai, C. K. S., Biodegradable Polymers- A Review on Recent Trends and Emerging Perspectives. *J. Polym. Environ.* **2011,** *19* (3), 637-676.
206. Sabir, M. I.; Xu, X.; Li, L., A review on biodegradable polymeric materials for bone tissue engineering applications. *J. Mater. Sci.* **2009,** *44* (21), 5713-5724.
207. Miller, R. A.; Brady, J. M.; Cutright, D. E., Degradation rates of oral resorbable implants (polylactates and polyglycolates): Rate modification with changes in PLA/PGA copolymer ratios. *Journal of Biomedical Materials Research* **1977,** *11* (5), 711-719.
208. Liu, Y.; Bai, X.; Liang, A., Synthesis, Properties, and In Vitro Hydrolytic Degradation of Poly(d,l-lactide-co-glycolide-co-ε-caprolactone). *Int. J. Polym. Sci.* **2016,** *2016*, 1-9.
209. Huang, M.-H.; Li, S.; Vert, M., Synthesis and degradation of PLA–PCL–PLA triblock copolymer prepared by successive polymerization of ε-caprolactone and dl-lactide. *Polymer* **2004,** *45* (26), 8675-8681.
210. Urquijo, J.; Guerrica-Echevarría, G.; Eguiazábal, J. I., Melt processed PLA/PCL blends: Effect of processing method on phase structure, morphology, and mechanical properties. *J. Appl. Polym. Sci.* **2015,** *132* (41).
211. Ostafinska, A.; Fortelny, I.; Nevoralova, M.; Hodan, J.; Kredatusova, J.; Slouf, M., Synergistic effects in mechanical properties of PLA/PCL blends with optimized composition, processing, and morphology. *RSC Adv.* **2015,** *5* (120), 98971-98982.
212. López-Rodríguez, N.; López-Arraiza, A.; Meaurio, E.; Sarasua, J. R., Crystallization, morphology, and mechanical behavior of polylactide/poly(ε-caprolactone) blends. *Polym. Eng. Sci.* **2006,** *46* (9), 1299-1308.
213. Maglio, G.; Migliozzi, A.; Palumbo, R.; Immirzi, B.; Volpe, M. G., Compatibilized poly(ϵ-caprolactone)/poly(L-lactide) blends for biomedical uses. *Macromol. Rapid Commun.* **1999,** *20* (4), 236-238.
214. Chavalitpanya, K.; Phattanarudee, S., Poly(Lactic Acid)/Polycaprolactone Blends Compatibilized with Block Copolymer. *Energy Procedia* **2013,** *34*, 542-548.
215. Vilay, V.; Mariatti, M.; Ahmad, Z.; Pasomsouk, K.; Todo, M., Improvement of microstructures and properties of biodegradable PLLA and PCL blends compatibilized with a triblock copolymer. *Mater. Sci. Eng.* **2010,** *527* (26), 6930-6937.
216. Wang, L.; Ma, W.; Gross, R. A.; McCarthy, S. P., Reactive compatibilization of biodegradable blends of poly(lactic acid) and poly(ε-caprolactone). *Polym. Degrad. Stab.* **1998,** *59* (1), 161-168.
217. Harada, M.; Iida, K.; Okamoto, K.; Hayashi, H.; Hirano, K., Reactive compatibilization of biodegradable poly(lactic acid)/poly(ε-caprolactone) blends with reactive processing agents. *Polym. Eng. Sci.* **2008,** *48* (7), 1359-1368.

218. Tsuji, H.; Ikada, Y., Blends of aliphatic polyesters. II. Hydrolysis of solution-cast blends from poly(L-lactide) and poly(E-caprolactone) in phosphate-buffered solution. *J. Appl. Polym. Sci.* **1998,** *67* (3), 405-415.
219. Kaihara, S.; Matsumura, S.; Mikos, A. G.; Fisher, J. P., Synthesis of poly(L-lactide) and polyglycolide by ring-opening polymerization. *Nat. Protoc.* **2007,** *2* (11), 2767-2771.
220. Pitt, C. G.; Chasalow, F. I.; Hibionada, Y. M.; Klimas, D. M.; Schindler, A., Aliphatic polyesters. I. The degradation of poly(ϵ-caprolactone) in vivo. *J. Appl. Polym. Sci.* **1981,** *26* (11), 3779-3787.
221. Fukushima, K.; Tabuani, D.; Dottori, M.; Armentano, I.; Kenny, J. M.; Camino, G., Effect of temperature and nanoparticle type on hydrolytic degradation of poly(lactic acid) nanocomposites. *Polym. Degrad. Stab.* **2011,** *96* (12), 2120-2129.
222. Cam, D.; Hyon, S.-h.; Ikada, Y., Degradation of high molecular weight poly(l-lactide) in alkaline medium. *Biomaterials* **1995,** *16* (11), 833-843.
223. Gilding, D. K.; Reed, A. M., Biodegradable polymers for use in surgery—polyglycolic/poly(actic acid) homo- and copolymers: 1. *Polymer* **1979,** *20* (12), 1459-1464.
224. von Burkersroda, F.; Schedl, L.; Göpferich, A., Why degradable polymers undergo surface erosion or bulk erosion. *Biomaterials* **2002,** *23* (21), 4221-4231.
225. Arias, V.; Höglund, A.; Odelius, K.; Albertsson, A.-C., Tuning the Degradation Profiles of Poly(l-lactide)-Based Materials through Miscibility. *Biomacromolecules* **2014,** *15* (1), 391-402.
226. Lyu, S.-P.; Bates, F. S.; Macosko, C. W., Coalescence in polymer blends during shearing. *AIChE Journal* **2000,** *46* (2), 229-238.
227. Van Hemelrijck, E.; Van Puyvelde, P.; Velankar, S.; Macosko, C. W.; Moldenaers, P., Interfacial elasticity and coalescence suppression in compatibilized polymer blends. *J. Rheol.* **2003,** *48* (1), 143-158.
228. Lazzari, S.; Codari, F.; Storti, G.; Morbidelli, M.; Moscatelli, D., Modeling the pH-dependent PLA oligomer degradation kinetics. *Polym. Degrad. Stabil.* **2014,** *110,* 80-90.
229. Jung, J. H.; Ree, M.; Kim, H., Acid- and base-catalyzed hydrolyses of aliphatic polycarbonates and polyesters. *Catal. Today* **2006,** *115* (1), 283-287.
230. Parithimarkalaignan, S.; Padmanabhan, T. V., Osseointegration: an update. *J. Indian Prosthodont. Soc.* **2013,** *13* (1), 2-6.
231. Doi, K.; Kubo, T.; Makihara, Y.; Oue, H.; Morita, K.; Oki, Y.; Kajihara, S.; Tsuga, K., Osseointegration aspects of placed implant in bone reconstruction with newly developed block-type interconnected porous calcium hydroxyapatite. *J. Appl. Oral Sci.* **2016,** *24* (4), 325-331.
232. Phillips, J. H.; Rahn, B. A., Fixation effects on membranous and endochondral onlay bone graft revascularization and bone deposition. *Plast. Reconstr. Surg.* **1990,** *85* (6), 891-897.
233. Moghadam, H. G., Vertical and Horizontal Bone Augmentation with the Intraoral Autogenous J-Graft. *Implant Dent.* **2009,** *18* (3).

234. Shah, A. M.; Jung, H.; Skirboll, S., Materials used in cranioplasty: a history and analysis. *Neurosurg. Focus* **2014,** *36* (4), E19.
235. Haleem, A.; Javaid, M., Polyether ether ketone (PEEK) and its 3D printed implants applications in medical field: An overview. *Clin. Epidemiol. Glob. Health* **2019,** *7* (4), 571-577.
236. Park, S.-H.; Gil, E. S.; Kim, H. J.; Lee, K.; Kaplan, D. L., Relationships between degradability of silk scaffolds and osteogenesis. *Biomaterials* **2010,** *31* (24), 6162-6172.
237. Langer, R.; Tirrell, D. A., Designing materials for biology and medicine. *Nature* **2004,** *428* (6982), 487-492.
238. Bose, S.; Roy, M.; Bandyopadhyay, A., Recent advances in bone tissue engineering scaffolds. *Trends Biotechnol.* **2012,** *30* (10), 546-554.
239. Wu, W.; Wang, W.; Li, J., Star polymers: Advances in biomedical applications. *Prog. Polym. Sci.* **2015,** *46*, 55-85.
240. Jahandideh, A.; Muthukumarappan, K., Star-shaped lactic acid based systems and their thermosetting resins; synthesis, characterization, potential opportunities and drawbacks. *Eur. Polym. J.* **2017,** *87*, 360-379.
241. Michalski, A.; Brzezinski, M.; Lapienis, G.; Biela, T., Star-shaped and branched polylactides: Synthesis, characterization, and properties. *Prog. Polym. Sci.* **2019,** *89*, 159-212.
242. Li, Y.; Kissel, T., Synthesis, characteristics and in vitro degradation of star-block copolymers consisting of l-lactide, glycolide and branched multi-arm poly(ethylene oxide). *Polymer* **1998,** *39* (18), 4421-4427.
243. Kim, E. S.; Kim, B. C.; Kim, S. H., Structural effect of linear and star-shaped poly(L-lactic acid) on physical properties. *J. Polym. Sci. B Polym. Phys.* **2004,** *42* (6), 939-946.
244. Ghoorchian, A.; Holland, N. B., Molecular Architecture Influences the Thermally Induced Aggregation Behavior of Elastin-like Polypeptides. *Biomacromolecules* **2011,** *12* (11), 4022-4029.
245. Breitenbach, A.; Li, Y. X.; Kissel, T., Branched biodegradable polyesters for parenteral drug delivery systems. *J. Control Release* **2000,** *64* (1-3), 167-78.
246. Burke, J.; Donno, R.; d'Arcy, R.; Cartmell, S.; Tirelli, N., The Effect of Branching (Star Architecture) on Poly(d,l-lactide) (PDLLA) Degradation and Drug Delivery. *Biomacromolecules* **2017,** *18* (3), 728-739.
247. Atthoff, B.; Trollsås, M.; Claesson, H.; Hedrick, J. L., Poly(lactides) with controlled molecular architecture initiated from hydroxyl functional dendrimers and the effect on the hydrodynamic volume. *Macromol. Chem. Phys.* **1999,** *200* (6), 1333-1339.
248. Huang, C.-F.; Kuo, S.-W.; Lin, H.-C.; Chen, J.-K.; Chen, Y.-K.; Xu, H.; Chang, F.-C., Thermal properties, miscibility and specific interactions in comparison of linear and star poly(methyl methacrylate) blend with phenolic. *Polymer* **2004,** *45* (17), 5913-5921.
249. Theodorakis, P. E.; Avgeropoulos, A.; Freire, J. J.; Kosmas, M.; Vlahos, C., Effects of the Chain Architecture on the Miscibility of Symmetric Linear/Linear and Star/Star Polymer Blends. *Macromolecules* **2006,** *39* (12), 4235-4239.

250. Singh, C.; Balazs, A. C., Effect of polymer architecture on the miscibility of polymer/clay mixtures. *Polym. Int.* **2000,** *49* (5), 469-471.

251. Bian, X.; Zhang, B.; Sun, B.; Sun, Z.; Xiang, S.; Li, G.; Chen, X., Preparation of high toughness and high transparency polylactide blends resin based on multiarmed polycaprolactone-block-poly(l-lactide). *Polym. Eng. Sci.* **2016,** *56* (10), 1125-1137.

252. Mauck, S. C.; Wang, S.; Ding, W.; Rohde, B. J.; Fortune, C. K.; Yang, G.; Ahn, S.-K.; Robertson, M. L., Biorenewable Tough Blends of Polylactide and Acrylated Epoxidized Soybean Oil Compatibilized by a Polylactide Star Polymer. *Macromolecules* **2016,** *49* (5), 1605-1615.

253. Lu, Y.; An, L.; Wang, Z.-G., Intrinsic Viscosity of Polymers: General Theory Based on a Partially Permeable Sphere Model. *Macromolecules* **2013,** *46* (14), 5731-5740.

254. Douglas, J. F.; Roovers, J.; Freed, K. F., Characterization of branching architecture through "universal" ratios of polymer solution properties. *Macromolecules* **1990,** *23* (18), 4168-4180.

255. Zong, C.; Xue, D.; Yuan, W.; Wang, W.; Shen, D.; Tong, X.; Shi, D.; Liu, L.; Zheng, Q.; Gao, C.; Wang, J., Reconstruction of rat calvarial defects with human mesenchymal stem cells and osteoblast-like cells in poly-lactic-co-glycolic acid scaffolds. *Eur. Cell Mater.* **2010,** *20*, 109-20.

256. Shirakata, Y.; Nakamura, T.; Shinohara, Y.; Taniyama, K.; Sakoda, K.; Yoshimoto, T.; Noguchi, K., An exploratory study on the efficacy of rat dedifferentiated fat cells (rDFATs) with a poly lactic-co-glycolic acid/hydroxylapatite (PLGA/HA) composite for bone formation in a rat calvarial defect model. *J. Mater. Sci. Mater. Med.* **2014,** *25* (3), 899-908.

257. Wierzbicki, M. A.; Bryant, J.; Miller, M. W.; Keller, B.; Maitland, D. J., Mechanical and in vitro evaluation of an experimental canine patent ductus arteriosus occlusion device. *J. Mech. Behav. Biomed. Mater.* **2016,** *59*, 156-167.

258. Abbasi, N.; Hamlet, S.; Love, R. M.; Nguyen, N.-T., Porous scaffolds for bone regeneration. *J. Sci-Adv. Mater. Dev.* **2020,** *5* (1), 1-9.

259. Velasco, M. A.; Narváez-Tovar, C. A.; Garzón-Alvarado, D. A., Design, materials, and mechanobiology of biodegradable scaffolds for bone tissue engineering. *Biomed. Res. Int.* **2015,** *2015*, 729076-729076.

260. Bosch, C.; Melsen, B.; Vargervik, K., Importance of the critical-size bone defect in testing bone-regenerating materials. *J. Craniofac. Surg.* **1998,** *9* (4), 310-316.

261. Janik, H.; Marzec, M., A review: fabrication of porous polyurethane scaffolds. *Mat. Sci. Eng. C-Mater.* **2015,** *48*, 586-591.

262. Chan, B. P.; Leong, K. W., Scaffolding in tissue engineering: general approaches and tissue-specific considerations. *Eur. Spine J.* **2008,** *17 Suppl 4* (Suppl 4), 467-479.

263. Nguyen, P. K.; Baek, K.; Deng, F.; Criscione, J. D.; Tuan, R. S.; Kuo, C. K., 2.6.5 - Tendon Tissue-Engineering Scaffolds. In *Biomaterials Science (Fourth Edition)*, Wagner, W. R.; Sakiyama-Elbert, S. E.; Zhang, G.; Yaszemski, M. J., Eds. Academic Press: 2020; pp 1351-1371.

264. Mistry, A. S.; Pham, Q. P.; Schouten, C.; Yeh, T.; Christenson, E. M.; Mikos, A. G.; Jansen, J. A., In vivo bone biocompatibility and degradation of porous fumarate-

based polymer/alumoxane nanocomposites for bone tissue engineering. *J. Biomed. Mater. Res. A* **2010,** *92* (2), 451-462.
265. He, S.; Timmer, M. D.; Yaszemski, M. J.; Yasko, A. W.; Engel, P. S.; Mikos, A. G., Synthesis of biodegradable poly(propylene fumarate) networks with poly(propylene fumarate)–diacrylate macromers as crosslinking agents and characterization of their degradation products. *Polymer* **2001,** *42* (3), 1251-1260.
266. Timmer, M. D.; Ambrose, C. G.; Mikos, A. G., In vitro degradation of polymeric networks of poly(propylene fumarate) and the crosslinking macromer poly(propylene fumarate)-diacrylate. *Biomaterials* **2003,** *24* (4), 571-577.
267. Timmer, M. D.; Horch, R. A.; Ambrose, C. G.; Mikos, A. G., Effect of physiological temperature on the mechanical properties and network structure of biodegradable poly(propylene fumarate)-based networks. *J. Biomater. Sci. Polym. Ed.* **2003,** *14* (4), 369-382.
268. Le Fer, G.; Luo, Y.; Becker, M. L., Poly(propylene fumarate) stars, using architecture to reduce the viscosity of 3D printable resins. *Polym. Chem.* **2019,** *10* (34), 4655-4664.
269. Timmer, M. D.; Carter, C.; Ambrose, C. G.; Mikos, A. G., Fabrication of poly(propylene fumarate)-based orthopaedic implants by photo-crosslinking through transparent silicone molds. *Biomaterials* **2003,** *24* (25), 4707-4714.
270. Peter, S. J.; Kim, P.; Yasko, A. W.; Yaszemski, M. J.; Mikos, A. G., Crosslinking characteristics of an injectable poly(propylene fumarate)/β-tricalcium phosphate paste and mechanical properties of the crosslinked composite for use as a biodegradable bone cement. *J. Biomed. Mater. Res.* **1999,** *44* (3), 314-321.
271. Gresser, J. D.; Hsu, S.-H.; Nagaoka, H.; Lyons, C. M.; Nieratko, D. P.; Wise, D. L.; Barabino, G. A.; Trantolo, D. J., Analysis of a vinyl pyrrolidone/poly(propylene fumarate) resorbable bone cement. *J. Biomed. Mater. Res.* **1995,** *29* (10), 1241-1247.
272. Chang, C.-H.; Liao, T.-C.; Hsu, Y.-M.; Fang, H.-W.; Chen, C.-C.; Lin, F.-H., A poly(propylene fumarate) – Calcium phosphate based angiogenic injectable bone cement for femoral head osteonecrosis. *Biomaterials* **2010,** *31* (14), 4048-4055.
273. Walker, J. M.; Bodamer, E.; Krebs, O.; Luo, Y.; Kleinfehn, A.; Becker, M. L.; Dean, D., Effect of Chemical and Physical Properties on the In Vitro Degradation of 3D Printed High Resolution Poly(propylene fumarate) Scaffolds. *Biomacromolecules* **2017,** *18* (4), 1419-1425.
274. Lee, K.-W.; Wang, S.; Fox, B. C.; Ritman, E. L.; Yaszemski, M. J.; Lu, L., Poly(propylene fumarate) Bone Tissue Engineering Scaffold Fabrication Using Stereolithography: Effects of Resin Formulations and Laser Parameters. *Biomacromolecules* **2007,** *8* (4), 1077-1084.
275. Alge, D. L.; Bennett, J.; Treasure, T.; Voytik-Harbin, S.; Goebel, W. S.; Chu, T.-M. G., Poly(propylene fumarate) reinforced dicalcium phosphate dihydrate cement composites for bone tissue engineering. *J. Biomed. Mater. Res. A* **2012,** *100A* (7), 1792-1802.
276. Jo, S.; Shin, H.; Shung, A. K.; Fisher, J. P.; Mikos, A. G., Synthesis and Characterization of Oligo(poly(ethylene glycol) fumarate) Macromer. *Macromolecules* **2001,** *34* (9), 2839-2844.

277. Temenoff, J. S.; Athanasiou, K. A.; Lebaron, R. G.; Mikos, A. G., Effect of poly(ethylene glycol) molecular weight on tensile and swelling properties of oligo(poly(ethylene glycol) fumarate) hydrogels for cartilage tissue engineering. *J. Biomed. Mater. Res.* **2002,** *59* (3), 429-437.
278. Liu, X.; Miller, A. L., 2nd; Waletzki, B. E.; Yaszemski, M. J.; Lu, L., Novel biodegradable poly(propylene fumarate)-co-poly(l-lactic acid) porous scaffolds fabricated by phase separation for tissue engineering applications. *RSC Adv.* **2015,** *5* (27), 21301-21309.
279. Brett Runge, M.; Dadsetan, M.; Baltrusaitis, J.; Knight, A. M.; Ruesink, T.; Lazcano, E. A.; Lu, L.; Windebank, A. J.; Yaszemski, M. J., The development of electrically conductive polycaprolactone fumarate–polypyrrole composite materials for nerve regeneration. *Biomaterials* **2010,** *31* (23), 5916-5926.
280. Moroder, P.; Runge, M. B.; Wang, H.; Ruesink, T.; Lu, L.; Spinner, R. J.; Windebank, A. J.; Yaszemski, M. J., Material properties and electrical stimulation regimens of polycaprolactone fumarate–polypyrrole scaffolds as potential conductive nerve conduits. *Acta Biomater.* **2011,** *7* (3), 944-953.
281. Ajji, A.; Utracki, L. A., Interphase and compatibilization of polymer blends. *Polym. Eng. Sci.* **1996,** *36* (12), 1574-1585.
282. Aparna, S.; Purnima, D.; Adusumalli, R. B., Review on Various Compatibilizers and its Effect on Mechanical Properties of Compatibilized Nylon Blends. *Polym. Plast. Technol. Eng.* **2017,** *56* (6), 617-634.
283. Utracki, L. A., Compatibilization of Polymer Blends. *Can. J. Chem. Eng.* **2002,** *80* (6), 1008-1016.
284. Luo, Y.; Dolder, C. K.; Walker, J. M.; Mishra, R.; Dean, D.; Becker, M. L., Synthesis and Biological Evaluation of Well-Defined Poly(propylene fumarate) Oligomers and Their Use in 3D Printed Scaffolds. *Biomacromolecules* **2016,** *17* (2), 690-697.
285. DiCiccio, A. M.; Coates, G. W., Ring-Opening Copolymerization of Maleic Anhydride with Epoxides: A Chain-Growth Approach to Unsaturated Polyesters. *J. Am. Chem. Soc.* **2011,** *133* (28), 10724-10727.
286. Chang, B.; Song, W.; Han, T.; Yan, J.; Li, F.; Zhao, L.; Kou, H.; Zhang, Y., Influence of pore size of porous titanium fabricated by vacuum diffusion bonding of titanium meshes on cell penetration and bone ingrowth. *Acta Biomater.* **2016,** *33*, 311-321.
287. Takahashi, Y.; Tabata, Y., Effect of the fiber diameter and porosity of non-woven PET fabrics on the osteogenic differentiation of mesenchymal stem cells. *J. Biomater. Sci. Polym. Ed.* **2004,** *15* (1), 41-57.
288. Gilardino, M. S.; Chen, E.; Bartlett, S. P., Choice of internal rigid fixation materials in the treatment of facial fractures. *Craniomaxillofac. Trauma Reconstr.* **2009,** *2* (1), 49-60.
289. Gleadall, A.; Pan, J.; Atkinson, H., A simplified theory of crystallisation induced by polymer chain scissions for biodegradable polyesters. *Polym. Degrad. Stabil.* **2012,** *97* (9), 1616-1620.

290. Tsuji, H.; Mizuno, A.; Ikada, Y., Properties and morphology of poly(L-lactide). III. Effects of initial crystallinity on long-term in vitro hydrolysis of high molecular weight poly(L-lactide) film in phosphate-buffered solution. *J. Appl. Polym. Sci.* **2000,** *77* (7), 1452-1464.

291. Suresh, K.; Chandrashekara, S., Sample size estimation and power analysis for clinical research studies. *J. Hum. Reprod. Sci.* **2012,** *5* (1), 7-13.

292. Lee, K. G.; Lee, K. S.; Kang, Y. J.; Hwang, J. H.; Lee, S. H.; Park, S. H.; Park, Y.; Cho, Y. S.; Lee, B. K., Rabbit Calvarial Defect Model for Customized 3D-Printed Bone Grafts. *Tissue Eng. Part C Methods* **2018,** *24* (5), 255-262.

293. Lee, S. H.; Lee, K. G.; Hwang, J. H.; Cho, Y. S.; Lee, K. S.; Jeong, H. J.; Park, S. H.; Park, Y.; Cho, Y. S.; Lee, B. K., Evaluation of mechanical strength and bone regeneration ability of 3D printed kagome-structure scaffold using rabbit calvarial defect model. *Mater. Sci. Eng. C Mater. Biol. Appl.* **2019,** *98*, 949-959.

294. Pattnaik, S.; Subramanyam, V. R.; Bapaji, M.; Kole, C. R., Antibacterial and antifungal activity of aromatic constituents of essential oils. *Microbios.* **1997,** *89* (358), 39-46.

295. Kricheldorf, H. R.; Boettcher, C., Polylactones, 24. Polymerizations of racemic and meso-D,L-lactide with Al□O initiators. Analyses of stereosequences. *Macromol. Chem. Phys.* **1993,** *194* (6), 1653-1664.

296. Trombetta, D.; Castelli, F.; Sarpietro, M. G.; Venuti, V.; Cristani, M.; Daniele, C.; Saija, A.; Mazzanti, G.; Bisignano, G., Mechanisms of antibacterial action of three monoterpenes. *Antimicrob. Agents Chemother.* **2005,** *49* (6), 2474-2478.

297. Wang, X.; Fang, L.; Wang, S.; Chen, Y.; Ma, H.; Zhao, H.; Xie, Z., Antibiotic treatment regimens for bone infection after debridement: a study of 902 cases. *BMC Musculoskelet. Disord.* **2020,** *21* (1), 215-215.

298. Sendi, P.; Zimmerli, W., Antimicrobial treatment concepts for orthopaedic device-related infection. *Clin. Microbiol. Infect.* **2012,** *18* (12), 1176-84.

299. Di Giulio, M.; Zappacosta, R.; Di Lodovico, S.; Di Campli, E.; Siani, G.; Fontana, A.; Cellini, L., Antimicrobial and Antibiofilm Efficacy of Graphene Oxide against Chronic Wound Microorganisms. *Antimicrob. Agents Chemother.* **2018,** *62* (7), e00547-18.

300. Aunkor, M. T. H.; Raihan, T.; Prodhan, S. H.; Metselaar, H. S. C.; Malik, S. U. F.; Azad, A. K., Antibacterial activity of graphene oxide nanosheet against multidrug resistant superbugs isolated from infected patients. *R. Soc. Open Sci.* **2020,** *7* (7), 200640.

301. Kang, Y.; Wang, C.; Shi, X.; Zhang, G.; Chen, P.; Wang, J., Crystallization, rheology behavior, and antibacterial application of graphene oxide-graft-poly (l-lactide)/poly (l-lactide) nanocomposites. *Appl. Surf. Sci.* **2018,** *451*, 315-324.

302. Smith, A. T.; LaChance, A. M.; Zeng, S.; Liu, B.; Sun, L., Synthesis, properties, and applications of graphene oxide/reduced graphene oxide and their nanocomposites. *NMS* **2019,** *1* (1), 31-47.

303. Thangamuthu, M.; Hsieh, K. Y.; Kumar, P. V.; Chen, G.-Y., Graphene- and Graphene Oxide-Based Nanocomposite Platforms for Electrochemical Biosensing Applications. *Int. J. Mol. Sci.* **2019,** *20* (12), 2975.

304. Sohn, J.; Lin, H.; Fritch, M. R.; Tuan, R. S., Influence of cholesterol/caveolin-1/caveolae homeostasis on membrane properties and substrate adhesion characteristics of adult human mesenchymal stem cells. *Stem Cell Res. Ther.* **2018,** *9* (1), 86.

APPENDIX A

MACROMER SCHEMES AND ^{1}H NMR

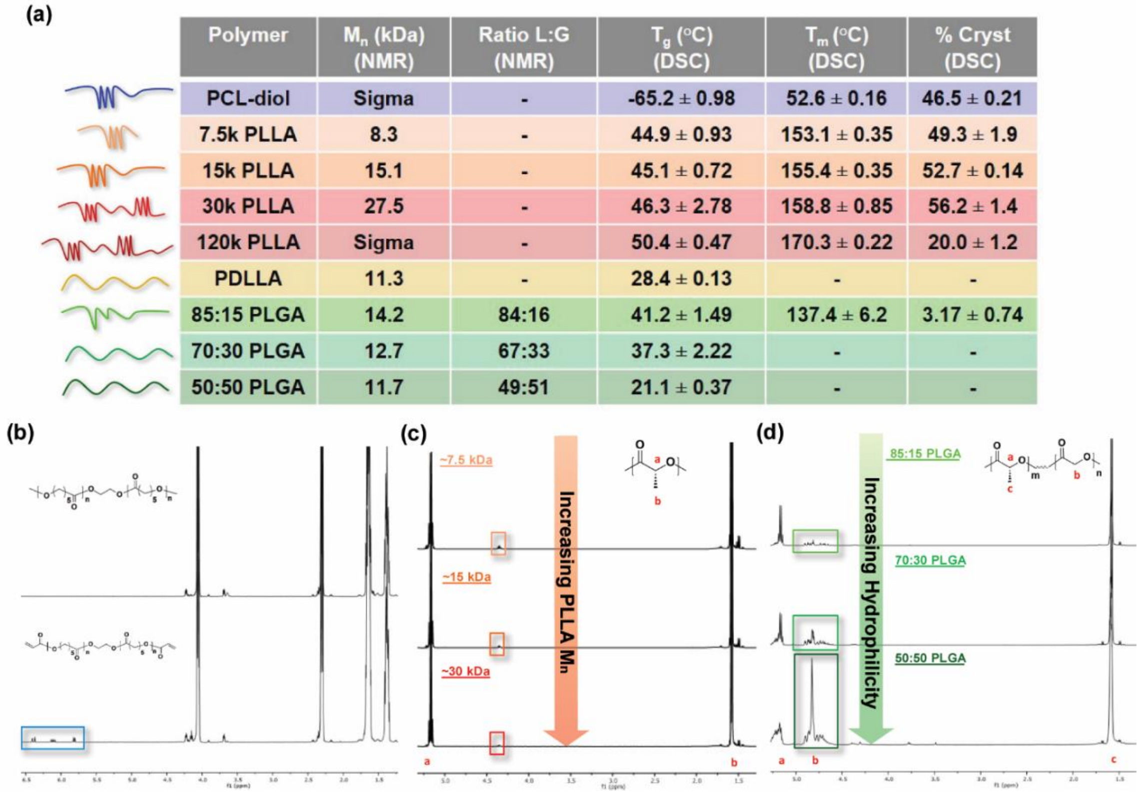

(a)

Polymer	M_n (kDa) (NMR)	Ratio L:G (NMR)	T_g (°C) (DSC)	T_m (°C) (DSC)	% Cryst (DSC)
PCL-diol	Sigma	-	-65.2 ± 0.98	52.6 ± 0.16	46.5 ± 0.21
7.5k PLLA	8.3	-	44.9 ± 0.93	153.1 ± 0.35	49.3 ± 1.9
15k PLLA	15.1	-	45.1 ± 0.72	155.4 ± 0.35	52.7 ± 0.14
30k PLLA	27.5	-	46.3 ± 2.78	158.8 ± 0.85	56.2 ± 1.4
120k PLLA	Sigma	-	50.4 ± 0.47	170.3 ± 0.22	20.0 ± 1.2
PDLLA	11.3	-	28.4 ± 0.13	-	-
85:15 PLGA	14.2	84:16	41.2 ± 1.49	137.4 ± 6.2	3.17 ± 0.74
70:30 PLGA	12.7	67:33	37.3 ± 2.22	-	-
50:50 PLGA	11.7	49:51	21.1 ± 0.37	-	-

Figure A-1. NMR and DSC results for each polymer are summarized in the table (a), stacked NMR showing successful acrylation of PCL [acrylate peaks boxed in blue] (b), stacked NMR showing PLLA with increasing M_n [as reference peak, boxed in orange, decreases] (c) and stacked NMR showing PLGAs with increasing glycolide content [boxed in green] (d).

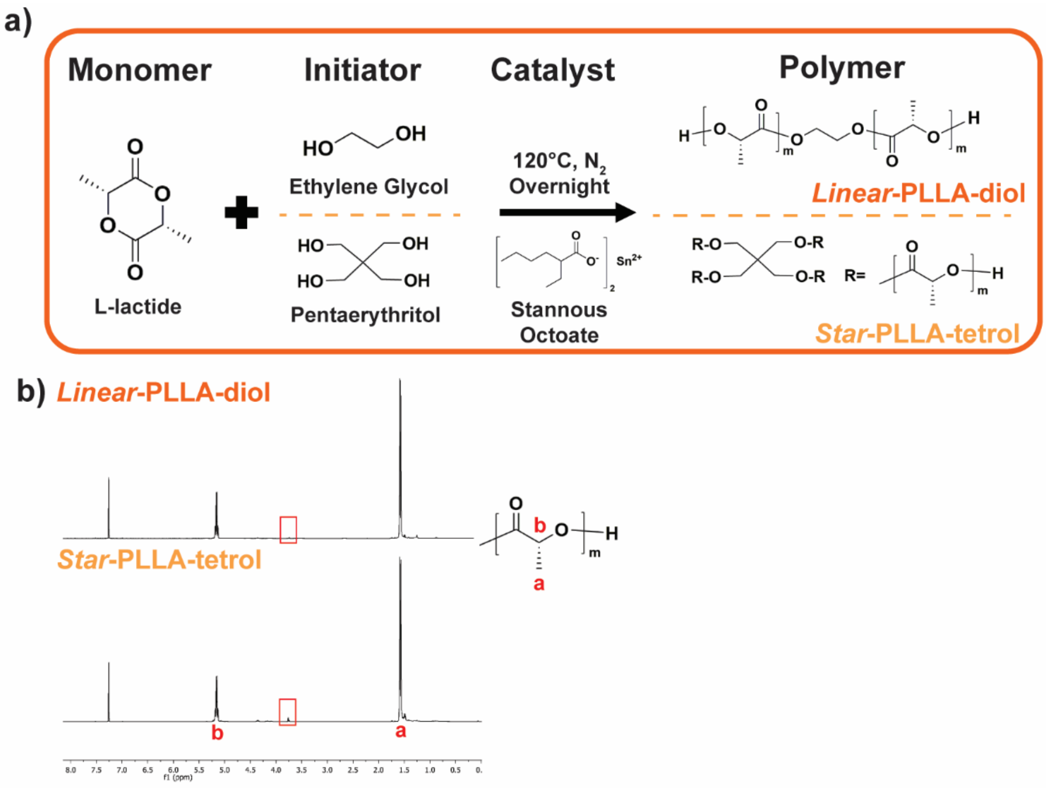

c)

	DSC			NMR
	T_g (°C)	T_m (°C)	% Crystallinity	M_n (kg/mol)
Linear-PLLA-diol	45.1 ± 0.90	155 ± 0.36	49.8 ± 0.56	15.6
Star-PLLA-tetrol	49.2 ± 0.54	152 ± 0.47	15.0 ± 1.9	14.7

Figure A-2. (a) Synthetic scheme for *linear*- and *star*-PLLA. (b) NMR spectra with red boxes to indicate the reference peaks representing the terminal C**H** used to calculate M_n. (c) Summary of thermal properties from DSC and M_n from NMR.

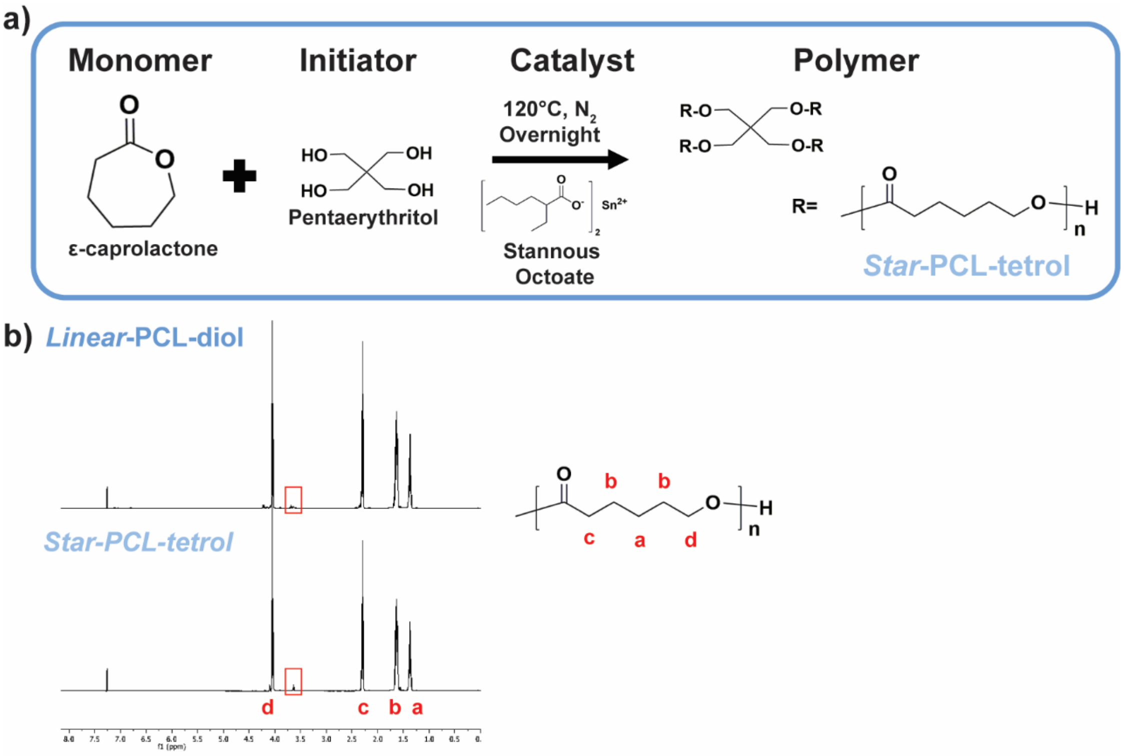

c)

	DSC			NMR
	T_g (°C)	T_m (°C)	% Crystallinity	M_n (kg/mol)
***Linear*-PCL-diol**	**-65.1 ± 0.82**	**52.7 ± 0.16**	**47.7 ± 1.3**	**10.3**
***Star*-PCL-tetrol**	**-63.2 ± 1.2**	**50.0 ± 0.37**	**44.8 ± 1.6**	**10.9**

Figure A-3. (a) Synthetic scheme for *star*-PCL-tetrol. [Note: *linear*-PCL-diol was purchased.] (b) NMR spectra with red boxes to indicate the reference peaks representing terminal CH_2 used to calculate M_n. (c) Summary of thermal properties from DSC and M_n from NMR.

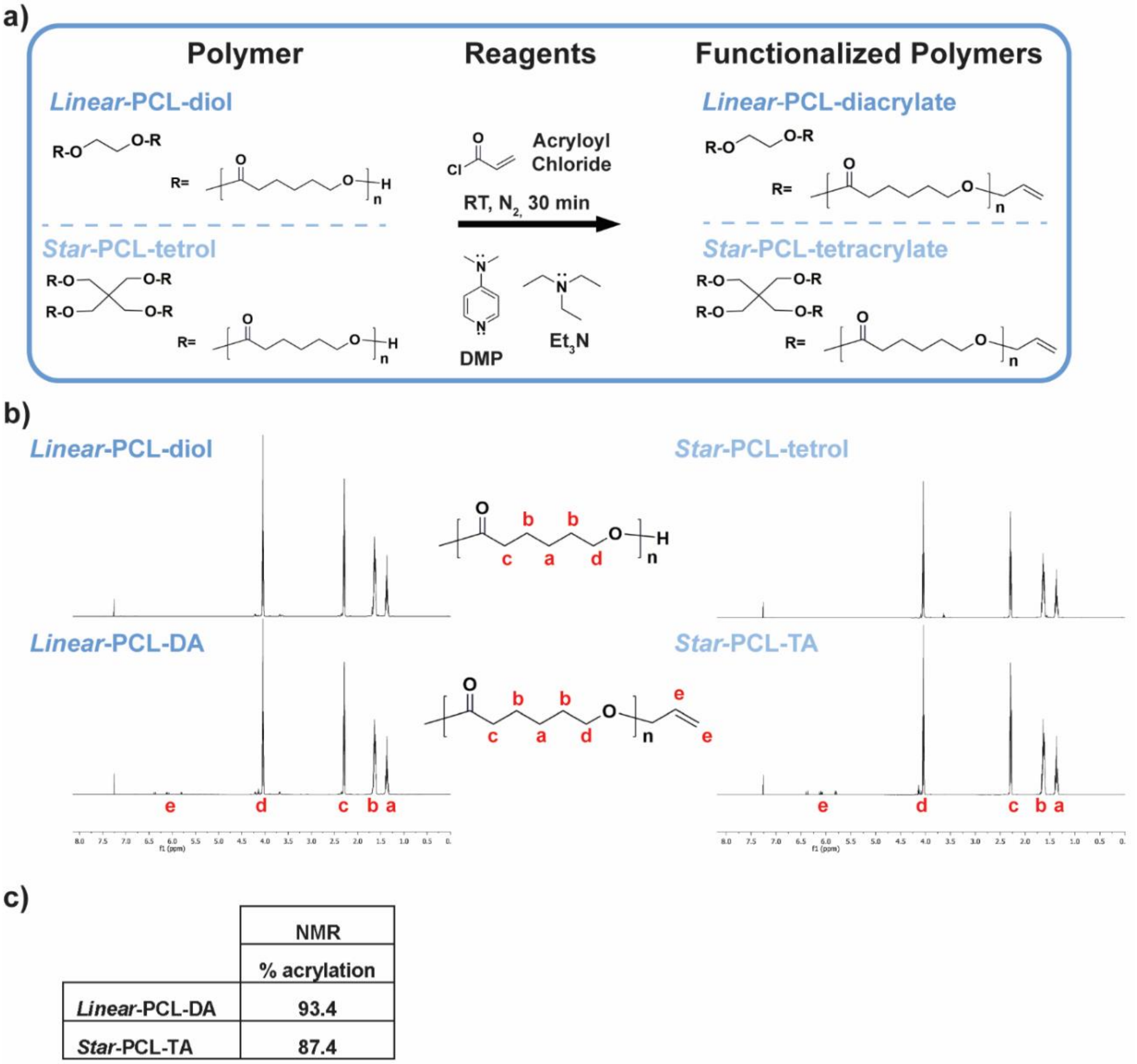

	NMR
	% acrylation
Linear-PCL-DA	93.4
Star-PCL-TA	87.4

Figure A-4. (a) Synthetic scheme for acrylation of *linear*-PCL-diol and *star*-PCL-tetrol. NMR spectra for (b) *linear*-PCL-DA and (c) *star*-PCL-TA. (d) Summary of NMR % acrylation calculations.

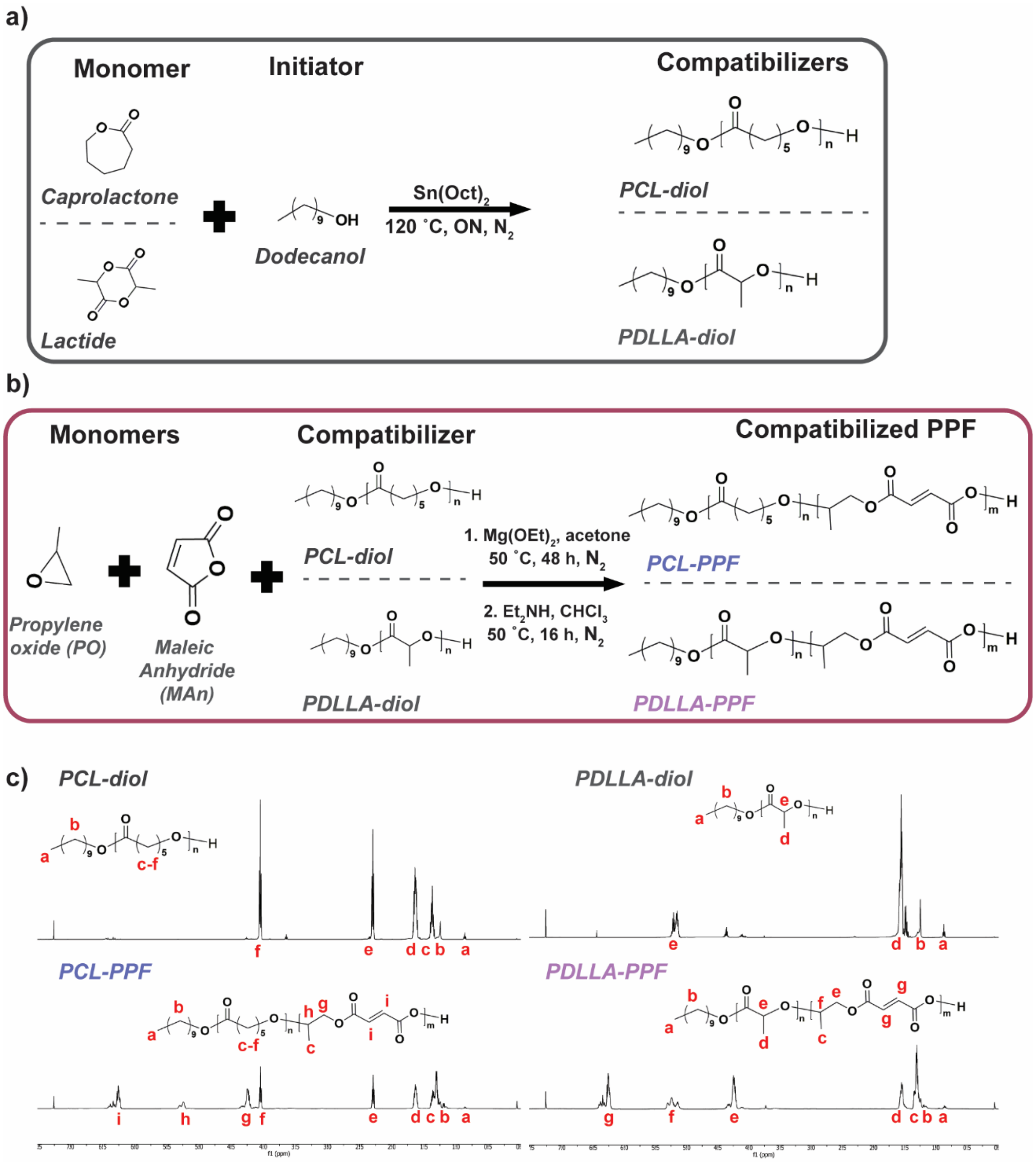

Figure A-5. (a) Synthetic scheme for ROPs of ~3 kg/mol PCL-diol and PDLLA-diol. (b) Schemes for synthesis of compatibilized PPF diblock copolymers: PCL-PPF and PDLLA-PPF. (c) Corresponding NMR spectra are shown.

APPENDIX B

SUPPLEMENTAL TABLES

Table B-1. Bone quantification values for volume corresponding to **Figure 2-10-a.**

	SMP Scaffold	**Untreated Defect**
Group 1	30.85 ± 12.9	34.88 ± 12.1
Group 2	17.56 ± 9.99	31.99 ± 15.9
Group 3	80.56 ± 40.8	87.1 ± 20.6

Table B-2. Bone quantification values for surface area corresponding to **Figure 2-10-b**.

	SMP Scaffold	**Untreated Defect**
Group 1	223.8 ± 44.7	176.5 ± 45.7
Group 2	157.7 ± 49.3	173.8 ± 42.0
Group 3	343.3 ± 55.6	304.6 ± 19.8

Table B-3. Stiffness values and statistical analysis corresponding to **Figure 2-11-a**.

	SMP Scaffold (N/mm)	**PEEK (N/mm)**	**Difference (N/mm)**
Rabbit 17145	247.5	166.4	81.1
Rabbit 17146	208.7	119.2	89.5
		Mean (μ)	85.3 ± 5.9
		p-value	.0313*

Table B-4. Failure load values and statistical analysis corresponding to **Figure 2-11-b**.

	SMP Scaffold (N)	**PEEK (N)**	**Difference (N)**
Rabbit 17145	355.2	267.4	87.8
Rabbit 17146	265.6	181.9	83.7
		Mean (μ)	85.7 ± 2.9
		p-value	.0152*

Table B-5. List of primary antibodies used in western blot analysis.

Antibody	Clone	Dilution	Source
Osterix	M-15-R	1:500	Santa Cruz Biotechnology
RUNX2	SAB2106220	1:1000	Sigma-Aldrich
Osteopontin	Akm2A1	1:500	Santa Cruz Biotechnology
SOX-9	E-9	1:500	Santa Cruz Biotechnology
COL2A1	M2139	1:500	Santa Cruz Biotechnology
COL10A1	E-14	1:2000	Santa Cruz Biotechnology
C/EBP-α	14AA	1:500	Santa Cruz Biotechnology
AFABP	B-4	1:500	Santa Cruz Biotechnology
β-actin	ab8226	1:8000	Abcam

Table B-6. Water uptake (%) and mass loss (%) values for U-PCL-DA, PD-PCL-DA, U-PCL-DA/PLLA, and PD-PCL-DA/PLLA following 14-day incubation at 37 °C in PBS.

	U-PCL-DA	PD-PCL-DA	U-PCL-DA/PLLA	PD-PCL-DA/PLLA
Water Uptake (%)	97.9 ± 0.5	105.5 ± 6.7	118.0 ± 13.4	118.1 ± 12.9
Mass Loss (%)	2.64 ± 0.2	2.2 ± 0.4	3.2 ± 0.4	3.0 ± 0.4

Table B-7. Calcium to phosphorous (Ca/P) ratios obtained from EDS.

	U-PCL-DA	PD-PCL-DA	U-PCL-DA/PLLA	PD-PCL-DA/PLLA
Ca/P	--	2.14 ± 0.13	--	2.00 ± 0.12

. **Table B-8.** Thermal properties of scaffolds.

	PCL			**PLLA**		
	T_m onset (°C)	**T_m midpoint (°C)**	**% Cryst.**	**T_m onset (°C)**	**T_m midpoint (°C)**	**% Cryst.**
L*PCL*	50.5 ± 0.41	56.1 ± 0.56	42.7 ± 1.7	--	--	--
L/L	50.5 ± 0.61	56.6 ± 0.21	42.0 ± 1.9	153.9 ± 1.8	164.0 ± 1.5	37.6 ± 7.3
L/S	51.1 ± 0.27	56.3 ± 0.25	42.5 ± 2.0	152.2 ± 0.84	157.5 ± 0.44	19.5 ± 1.8
S*PCL*	42.6 ± 0.20	49.2 ± 0.02	30.4 ± 3.5	--	--	--
S/L	41.0 ± 0.83	50.0 ± 0.12	33.5 ± 1.6	155.2 ± 0.56	160.0 ± 0.19	23.0 ± 7.1
S/S	39.7 ± 2.0	50.3 ± 0.20	39.2 ± 4.3	147.9 ± 2.2	156.5 ± 0.13	24.7 ± 5.8

Table B-9. Mechanical properties of scaffolds.

	Modulus (MPa)	**Compressive Strength (MPa)**	**Toughness (mJ)**
L*PCL*	9.65 ± 2.8	21.6 ± 4.0	238 ± 74
L/L	23.8 ± 3.6	28.0 ± 5.2	275 ± 66
L/S	17.4 ± 4.2	34.3 ± 6.0	325 ± 61
S*PCL*	3.57 ± 0.58	15.0 ± 3.2	115 ± 25
S/L	11.9 ± 2.3	24.5 ± 7.7	184 ± 45
S/S	11.3 ± 2.4	15.3 ± 6.8	138 ± 58